Spatially Controlled Presentation of Biochemical Ligands on Biomaterial Surfaces Using Comb Polymers

By
Darrell J. Irvine

B.S. Engineering Physics, College of Engineering
B.Phil. Engineering Physics, University Honors College
University of Pittsburgh, 1995

Submitted to the Department of Materials Science and Engineering
in Partial Fulfillment of the Requirements for the Degree of
Doctor of Philosophy in Polymer Science
at the
Massachusetts Institute of Technology

June 2000

Signature Redacted

Signature of Author: _____
Department of Materials Science and Engineering
May 15, 2000

Signature Redacted

Certified by: _____ Signature Redacted
Anne M. Mayes, Associate Professor of Polymer Physics
Linda G. Griffith, Associate Professor of Chemical Engineering
Thesis Supervisors

Signature Redacted

Accepted by: _____
Carl V. Thompson
Stavros Salapatas Professor of Materials Science & Engineering
Chairman, Departmental Committee on Graduate Students

Spatially Controlled Presentation of Biochemical Ligands on Biomaterial Surfaces Using Comb Polymers

By
Darrell J. Irvine

Submitted to the Department of Materials Science and Engineering

On May 15, 2000 in Partial Fulfillment of the Requirements for the Degree of

Doctor of Philosophy in Materials Science and Engineering

ABSTRACT

The mechanisms used by cells to communicate with their environment *in vivo* are being rapidly elucidated due to advances in molecular biology and genetics. Knowledge of the molecular players controlling the information which cells receive from their environment has made possible biomimetic synthetic materials which use natural ECM signals to guide cell behavior. Recent research has demonstrated the feasibility of designing surfaces that eliminate nonspecific cell-materials interactions and signal cells through peptides incorporated at the surface of materials to manipulate a variety of cell functions. The present studies have been undertaken with the objective of *combining the ideal properties of model surfaces, including protein resistance and control of ligand distribution, with flexible surface modification routes that can be directly incorporated in relevant device fabrication processes.*

The agent of surface property modification in this work is an amphiphilic comb polymer designed to provide a hydrophilic polymer brush-like surface layer which resists protein adsorption while simultaneously presenting covalently tethered minimal peptide signals to elicit predictable cell behavior at the surface. We have carried out theoretical and experimental studies of comb polymer systems in order to predict, prepare, and characterize the surface structure of such materials and their influence on cells *in vitro*.

Two theoretical methods were used for predicting the properties of comb polymer surfaces. The first was a Monte Carlo simulation of tethered ligand surface-cell membrane interactions, modeling the interaction of a cell with a tethered ligand surface as a function of the nature of the cell receptor-ligand interactions and the spatial distribution of ligand on the surface. The relative importance of experimental parameters such as receptor-ligand affinity, cluster size, and total ligand density were determined. Under certain conditions, ligand cluster sizes up to a few hundred nanometers in diameter were shown to be effective in increasing the number of receptors bound for a given total ligand density.

The second theoretical tool used was a self-consistent field lattice model for the description of amphiphilic comb polymer and comb polymer/homopolymer blend surface compositions at the water/polymer interface. Surface segregation in a polymer blend is proposed as an effective route to create comb polymer-rich surfaces on biomaterials with desirable bulk properties. Results from the model calculations allowed us to predict the effects of comb architecture and composition on the surface composition of comb/homopolymer blends where the comb polymer is surface segregated to provide a protein-resistant tethered ligand surface. Calculations of comb

polymer-water or blend-water interface structures predict a quasi-two-dimensional organization of the top molecular layer of comb polymer with the backbone aligned parallel to the interface and hydrophilic side chains extended in a brush-like layer into solution.

Experimentally, a comb polymer was synthesized comprised of a hydrophobic backbone of poly(methyl methacrylate), which imparts stability to the comb polymer surface in contact with aqueous solution, and short poly(ethylene glycol) side chains, which provide protein resistance and sites (at the chain ends) for tethering peptides. Optimization of the comb polymer architecture and chemical makeup was performed to maximize resistance of the comb polymer to nonspecific cell interactions with comb surfaces. Comb polymers containing 40-50 wt% of short (6-9 unit) PEG side chains completely resist nonspecific adhesion of a model fibroblast cell line in the presence of 7.5% serum. Regulated cell response to comb polymer surfaces was achieved by tethering peptide ligands at the surface. Differentiation of PC12 neuronal cells was induced using tethered epidermal growth factor, and control of WTNR6 fibroblast adhesion was established via tethered Arg-Gly-Asp (RGD) adhesion peptides.

Incorporation of the comb surface structure on bulk materials of interest for biomedical applications was experimentally achieved by two novel methods: latex film formation and surface segregation. Latex beads, of sizes ranging from 0.2-2 microns were prepared using the comb polymer as a stabilizer during dispersion polymerization. The resulting beads contain a permanent monolayer coverage of the comb at their surface, and films formed by embedding the beads in comb polymer films or coalescing confluent layers of the beads yield surfaces with cell-function-controlling characteristics similar to films of the pure comb polymer. Latexes provide the additional advantage of allowing ligand to be clustered at 0.1 – 1 μm length scales.

Implementation of comb polymer surfaces for biodegradable devices was demonstrated using comb polymer surface segregation in a biodegradable homopolymer matrix. Blends of poly(L-lactide) (PLA) with the comb polymer were annealed in water to drive surface segregation of the comb via its hydrophilic side chains, forming a surface layer enriched in the comb polymer. The surface segregated blend again presents a surface that controls cell function in a manner similar to the pure comb polymer, allowing a spatially variable presentation of peptides on a protein-resistant background.

Control of nanometer-scale clustering of peptides at the surface of comb polymer films, latex films, or surface segregated blends is readily accomplished through functionalization of multiple side chains per ligand-bearing comb. In a study of the adhesion strength of cells on comb surfaces, manipulation of local ligand density by controlling ligand clustering was found to dramatically influence the adhesion of cells on tethered RGD. Cells on clustered RGD showed a strengthening of adhesion for certain ranges of increasing detachment force. Clustering could induce an approximate 3-fold increase in cell adhesion strength at equivalent total densities of RGD at the surface. Strengthening depended on both cluster size and total ligand density in a manner consistent with a model of integrin-based force-dependent signaling. Control of ligand presentation in this manner has implications for the design of biomaterials with engineered, predictable cell responses that can be tailored for specific applications. Comb surfaces may readily present combinations of ligand (such as growth factors and adhesion peptides), for further control over specific cell functions that require a controlled integration of multiple cell inputs.

Taken as a whole, this work presents a facile route for modifying the surface properties of a large variety of biomaterials, using comb polymers to provide a surface structure that specifically directs cell function. Control of ligand distribution through clustering of peptides on these surfaces allows fine-tuning of cell function and we have demonstrated how this parameter plays a significant role in cell adhesion. Comb polymers of this type are inexpensive, readily synthesized, and combined with the several application methods demonstrated here (thin films, latex films, embedded latexes, and surface segregation) provide a flexible means to generate cell-signaling surfaces by a clinically-relevant, practical method which offers more ways to control cell function than any approach yet devised.

Thesis Supervisor:	Anne M. Mayes
Title:	*Associate Professor of Polymer Physics*
Thesis Supervisor:	Linda G. Griffith
Title:	*Associate Professor of Chemical Engineering*

Table of Contents

1 List of Figures and Illustrations

2 List of Tables

3 Acknowledgments

This thesis is dedicated to Professor Anna C. Balazs, who first shared with me such enthusiasm for science and love of this endeavor.

Deep thanks are due my thesis advisors, Professors Anne M. Mayes and Linda G. Griffith. This document is the starting point of what I hope to be an exciting and fruitful career, and for anything that is well done here or in the future, you can surely take credit for teaching me how it was done. I would only lay claim to the mistakes.

To my wife Jennifer, I cannot possibly express adequately my thanks, my joy, or my love. I could not have succeeded without you.

I would like to express heartfelt thanks to the people I've worked with and matured with at MIT. My longtime lab mates Michael Fasolka, Jonathan Hester, Anne-Valerie Ruzette, Philip Soo, Pallab Banerjee, and David Walton made an immeasurable difference in my experience here. I cannot imagine a group of people who could better offer their time to help one another, a laugh when that was needed, or a sympathetic ear.

To my family, I thank you all for your constant support. I owe whatever work ethic I have to the example set by my father, and both my parents for whatever gift for teaching and helping others I have been given. I have to specially thank Kent and Beth Fager for taking me in and allowing their dining room to be occupied by computer equipment for months, feeding me, and getting me to the train!

Several researchers at MIT contributed to the present work. All of the studies of comb polymer-based latexes were done in collaboration with Dr. Pallab Banerjee during his postdoctoral work at MIT. Adhesion strength experiments on clustered ligand comb polymer surfaces were performed by Graduate Research Assistant Lily Koo on surfaces I prepared, without whom such an exhaustive study would not have been feasible. Graduate Research Assistant Terry Johnson carried out experiments performed with the PC12 cell line on tethered EGF surfaces on comb surfaces I prepared. Both Lily and Terry gave generously of their time in

discussions of this work. Graduate Research Assistant Anne-Valerie Ruzette made bulk characterization measurements of PLA/comb polymer blends.

Important technical support was provided in many experiments. Libby Shaw in the MIT Center for Materials Science and Engineering provided careful training and guidance in obtaining atomic force microscopy and ellipsometric data. Yuan Lu supervised collection of XPS data at the Harvard Surface Science Center. Steve Kline, Boualem Hammouda, and Tania Slawecki aided A.-V. Ruzette at the National Institute of Standards and Technology in the collection of SANS data. I am grateful to Professors Chris Scott, Paula Hammond, and Michael Rubner of MIT for access to the rheometer, UV-detector GPC, and contact angle instruments used in this work. Alan Wells of the University of Pittsburgh supplied the fibroblast cell line used throughout these studies.

Financial support was provided by the National Science Foundation through a Graduate Research Fellowship to myself, as well as DMR award number 98-17735. This work was also funded in part by grants from the Whitaker Foundation and the National Institutes of Health. This work made use MRSEC Shared Experimental Facilities supported by the National Science Foundation under award number DMR98-08941.

4 Background and Scope of Thesis

4.1 The Role of Materials in Bioengineering

The design of materials for biotechnological and biomedical uses is being transformed by the application of the signaling principles and components of cells' natural macromolecular environment, the extracellular matrix (ECM), to fundamentally alter the function of cells in contact with biomaterials. These biologically *active* systems are being designed to have surfaces that appear to cells less like foreign entities and more like the ECM proteins and sugars composing native tissue[1, 2]. Advances in such biomimetic materials have led progress in both research and commercial development of drug delivery systems[3-5], prosthetic implant devices[1, 6], hybrid cell-materials *in vivo* and *ex vivo* biomedical devices[2, 7, 8], and *in vitro* assay systems and biosensors[1, 6]. The rapid expansion of research in these areas, especially within the nascent field of tissue engineering, has been made possible by parallel advances in materials science, chemical engineering, and molecular and cell biology, as well as in the training of scientists who have the necessary background to work at the interface of these disparate fields. While the work in this thesis has as its focus the design of materials, it is clearly the recent revolution in understanding of the molecular components of cellular communication that makes such research possible[9].

It is only in recent years (coincident with the unraveling of many unknown aspects of cell function as mentioned above) that research in biomaterials based on a rational scientific rather than an empirical engineering approach has become possible. The current work is motivated by the desire to use a fundamental understanding of cell and molecular biology to design devices that directly interact with cells via their natural routes of communication, to dictate cell functions rather than respond to them. We view this achievement as the first step toward biomaterials which have, literally, dialog with living systems (implying *two-way* communication) to guide cell functions, to provide aid and protection for cells, and to replace lost or damaged cell functions.

4.2 Importance of the Surface of Biomaterials

For the purposes of the following discussion we will define biomaterials as materials used in contact with living systems *in vivo* or *in vitro* that do not originate from a living cell. In the design of biomaterials that can effectively communicate with cells, the surface of these materials plays a pivotal role. In tissue engineering and implant design (with which the current work is most directly connected) the surfaces of artificial materials are placed in contact with the host tissue as an artificial extracellular matrix- a non-cellular substrate that both the living and non-living components of the body will begin to immediately interact with. The first event in virtually any cell-materials system (*in vivo* or *in vitro*) is the rapid adsorption of ECM proteins on the biomaterials surface. Cells interact with this intervening protein layer; thus cell function at the interface, beginning with adhesion and including subsequent growth, migration, or changes in differentiated function, is controlled by the composition and conformation of the adsorbed layer. Uncontrolled cell attachment (and subsequent function) is a ubiquitous phenomenon complicating the design of devices for *in vitro* as well as *in vivo* biotechnological and biomedical

applications, since defined media for many important cell lines and primary cell cultures remains unknown.

Proteins adsorb at surfaces via many molecular interactions (van der Waals, ionic, the hydrophobic effect, etc.)[10, 11], thus the exact nature of the adsorbed layer is extremely sensitive to the concentration and composition of proteins present in solution and the particular surface structure in contact. In addition, proteins readily adsorb in multiple conformations that may change the affinity of receptor interactions with binding sites or mask interactive sites entirely[12, 13]. Because the nature of the adsorbed layer can change with the type, number, and state of differentiation of cells present (each cell being a potential source of extracellular proteins), control of cell function at surfaces by manipulating the adsorbed layer is problematic. How then might we engineer cell responses at surfaces? It is helpful to first consider the adhesion of cells *in vivo* and the signals they receive from native ECM.

4.3 The ECM, Integrins, and Cell Adhesion

The native extracellular matrix consists of soluble and insoluble proteins, peptides, sugars, and small molecules that surround cells and provide the framework within which the cells of any given tissue are organized[14-16]. The chemical and physical makeup of a given ECM varies from tissue to tissue; however any ECM provides multiple functions in the body. These include provision of a space-filling scaffold for three-dimensional organization of cells, mechanical integrity as needed, control over cell polarity, and regulation of cell function[15].

Adhesion of cells to the fibrous proteins that form the mechanical scaffolding for cells *in vivo* is mediated in large part by the binding of a family of cell surface receptors known as integrins. These cell surface receptors bind either directly to the substrate proteins (e.g. binding

of integrins to collagen) or via an intermediate adhesion protein that adsorbs in a specific manner to the underlying substrate protein. These two alternatives are depicted schematically in Figure 4.1. Integrins are heterodimeric transmembrane proteins comprised of an α and β subunit, as depicted in Figure 4.2. 13 α and 8 β chains are currently known, and various α-β pairs give rise to integrins with a breadth of affinities and a variety of target ligands[17-19].

Most integrins recognize a specific short amino acid target sequence on ECM protein ligands. These peptide oligomer targets alone are often ligands that bind integrin receptors, usually with much lower affinity than the complete proteins[18-23]. Table 4.1 summarizes several examples of α-β pairs, the target amino acid sequence(s) to which they bind, and some of the proteins that contain the target sequence.

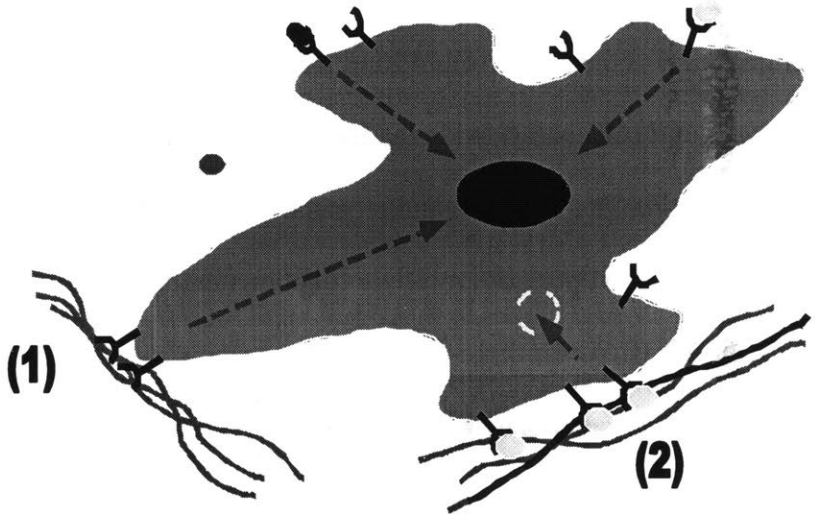

Figure 4.1. Mechanisms for cell adhesion *in vivo*. Cell adhesion is supported by (1) binding of cell surface receptors directly to receptor sites on ECM scaffolding proteins such as collagen, or (2) binding of receptors to adhesion proteins such as fibronectin or laminin adsorbed to the underlying matrix.

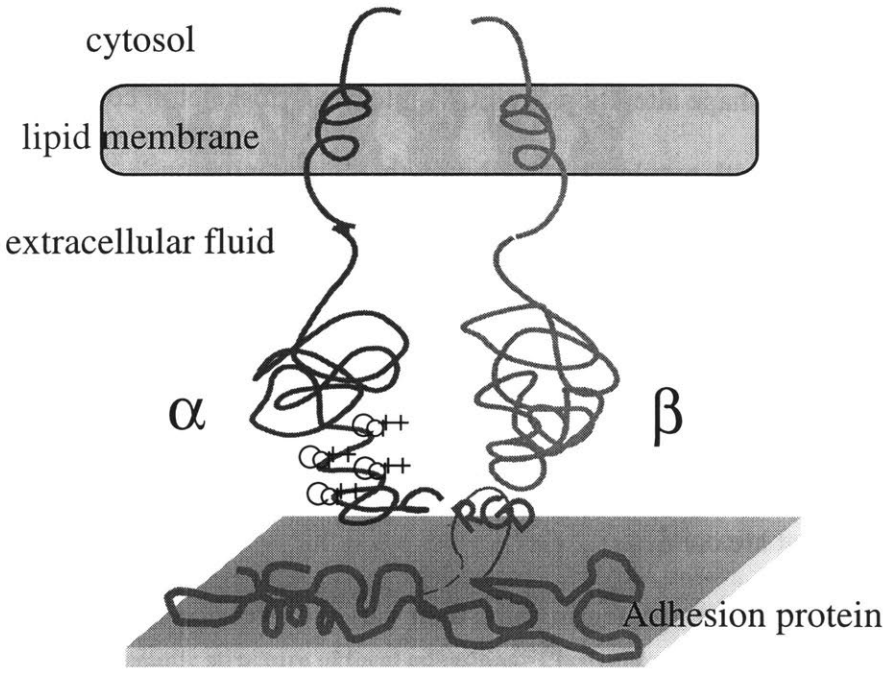

Figure 4.2. Structure of integrin cell surface receptors[17]. Integrins are composed of two distinct macromolecular subunits that noncovalently associate in the cell membrane. Metal cations bound to the α subunit are necessary for ligand recognition. A common motif recognized by many integrins is the RGD amino acid sequence.

Table 4.1. Example integrin α-β pairs and their ligands[17].

Integrin α-β pair	Target amino acid sequence	Example proteins containing the target sequence
$\alpha_5\beta_1$	RGDSP[18]	fibronectin, collagen
$\alpha_4\beta_1$	REDV[22]	fibronectin
$\alpha_6\beta_1$	YIGSR[21]	laminin
$\alpha_2\beta_1$	DGEA[23]	laminin, collagen

Integrins manipulate cell behavior through mechanical stimulus from adhesion-derived tension generation and by biochemical signaling. Mechanically, the generation of tension through integrin-ECM contacts is necessary for cell migration[24-26]. Cells respond to the

compliance of their surrounding matrix, and mechanical probing of the environment may serve as a "mechanotaxis" mechanism for guiding cell migration during wound healing and development[27, 28]. Cell shape alterations by ECM-integrin-cytoskeleton connections also have been correlated *in vitro* with regulation of cell growth[29], differentiation[30, 31], and cell polarity[32]. Integrin-ECM contacts are a source of biochemical signaling as well. While the receptors themselves do not possess cytoplasmic kinase domains, they serve as docking sites for adaptor proteins that link them to cytosolic kinases such as FAK[33] and cytoskeletal components such as actin, tensin, and vinculin[34]. Recruitment of proteins to the site of integrin binding initiates signaling cascades that are connected to cell cycle decisions: whether a cell will rest, grow, or differentiate[33]. The diversity of integrin pairs, their varied expression in cells of differing phenotype, and the multiple substrates which serve as their targets help organize the variety of tissue compositions and structures found in higher organisms[19].

Cell function is regulated not only by the chemical diversity in integrin receptors and ligands, but also their spatial distribution. Clustering of integrins leads to the formation of large (up to ~1 μm)[35] supramolecular structures inside the cell membrane at points of cell-ECM contact known as focal adhesions, focal contacts, or ECM contacts[34-37]. The hypothesized structure of such adhesive contacts is shown schematically in Figure 4.3. The formation of these complexes is accompanied by the reorganization of connected actin filaments into stress fibers that provide a stronger mechanical link between the cell and its substrate[35, 36]. Stress fibers also serve as scaffolds for the recruitment of focal contact proteins, and their reorganization serves as a positive feedback mechanism that brings more integrins to the adhesion site. Biochemical signaling at the focal adhesion is enabled through the presence of protein kinases, and by the co-clustering of other receptors (e.g. growth factor receptors) that have intrinsic kinase ability[38].

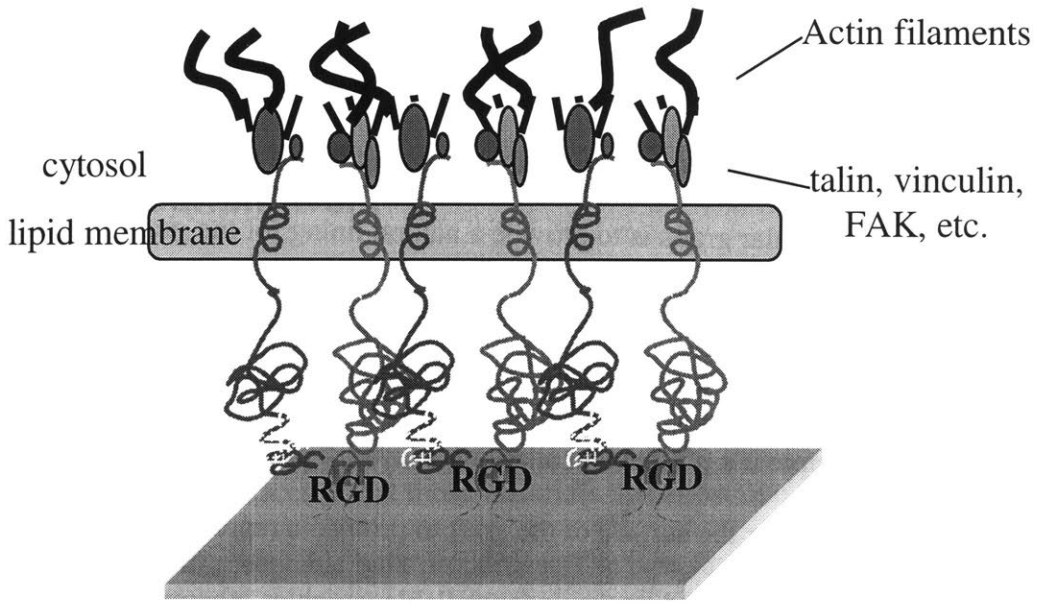

Figure 4.3. Simplified schematic structure of focal adhesions. Clustering of integrins leads to aggregation of a variety of cross-linking and signaling proteins as well as organization of actin filaments into mechanically robust stress fibers.

Because the biochemical signals delivered depend on the protein components recruited to focal contacts, a multidimensional matrix of possible responses is generated by different physical states of integrins: unclustered ligated receptors, clustered ligated receptors, unclustered unligated receptors, and clustered ligated receptors all give rise to different biochemical outcomes[38].

4.4 A Paradigm for Controlling Cell Function: Protein Resistance + Tethered Ligands

Cell adhesion *in vivo* is controlled by integrin binding to ECM ligands of appropriate type and spatial distribution. However, typical biomaterials when implanted adsorb a non-physiological layer of protein, leading to uncontrollable cell-biomaterial interactions and cell responses. The goal of much current biomaterials research is to eliminate adsorbed layer-signaling in favor of

tailored biochemical signaling based on the growing body of knowledge in cell-ECM communication[39-47].

Consider the following example to illustrate the goals of controlled cell responses envisioned. A proposed approach for reducing thrombogenicity and the danger of stroke in patients with synthetic vascular grafts is to provide a natural lining for the graft by seeding endothelial cells[48]. However, to minimize the likelihood of infection, seeding and adhesion must occur quickly[48]. Promotion of cell adhesion has been attempted with limited success by simply exposing grafts to the recipient's plasma and allowing a layer of proteins to adsorb[49]. A better approach would be to engineer the surface of the graft to provide a reproducible, tailored degree of cell adhesion that does not depend on the uncontrollable variables inherent to protein adsorption[43]. The surface structure and the target cell type alone would ideally determine kinetics of spreading and the strength of adhesion. We might also hope to further manipulate other aspects of cell function on the graft surface, such as the ability of the cells to move and grow on the graft surface, in order to effect uniform coverage of the graft *in situ* by cell proliferation and migration. How can such results be achieved in an economical, reproducible manner?

Early studies aimed at controlling cellular interactions with materials (primarily for permanent implants) focused on eliminating the first event when materials come in contact with native tissue: adsorption of serum proteins. Biomaterials research in the last ten years has developed a second focus in parallel with inhibited nonspecific protein adsorption, namely, *controlled cell signaling* at surfaces. This problem has been approached by seeking to guide the adsorption of specific proteins in specific orientations[50] or by directly incorporating peptides or proteins into the materials[39-47, 51]. Presentation of signals by incorporation of peptide ligands at biomaterials surfaces has been used to guide cell adhesion, growth, migration, and

differentiation[39-47, 51]. In addition to avoiding the inherent complications present when trying to use controlled protein adsorption to guide cell function, immobilized peptide ligands are more robust and stable under conditions of varied solvents and pH[52].

4.5 Scope of Current Work

4.5.1 Problems in Practical Application

A paradox that bears on much of the current research aimed at developing protein-resistant tethered ligand surfaces is that those materials that allow one to control protein adsorption often have unacceptable bulk properties. The best surfaces currently known for eliminating nonspecific cell-material interactions are hydrogels of poly(ethylene oxide) (PEO)[40, 42, 45, 53], which, however, have low mechanical strength and limited processability. These are serious issues limiting the use of such approaches outside the laboratory. Conversely, synthetic materials with desirable bulk properties typically have none of the biological recognition described above characteristic of native ECM. Polylactide (PLA) is a good example; it is highly favored for implant applications requiring biodegradability, reasonable mechanical strength, and stiffness (it is also one of the few degradable synthetic polymers in devices approved by the FDA for implantation)[54-57], yet its surface is prone to the nonspecific protein adsorption and subsequent cellular responses seen on virtually all synthetic materials placed in contact with cells *in vivo* or *in vitro*[58]. The current work was motivated by the desire to meet both bulk and surface structure-function requirements, by using surface modification to provide an ECM-like surface structure on materials which retain favorable device-specific bulk properties.

A diverse collection of approaches has been used for surface modification of biomaterials, and in particular for incorporating PEO at surfaces for protein resistance.

Examples include physisorption[59], chemisorption[60], covalent grafting[61-65] of polymers (including graft polymerization), and glow discharge treatment[66]. Of these, adsorption (chemical or otherwise) has been the most actively investigated for biomaterials surface modification.

To date, most of the approaches listed above offer only imperfect protein resistance and thus allow varying degrees of nonspecific cell attachment (in practice, the most important end-result of protein adsorption, since most normal cells are anchorage-dependent[67]). Further, the approaches reported to provide full cell resistance coupled with immobilized ligand signaling are typically the most inflexible from an application standpoint and require processing that is difficult to employ on a commercial scale. For example, several approaches have been demonstrated for control of cell adhesion on materials via tethered biochemical ligands on a non-adhesive background by coupling surface modification agents such as self-assembled monolayers to surfaces from solution[40, 42, 43, 47]. However, such approaches require chemistry to be carried out on the surface of the biomaterial, which limits the applicability of the approach to materials with the appropriate reactive sites, and introduces multiple steps of incubating the biomaterial surface with various solutions, which is both inefficient and difficult to employ for mass production of three-dimensional devices.

In addition to synthesis and processing issues, biomaterials have yet to implement biophysical aspects of cell signaling hypothesized by cell biologists. In particular, integrin-ECM contacts in cell adhesion are known to have important spatial distribution aspects[34-36, 68], as discussed above. Promising results demonstrating the significance of ligand spatial distribution were obtained by Maheshwari et al. in a model tethered-adhesion ligand system[45]. They tethered ligands in clusters on nanometer length scales by covalently linking RGD peptides to the chain ends of star PEO molecules on a PEO hydrogel. Cell adhesion strength and migration speeds were dramatically affected by the spatial distribution of the ligand. However, this model system

again suffers from difficult implementation in clinical device design. Development of biomaterials that can control spatial distribution of ligand in commercially relevant materials is an unsolved challenge.

The hypothesis of this thesis is that the requirements for a cell-signaling surface can be met by rational design of materials that are simply prepared, inexpensive, and readily applied as a surface modification to a variety of biomaterials. Further, these materials can be designed to practically direct cell signaling through the control of ligand spatial distribution at the surface, which to date has been considered only in a model system[44, 45]. The first half of this work focuses on meeting these goals within the framework of a non-degradable, permanent implant coating applicable by simple aqueous-based coating operations. The second goal of this work is to demonstrate through an alternative surface modification method, surface segregation, that such materials are readily applicable to the further requirements of materials for tissue engineering.

4.5.2 Materials Design

To develop this thesis, careful consideration was given to the polymer composition and architecture. The materials must meet three requirements. First, they must impart protein resistance and allow ligand spatial distribution at the surface to be tailored. Second, they must be easily synthesized and economically prepared. Third, they must be applicable for surface modification of a broad range of biomaterials via flexible, preferably aqueous-based processing. We chose to study amphiphilic comb polymers to marry these characteristics into one material.

Protein Resistance

The successful candidate material must first and foremost provide protein adsorption resistance at the surface. A large body of scientific literature in biomaterials (both experimental and theoretical) is devoted to identifying criteria for the creation of protein- and cell-resistant surfaces, and much of this work is relevant to the design of effective comb polymers. Of synthetic materials, poly(ethylene oxide) (a.k.a. poly(ethylene glycol) for lower molecular weights) has been found to provide uniquely high protein resistance when used as a coating for biomaterials surfaces. PEO-modified biomaterials show lower protein adsorption [11, 60, 62, 69, 70] and resistance to nonspecific bacterial[71], platelet[69], and cell[72, 73] adhesion. PEO-based protein-resistant surfaces can also present tethered ligands, by end-functionalizing PEO chains at the surface[39, 40, 45, 74].

The current (imperfect) understanding of PEO's ability to shield surfaces from protein adsorption is based on a broad range of theoretical and experimental work. The unique resistance of PEO to protein adsorption is likely a combination of factors: PEO has an extremely low interfacial free energy with water, it has the highest known chain mobility in water, it lacks ionic binding sites, and it hydrogen bonds with water[65]. Theoretical treatments of the interaction of proteins with grafted PEO surfaces show an interdependence of chain length and grafting density (number of end-attached chains per unit surface area) on the amount of protein adsorbed[10, 75]. At high surface density, even short PEO chains are predicted to exhibit equilibrium protein resistance by complete steric exclusion of protein from the interface[10, 75]. Conversely, at low chain density but high molecular weight, the highly mobile PEO chains present a large kinetic barrier to adsorption[75].

This picture of protein-surface interactions is consistent with experimental observations. Experimentally, increasing the surface density of grafted PEO at fixed molecular weight or increasing molecular weight at fixed density has been found to improve protein resistance[11, 60, 70]. Atomic force microscopy studies of the interaction between albumin and PEO-coated poly(styrene) surfaces using atomic force microscopy have shown that increasing surface coverage by PEO decreases the force of adhesion between albumin and the underlying polymer surface; at high surface coverages (even for very short PEO chains of only three repeat units) this adhesion force is completely eliminated[76]. Alternatively, higher molecular weight PEO chains at lower surface densities can be equally effective, even for low volume fractions of highly swollen PEO near the surface[62].

The use of comb polymers allows a PEO layer to be presented at the surface by anchoring the hydrophilic chains to a hydrophobic backbone, as schematically shown in Figure 4.4(a). The surface "grafting density" of PEO chains is controlled by the spacing between units on the backbone. PEO macromonomers containing a methacrylate end-group are commercially available in a variety of chain lengths and comb polymers containing a backbone of methacrylate monomers are readily synthesized by inexpensive free radical techniques, making them easily and economically prepared. Use of PMMA/PEO-based comb polymers was further motivated by the fact that both PMMA and PEO are components of FDA-approved biomedical devices for use *in vivo*, which makes the regulatory approval of new biomaterials based on these components more likely[39, 52]. Finally, amphiphilic polymers such as the proposed comb molecules are often soluble in water/alcohol mixtures[77], eliminating the need for toxic organic solvents during processing.

Amphiphilic combs having the basic structure depicted in Figure 4.4(a) have been studied previously for improving the protein resistance of biomaterials. Combs with methacrylate

backbones and PEO side chains have been studied as adsorbed layers for increasing the hydrophilicity of polymer surfaces[59, 78], and in blends with methacrylate homopolymers to increase wettability of biomaterials[79, 80]. Surface grafting of PEO side chains to polyurethanes, creating comb polymers *in situ* at a surface, has also been used to achieve protein-resistant surfaces[81, 82]. These studies demonstrate the great potential of comb polymers to realize cell-*resistant* surfaces, but the design of cell-*signaling* surfaces using such materials has not been pursued.

Surface Tethering of Clustered Ligands

Polymers with a comb architecture provide a convenient means for tethering biochemical ligands at a surface with control over local spatial distribution of the peptide signals. Peptide or protein ligands can be tethered at comb polymer surfaces by functionalization of the ends of the comb side chains; clustering of ligand on nanometer length scales can be achieved by functionalizing multiple branch ends per molecule, as depicted in Figure 4.4(a). Control of the surface density of ligand clusters on comb polymer films should be readily achieved by mixing functionalized and unfunctionalized combs in different ratios. Thus three parameters of interest, cluster size, ligand density within clusters, and cluster surface density can be easily tuned by control over the comb molecular weight, functionalization, and film composition.

Comb polymers as described thus far might meet all the prescribed objectives, but only allow nanoscale ligand clustering on length scales determined by the size of the molecules, a few tens of nm at most. However, amphiphilic comb polymers can also be used to prepare polymer latexes, which were studied here to further broaden the applicability of the comb polymer approach. Polymer latexes have been used for many years in a wide variety of applications such as paints, inks, adhesives, and paper making[83]. These applications exploit the easily tuned

physical properties of latexes such as particle size and glass transition (T_g), as well as the simple, economic route of emulsion or dispersion polymerization for their synthesis. Latexes that consist of particles exhibiting surface functionalities have opened up further areas of interest, including biomedical applications. Polymer latexes conjugated with antibodies or other proteins have been used for delivering drugs to cells[83], as marking agents for microscopy[84], and as agents for immunoassays and separations[84-86]. However, to our knowledge, no studies have examined the use of latexes to create cell-interactive surfaces.

Latex particles functionalized with ligand could be applied as coalesced solid films or embedded into protein-resistant comb polymer surfaces, as shown schematically in Figure 4.4(b) and (c), respectively. Mixtures of ligand-functionalized and unmodified latexes on a surface would allow clustering of ligand similar to thin film blends of functionalized and unmodified comb polymers. Because these colloids typically range in size from ~50 nm up to ~10 μm[87-89], they extend the range of accessible clustered ligand domain sizes by two orders of magnitude. In addition, synthesis can be carried out by free radical methods in water/alcohol media[77] and the completed spheres stored in pure water- again eliminating hazardous organic solvent-based processing.

Together, these comb polymer-based approaches, comb polymer films and comb-stabilized latex films were explored as candidates for biomaterials surface modification. Optimum chemical composition and architecture for comb polymers as cell-signaling surfaces were investigated, including effects of PEO content and side chain length on resistance of surfaces to nonspecific cell adhesion. A theoretical self-consistent field model of the comb polymer/water interface was implemented to aid in the understanding and design of these surfaces. Preparation of clustered ligand surfaces using these systems was demonstrated with tethered adhesion peptides as well as growth factors. Tethered ligand surfaces prepared by comb

polymer systems elicit controlled cell responses, providing a broad range of possible processing schemes for implementation of clustered ligand surfaces on biomaterials.

4.5.3 Application to Tissue Engineering

A large number of *in vivo* biomedical applications would best be addressed by a system with cell-signaling properties *and* bioresorbability or biodegradability. Examples of such applications include targeted drug delivery[3-5], temporary tissue barriers[2], and cell delivery scaffolds for gene therapy or tissue engineering[54, 90-92]. To demonstrate the *general* applicability of comb polymers for biomaterials surface modification, the second focus of this thesis was to develop a surface modification method suitable for providing spatially controlled ligand presentation on resorbable, three-dimensional devices where a simple coating approach is problematic. We chose to focus on the particular application of tissue engineering scaffolds for these studies.

Tissue engineering is a field that focuses on the repair of lost or damaged metabolic function through the transplantation of cells using an open or closed scaffold delivery system[2]. Tissue engineering as a discipline developed in response to the need for an alternative to organ transplantation. One quarter of all patients yearly in need of an organ transplant die before receiving treatment, due to the severe shortage of donor organs[2]. Unfortunately, current statistics predict a steadily increasing gap in the number of available organs vs. the number of needy patients, and optimism for increasing the donor pool is low[2].

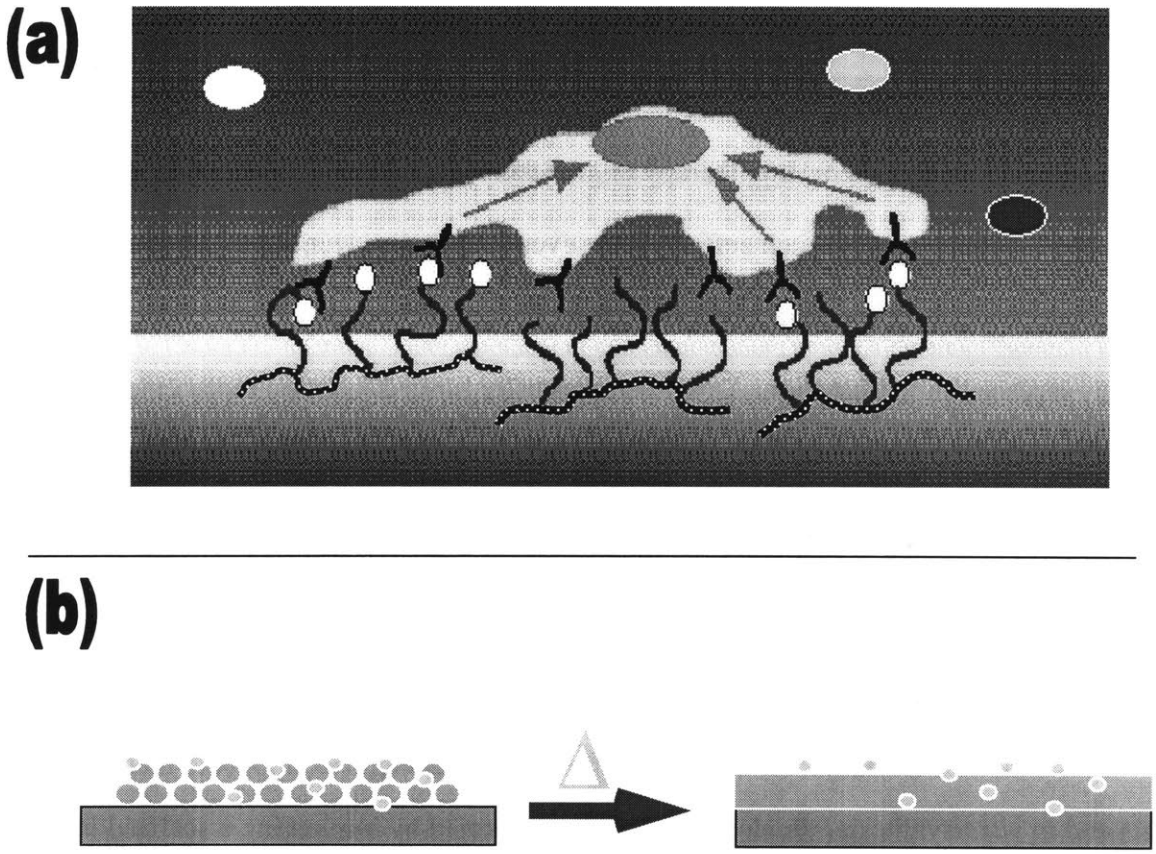

Figure 4.4. Schematic representation of comb polymer systems. (a) Comb polymer thin films. (b) Coalesced latex films. (c) Embedded latex films.

As an alternative to transplantation, patients traditionally receive one of three procedures when available: surgical reconstruction (e.g. heart), mechanical devices to replace the lost organ function (e.g. kidney dialysis), or drug therapy (e.g. diabetes patients)[93]. While these approaches are not limited by donor supply, each suffers from several other disadvantages. Surgical reconstruction often fails in the long term (e.g. a few years post-procedure), while mechanical devices only replace limited function. Drug therapies offer limited function replacement and undesirable, sometimes dangerous side effects[1]. Replacement of failed organs and tissues by tissue engineering offers the promise of complete or near-complete permanent restoration of function with no donor supply limitations, reduced risk of rejection of transplanted cells, and no long-term side effects.

Tissue engineering approaches can be broadly classified into two categories; *in vivo* synthesis and *in vitro* synthesis. *In vivo* synthesis is performed by implanting a scaffold into which cells grow from surrounding tissues *in situ*, regenerating the lost tissue under the guidance of the scaffold[2, 93]. *In vitro* synthesis is performed by seeding autologous or donor cells on a scaffold in culture, regenerating the tissue *in vitro*, followed by implantation of the finished structure[2, 93]. Tissue engineering is a topic of current research for all 4 types of tissue (epithelial, connective, muscle, and nerve). Cell transplantation approaches are being studied to replace or repair cartilage[2], bone[94], skin[95-98], nerve[99-101], kidney[8], blood vessels[102], and liver[103].

Tissue Engineering Scaffolds

The design of artificial matrices for *in vivo* or *in vitro* tissue synthesis presents an exciting challenge for the materials scientist. Tissue engineering requires a means to deliver cells to an implant site, to provide a template for their organization, to guide cell function, and to provide protection (mechanical and chemical) from the surrounding tissue over a prescribed time

period[2, 90, 91, 99]. Further, cell scaffolds must not induce an intense or prolonged inflammatory response *in vivo* and must degrade in a controlled manner without toxic byproducts[2, 6, 104]. Ideally, the scaffold surface would be protein-resistant and guide cell function via controlled presentation of peptide signals[43, 54].

Cell scaffolds prepared in current research are typically open cell foams with pores ranging from a few tens to several hundred microns in diameter, depending on the application, with porosities $\geq 95\%$[90, 93, 104, 105]. The vast majority of studies on the fabrication and use of these structures for cell delivery have focused on the development of a suitable morphology using a polymer with the desired biodegradation characteristics[56, 57, 91, 92, 106]. Few studies have been concerned with tailoring the surface of biodegradable materials to incorporate protein resistance and biochemical signaling. This is due in part to the difficulty in chemically modifying the surface of biodegradable materials in a controlled manner. Preparation of biodegradable polymers with pendant functional groups is difficult and achieved with poor yield, low functionalities, and/or low molecular weights[107, 108]. Black et al.[41] investigated one route to functionalize biodegradable poly(lactide) with peptide ligands by preparing block copolymers of PLA with short poly(ethylene oxide) blocks that had functionalized end-groups. Films of the block copolymer present a protein resistant PEO surface layer end-capped with the ligand of interest. However, these copolymers provide no route for controlling ligand distribution, except through macroscopic patterning of the polymer functional groups.

As an alternative to direct chemical modification of a biodegradable polymer, Park et al. investigated the use of a solid free-form fabrication process (3DP™) to incorporate end-functionalized PEO-PPO-PEO block copolymers into the surface of degradable poly(lactide) devices[54]. Devices were fabricated by the 3DP process, by "printing" microdroplets of block copolymer solution onto the surface of PLA. The printed polymer is permanently entangled with

the surface after evaporation of the solvent. Cell-resistant PLA surfaces were prepared in this manner. To present ligands for cell adhesion at the surface, Park et al. functionalized the PEO chain ends of the triblock with a sugar residue recognized by a hepatocyte cell-surface receptor. Surfaces presenting the tethered sugar were resistant to nonspecific cell attachment but also did not support strong spreading of hepatocytes. They reasoned that much of the ligand was inaccessible at the surface due either to steric interference from unfunctionalized PEO chains or burial of the ligand within the bulk during the printing process.

Surface Modification of Polylactide

To address the issues described above, we explored the use of surface segregation to surface modify polylactide biomaterials by blending PMMA/PEO comb polymers with polylactide. PLA has excellent bulk properties, but as stated above, PLA devices have no controlled cell interactions. Surface segregation was studied as a means to provide a protein-resistant cell-signaling comb polymer surface layer on devices which could be fabricated by typical processing routes used for tissue engineering scaffold preparation.

Surface segregation is the formation of a layer enriched in one of the components of a blend at a substrate interface or free surface. Segregation can be a consequence of bulk phase separation coupled with preferential surface interactions of one of the components, or in miscible blends, driven solely by surface free energy minimization. Segregation has been predicted and observed for homopolymers[109-116], block copolymers[117-120], end-modified copolymers[121-125], graft (comb) copolymers[80, 126, 127], and star homopolymers and copolymers[127]. Of these architectures, comb polymers appear to have the greatest potential as surface segregation agents for creating clinically-relevant clustered ligand surfaces. Homopolymers are unsuitable surface segregation agents as the repeat units which one might use for eliminating nonspecific cell

interactions with biomaterials (e.g. ethylene oxide, dextran) are water soluble and the resulting surface structure would be unstable *in vivo*. Block and star copolymers, on the other hand, are typically prepared by anionic methods that are both costly and time intensive [128]. In addition, PEO blocks of greater than ~10 repeat units may crystallize[79, 129], making them inefficient surface modification agents, and PEO-containing block or star copolymers may also form micelles in the bulk of the material[79], compromising both their surface activity and bulk mechanical properties. In contrast, comb polymers with short PEO side chains can be economically synthesized with a large fraction of PEO units while remaining water insoluble, noncrystalline, and less subject to micellization.

To avoid bulk amorphous phase separation and an accompanying loss of mechanical properties[130], a miscible surface-segregated blend is desirable, i.e. a blend that contains a surface layer enriched in cell-guiding comb polymer but remains homogeneously mixed in the bulk amorphous phase of PLA. While PLA blended with P(MMA-r-POEM) has not been studied to date, the miscibility of blends of PLA with PMMA or PEO has been previously examined by thermal techniques. Eguiburu et al.[131] studied blends of PMMA with poly(D,L-lactide) or poly(L-lactide) by DSC. They showed that amorphous PMMA/PLA blends are fully miscible, while semicrystalline PMMA/PLA blends appear to be miscible if the blend is annealed to allow rearrangement of the crystal structure. Younes and Cohn[132] found evidence of miscibility in the amorphous phase for PLA blended with low molecular weight PEO ($M < 10K$ g/mol), although crystallization of both components led to phase separation for some compositions. Nijenhuis et al.[133] and Yang et al.[134] studied blends of high molecular weight PEO with PLA, also by calorimetry, and found the blends to be completely miscible in the amorphous phase.

In the present work, a theoretical self-consistent field model of PLA/comb polymer blends was used to predict the composition profiles of surface-segregated materials. The effect of

changing thermodynamic driving forces on blend surface compositions was studied. Surface segregation of the amphiphilic comb polymer driven by annealing of blends in water was predicted to provide excellent surface enrichment of the cell-signaling component. Molecular weight and film thickness effects on surface segregation were also investigated.

Experimentally, thin film blends of poly(lactide) and comb polymer were studied, and conditions for surface segregation of comb polymers in PLA were identified which provide a comb-enriched surface layer suitable for controlling ligand spatial distribution by nanoscale ligand clustering. Tailoring of cell adhesion on PLA was achieved through surface segregation of adhesion ligand-bearing comb polymer, recapitulating the cell-signaling comb polymer structure at the surface of PLA films. This thermodynamic self-assembly process provides a straightforward route to implement comb polymer-based control of cell-surface interactions on a great variety of complex three-dimensional biomedical devices.

4.5.4 Spatial Distribution of Ligand in Integrin Signaling

Because integrin clustering is the key feature of focal adhesions and appears to be required for full integrin mechanical and chemical signaling[34, 38], the distribution integri-binding ligands on a substrate should have a strong influence on cell adhesion. One possible mechanism for focal adhesion formation would be nucleation of protein aggregates at sites where several receptors cluster due to binding with closely apposed ligands. If this were the case, the strength and organization of cytoskeletal connections to sites of clustered ligand (via integrins) would be influenced by both the total ligand density as well as its local distribution, i.e. the true (not average) distance between neighboring ligands at 10-100 nm length scales. Receptor binding might thus be dramatically affected by ligand clustering. In addition, if the strength or

organization of integrin-cytoskeletal linkages depends on integrin clustering, then control of both total ligand density and ligand clustering would have quantitative effects on cell attachment strength and the response of cells to applied forces.

To complement studies on the preparation of clustered ligand surfaces using comb polymers, we carried out a theoretical analysis of potential effects of ligand nanoscale clustering on receptor binding. A simple analytical model and a Monte Carlo lattice model of the interface between a cell membrane and substrate presenting clustered ligands were developed. These models predict potentially large increases in receptor binding induced by ligand clustering under conditions where the effective affinity of receptor-ligand interactions is influenced by receptor clustering. Thus a mechanism is proposed by which strong increases in receptor binding, and as a consequence, increases in cell-cytoskeletal connectivity, might be expected by presentation of nanoscale-clustered ligand.

Finally, in order to indisputably demonstrate the potential effects of controlling ligand spatial distribution using comb polymer surfaces, studies were made of the adhesion of cells to clustered adhesion peptide surfaces. Cell adhesion strengths were quantified using a centrifugal force detachment assay. Comb polymer surfaces presenting ligands clustered on 100-300 nm length scales were used to control cell adhesion. Clear functional dependence of cell adhesion on ligand surface distribution was demonstrated in these experiments. The results indicate that comb polymers do allow effective clustering of ligand and that this local-scale distribution can be used to modulate cell adhesion and response to external forces. Comb polymers are thus a facile route to control cell adhesion via nanoscale ligand clustering.

4.5.5 Outline of the Thesis

The experimental and theoretical work carried out to fulfill the objectives discussed in sections 4.5.2, 4.5.3, and 4.5.4 is presented in Chapters 5 through 10 of this thesis. Chapter 5 describes the theoretical models used to study receptor binding to clustered ligand surfaces and comb polymer surface segregation, as well as group contribution calculations used to predict several properties of P(MMA-r-POEM) comb polymers. Chapter 6 describes in detail the preparation of the materials and the analytical techniques used to characterize them. Surface preparation and analysis techniques are described, as well as cell culture experiments carried out on comb polymer surfaces. Chapter 7 presents the results from theoretical studies of clustered ligand-receptor binding, and discusses design criteria for clustered ligand surfaces. This is followed in Chapter 8 by experimental studies on the implementation of protein-resistant tethered ligand surfaces with control over ligand clustering using PMMA-based comb polymers. Results identifying the structure and composition of comb thin films resistant to nonspecific cell adhesion are discussed, followed by results obtained for comb-stabilized latexes. Secondly, experiments on comb thin films and latex films permitting controlled cell adhesion via tethered RGD peptides are discussed. Finally, results for tethered epidermal growth factor-induced PC12 cell differentiation on comb thin films are presented. In Chapter 9 the use of comb polymers for surface modification of complex 3D structures in the context of tissue engineering is discussed, through studies of comb polymer surface segregation in biodegradable polylactide. Theoretical predictions for surface segregation from SCF calculations are presented. This is followed by experimental results for polylactide/comb polymer thin films blends. Creation of cell-resistant layers on polylactide blends or tuned cell adhesion via tethered RGD is demonstrated through water annealing of blend thin films. Chapter 10 unites the theoretical and experimental work on comb polymer surface design in a study of clustered adhesion ligand effects on cell adhesion

strength. Adhesion of cells on nanoscale-clustered RGD peptides is compared with cell adhesion on adsorbed fibronectin, and a model describing clustered ligand effects is proposed. The thesis closes with a summary of conclusions gathered in this work and a discussion of important future directions.

5 Theoretical Methods

5.1 Modeling Cell Interactions With Clustered Ligand Surfaces

5.1.1 Description of the Cell-Substrate Interface

An analytical model and a Monte Carlo simulation were developed to model the interface between a cell membrane and a rigid substrate presenting tethered ligands for membrane-bound receptors. The models consider the interaction of cell surface integrin receptors with ligand immobilized on the substrate discretely or in clusters (groups of multiple ligands confined to a defined area). The physical picture is schematically shown in Figure 5.1. The cell membrane is flat against the substrate with a constant separation of 300×10^{-8} cm, comparable to the distance over which integrins can interact with ligand[9]. Unligated integrins can diffuse freely in the plane of the membrane[135] and interactions between integrins and other membrane components are neglected. Ligand is immobile on the surface, modeling the case of adsorbed adhesion proteins or (as depicted in Figure 5.1) peptide ligand immobilized on an artificial substrate via short tethers [40, 41, 45, 47, 51].

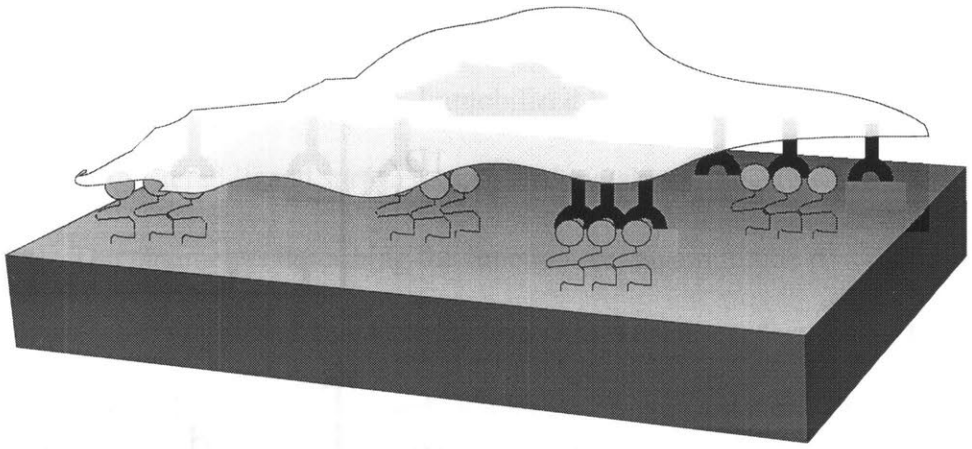

Figure 5.1. Schematic of cell membrane-substrate interface modeled.

5.1.2 Analytical Model

The effect of ligand surface distribution on equilibrium receptor binding was first analyzed for the case of receptors binding clustered ligands when the binding energy of the receptor-ligand pair is *unaffected* by nearest-neighbor interactions between receptors. For analysis, a one-dimensional strip of the 2D cell-substrate interface is considered. It is assumed for simplicity in this calculation that the ligand clusters are regularly distributed on the surface, with a line density profile in 1D as shown in Figure 5.2. The equilibrium reaction between a free receptor R and unoccupied ligand L is:

$$\mathbf{R + L \Leftrightarrow C} \qquad \textbf{(Eqn 5.1)}$$

where C is the complex formed by the bound receptor-ligand pair.

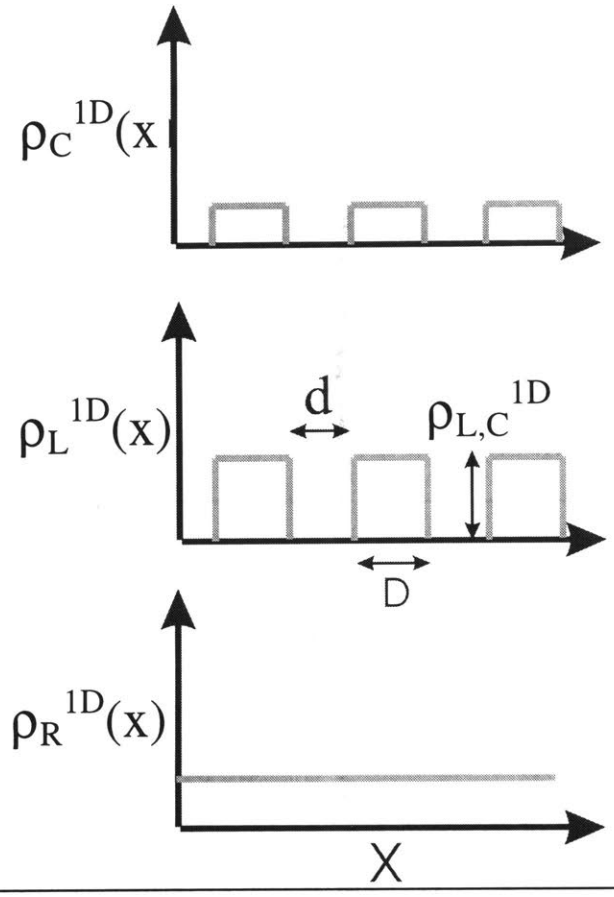

Figure 5.2. One-dimensional representation of a clustered ligand substrate/cell membrane interface. Free receptor concentration within the plasma membrane is uniform, but the ligand distribution (and thus the complex distribution) at the surface is spatially variant.

To determine the effect of ligand clustering on binding for the case where this single reaction describes receptor-ligand interactions in the system, the total number of complexes in the system at equilibrium is calculated from a spatially-dependent mass action law. The receptor-ligand binding reaction at equilibrium is governed by:

$$\rho_C^{1D} = \rho_L^{1D}\rho_R^{1D}/K_D^{1D} \qquad \textbf{(Eqn 5.2)}$$

where ρ_C^{1D}, ρ_R^{1D}, and ρ_L^{1D} are the line densities (#/length) of receptor-ligand complexes, unoccupied cell receptors, and unoccupied ligand, respectively, and K_D^{1D} is the 1D equilibrium dissociation constant (with units #/length). Because receptors are free to diffuse along the slice of the interface, the free receptor concentration profile is spatially invariant at equilibrium-diffusion will continue to adjust the local unbound receptor concentration to maintain a flat

density profile as ligand binding occurs. *Note that steric interactions between receptors within clusters are neglectied in this calculation.* Immobilized ligands provide a varying function in x for ρ_L^{1D}, $\rho_L^{1D}(x)$. A clustered ligand surface is modeled by taking a square wave for the ligand density $\rho_L^{1D}(x)$. The parameters describing the function are the amplitude $\rho_{L,C}^{1D}$ (local line concentration of ligand within a cluster), cluster size D, and cluster separation d. For a total number of clusters n within our 1D slice and total length of interface $X = n(D + d)$, the average ligand line density is:

$$\langle\rho_L^{1D}\rangle = nD\rho_{L,C}^{1D}/X \qquad \textbf{(Eqn 5.3)}$$

Because the ligand density is a spatially varying function, the receptor-ligand complex line density will also have an x dependence, as schematically shown in Figure 5.2. $\rho_C^{1D}(x)$ will be a step function:

$$\rho_C^{1D}(x) = \begin{cases} \rho_{C,C}^{1D} = \rho_{L,C}^{1D}\,\rho_R^{1D}/K_D^{1D} & \textbf{for } x \textbf{ within clusters} \\ 0 & \textbf{elsewhere} \end{cases} \qquad \textbf{(Eqn 5.4)}$$

where ρ_R^{1D} (no x dependence) is the free receptor density everywhere along the interface:

$$\rho_R^{1D} = (X\rho_{R,T}^{1D} - nD\rho_{C,C}^{1D})/X = \rho_{R,T}^{1D} - \langle\rho_C^{1D}\rangle \qquad \textbf{(Eqn 5.5)}$$

where $\rho_{R,T}^{1D}$ is the total initial receptor density. Substituting equation (Eqn 5.5) into (Eqn 1.4), we obtain for the local line concentration $\rho_{C,C}^{1D}$ of complexes within a cluster:

$$\rho_{C,C}^{1D} = (\rho_{L,C}^{1D}\,\rho_{R,T}^{1D})/(K_D^{1D} + \langle\rho_L^{1D}\rangle) \qquad \textbf{(Eqn 5.6)}$$

The total number of complexes (C) in the 1D strip will be:

$$C = X\sum_{x=0}^{X} \rho_C^{1D}(x) = nD\rho_{C,C}^{1D} = (X\langle\rho_L^{1D}\rangle\rho_{R\,T}^{1D})/(K_D^{1D} + \langle\rho_L^{1D}\rangle) \qquad \textbf{(Eqn 5.7)}$$

which is exactly equivalent to the result expected for the case of a homogeneous distribution of ligand where $\rho_L^{1D}(x) = \langle\rho_L^{1D}\rangle$ for all x. Thus clustering ligand without changing the nature of receptor-ligand interactions (or introducing other molecules for receptors to interact with) *does not increase* the total number of complexes formed. Comparing the same total density of ligand clustered and unclustered, the total number of complexes formed is the same because the local increase in ρ_C induced by increased ligand concentration within clusters is exactly offset by the decrease in ligand density outside the clusters. Only *local* complex densities (within clusters) can be affected. The local complex density within ligand clusters along a strip of the cell-substrate interface in terms of the mean complex density for the same total amount of ligand distributed randomly is:

$$\rho_{C,clustered}^{1D} = (\rho_{L,C}^{1D}\rho_{C,unclustered}^{1D})/\langle\rho_L^{1D}\rangle = (X\rho_{C,unclustered}^{1D})/nD \qquad \textbf{(Eqn 5.8)}$$

For example, nanoscale clustering of 5 ligands within a 400 nm^2 area, at a total ligand density of 500 ligands/μm^2, would give an increase in local complex density *within* clusters of 5 times the average total complex density on a surface with a homogeneous random ligand distribution. . It should be emphasized, however, that steric interactions between receptors within a single cluster are not accounted for in this model and may influence this result.

5.1.3 Monte Carlo Simulations

Model description

To probe the role of steric effects as well as binding affinity effects with varying ligand spatial distribution, a Monte Carlo simulation of the cell-substrate interface was developed. The model is schematically shown in Figure 5.3. The contact area of the cell membrane against the

substrate is modeled as a planar square lattice (500x500 sites). Coarse-graining the model at the level of 100 nm^2 of surface area per lattice site (approximately the size of integrin receptors [15]), gives a total model area of 25 μm^2, approximately 2.5% of the total real area of contact (~1,000 μm^2) [136] of a well spread fibroblast on a substrate. Diffusion of receptors or ligand in the third dimension (the height between the surface and cell membrane) has been neglected, as the separation between the cell membrane and the surface is comparable to the size of the receptors and small relative to the lateral length of the lattice.

The lattice is occupied by three components: tethered (immobilized) ligands, mobile cell surface receptors, and immobilized receptor-ligand complexes. The number of receptors on the lattice is fixed at 2,500, modeling a cell with 100,000 total receptors[136, 137]. A ligand or complex located on a given lattice site is immobilized to that 100 nm^2 area. Receptor diffusion in the cell membrane is modeled by allowing receptors (labeled "R" in the schematic) to move during the simulation to nearest neighbor sites on the lattice. When a receptor diffuses into a site occupied by a ligand, a complex is formed ("C" in the schematic). Volume exclusion of the receptors and complexes is maintained by disallowing moves which place one receptor in the same lattice site as another free receptor or complex. To minimize finite size effects, periodic boundary conditions are employed at the edges of the lattice.

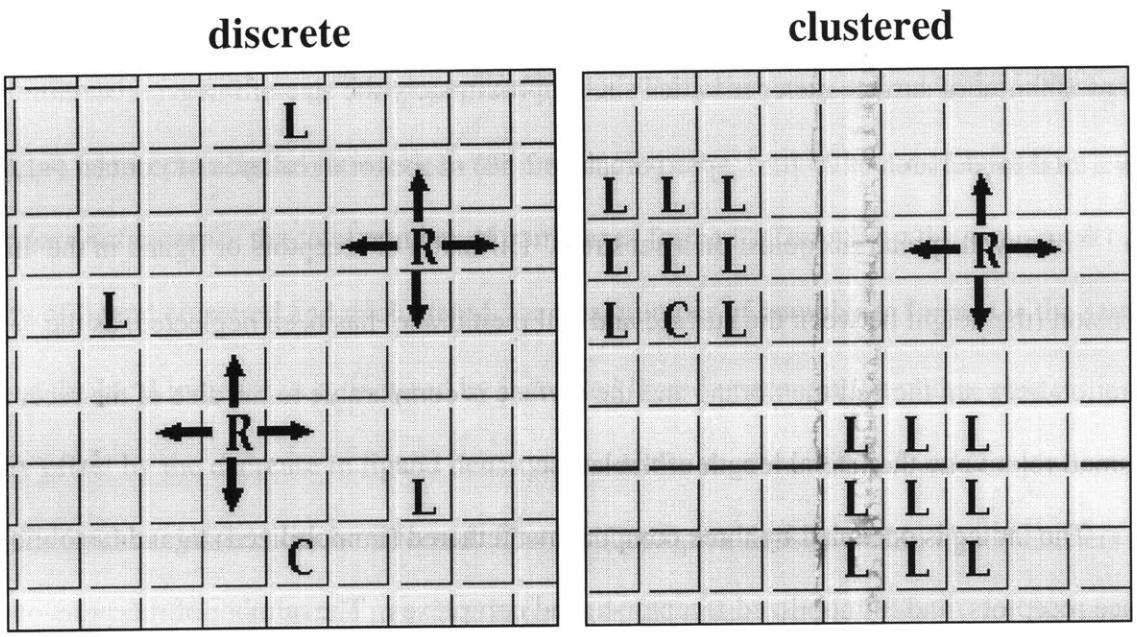

Figure 5.3. Schematic of lattice model for cell membrane-substrate interface. A cell membrane apposed with a surface presenting tethered ligands for cell surface receptors is modeled as a two-dimensional square lattice. Each site of the lattice may be occupied by either a tethered ligand (L), mobile receptor (R), or tethered ligand-receptor complex (C). Clustered ligand surfaces are modeled by placing ligands in ordered arrays placed randomly on the 2D lattice.

The spatial distribution of ligands is determined at the outset of the simulation and remains static during equilibration of the system. The ligand distribution for a given simulation is determined by the total fraction of lattice sites to be occupied by ligand and the cluster size D (the number of sites comprising the linear dimension of the cluster). Clustered ligand presentation is modeled by placing ligand in square arrays of 1-20 lattice sites per side ($D = 3 \rightarrow$ 3x3 arrays of ligand). At the outset of the simulation, clusters are placed randomly on the lattice (preserving volume exclusion of the ligands; only one ligand is allowed to occupy any given site), until the prescribed fraction of lattice sites is filled. Unclustered ligand presentation is modeled by setting $D = 1$. Total ligand densities in simulations were varied two orders of magnitude from 30 ligands/μm^2 to 4,000 ligands/μm^2. After placing ligands, receptors are also initially placed randomly on the lattice, on unoccupied sites, until the prescribed number of receptors is allocated.

Dynamics of the system and evolution of the equilibrium state from the initial placement of receptors and ligands are simulated by diffusion of receptors and receptor-ligand binding/unbinding. At each cycle of the simulation, one receptor is chosen at random, a direction to attempt moving that receptor is also randomly chosen (up, down, left, or right on the lattice), and the attempted move is accepted or rejected according to excluded volume constraints and the Metropolis criterion. Excluded volume rejects any move that will place a receptor on a site already occupied by either another receptor or receptor-ligand complex, while the Metropolis criterion ensures sampling of the equilibrium distribution of the system [138]. For the current model, the Metropolis criterion sets the probability for accepting a move of a receptor to an unoccupied site or unoccupied ligand, based on energetic interactions between the components of the system. We define for convenience the energy of receptors to be 0 in the unbound state, while the energy of the receptor-ligand complex is E ($E < 0$). Moves which leave the energy of the system unchanged or which lower the energy of the system are automatically accepted. Thus moves of unbound receptors through the lattice or moves of an unbound receptor onto a free ligand (forming a complex) are accepted with unit probability. Diffusion of a receptor off a ligand site (breaking a receptor-ligand bond) is allowed with probability $p = \exp(-\Delta E/kT) = \exp(E/kT)$: the energetically unfavorable process of breaking the ligand-receptor bond is allowed, but only with a likelihood determined by a Boltzmann weight for the bound state. Simulations using one binding energy to describe receptor-ligand interactions are hereafter referred to as the *single-state model.*

Modeling Complex-Complex Interactions

In order to examine the effect of binding energy changes due to clustering of ligated receptors, a two-state binding energy model was used. Two different possible energies for the bound

receptor state were introduced, E_1 and E_2 ($E_2 < E_1 < 0$), which represent the energy of discrete receptor-ligand pairs and clustered complexes, respectively. Clustering changes the binding energy via nearest neighbor complex interactions: complexes which form adjacent to an existing receptor-ligand pair break with a probability $p_2 = \exp(E_2/kT)$, while discrete complexes break with probability $p_1 = \exp(E_1/kT)$ ($p_2 < p_1$). This simple model allows us to account for an effective increase in the affinity of receptor-ligand interactions within clusters.

Two types of immobilized ligand were modeled: adsorbed adhesion proteins (e.g. fibronectin, laminin, etc.) and immobilized low molecular weight adhesion peptides. Adsorbed proteins present ligand to cells *in vivo* and are also important experimental models. Immobilized peptide ligands, on the other hand, are of interest in biotechnological applications for controlling cell adhesion on artificial substrates. For modeling purposes, these two different types of ligand differ primarily in their affinities for integrins. Adhesion proteins have K_Ds on the order of 10^{-6} – 10^{-7} M, while linear adhesion peptides such as GRGDS have much lower affinities[19, 139], $K_D \sim 10^{-3}$ – 10^{-4} M. Simulations were run using discrete receptor-ligand binding energies E_1 corresponding with these solution K_Ds. To model tethered RGD peptides, E_1 was set to -1.0kT ($K_D \sim 2\times10^{-4}$ M); to model adsorbed full adhesion proteins E_1 was set to -5.0kT ($K_D \sim 3.7\times10^{-6}$ M). To investigate the effects of increased affinity on clustering, we varied the clustered-state binding energy E_2 from $1E_1 - 8E_1$.

Equilibration of Systems

Equilibration was effected by repeating the cycle of receptor selection and attempted movement. The equilibrium state of the system evolves after many Monte Carlo (MC) steps, defined as the average number of cycles required to randomly select and attempt moving each receptor once. For the receptor density studied (2,500 receptors on the lattice, or 100 receptors/μm^2), the

average number of cycles per MC step was ~20,000. Given known diffusivities of membrane receptors (10^{-9}-10^{-10} cm^2/s) [9], we can correlate one Monte Carlo step with approximately 100-1,000 microseconds of real time. From the stochastic initial receptor distributions, the equilibrium state of the cell-surface interface was found to evolve within ~250 MC steps for clustered ligand systems (and much faster for D = 1 unclustered ligand distributions). In real time, this correlates with a timescale on the order of a few seconds. Two examples illustrating system equilibration are shown in Figure 5.4, where the instantaneous percent of bound receptors for D = 1 in the single-state model and D = 5 in the two-state model are shown.

Equilibrium values for system properties were determined by averaging steady-state values over 10^8 cycles (beginning after 10^7 cycles for equilibration) for 3 separate random cluster distributions. The primary attribute of interest for each simulation is the number of receptors (or fraction of receptors) bound at equilibrium.

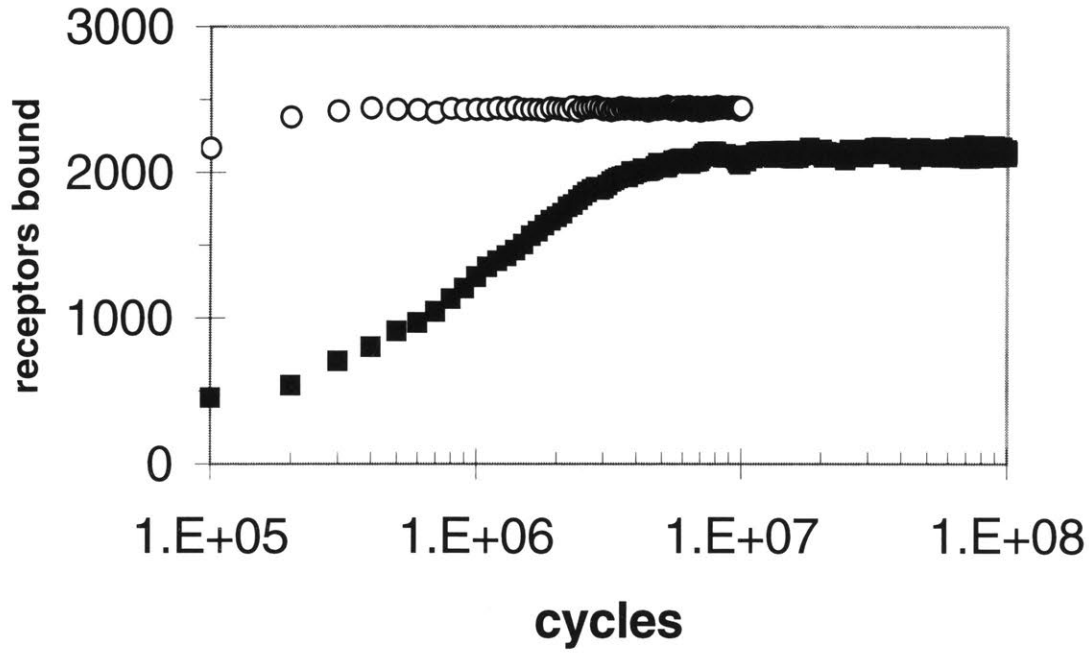

Figure 5.4. Evolution of equilibrium state for two example simulations. (•) Instantaneous number of bound receptors for an example single-state simulation. D = 1, ligand density 100/μm^2, 2,500 receptors, and E = -2.0kT. (•) Bound receptors for an example two-state simulation. D = 5; 1,000 ligands/μm^2; E_1 = -2.0kT and E_2 = -6.0kT.

Relationship Between Model Parameters and Solution Affinities

The equilibrium receptor-ligand dissociation constant K_D is related to the bond break probability p. At equilibrium, the number of bonds formed per unit time must equal the number of bonds broken. For the lattice model, this is expressed as:

$$(p_{on}/\tau)(\rho_L A/N^2)((\rho_{R,T} - \rho_C)A/N^2) = (p_{off}/\tau)(\rho_c A/N^2) \quad \textbf{(Eqn 5.9)}$$

where p_{on} is the probability for bond formation per site occupied by both receptor and ligand per simulation cycle, p_{off} is the probability for breaking a bond per site occupied by a receptor-ligand complex per MC step, τ is the amount of real time per MC step, ρ_L is the total ligand surface density, $\rho_{R,T}$ is the total receptor surface density, ρ_c is the complex surface density, A is the area modeled, and N^2 is the total number of lattice sites in the model (N sites per side in the lattice). The quantities $(\rho_L A/N^2)$, $((\rho_{R,T} - \rho_C)A/N^2)$, and $(\rho_C A/N^2)$ are probabilities a given site on the lattice is occupied by a ligand, unbound receptor, or complex, respectively. The bond formation/break probabilities p_{on} and p_{off} are:

$$p_{on} = 1 \quad \textbf{(Eqn 5.10)}$$

$$p_{off} = p = e^{-\Delta E/kT} \quad \textbf{(Eqn 5.11)}$$

Equation (Eqn 5.9) is the lattice equivalent of the real-space mass action equation:

$$k_{on}\rho_L(\rho_R - \rho_C) = k_{off}\rho_C \quad \textbf{(Eqn 5.12)}$$

Thus the bond break probability p is related to the two-dimensional affinity constant K_D^{2D}:

$$K_D^{2D} = k_{off}/k_{on} = \rho_L(\rho_R - \rho_C)/\rho_C = p/a = [\text{area}^{-1}] \quad \textbf{(Eqn 5.13)}$$

Where a is the area per lattice site ($= A/N^2 = 1\text{x}10^{-12}$ cm^2/site). K_D^{2D} can in turn be related to the standard solution 3D K_D by considering the volume of the surface-localized receptor-ligand interactions. We assume the cell-substrate interface is planar in this model with a separation $d \sim 300\text{x}10^{-8}$ cm, consistent with the separation required for receptor-ligand interactions[9]. The 3D K_D is (in its standard units, assuming K_D^{2D} is in units of cm^{-2}):

$$\mathbf{K_D = (1{,}000K_D^{2D})/(dN_a) = (1{,}000}p\mathbf{)/(}d\ a\ \mathbf{N_a) = [mol/L]} \qquad \textbf{(Eqn 5.14)}$$

where N_a is Avogadro's number. Using our model parameters for d and a, the 3D $K_D = 5.53\text{x}10^{-4}p$. Figure 5.5 plots the equivalent 2D and 3D K_D's as a function of the binding probability p and the dimensionless binding energy $\Delta E/kT$.

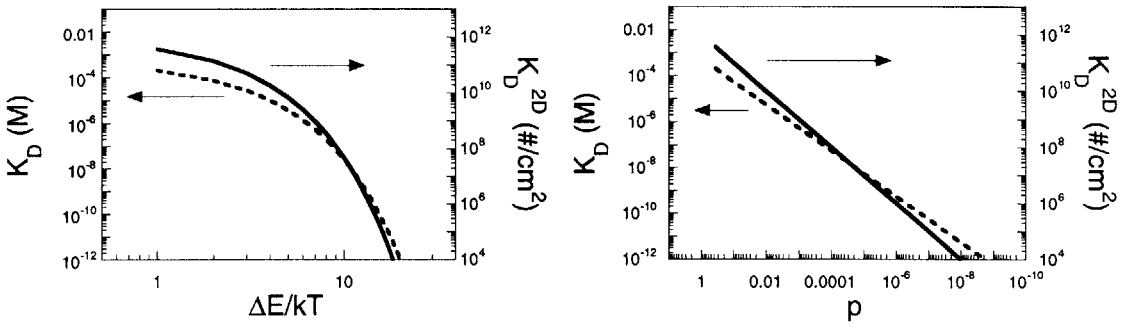

Figure 5.5. Two-dimensional and three-dimensional K_D's as a function of model parameters p and $\Delta E/kT$.

5.2 SCF Calculations of Comb Surface Segregation and Polymer/Water Interface Structures

5.2.1 Self-Consistent Field Description of Polymer Blend System

Self-consistent field (SCF) calculations were used to predict the one-dimensional concentration profiles of comb polymer/homopolymer surface-segregated blends and comb polymer/water or blend/water interfaces. An extension of the Scheutjens and Fleer lattice SCF theory[140-142] was used, which has been extensively treated in the literature[109, 115, 126, 140-144]. Polymer chains are modeled as chains of connected segments, each of which has the same size as a solvent molecule, equal to one lattice site in volume. No "free volume" is allowed in the system and every lattice site must be filled (statistically) by either a polymer or solvent segment. Any symmetries present in the system of interest are identified and used to limit the number of explicit contacts that must be counted when calculating the equilibrium segment distributions. Here the composition profiles of polymer/solution interfaces and blend surfaces modeled are inherently one-dimensional, varying only in the direction perpendicular to the substrate. Concentrations of the components will be uniform in a given plane parallel to the interface.

Our objective with these theoretical calculations is to predict the component concentration profiles of 1) comb polymer/homopolymer blends at equilibrium with water at the free surface, and 2) comb polymer/water interfaces.

5.2.2 Surface Segregation Calculations

Calculations were made for the case of blend thin films confined between two impenetrable planes, representing the substrate and contacting aqueous solution, respectively. Similar calculations for homopolymer blends were made previously by Hariharan et al.[115] The

lattice orientation for these calculations is shown in Figure 5.6. We modeled miscible polymer blends, so that the only expected gradients in the concentration profiles of the blend components will occur at the polymer/water interface, perpendicular to the plane of the film. Figure 5.6(a) depicts example one-dimensional volume fraction (ϕ) profiles for the matrix and comb polymer as might be obtained from the calculations. Polymer chains in the blend are modeled as connected segments on the three-dimensional lattice as shown in Figure 5.6(b). A mean-field approximation is applied within the plane of the substrate and the system is subdivided into layers (each one lattice site deep) of homogeneous polymer concentration (Figure 5.6(c)).

The polymer blend is comprised of two polymer chemical species, hydrophobic segments and hydrophilic segments, designated *A* and *B* respectively. Water at the free surface of the blend is considered as a single-segment molecule of a third chemical species, type *S*. Blends were modeled as mixtures of linear *A* homopolymer with comb polymers having *A* segment backbones and *B* segment side chains (or teeth). Contacts between polymer segments of type *A* and *B* are calculated statistically within the mean field approximation. The number of contacts of *A* on a given lattice site in layer z with neighboring *B* segments within the same layer, for example, is equal to the *A* segment concentration on the site $\phi_A(z)$, which is the same for all sites within layer *z*, multiplied by the statistical number of *B*-segment nearest neighbors within the same layer (the product of the *B* segment concentration within layer *z*, $\phi_B(z)$, and λ_0, the fraction of nearest-neighbor sites within layer *z*- for a hexagonal lattice, 6/8). Contacts between segments in adjacent layers are also calculated by mean-field approximation: the average number of contacts between a segment in layer *z* and layer *z+1* is simply the product of the volume fraction of polymer in sites at layer *z+1*, the volume fraction at sites in layer *z*, and the fraction of nearest neighbors connecting a given single site in layer *z* to layer *z+1* (λ_1, for a hexagonal lattice, 1/8).

Contacts between layer z and layer z-1 are found in a similar manner. Thus the total number of contacts n_{AB} between an A segment in layer z and adjacent B segments is:

$$n_{AB}(z) = \phi_A(z)[\lambda_1\phi_B(z-1) + \lambda_0\phi_B(z) + \lambda_1\phi_B(z+1)] = \phi_A(z)<\phi_B(z)> \qquad \text{(Eqn 5.15)}$$

The energy of contacts between the components of the system is given by the magnitude of the Flory-Huggins segmental interaction parameter χ for each chemical pair multiplied by the number of contacts and kT; increasing values of χ_{ij} correspond with increasingly unfavorable interactions between two segments of chemical type i and j. To model a miscible blend, χ_{AB} is fixed at 0.0. (Miscible polymers typically have interaction parameters near zero or very small negative values[145]). A relative attraction of the hydrophilic surface units to the water-contacting surface of the blend is modeled by setting $\chi_{BS} < \chi_{AS}$ (S designating the solvent contacting the blend at the free surface). In calculations specifically modeling polylactide/PMMA comb polymer blends, the B segment interaction with the surface is set to that of PEO with water[146], $\chi_{BS} = 0.4$, and the A segment interaction with the surface is set to $\chi_{AS} = 1.25$, providing a repulsion of the hydrophobic segments from the surface. This simple lattice model does not, however, allow explicit accounting of the entropic nature of the hydrophobic effect at the water/polymer interface. The relatively favorable localization of hydrophilic species at the surface is approximated only through the magnitude of each χ parameter.

The equilibrium distribution of polymer segments within the lattice is calculated by solving for concentration profiles of the components that satisfy a diffusion equation (maintaining chain connectivity and accounting for the configurational degeneracy of the system) subject to an external potential that maintains the constraint of incompressibility; the potential must be simultaneously self-consistent with the polymer concentration profiles. SCF calculations can provide a wealth of information on the system, including the 1D concentration

profiles of the polymer and solvent molecules, of individual segments of molecules, and also provides thermodynamic quantities such as the free energy or entropy of the system. The set of nonlinear equations governing the components and system constraints are solved by numerical iteration using an unconstrained nonlinear optimization routine[147]. The set of nonlinear equations used to describe the system and their solution are explained in more detail in Appendix B.

Calculation of theoretical concentration profiles for blends of comb polymers mixed with high molecular weight linear homopolymer having 1000 segments per chain (N = 1000, segment type *A*) were made. The comb consists of short teeth of type *B* ($N_{teeth} = 4$) spaced evenly every 7 units along a backbone of 150 *A* segments (20 total teeth per comb), providing a repeating structure as shown schematically in Figure 5.7. This architecture and composition models the C1 comb polymer prepared for experimental studies, providing similar mole and weight fractions of the hydrophilic side chain segments. The number of lattice layers (*M*) in blend calculations was fixed at 450 (assuming a segment size of ≈5 Å, this models a blend film ≈2,200 Å thick), except for calculations where the effect of film thickness was explicitly examined.

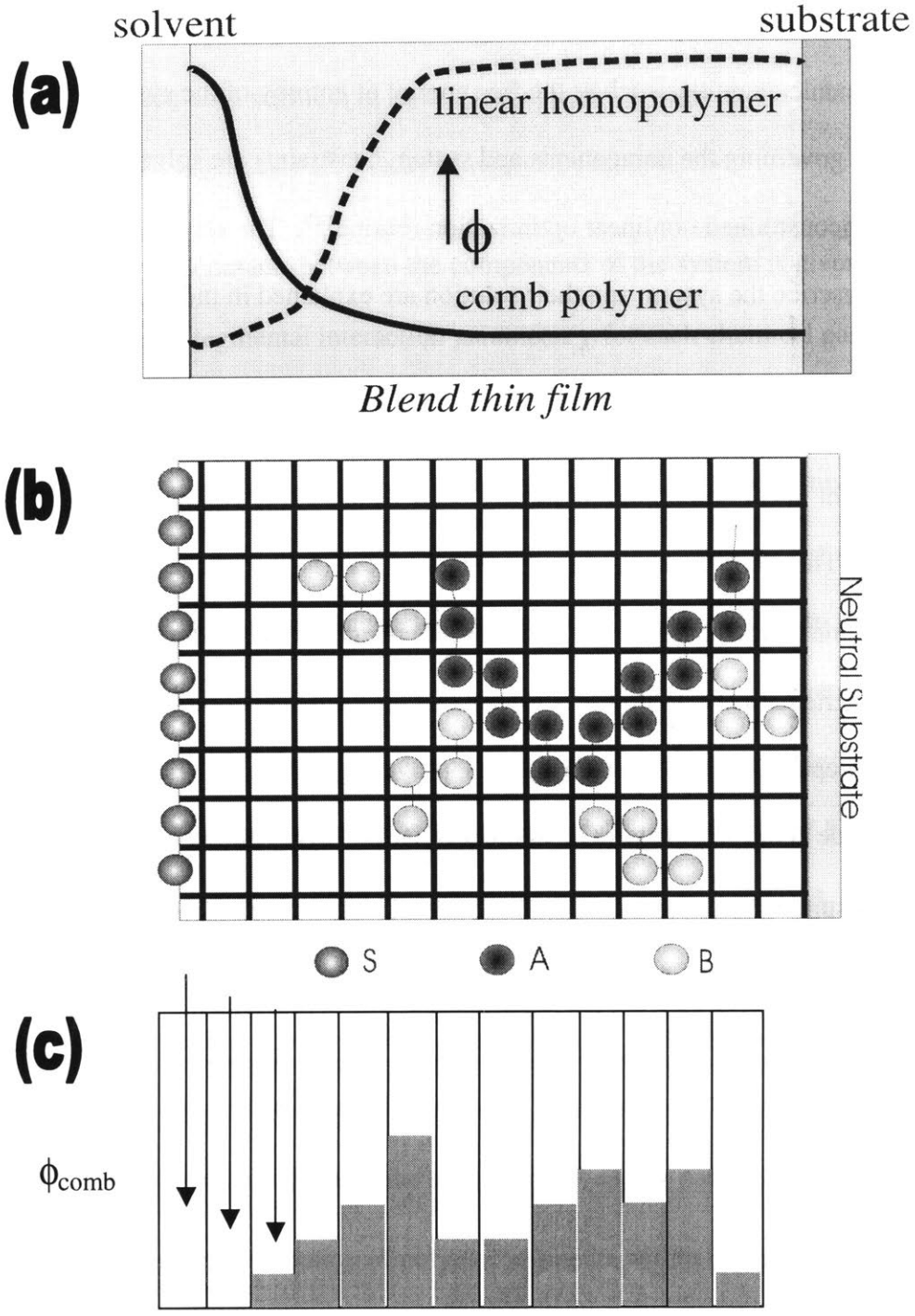

Figure 5.6. Schematic of blend systems and orientation of lattice for surface segregation calculations. (a) Schematic of blend thin film and concentration profiles in the blend. (b) Polymer chains are modeled as connected segments on a three-dimensional hexagonal lattice, confined between an impenetrable water interface and solid neutral substrate. (c) Lattice layer orientation for SCF model. Concentration variations are only considered in layers parallel with the substrate.

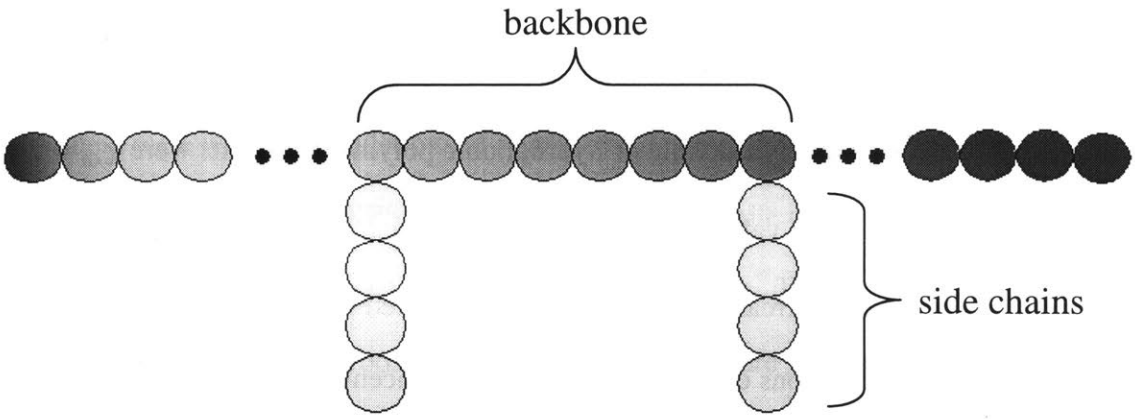

Figure 5.7. Comb Architecture for SCF Model. The comb additive consists of 20 side chains (chemical type *B*) of 4 units each, evenly spaced every 7 segments along a backbone (chemical type *A*) of 150 units.

5.2.3 Polymer/Water Interface Calculations

A second set of SCF calculations was made to predict the composition of comb polymer/water and blend/water interfaces. The lattice description of these systems remains as depicted in Figure 5.6, however, water is now explicitly included in the calculations as a single-segment molecule of type *S*. An example of the type of concentration profiles generated in these calculations is shown in Figure 5.8. The water/polymer interface is initially created by making calculations for a system with segment potentials biased to place polymer and solvent at opposite boundaries with χ interaction parameters set to induce phase separation. A semi-infinite system is modeled by using reflecting boundary conditions (component concentrations at the boundaries are set equal to those present in the adjacent lattice layer)[142]. The influence of system variables on the interface structure can then be examined in subsequent calculations, using the initial semi-infinite interface result to start numerical solutions of the model.

Interface structure calculations were made for comb polymer films in contact with water (presented in Chapter 8) and comb polymer/PLA blends in contact with water (presented in

Chapter 9). The architecture of the comb polymer and PLA used for these calculations was the same as that described above for SCF calculations of surface segregation. χ parameters modeling interactions between water and the hydrophilic or hydrophobic polymer segments were $\chi_{AB} = 0$, $\chi_{BS} = 0.4$, and $\chi_{AS} = 2.5$. This larger value of χ_{AS} vs. that used in the hard-wall segregation calculations counterbalances the increased entropy of mixing created by including the monomeric solvent in the calculations explicitly. Equilibrium concentration profiles calculated for each system component are presented.

5.3 Group Contribution Predictions of Polymer Physical Properties

Group contribution calculations were made following the procedure of Van Krevelen[148] to predict the molar volume and glass transition temperature (T_g) of the P(MMA-r-POEM) comb polymers synthesized in this work. Group contribution calculations predict physical properties of materials based on aggregate accounting of contributions due to individual chemical units of the molecules.

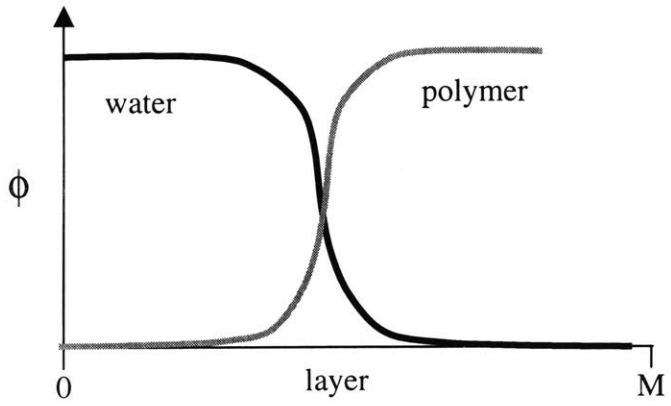

Figure 5.8. Concentration profiles as obtained in SCF interface structure calculations.

Properties are typically calculated as a sum of group contributions weighted by the mole or weight fraction of each group present in the material. Predicted molar volumes of comb polymers were used in calculations of near-surface compositions of poly(lactide)/comb polymer blends from experimental XPS data on blend surfaces, while the T_g calculations served to guide the choice of annealing temperatures in blend experiments. The results for each of these quantities calculated for carboxylated P(MMA-r-POEM) are summarized in Table 5.1 along with the values of polylactide (PLA, the matrix polymer for biodegradable blend studies) for comparison. Calculations were made for C1 P(MMA-r-POEM) (physical parameters and structure of this polymer are described in Chapter 6) assuming 100% carboxylation of POEM chain ends. The polymer contains 62 wt% methyl methacrylate, 18 wt% POEM, and 20 wt% methoxy-POEM.

P(MMA-r-POEM) Molar Volume Calculation

Molar volumes (V_a, amorphous state) were calculated as a sum of group contributions listed in Table 5.2 weighted by the mole fraction of each group in the materials. The amorphous/crystalline molar volumes of poly(lactide) have been determined experimentally in previous work by X-ray diffraction and densitometry[149] (amorphous molar volume V_a = 57.7 cm^3/mol, crystalline molar volume V_c = 55.8 cm^3/mol). However, to obtain an estimate of the molar volume of the carboxylated comb polymer, we used group contribution calculations, as predicted molar volumes for pure PMMA and PEO were in good agreement with experimentally measured volumes.

Table 5.1. Calculated physical properties of P(MMA-r-POEM) comb polymer and corresponding experimental data for polylactide.

Polymer	V (cm^3/mole)**	ρ (g/cm^3)**	T_g (°C)
PLA	55.72/50.85*	1.248/1.290*[149]	60[150]
C1	139.33	1.08	43

Calculated P(MMA-r-POEM) properties are compared with the experimentally measured values for PLA. *Amorphous and crystalline values, respectively. **Values at 298K and 1 atm pressure.

The molar volume of carboxylated P(MMA-r-POEM) was calculated as:

$$V_{comb} = \Sigma X_i V_i \qquad \textbf{(Eqn 5.16)}$$

Where X_i is the mole fraction of group i, V_i is the amorphous molar volume contribution from group i, and the summation was carried out for all groups present in the polymer, as outlined in Table 5.2. The calculated molar volume of the comb polymer and density are 139.3 cm^3/mol and 1.09 g/cm^3, respectively.

P(MMA-r-POEM) Glass Transition Temperature Calculation

The glass transition temperature of carboxylated P(MMA-r-POEM) was estimated using a group contribution formalism, in a manner similar to the calculation of molar volume. The glass transition is estimated as:

$$T_g = Y_g/M_0 = \Sigma Y_{g,i}/M_0 \qquad \textbf{(Eqn 5.17)}$$

where Y_g is the molar glass transition function, M_0 is the average repeat unit molecular weight, and $Y_{g,i}$ is the glass transition contribution of chemical group i in the polymer. The summation is carried out over each of the groups present on average per repeat unit. Using the composition of P(MMA-r-POEM) described above and the empirically determined values for $Y_{g,i}$ listed in Table 5.2 from Van Krevelen, we obtain a value of 43°C for T_g.

Table 5.2. Molecular contributions used in group contribution calculations.

Group	V_a (cm^3/mol)	$Y_{g,i}$ (K•g/mol)
$-CH_2-$	16.37	2700
$-C(CH_3)(COOCH_3)-$	74.7	35,100
-O-	8.5	4,000
-(CO)O-	23.0	8,000
$-CH(CH_3)-$	32.72	-
	-	-
$-CH_3$	-	-
	-	-
-COOH	-	8,000

From Van Krevelen[148].

6 Materials and Experimental Methods

6.1 Reagents, Polymers, and Peptides

Monomers and Chemicals. Methyl methacrylate (MMA), ethyl methacrylate (EMA), methyl acrylate (MA), butyl acrylate (BA), poly(oxyethylene) methacrylate (POEM, M_n ~ 360 g/mol), methoxy poly(oxyethylene) methacrylate (MPOEM, M_n ~ 300 g/mol, 475 g/mol, 1,100 g/mol, or 2,080 g/mol), tetrahydrofuran (THF), azo(bis)isobutyronitrile (AIBN), 1-methoxyphenol, succinic anhydride, anhydrous dichloroethane, N-methylimidazole, N-hydroxysuccinimide, dicyclohexylcarbodiimide, sodium cyanoborohydride, 9-anthracenemethanol, methacryloyl chloride, Tween 20 surfactant, diiodomethane, tritolyl phosphate, ammonium persulfate, anhydrous sodium sulfate, triethylamine, 2,2,2-trifluoroethanesulfonyl chloride, and dimethylformamide (DMF) were obtained from Aldrich. Phosphate buffered saline pH 7.4 and N-(2-Hydroxyethyl)piperazine-N'-(2-ethanesulfonic acid) (HEPES) buffer pH 7.4 were prepared from prepackaged dry packets from Sigma. Butyl methacrylate was obtained from PolySciences. Sodium hydroxide, petroleum ether, methanol, dichloromethane, anhydrous ethyl ether, ethyl acetate, and deuterated solvents were obtained

from VWR Scientific. N-(3-Dimethylaminopropyl)-N'-ethylcarbodiimide hydrochloride (EDC) was obtained from Pierce Chemical Company. All reagents were used as received unless otherwise noted.

Polymers. Poly(L-lactide) (M_n ~ 80,000-160,000 g/mol) and poly(D,L-lactide) (M_n ~ 100,000 g/mol) were obtained from Sigma. Poly(methyl methacrylate) (M_n = 168,000 g/mol, PDI = 1.07) was purchased from PolySciences.

Peptides and Proteins. Gly-Arg-Gly-Asp-Ser-Pro (GRGDSP) and Gly-Arg-Gly-Glu-Ser-Pro (GRGESP) peptides were obtained from Gibco. Gly-Arg-Gly-Asp-Ser-Pro-Lys (GRGDSPK) was obtained from American Peptide Company. Murine epidermal growth factor, human fibronectin, rat tail collagen, and bovine serum albumin were purchased from Sigma.

6.2 Comb Polymer Synthesis and Molecular Characterization

6.2.1 Comb Polymer Synthesis

The chemical structure of the comb copolymers prepared for these studies is shown in Figure 6.1. The combs are random terpolymers of MMA and two poly(ethylene glycol)-side chain units, poly(oxyethylene) methacrylate and methoxy-poly(oxyethylene) methacrylate. The comb polymers prepared for these studies all contained ~50:50 weight ratios of POEM (~6 EO repeat units) and MPOEM (~9 EO repeat units) except for two experiments where PEO content of combs and side chain length were specifically varied, as noted below. For brevity, the POEM/MPOEM/MMA comb polymers are referred to generically throughout as P(MMA-r-POEM). Combs were synthesized by free radical copolymerization of MMA and POEM monomers in THF, initiated by AIBN. The following represents a typical synthesis protocol: 21 mL MMA (19.7 g, 0.197 mol), 6.55 g POEM (0.0182 mol), 6.55 g methoxy-POEM (0.0138 mol), and 0.239 g AIBN (0.00146 mol) were added to 500 mL THF in a 1000-mL round bottom

flask equipped with a condenser. The solution was degassed by bubbling nitrogen 20 minutes, followed by refluxing at 70° C for 18 hours. The reaction was terminated by addition of 20-50 mg 1-methoxyphenol. The resulting copolymer was purified by two precipitations in 8:1 vol:vol petroleum ether:methanol and dried *in vacuo* at 25°C for 24 hours.

Physical characteristics of P(MMA-r-POEM) comb copolymers used in the majority of these studies are listed in Table 6.1. In order to maximize both the protein resistance of comb surfaces as well as the potential ligand density at comb surfaces, combs were prepared which maximized the weight fraction of PEO side chain units while maintaining water insolubility. Our criteria was a solubility of the comb in water < 0.001 g/mL. Combs comprised of ≤ 50 wt% POEM/methoxy-POEM monomers were by this definition water insoluble.

In addition to C1 and C2 listed in Table 6.1, two series of comb polymers were prepared to assess the effect of composition and side chain length on the resistance of comb surfaces to nonspecific cell adhesion. For these two experiments, comb polymers with molecular weights comparable to C1 were prepared as described above containing only MMA and methoxy-POEM (no POEM monomer).

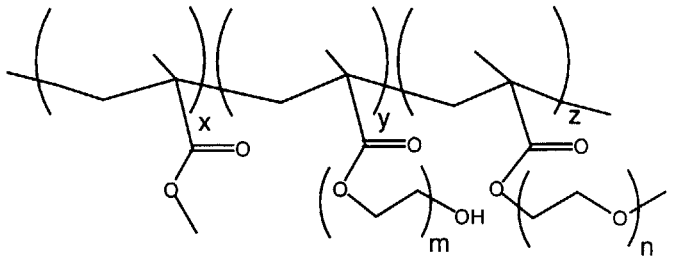

Figure 6.1. Base comb polymer structure. Repeat units are (x) methyl methacrylate (MMA), (y) poly(oxyethylene) methacrylate (POEM), and (z) methoxy-poly(oxyethylene) methacrylate (MPOEM). Side chain lengths used in the majority of these studies are m ~ 6 and n ~ 9.

Table 6.1. Comb polymer physical data.

Comb polymer	M_n (g/mol)	M_w (g/mol)	PDI	Composition (wt:wt:wt MMA:POEM:MPOEM)
C1	25,870	44,870	1.73	62:18:20
C2	93,900	192,000	2.04	66:16:18

To assess composition effects, combs were prepared containing 20, 30, or 45 wt% MPOEM (compositions determined by NMR). To examine side chain length effects, combs were prepared with 45 wt% total MPOEM, using MPOEM monomer having 5, 9, 23, or 45 ethylene oxide repeat units.

Fluorophore-labeled comb synthesis. Experiments to examine changes in comb stabilizer molecular weight during dispersion polymerization of latexes were performed using a comb containing a fluorescent monomer label. The fluorophore monomer was prepared by reacting 9-anthracenemethanol (2 g) with methacryloyl chloride (1.0 ml) in the presence of triethylamine (1.53 ml) in freshly distilled THF (50 ml) at 0° C for 2 hours, followed by stirring overnight at room temperature. The mixture was filtered, the solvent evaporated, and the monomer redissolved in dichloromethane. The solution was washed with 2 wt% aq. sodium hydroxide for 20 minutes followed by washing with several fractions of deionized water until the pH of the water fraction was neutral. The organic fraction was dried over anhydrous sodium sulfate and concentrated by evaporation. The resulting anthracene-methyl methacrylate (AnMMA) monomer was refrigerated until used. Fluorophore-labeled comb was prepared by copolymerization of MPOEM, MMA, and AnMMA (43:55:2 by weight) with AIBN followed by purification as described for comb polymer syntheses above.

NMR and Elemental Analysis

Comb compositions were determined using a Bruker Avance DPX400 proton NMR operating at 400 MHz. ^{1}H-NMR spectra were obtained for 1% copolymer solutions in deuterated chloroform or dimethyl sulfoxide. Yields of functionalization reactions were calculated from elemental analysis performed on samples by Quantitative Technologies, Inc.

Size Exclusion Chromatography

Molecular weights of the comb were determined using a Waters Associates gel permeation chromatography-laser light scattering system comprised of a model 510 pump, model 410 differential refractometer, miniDawn laser light scatterer, and two linear Styragel columns connected in series. Filtered copolymer solutions (0.004 g/mL) in THF were eluted at 30° C. Absolute number average and weight average molecular weights were obtained using the comb polymer *dn/dc* calculated according to[148]:

$$\mathbf{dn/dc = (n_{comb} - n_{THF})/\rho_{comb}} \qquad \textbf{(Eqn 6.1)}$$

Where n_{comb} is the refractive index of the comb polymer, n_{THF} is the refractive index of the solvent, and ρ_{comb} is the density of the comb polymer. The polymer refractive index was measured by ellipsometry (≈1.491), ρ_{comb} was estimated by group contribution methods as described in Chapter 6 (≈1.09 g/cm^3), and the value for n_{THF} used was 1.407[151]. This gives a value of *dn/dc* = 0.077 cm^3/g, intermediate between the values for PEO (0.068) and PMMA (0.089) in THF[152].

For characterization of comb polymer grafting to latexes (prepared as described below), anthracene fluorophore-labeled comb and a PMMA latex prepared using this labeled stabilizer were analyzed by a second GPC system in the laboratory of Professor Paula Hammond. This system utilized an ultraviolet detector measuring absorbence at 254 nm to detect only

fluorophore-labeled molecules in eluted samples of labeled and unlabeled polymers (Waters 515 pump, Waters 440 UV detector, and two Styragel columns, with THF as eluent at 1.0 ml/minute). At this wavelength, P(MMA-r-POEM) combs and PMMA latexes have no absorption band and are invisible to the detector, while the anthracene-labeled comb polymer or latexes prepared with this labeled comb provide a strong UV signal.

Peptide Coupling

Three different methods were demonstrated for coupling peptides to comb polymers or comb polymer surfaces as outlined in Figure 6.2: pre-coupling the peptide to comb in solution (before preparing surfaces), surface coupling peptide to pre-activated comb surfaces, or activating surfaces *in situ* just prior to surface coupling. Surface coupling allows one to minimize the amount of a precious peptide used, as coupling can be carried out with a minimal volume of dilute peptide solution. However, the solution pre-coupling method (Figure 6.2(a)) was used for the majority of tethered RGD studies, as this route allows the preparation of many surfaces with controlled, repeatable total ligand density and ligand cluster size by using the same batch of RGD-comb polymer in each experiment. These chemistries were performed through activation of the hydroxyl ends of the POEM side chains with an amine-reactive group, as outlined in Figure 6.3 for NHS activation and Figure 6.4 for tresyl chloride activation.

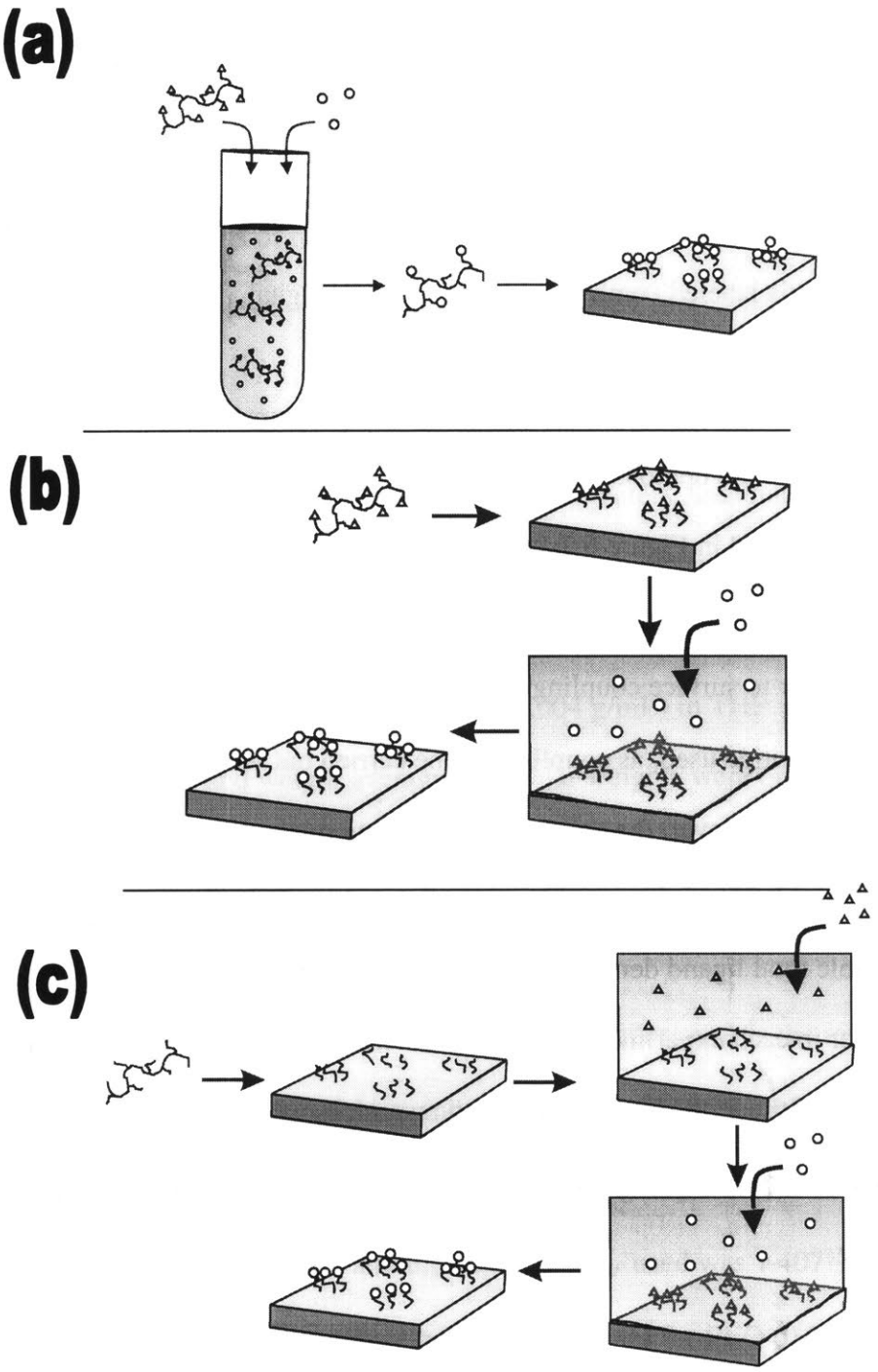

Figure 6.2. Chemical routes used to couple peptides to comb polymer. Symbols: (•) activated comb polymer end group. (•) peptide. (a) Activated comb polymer is coupled to peptide in solution. (b) Films of activated comb polymer are prepared and peptide is coupled to surfaces from solution. (c) Films of comb polymer are prepared and activated *in situ*, followed by peptide coupling to the surface from solution.

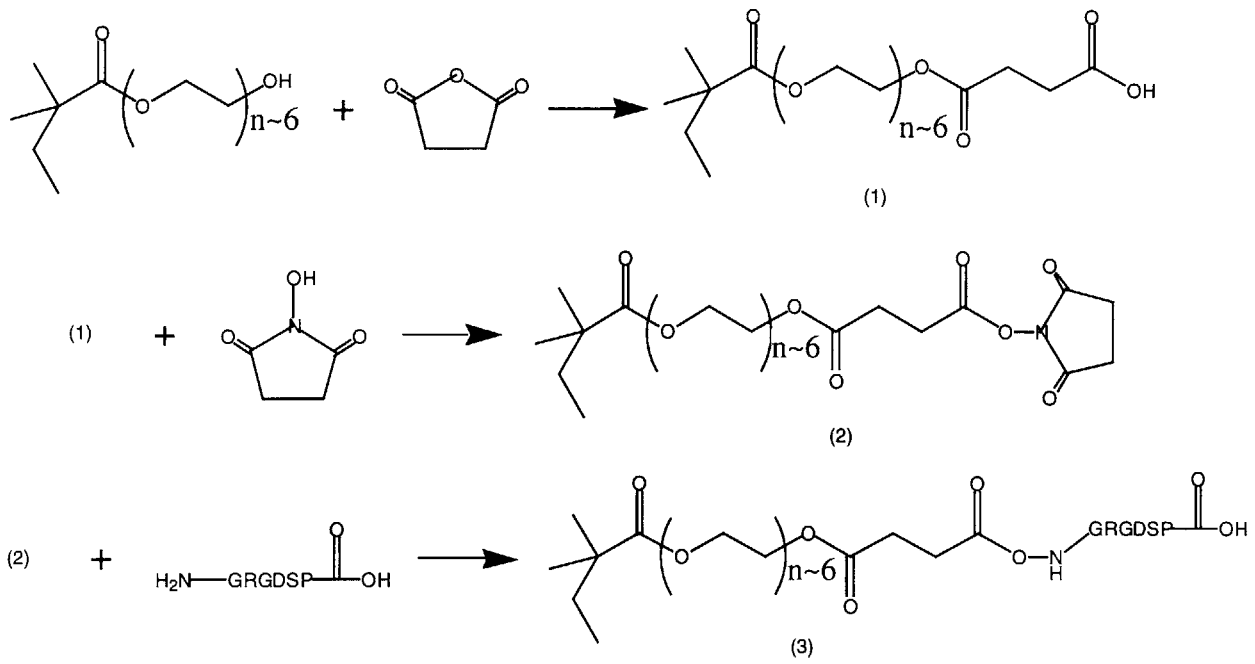

Figure 6.3. Carboxylation, NHS activation, and peptide coupling chemistries used for modification of comb polymers. Products in each step are (1) carboxylated comb, (2) NHS-activated comb, and (3) RGD-comb.

$$R\text{-}(O\text{-}CH_2\text{-}CH_2)_n\text{-}OH \;+\; Cl\text{-}SO_2\text{-}CH_2\text{-}CF_3$$

$$\downarrow \text{(TEA)}$$

$$R\text{-}(O\text{-}CH_2\text{-}CH_2)_n\text{-}O\text{-}SO_2\text{-}CH_2\text{-}CF_3 + NH_2\text{-}\mathbf{R'}$$

$$\downarrow$$

$$R\text{-}(O\text{-}CH_2\text{-}CH_2)_n\text{-}O\text{-}SO_2\text{-}CH_2\text{-}CO\text{-}NH\text{-}\mathbf{R'}$$

Figure 6.4. Tresyl Chloride Activation Chemistry.

Carboxylation of comb polymer. The first step for peptide linking via the NHS route was carboxylation of the comb polymer, carried out using a modification of the procedure of Storey and Hickey[153]. The following represents a typical synthesis: 8 g comb polymer (0.00889 mol -OH) and 4 g succinic anhydride (0.0889 mol) were added with magnetic stir bar to a hot 500-mL round bottom flask removed from a drying oven (T ~ 150°C). The reactor was capped

with a rubber septum and purged with nitrogen until cool. 200 mL anhydrous dichloroethane was cannulated into the flask. The copolymer was observed to quickly dissolve while the succinic anhydride remained suspended in the solvent. The mixture was degassed 15 minutes by bubbling nitrogen, then 48 μL N-methylimidazole (NMIM) was added dropwise to the reactor. Upon addition of NMIM, the solution rapidly cleared. The flask was connected to a condenser and refluxed 15 hours at 65° C. The carboxylated comb polymer was separated from unreacted succinic anhydride and NMIM by concentrating in a rotovaporator, precipitating in petroleum ether, redissolving in THF, and precipitating in 5 vol% aqueous HCl. The polymer was washed 18 hours by stirring in 5 vol% aq. HCl, recovered by filtration, and dried at 60° C *in vacuo*.

NHS-activation of carboxylated comb polymer. Carboxylic acid groups of the comb polymer were activated using N-hydroxysuccinimide and carbodiimide, following a modification of the procedure of Jo and Mikos[154]. The following is a representative synthesis: 4.75 g carboxylated comb, 0.526 g N-hydroxysuccinimide, and 45 mL dichloromethane (DCM) were added to a 100-mL round bottom flask. The carboxylated copolymer swelled but did not dissolve in DCM. 0.942 g dicyclohexylcarbodiimide (DCC) was dissolved in 5 mL DCM and immediately added dropwise to the stirring comb/NHS/DCM mixture. Within 15 minutes the mixture became briefly clear (comb polymer dissolves as carboxylate groups are activated by DCC) then cloudy again as the dicyclohexylurea side product of the reaction was produced. The mixture was stirred 12 hours at room temperature. The NHS-activated polymer was purified by precipitating in anhydrous ethyl ether 2-3 times (redissolving in ethyl acetate at 0.05 g/mL for second and third precipitations). NHS-activated comb polymer was stored at -20°C until used.

Example NMR spectra of C1 P(MMA-r-POEM), carboxylated C1, and NHS-activated C1 are shown in Figure 6.5. The spectrum of the unmodified copolymer is characterized by the

strong peaks at ~3.6 ppm due to the MMA -OC$\underline{H}_3$ protons and the side chain -C$\underline{H}_2$C$\underline{H}_2$O- protons, as well as the backbone vinyl/methyl group peaks at ~1-2 ppm. The carboxylated product shows the introduction of a signal at 12.17 ppm due to the -COO$\underline{H}$ proton and a shift of the peak for the last pair of protons in the POEM side chains from 4.03 to 4.13 ppm. Activation of the carboxylated comb with NHS removes the carboxylate proton signal and introduces peaks for the succinimidal protons at 2.76 to 2.95 ppm. Separation of unreacted reagents and by-products in each functionalization step was confirmed by GPC (data not shown). Yields from each of the comb modification reactions were calculated from elemental analysis of polymer samples. Example results for the C1 P(MMA-r-POEM) before and after functionalization are listed in Table 6.2, along with the calculated yields.

Tresyl chloride activation of comb polymer. As an alternative to functionalizing carboxylate groups on the comb polymer, tresyl chloride chemistry was used to bond amine-reactive groups to hydroxyl chain ends[155]. Activation of hydroxyl groups was achieved by reacting the comb polymer with tresyl chloride (2,2,2-trifluoroethanesulfonyl chloride). The comb polymer (150 mg) was dissolved in 25 ml dry THF at 4° C. Triethylamine (200 µl) and tresyl chloride (250 µl) were added dropwise and the reaction was allowed to proceed with stirring at 4°C for 3 hours. The activated polymer was then recovered by filtration and precipitation in petroleum ether, dried *in vacuo*, and stored at -20°C until used.

Table 6.2. Example elemental analysis results for functionalized comb polymers.

Sample	*Wt% C*	*Wt% H*	*Wt% N*	*Wt% O*	*mol % groups functionalized*	*μg peptide/mg copolymer*
carboxylated C1	57.08	8.15	<0.05	33.36	100.0*	-
NHS-activated C1	56.95	7.98	0.55	34.19	86.0**	-
GRGDSP-coupled C1	56.55	8.11	1.16	32.33	88.0***	50.95

***mol% available hydroxyl groups converted to carboxylate, calculated from wt% C. **mol% available carboxyl groups activated by NHS, calculated from wt% N. ***mol% available NHS groups converted to amide linkages, calculated from wt% N.**

Table 6.3. RGD-functionalized comb polymer physical data.

polymer	*base material*	*peptide linked*	*μg peptide/mg polymer*	*# peptides/molecule*
C1-RGD1	C1	GRGDSP	50.9	2.10
C2-RGD1	C2	GRGDSPK	12.4	1.69
C2-RGD2	C2	GRGDSPK	16.0	2.18
C2-RGD3	C2	GRGDSPK	26.6	3.62
C2-RGD4	C2	GRGDSPK	40.0	5.44
C1-RGE1	C1	GRGESP	37.9	1.6

RGD coupling to activated comb polymers. GRGDSP, GRGDSPK, or the inactive analog GRGESP was covalently linked via an amide bond to the POEM side chain ends. GRGDSPK peptides were utilized in order to facilitate labeling of surface peptide by fluorescent markers. RGD-functionalized comb polymers were prepared in solution by coupling RGD to the NHS-activated comb polymers in DMF/water mixtures using a modification of the procedure of Jo and Mikos[154].

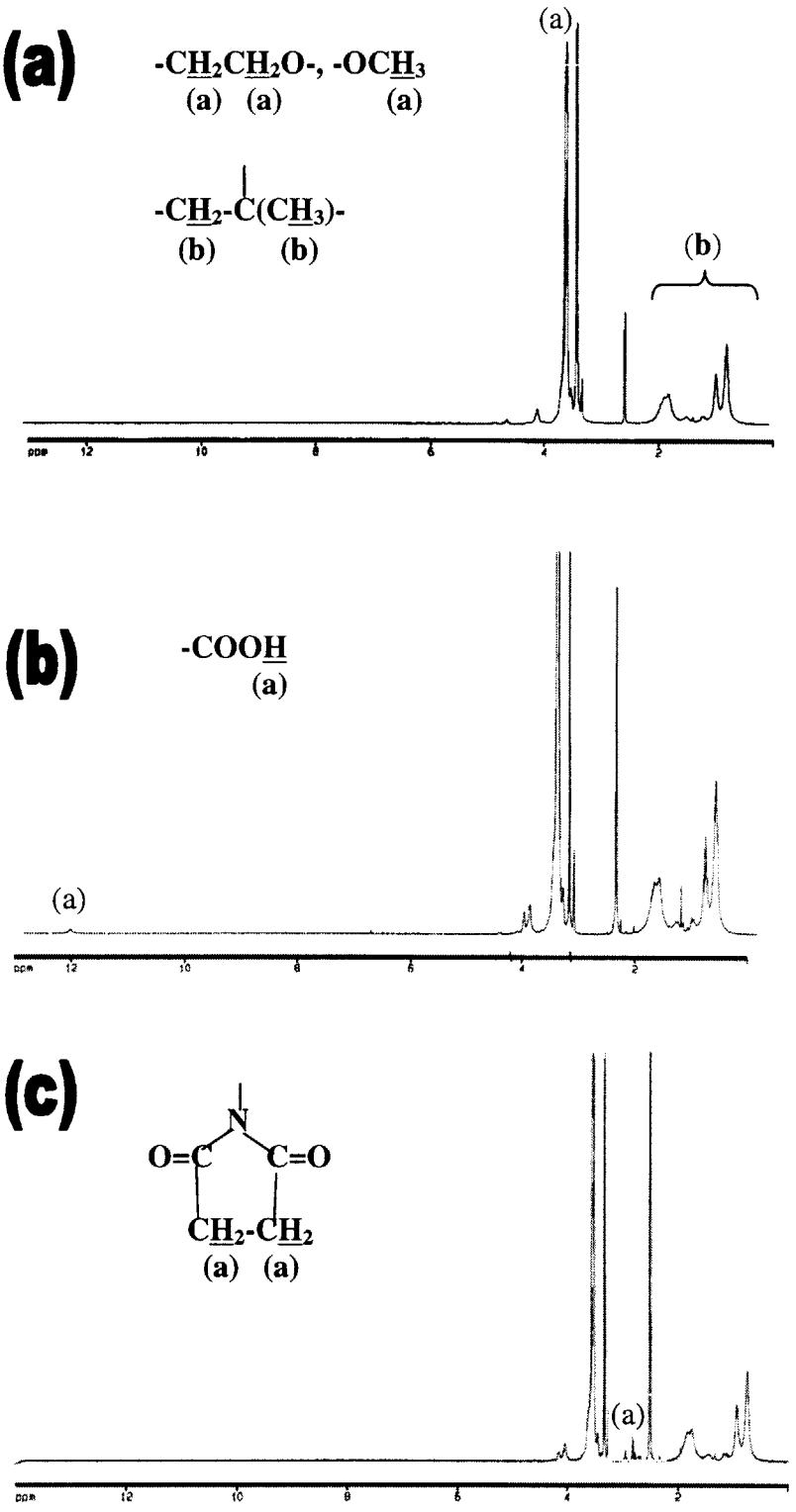

Figure 6.5. ^{1}H NMR spectra of P(MMA-r-POEM) comb polymer after activation reactions. NMR spectra obtained for copolymers in 0.01 g/mL deuterated DMSO. (a) C1 P(MMA-r-POEM) polymer; (b) carboxylated C1; (c) NHS-activated C1.

In a typical reaction, 6.2 mg GRGDSP was dissolved in 2 mL PBS. 100 mg NHS-activated comb copolymer (4.5X excess carboxylate groups) was dissolved in 2 mL anhydrous DMF. Peptide and comb solutions were chilled with stirring at 4° C for 30 minutes. The comb solution was then added dropwise to the stirring peptide solution at 4° C. As the reaction progressed, a milky emulsion formed. The reaction was allowed to proceed with stirring at 4° C for 12 hours, after which the emulsion was evaporated under low heat (T = 35-40°C) in a chemical hood. The recovered polymer was separated from any remaining free peptide and hydrolyzed NHS by dialysis: the polymer was redissolved in 3 mL 50/50 vol/vol water/ethanol and injected into a dialysis cassette (Pierce Slide-A-Lyzer, 3500 g/mol molecular weight cutoff). The cassette was immersed in 2 L 50/50 vol/vol water/ethanol and stirred for 3 days with periodic changes of the medium. Finally, the purified copolymer was recovered by evaporating the dialyzed solution under low heat (T = 35-40°C) and drying the product *in vacuo* at 25° C for 24 hours. Peptide-linked combs were stored at room temperature. Variations in the total RGD content were obtained by changing the ratio of peptide to polymer during the solution coupling reaction. Solution coupling of GRGESP and GRGDSPK was carried out in a similar manner. Coupling of GRGDSPK through the ε-amine of the lysine (K) group is expected to be negligible due to the much lower reactivity of the Lys amine relative to the N-terminal amine (Pierce Chemical Co., private communication). Table 6.3 lists the physical data for the number of peptides incorporated per molecule in each polymer, calculated from elemental analysis results.

To demonstrate flexibility in ligand coupling to comb polymer surfaces, two alternative approaches were used. First, peptides were coupled to NHS-activated thin films of comb polymer (1,500 Å-thick films prepared on tissue culture polystyrene dishes as described below). GRGDSP peptides were dissolved at 1.0 mg/mL in pH 7.4 PBS followed by incubation of the solution over the comb film surface at 4°C for 6 hours. The surfaces were rinsed twice briefly in

PBS, then stored in PBS at 4°C until use. GRGESP was coupled to NHS-activated C1 surfaces in a similar manner. Controls for the nonspecific adsorption of peptides to comb surfaces were prepared by exposing unactivated carboxy-comb films to peptide solutions and rinsing in the same manner used for linkage of peptides to the NHS-activated films.

As an alternative coupling route, a "one step" coupling procedure was performed through *in situ* NHS activation and immediate peptide coupling to comb polymer films. Carboxylated comb films (1,500 Å thick) were first prepared by spincoating from water/ethanol solution onto tissue culture polystyrene 35mm diameter dishes (as described below). For peptide linking, 9 mg EDC and 15 mg NHS were dissolved in 4 mL PBS and immediately applied (1 mL per surface) to dishes. Surfaces were left in contact with the solution 20 minutes at room temperature, followed by 2X rinsing with 1mL PBS. 1 mL of GRGDSP solution (0.5 mg/mL in PBS) was immediately applied to each surface, and stored at 4°C for 6 hours. Each surface was subsequently rinsed twice with PBS for 20 minutes each wash. Surfaces were stored under PBS until used.

RGD-comb for the synthesis of an RGD-functionalized latex was prepared by solution coupling peptide to tresyl-activated C1. Tresylated comb polymer was prepared as described in section 6.2.1. Peptide was coupled to the chain ends of tresyl-activated comb polymer in solution: 150 µl GRGSP solution (1 mg/ml in pH 7.4 phosphate buffered saline) was added to 2.5 ml of activated comb solution (0.02 g/ml tresylated C1 in THF) at 5° C and stirred for 3 hours. The RGD-coupled comb was recovered by overnight precipitation in deionized water and purified by dialysis as described above.

EGF coupling to comb polymer surfaces. Tethered EGF surfaces were prepared in collaboration with MIT Graduate Research Assistant Terry Johnson. 6,100 g/mol murine epidermal growth factor was tethered to tresyl chloride-activated comb polymer films from

solution. The reaction of an amine-bearing peptide with the tresyl groups of the comb surface is outlined in Figure 6.4.

1,500 Å-thick comb polymer thin films were spincoated on glass coverslips as described below. EGF was coupled to tresyl-activated chain ends at the surface of comb polymer thin films via incubation of the activated surfaces in aqueous EGF solutions. In a typical reaction, 100 μL EGF (5 μg/mL in PBS) was applied to 0.785 cm^2 comb polymer surfaces and left over the activated film at 4°C for 3 hours. Excess peptide was removed by rinsing with PBS twice for 20 minutes each rinse. Yields of EGF coupling to comb surfaces were determined by T. Johnson by coupling ^{125}I radiolabeled-EGF to surfaces and measuring the radioactivity with a phosphor plate imager. Radioactivity was converted to EGF molecules/area by comparing the phosphor imager counts with standards of known ^{125}I-EGF concentration. Results are presented in Figure 6.6. EGF can be coupled at receptor-saturating surface densities (~ 1 ng/cm^2)[44] while maintaining low nonspecific peptide adsorption on the film.

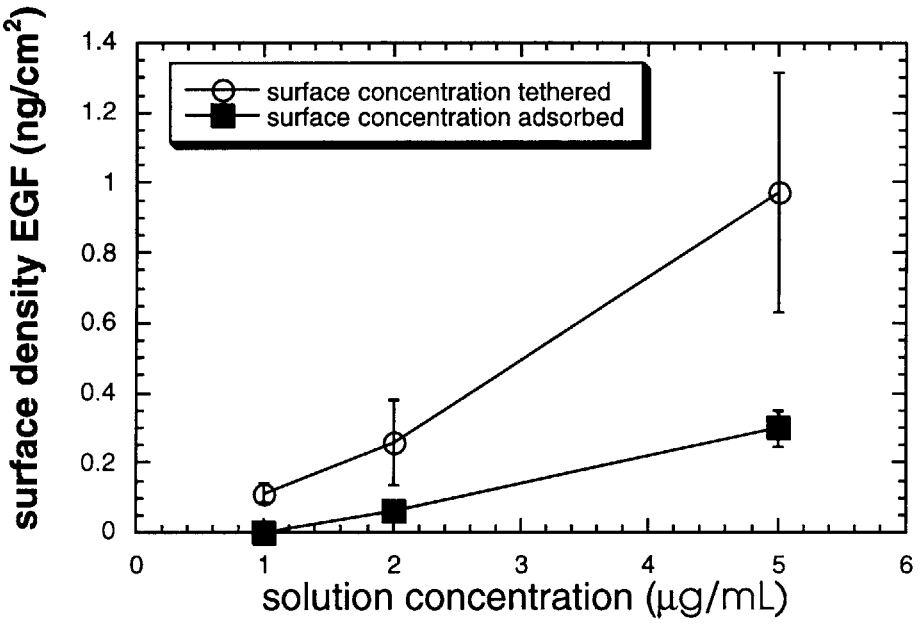

Figure 6.6. EGF covalent coupling and nonspecific adsorption during linkage to comb polymer surfaces.

Surfaces presenting 1 ng/cm^2 EGF were used in PC12 differentiation experiments on tethered EGF. To successfully induce differentiation of PC12 cells, the tethered growth factor might need to be stably presented at the surface for several days[156, 157]. Since the growth factor has an order of magnitude larger molecular weight than RGD ligands, slow dissolution of the ligand-functionalized molecules could be an issue. Stability of EGF surfaces was monitored by taking phosphor plate imager measurements on EGF surfaces after 7 days immersion in PBS at 4°C or 3 days immersion in PBS at 37°C. Over several days, only a few percent of the molecules were lost, as shown in Figure 6.7. As well, the small amount released may be untethered adsorbed peptide that became unbound from the surface. The amounts of EGF released, in the volume of the cell culture plates used for experiments, amount to concentrations well below the threshold level of soluble EGF required to elicit cellular responses from PC12 cells.

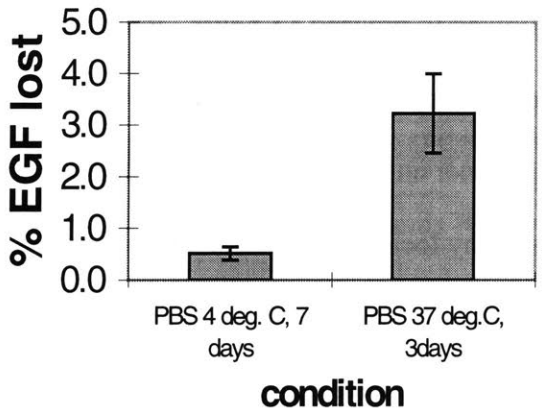

Figure 6.7. Stability of tethered EGF surfaces.

6.3 Synthesis and Characterization of Comb-Stabilized Latex Spheres

Latex spheres stabilized by P(MMA-r-POEM) comb polymer were prepared for the creation of large-domain clustered ligand surfaces. Dispersion polymerization was performed to obtain comb-stabilized beads with sizes ranging from ~0.1-1 μm in diameter. Four latex compositions were synthesized, using different methacrylate and acrylate monomers. Latex synthesis and characterization were carried out in collaboration with MIT Postdoctoral Research Scientist Dr. Pallab Banerjee.

Dispersion Polymerization

Methacrylate- and acrylate-based polymer latexes were synthesized by dispersion polymerization employing the comb polymers as stabilizing agents. Dispersion polymerization of vinyl monomers in the presence of the comb polymer proceeds as outlined in Figure 6.8[39]. Comb stabilizer (C1) was dissolved in 50 mL of a 1:1 vol:vol mixture of ethanol and water, followed by addition of methacrylate/acrylate monomers and 0.57 g ammonium persulfate. Table 6.4 lists the amounts of monomer and stabilizer used in each synthesis. Syntheses were initiated by heating at 60°C with stirring and allowed to proceed 18 hours. Reactions began as one phase, clear solutions, and became opaque white dispersions during polymerization. Upon progression of chain growth, the nascent polymer chains are insoluble in the medium and begin to precipitate. This agglomeration is arrested by localization of the stabilizer at the polymer/solution interface. As the synthesis proceeds, the comb-stabilized polymer particles grow homogeneously and provide nearly monodisperse latex spheres of submicron to micron size. At completion of the syntheses, dispersions were purified by repeated centrifugation and redispersion in water/ethanol 5 times. Suspensions were stable over >24 hour periods and could be resuspended after extended storage via ultrasonic mixing. All latexes were ultrasonically treated for at least 30

minutes prior to use. Comb-stabilized latexes of four different compositions were prepared: pure poly(methyl methacrylate), poly(methyl methacrylate-co-butyl acrylate), poly(ethyl methacrylate-co-methyl acrylate), and poly(ethyl methacrylate-co-butyl methacrylate).

Peptide-Linked Latex Sphere Synthesis

RGD-functionalized latexes were prepared by synthesizing latexes using peptide-functionalized comb stabilizer prepared as described in 6.2.1. The functionalized comb was used as a stabilizer for synthesis of a PMMA latex, using reagents as listed in Table 6.4. Interestingly, use of the RGD-coupled comb stabilizer caused a 10-fold reduction in average particle size and 2-fold increase in molecular weight. It is difficult to interpret this effect, due to the complex ionic and hydrophilic-hydrophobic interactions that the peptide introduces to the system.

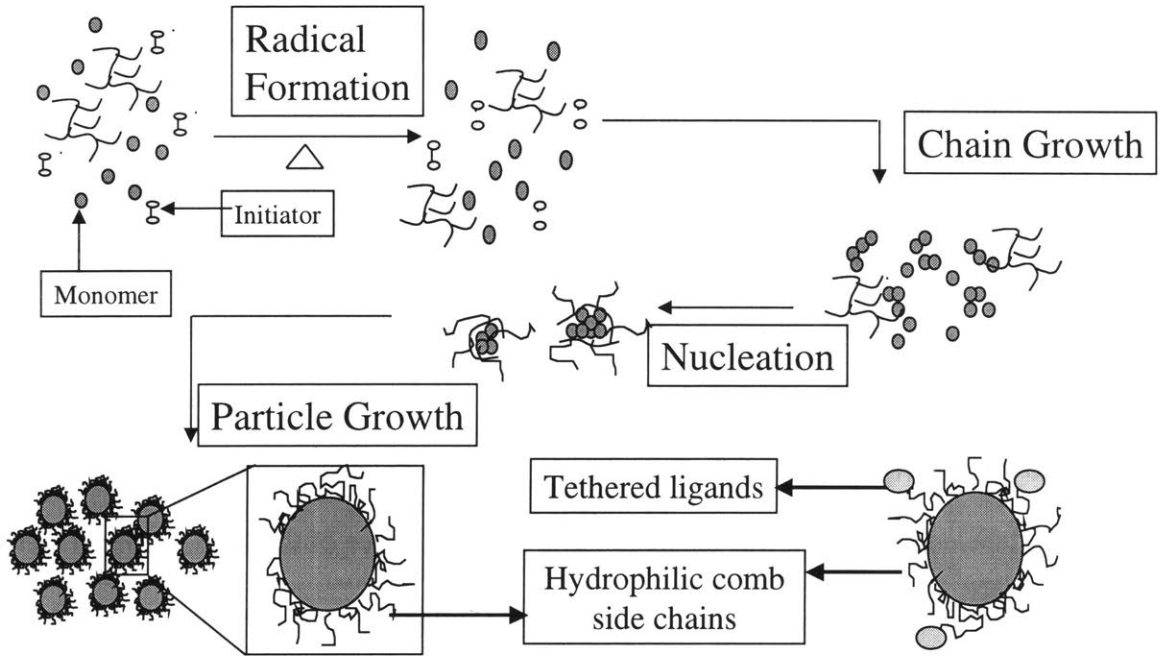

Figure 6.8. Dispersion polymerization of comb-stabilized latex nanospheres.

The RGD-bearing latexes were also found to be exceptionally stable in water/alcohol medium, presumably due to the increased solubility of the peptide-functionalized comb in water/alcohol mixtures.

Characterization of Latexes

Molecular weights and compositions of the latexes were obtained as described above for comb polymers using size exclusion chromatography and NMR, respectively. Molecular weights, glass transitions, average particle size/polydispersity, and composition of the latexes are listed in Table 6.4. From the NMR and GPC data, the stabilizer was found to comprise only ~1 wt% of the latex beads.

These latex nanospheres, as schematically shown in Figures 4.4(b) and (c), are expected to have a very thin layer of comb polymer localized at their surface; such latexes are typically stabilized by a monolayer of the surface-active polymer[83]. However, the stabilizer is often permanently grafted to the high-molecular weight core polymer chains[39, 195], providing well-anchored, highly entangled covalent tethers between the stabilizer and core of the beads- and thus a robust surface layer. To examine whether grafting of the stabilizer to the core occurs in P(MMA-r-POEM)-stabilized latexes, a PMMA latex was also prepared using a fluorescently-labeled comb polymer. GPC traces of the labeled comb polymer and the latex prepared using the labeled comb are shown in Figure 6.9. By using an ultraviolet detector, a GPC trace of only the fluorescently-labeled molecules was obtained. The UV GPC trace of the latex prepared using labeled P(MMA-r-POEM) shows that the fluorescent comb polymer is grafted to the core molecules, as the molecular weight of the polymer detected by UV is the same as that of the core polymer.

Morphology of the latex beads was assessed by examining beads cast onto glass coverslips with a JEOL 6320 field emission scanning electron microscope operating at a 4.0 kV

accelerating voltage. SEM images were obtained by Dr. Pallab Banerjee and MIT Graduate Research Assistant Jon Hester. Samples were shadowed with gold prior to imaging. Average particle diameters were measured from SEM micrographs, with at least 300 particles measured for each sample. Polydispersities were calculated as the weight average diameter divided by the number average diameter of the particles. All latexes were nearly monodisperse, as evidenced by the size polydispersities listed in Table 6.4. Variation of the methacrylate/acrylate monomers used in the synthesis (while maintaining constant overall concentration of monomer, stabilizer, and initiator) had a relatively strong influence on the final size of the latex beads. This is to be expected, since the solubility of the resulting polymers in the dispersion medium directly affects particle size[39, 87, 88].

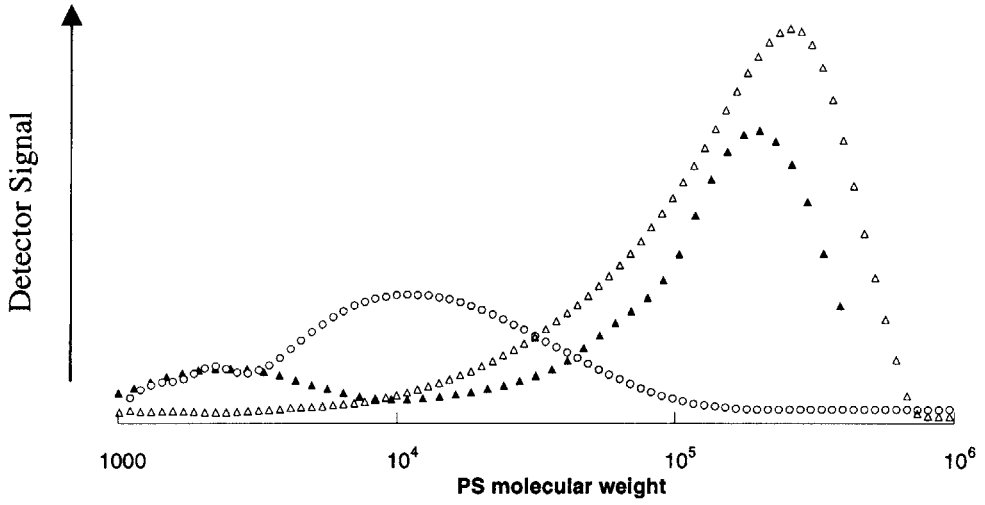

Figure 6.9. GPC traces showing grafting of P(MMA-r-POEM) to the high molecular weight core of PMMA latexes. Shown are the GPC detector signals from size exclusion chromatography of fluorescently labeled P(MMA-r-POEM) (○ refractive index detector) or a PMMA latex synthesized with fluorescent comb (△ refractive index detector, • UV detector).

Hydrophobicity of the product polymers increases in the order P(EMA-co-BMA), P(MMA-co-BA), P(EMA-co-MA), PMMA, and the average particle size similarly increased in this order.

Table 6.4. Comb polymer latex synthesis conditions and properties.

Sample	$[S]_0$ (g/mL)[a]	$[M]_0$ (g/mL)[b]	Final Composition (wt%)	M_W (g/mol)	T_G (°C)[d]	Diam. (μm)	PDI[c]
P(MMA-co-BA) latex	0.03	0.06 MMA, 0.04 BA	27:73 MMA:BA	515,218	-26	1.2	1.054
P(EMA-co-BMA)	0.025	0.09 EMA, 0.011 BMA	18:82 EMA:BMA	471,329	28	0.21	1.056
P(EMA-co-MA) latex	0.027	0.063 EMA, 0.03 MA	51:49 EMA:MA	591,960	35	1.3	1.035
PMMA latex	0.026	0.10	100 MMA	413,805	105	1.8	1.041
RGD-PMMA latex[c]	0.01	0.10	100 MMA	1,035,000	105	0.49	1.055

[a] **$[S]_0$ = initial comb stabilizer concentration**

[b] **$[M]_0$ = initial monomer concentration**

[c] **PMMA latex prepared with RGD peptide-linked comb stabilizer**

6.4 Sample Preparation and Characterization

6.4.1 Comb Polymer and Latex Thin Films

Comb Polymer Thin Film Preparation

Comb polymer thin films for surface characterization and cell culture experiments were prepared by spincoating or solvent casting, using glass, single crystal silicon, or tissue culture polystyrene (TCPS) substrates. Cell culture substrates were 30 mm glass dishes (Kontes) or TCPS culture plates (Falcon), while single crystal silicon wafers were used for contact angle and X-ray

photoelectron spectroscopy measurements. Glass and silicon substrates were cleaned by immersion in concentrated sulfuric acid for two hours, followed by rinsing with distilled deionized water and drying under a dry nitrogen stream.

Comb polymer thin films on glass or silicon were prepared by spincoating 0.01 g/mL chloroform solutions of the comb copolymer on substrates at 1000 rpm and drying *in vacuo* for 24 hours at 25°C, providing films ~1,500 Å thick. Films prepared on TCPS were solution cast from 0.002 g/mL solutions of comb polymer in 50/50 vol/vol water/ethanol, to obtain films ~5,000 Å thick. Solvent cast films were covered and dried at room temperature for 5 hours followed by drying *in vacuo* at 25°C for 24 hours. Films were stored *in vacuo* at 25° C until used, typically less than 48 hours.

Latex Film Preparation

Films were prepared from latex suspensions by spincoating the particles (0.02-0.03 g/ml in 50/50 vol/vol water/ethanol) at 1,000 rpm onto cleaned 18 mm No. 2 glass coverslips (VWR Scientific). To form contiguous films from the cast particles, short heat treatments (30 – 60 seconds) were applied to the samples by a heat gun set at 800-900° C from a distance of ~0.5 cm. Resulting films were optically clear; coalescence of the particles was confirmed by examining the surfaces in a light microscope. Poly(methyl methacrylate) homopolymer (not a latex) served as a control substrate. PMMA (PolySciences, 68K g/mole, M_w/M_n = 1.07) films were spincoated from a 0.03 g/ml toluene solution onto clean glass coverslips at 1,000 rpm, followed by drying *in vacuo* at 70°C for 24 hours. Films were stored *in vacuo* at 25° C until used, typically less than 48 hours.

Embedded Latex Film Preparation

Embedded latex films were prepared by first spincoating a film of the comb polymer ~2,000 Å thick from 0.02 g/ml 50/50 vol/vol water/ethanol solutions at 1,000 rpm, followed by immediate spincoating of a diluted water/ethanol suspension of the desired latex particles atop this film. The subsequent spincoating step thinned the underlying comb layer to ~500 Å. Latexes were embedded at three different surface densities using suspension concentrations of 0.001 g/ml, 0.01 g/ml, and 0.02 g/ml. Light microscope imaging of the embedded particle surfaces revealed particle separations of approximately 2 μm, 1 μm, and close packing for these concentrations, respectively. Swelling and partial dissolution of the comb films during casting of the latex suspension aided adhesion of the particles to the film once dried. Films were stored *in vacuo* at 25° C until used, typically less than 48 hours.

6.4.2 Poly(lactide)/Comb Polymer Blends

Blend Thin Film Preparation

Polymer blend thin films were prepared by co-dissolving 2 –20 wt% C1 or C2 comb polymers with PLA matrix homopolymers. Characteristics of the matrix homopolymers are listed in Table 6.5. Chloroform solutions (0.03 g/mL) were stirred • 3 hours to homogenize and subsequently spincoated at 1,000 rpm on 30 mm glass culture dishes (Kontes). Films were dried 24 hours at 25° C *in vacuo*. Film thicknesses for PLA/C1 blends measured by ellipsometry are listed in Table 6.6. The measured thickness of films prepared from 80:20 wt:wt PLA:C2 and PLA:C2/C2-RGD blends were not statistically different than that measured for PLA:C1 blends.

Blend Sample Preparation for Bulk Measurements

Blend samples for rheology and SANS measurements were prepared by solvent casting co-dissolved polymers from 0.10 g/mL chloroform solutions onto glass plates ~1 mm thick. The films were dried *in vacuo* at 100°C for 3 days then molded into 25 mm diam. discs 1 mm thick in a compression mold 10 minutes at 125°C.

XRD samples were prepared by solvent casting 100 μL of 0.10 g/mL chloroform solutions onto cleaned 18 mm glass coverslips (VWR Scientific). Samples were covered by shallow glass dishes and dried in a fume hood at 25°C for 24 hours, then dried *in vacuo* at 25°C for 48 hours.

Samples for measuring weight loss due to the aqueous annealing process were prepared by solvent casting poly(L-lactide) or its blends with comb polymers from 0.10 g/mL chloroform solutions on clean glass plates. Samples were dried 12 hours in air then moved to a vacuum oven to dry 24 hours at 25° C. 100-200 mg samples ~1.5 mm thick and 0.57 cm^2 in area were cut from the cast films, immersed in sealed vials containing filtered deionized water, and annealed for 1 to 4 days at 70° C. Mass loss was determined by subsequently drying the films *in vacuo* at 70° C until a constant mass was obtained and comparing with the pre-annealed mass.

Table 6.5. Physical characteristics of PLA matrix polymers used in blend studies.

Matrix polymer	M_w (g/mol)	T_g (°C)	T_m (°C)
poly(L-lactide)	1.20×10^5	60	180
poly(D,L-lactide)	1.06×10^5	57	-

Table 6.6. Dry thicknesses of spincoated PLA blend films.

Sample	Film Thickness (Å)
Cleaned silicon	35±11*
PLA	2072±62.0
98/2 PLA/C1	1935±26.0
95/5 PLA/C1	2035±52.0
90/10 PLA/C1	2600±145
80/20 PLA/C1	3329±114

Measurements were made by ellipsometry at 633 nm. Thickness of the native SiO_2 film at the surface of typical polished single-crystal substrates is also listed. *Average standard deviation for oxide thickness for a given substrate was 3.5±2.0 Å, indicating very low surface roughness for clean substrates; the larger std. dev. listed for the substrate oxide is due to variation in the oxide thickness measured on different substrates.

Annealing of Blend Samples

In order to effect surface segregation of the comb polymer to the exterior surface of PLA/comb blends, thin film samples were annealed at 70°C in 0.2-μm filtered deionized water. Aqueous annealing of blend samples was carried out in a sealed water bath with self-regulating temperature control. Films were annealed in water at 70±1°C for 1 to 4 days. After heat treating, samples for XPS, XRD, and contact angle measurements were dried 24 hours at 25° C *in vacuo*. For cell culture experiments, water was aspirated from samples, which were subsequently sterilized under a UV lamp 30 minutes, and used immediately.

The choice of annealing temperature was dictated by the need to impart mobility to the polymer chains while avoiding rapid hydrolysis of the polyester matrix. Reed and Gilding[55] studied the degradation of PLA as a function of temperature and found that the hydrolysis rate increases more rapidly with temperature above T_G (~60° C[150]). However, at 70° C we found no statistically significant degradation over the 1 to 4-day annealing periods in pure deionized

water. 100-200 mg PLA samples annealed 4 days in water at this temperature showed no statistically significant weight loss (1.36±1.39% measured weight loss). This annealing temperature imparts chain mobility in the amorphous phase while maintaining (and in fact, growing) the crystalline phase ($T_{m,PLA} \approx 180°C$[150, 158]). Blend thin films were annealed in water 1 to 4 days.

For comparison with water-annealed samples, surface composition was also examined by XPS for blend samples prepared by annealing in vacuum at 120°C. Samples were annealed 4 days, quenched to room temperature on large aluminum blocks, and immediately used for surface analysis. Vacuum annealing at a higher temperature (200°C), above the T_m of the matrix to impart better mobility to the chains in the melt resulted in thermal degradation of the matrix and sublimation of degradation by-products.

6.4.3 Bulk Characterization

Equilibrium Swelling of Comb Polymer in Water

Measurements of water uptake by bulk P(MMA-r-POEM) samples were made to assess the swelling of comb polymers in aqueous environments. Three samples of C2 comb polymer were prepared by compression molding 10 minutes at 125°C to obtain 150-220 mg of comb in 0.5 mm-thick discs 25 mm in diameter. Samples were immersed in 150 mL filtered deionized water at 37°C. Weight of the samples was periodically measured over 7 days by removing the samples, blotting excess water, and weighing. The measured equilibrium water content, reached between 24 and 48 hours, was 16±3.1 wt% water in these samples.

Dynamic Rheological Measurements on PLA/Comb Blends

Rheological characterization of PLA/comb polymer blends was carried out in collaboration with MIT Graduate Research Assistant Anne-Valerie G. Ruzette. Dynamic rheological measurements were made on poly(D,L-lactide)/comb polymer blends using a Rheometric Scientific ARES rheometer. Data was collected in a parallel plate geometry, with 25 mm plates and a 0.5 mm plate gap. Dynamic storage (G') and loss (G") moduli of polymer blends were determined isothermally as a function of angular frequency (10^{-1} rad/s < ω < 10^{5} rad/s). Strains were 1% to maintain a linearly elastic response from the materials. Storage and loss moduli measured at multiple temperatures were superimposed about a reference temperature of 140° C to obtain master rheological response curves for each blend composition. Rheology data from all temperatures (60-140°C) are superimposable, indicating no significant change in molecular weight or microstructure of the blends over this temperature range.

SANS Measurements on PLA/Comb Blends

SANS characterization of PLA/comb polymer blends was carried out in collaboration with MIT Graduate Research Assistant Anne-Valerie G. Ruzette. Small angle neutron scattering (SANS) measurements on poly(D,L-lactide)/comb polymer blends were made at the National Institute of Standards and Technology on the NG-3 beamline of the Cold Neutron Research Facility. Neutrons of wavelength $\lambda = 6$ Å were used, with resolution $\Delta\lambda/\lambda = 15\%$, and a sample-to-detector distance of 6 m. The available scattering vector range in this configuration is Q = 0.008 - 0.08 $Å^{-1}$. Scattered intensities were corrected for background and detector noise according to standard procedures and scaled to absolute units (cm^{-1}) using a silica standard. Scattering profiles were obtained at 4 temperatures in 25°C increments, with 30 minutes between scans for equilibration after temperature changes.

X-Ray Diffraction

X-ray diffraction spectra were collected with the assistance of MIT Graduate Research Assistant Simon Mui. Spectra were obtained on a Rigaku powder diffractometer using a rotating anode generator operating at 60 kV/300 mA. Pure PLA and 80:20 wt:wt PLA:C1 blend samples were prepared as described above. XRD spectra were collected for samples as cast or after 4 days water annealing. Scans were made in a $\theta/2\theta$ geometry for 2θ = 10-60° at 5° per minute in 0.02° intervals. Background spectra were collected for empty sample holders and subtracted from the sample data. The % crystallinity in the samples (X_c) was calculated for each sample based on the relative area under the intensity vs. 2θ curve for Bragg reflections vs. amorphous signal[159]:

$$X_c = A_{Bragg}/(A_{Bragg} + A_{amorph}) \qquad \textbf{(Eqn 6.1)}$$

Primary Bragg reflections were measured at 2θ = 14.6°, 16.6°, and 22.3°, in agreement with published values for semicrystalline PLA[160].

6.4.4 Surface Characterization of Polymer Films

Contact Angle Measurements

Contact angles of liquids on copolymer surfaces were measured using an Advanced Surface Technologies, Inc. VCA2000 video contact angle system in the laboratory of Professor Michael F. Rubner. Spreading contact angle measurements were made by repeatedly adding water to a droplet on polymer surfaces in 2 μL increments (up to 12-14 μL total on the surface) and digitally capturing an image of the droplet at each step. Withdrawing contact angle measurements were made in a similar manner by aspirating water from a droplet on the surface in 2 μL increments down to 2 μL total volume on the surface. Respreading measurements were

made by repeating spreading contact angle measurements immediately after a series of withdrawing measurements.

Surface energies of PMMA, PLA, and the comb polymers were determined using sessile drop measurements of three liquids on spincoated films of the polymers. Sessile drop contact angle measurements for the quantification of copolymer surface energies were made from a 4 μL drop of 3 different liquids (water, diiodomethane, and tritolyl (tricresyl) phosphate) on the surface. Reported contact angles are mean and standard deviations calculated from 4 measurements on 5 different samples of each surface. To enable direct comparison, data were collected on a single day to avoid systematic differences in contact angle values due to changes in room relative humidity and temperature. Contact angle values and standard deviations are listed in Table 6.7. Using these measured values, the surface energy of the polymers was calculated using the harmonic mean approximation of Young's equation[161]:

$$\left(1+\cos\theta_i\right)\left(\gamma_i^d+\gamma_i^p\right)=4\left(\frac{\gamma_i^d\gamma_s^d}{\gamma_i^d+\gamma_s^d}+\frac{\gamma_i^p\gamma_s^p}{\gamma_i^p+\gamma_s^p}\right) \qquad \textbf{(Eqn. 6.1)}$$

where θ_i is the contact angle of liquid *i* on the polymer surface, γ_i^d and γ_i^p are the dispersive and polar surface energy components of liquid *i*, and γ_s^d and γ_s^p are the dispersive and polar surface energy components of the polymer. The two unknowns (γ_s^d and γ_s^p) were found using pairs of liquid contact angle measurements and the known values for the surface energy components of the liquids[161], listed in Table 6.8 (diiodomethane measurements were not used for determination of the comb polymer surface energy as the comb was found to be partially soluble in this liquid).

Table 6.7. Sessile drop contact angles on polymers for surface energy calculations.

Polymer	*Water contact angle (°)*	*Diiodomethane contact angle (°)*	*Tritolyl phosphate contact angle (°)*
PMMA	74±0.75	36±3.4	29±2.8
C1	68±1.4	36±8.2	29±1.3
PLA	73±1.3	54±6.4	49±5.5

Table 6.8. Liquid surface energy parameters used for polymer surface energy calculations[161].

Liquid	γ^d *(dyn/cm)*	γ^p *(dyn/cm)*	γ*(dyn/cm)*
Water	22.1	50.7	72.8
Diiodomethane	44.1	6.7	50.8
Tritolyl phosphate	39.8	1.1	40.9

The interfacial tension of each of the blend components with water can be approximately calculated using the known γ_p of the polymers and water according to[161]:

$$\gamma_{pw} = \gamma_p + \gamma_w - W_{adh,PW} \approx \gamma_p + \gamma_w - 2(\gamma_p\gamma_w)^{1/2} \qquad \textbf{(Eqn 6.2)}$$

where $W_{adh,PW}$ is the work of adhesion between the polymer and water, calculated using a geometric mean approximation[162, 163].

Ellipsometry

Thicknesses and refractive indices of thin films on silicon substrates were measured using a Gaertner ellipsometer operating at a wavelength of 633 nm. For some samples, dry film thicknesses were confirmed using AFM topography measurements across defects in the surface created by scoring the film.

Atomic Force Microscopy

AFM on polymer surfaces was performed with a Digital Instruments Dimension3000 using Si_3Ni_4 "tapping mode" cantilevers. Topographical and phase images were obtained using tapping mode on films prepared on either glass or polished silicon substrates. Cantilever spring constants were 30-60 N/m, with resonant frequencies ~320 kHz. Scans were made at 1 Hz with 512x512 pixel sampling. The free vibration amplitude (A_0) of the cantilever near the surface but out of contact was typically ~2.2 V. Blend morphology investigations and nanosphere distribution imaging was performed with setpoints ~$0.5A_0$.

X-ray Photoelectron Spectroscopy

XPS chemical analysis of PLA/comb polymer blend film surfaces was performed using a Surface Science Instruments SSX-100 spectrometer (Mountain View, CA) with an electron take-off angle of 45° to the plane of the sample. Low resolution survey and high resolution C_{1s} spectra were obtained for each sample. Survey scans over 0-1000 eV binding energy range indicated the presence of C and O, as expected with no significant contaminant element peaks. High resolution C_{1s} spectra were fit by subtracting a linear background and introducing a Gaussian-Lorentzian function to describe peaks for each carbon bonding environment in the samples:

$$I(E) = 2A\left[\frac{m\sqrt{\ln 2}}{W\sqrt{\pi}}\exp\left(-4\ln 2\left(\frac{E-E_0}{W}\right)^2\right)+\frac{1-m}{\pi W\left[1+4\left(\frac{E-E_0}{W}\right)^2\right]}\right] \qquad \textbf{(Eqn 6.2)}$$

where I(E) is the intensity at binding energy E, A is the peak area, E_0 is the peak center, W is the full-width at half-maximum intensity, and *m* is the Gaussian-Lorentzian mixing ratio (1

= pure Gaussian, 0 = pure Lorentzian). The mixing ratio *m* was constrained between 0.7 and 1.0 for all fits, a range appropriate to the monochromated Al K_α line shape[164]. Good fits were obtained for peak widths ranging from 1.0 to 1.6 eV.

Spectra were deconvoluted using known peak positions of the blend components from the literature[164], as listed in Table 6.9. Relative theoretical area contributions were calculated as a function of the near-surface mole fraction of the PLA (θ) using the known compositions of the blend components. θ is related to the near-surface volume fraction of comb polymer (ϕ^s_{comb}) by the specific volumes of the system components:

$$\theta = \frac{\frac{(1-\phi^s_{comb})}{V_{PLA}}}{\frac{(1-\phi^s_{comb})}{V_{PLA}} + \frac{\phi^s_{comb}}{V_{comb}}} \qquad \textbf{(Eqn 6.3)}$$

where V_i is the specific volume of component *i*.

Concentration profiles obtained from theoretical SCF calculations were used to model XPS surface composition data. The area (A_i) of a C_{1s} photoelectron peak from a sample of pure *i* is[165]:

$$A_i = C\rho\sum_{n=1}^{\infty}\exp[\frac{-(n-1)d}{\lambda_E \cos\theta}] = C\rho\left[\frac{1}{1-\exp(\frac{-d}{\lambda\cos\theta})}\right] \qquad \textbf{(Eqn 6.4)}$$

where the summation is carried out over all molecular planes from the surface into the bulk of the sample. *C* is a constant dependent on the particular peak and instrument conditions, ρ is the mass density of the sample, *d* is the average spacing between molecular layers at the surface of the sample, λ_E is the photoelectron mean free path in the sample (= 2.3±0.3 nm for Cu

K_α radiation ejecting C_{1s} electrons from organic polymers[166]) and θ is the take-off angle. This equation assumes ρ and *d* are constant as a function of depth in the sample. For a blend of *i* with a second material *j*, the area (A_{ij}) of the same C_{1s} peak is:

$$A_{i/j} = C\rho\sum_{n=1}^{\infty} x_n \exp\left[\frac{-(n-1)d}{\lambda_E \cos\theta}\right] \qquad \textbf{(Eqn 6.5)}$$

where the density in the blend is assumed approximately equal to that of pure *i*. x_n is the mole fraction of carbon due to component *i* in layer *n*. The ratio of the C_{1s} peak for the blend to that in the pure sample is[165]:

$$A_{i/j} / A_i = \left[1-\exp(\frac{-d}{\lambda_E \cos\theta})\right]\left[\sum_{n=1}^{\infty} x_n \exp\left(\frac{-(n-1)d}{\lambda_E \cos\theta}\right)\right] \qquad \textbf{(Eqn 6.6)}$$

SCF concentration profiles for PLA/comb blends were used to fit measured $A_{EO\ blend}/\ A_{EO\ comb}$ ratio, where A_{EO} is the ethylene oxide carbon (BE = 286.5 eV) C_{1s} peak. The planar spacing was assumed equal to the size of 1 lattice layer in the SCF calculations, $d \approx 5$ Å.

Table 6.9. High resolution C1s spectra contributions used to deconvolute XPS spectra.

Carbon Bonding Environment	BE (eV)	Theoretical Area Contribution
-CH_2-, -C(-)(-)-CH_3	285.0	2 - θ
-C(-)(-)-	285.8	1 - θ
-O-CH_2-CH_2-O-	286.5	2.38(1 – θ)
-O-CH_3, -CH(CH_3)-(CO)O-	287.0	1
-(CO)O-	289.0	1

The volume fraction of comb polymer in each layer of the SCF calculations was directly converted to x_n using:

$$x_n = 1 - \theta_n \qquad \textbf{(Eqn 6.7)}$$

where θ_n is the mole fraction PLA in layer n obtained using (Eqn 6.3). SCF parameters representative of PLA/P(MMA-r-POEM) blends were used to calculate the concentration profiles using the hard-wall surface model of blends, as described in section 5.2.1. χ_{AS}, the only unknown, was varied over reasonable values (1.0-3.0) to obtain a best fit to the XPS $A_{EO\ blend}/ A_{EO\ comb}$ data as a function of ϕ^b_{comb}. Best fits were obtained for $\chi_{AS} = 1.25$.

Determination of RGD Peptide Densities at Polymer Film Surfaces

Peptide Labeling with Fluorescent Nanospheres. GRGDSPK peptides present at the surface of comb polymer films or PLA/comb blends were labeled by covalently linking fluorescent nanospheres bearing surface aldehyde groups (yellow-green aldehyde-sulfate Fluospheres™, nominal diameter 29 nm, Molecular Probes) to the ε-amine of the peptide's terminal lysine. Stock solutions of the nanospheres suspended in pH 7.4 HEPES buffer were prepared (2.0×10^{13} nanospheres/mL) and stored at 4°C in the dark until used. Coupling of the nanospheres to peptide-presenting surfaces was performed by sonicating the stock solution for 1 hour then applying 625 μL/cm^2 to surfaces. Condensation of the aldehyde with the amine group of the peptide is reversible, but addition of a reducing agent converts this bond to a permanent amide linkage. This was effected by the immediate addition of 62.5 μL/cm^2 sodium cyanoborohydride (0.033 g/mL in deionized water) to each surface. Samples were subsequently stored at 4°C in the dark for 24 hours to allow reaction of the nanospheres with the surface peptide. Removal of excess nanospheres from the surfaces was accomplished by rinsing 3X with 625 μL/cm^2 Tween 20 solution (0.3 vol% in PBS), 5 minutes per wash, followed by one wash

with deionized water. Measurements of total fluorescence on surfaces after further rinsing treatments showed no further reduction in label present.

Peptide Surface Density Determination Via Fluorescence Measurements. Measurement of total peptide at the surface of comb polymer films was performed by coupling nanospheres to polymer films cast in opaque 96-well plates, followed by measurement of total fluorescence on each surface in a Molecular Devices SpectraMax Gemini fluorescence plate reader (excitation at 488 nm, emission at 520 nm). Fluorescence measurements were converted to nanosphere surface densities by comparing readings with standard curves prepared from nanospheres at various dilutions in a 96-well plate. Nonspecific adsorption of nanospheres on film defects was accounted for by measuring the fluorescence of control comb surfaces presenting no ligand, and subtracting this baseline signal from that measured on RGD surfaces. As the nanospheres were present in large excess (~1000X) to the surface peptides for extended time periods during coupling, labeling of accessible peptide clusters for cluster spacings significantly greater than the nanosphere diameter is expected to be quantitative. Qualitative examination of the label distribution on polymer surfaces was made by fluorescence microscopy on films using a Zeiss 35 inverted fluorescence microscope.

Peptide Surface Density Determination Via AFM Measurements. RGD peptide density at the surface of PLA/comb polymer blends was determined by imaging nanosphere-labeled blend surfaces with AFM. 8-12 2.5x2.5 μm AFM scans taken from 2-3 different labeled samples were collected. The high-T_g poly(styrene) nanosphere labels (T_g ~ 100°C) were well resolved in the AFM phase images. AFM phase images were analyzed by first thresholding the data and creating a binary black/white image from the original scan. The nanospheres exhibited a large phase contrast with blend surfaces, rendering the binary image insensitive to the exact threshold used for creating the black and white image. Density of nanospheres in the binary

images was determined using NIH Image™ software. Particles were counted in each image, neglecting holes not probed by the AFM tip or gross film defects, to arrive at the density of peptide clusters on the surface. Cluster densities were converted to total RGD densities at the surface by multiplying by the number of peptides per cluster (i.e. per chain) for the given comb polymer.

Ligand Loss Measurements of PLA/RGD-comb Blend Degradation Kinetics

In order to assess the stability of ligand at the surface of surface-segregated PLA/RGD-comb polymer blends, a degradation study was carried out to measure the loss of ligand from thin film surfaces in collaboration with MIT undergraduate Catherine Reyes. 10mm glass coverslips were cleaned by immersion for 2 hours in sulfuric acid, followed by a deionized water rinse and drying by a nitrogen stream. 80:20 wt:wt PLA:C2-RGD1 blends were prepared by solvent casting 20 μL per coverslip from 0.03 g/mL chloroform solutions. Films were allowed to dry in a hood under a glass cover for 24 hours, followed by 12 hours *in vacuo* at 25°C. Samples were annealed 1 day in 70°C water as described in section 6.4.2. Peptides present at the surface of annealed blends were subsequently labeled using fluorescent nanospheres as described in section 6.4.4, and rinsed to remove unreacted label. Blend films were floated off the coverslips onto the surface of a water bath, recovered with tweezers, and placed in the wells of an opaque 96-well assay plate. Samples were each immersed in 300 μL of phosphate buffered saline (PBS). Degradation was carried out by incubating the covered 96-well plate at 37°C in a closed dark incubator. PBS was added to sample wells as necessary on alternate days in order to avoid significant change in the PBS volume due to evaporation. Every 7 days, PBS was aspirated from the sample wells, samples were rinsed once with 300 μL PBS and aspirated, 300 μL fresh PBS was added, and fluorescence of the samples in the plate was measured using a Molecular Devices

SpectraMax Gemini fluorescence plate reader. A standard curve of fluorescence vs. nanosphere number was prepared from standard dilutions of nanospheres. Percent label lost at each time point was calculated with respect to the initial average number present.

6.5 Cell Interactions With Comb Polymer Surfaces

6.5.1 Cell Culture

All cell culture reagents were obtained from Gibco unless otherwise noted.

WTNR6 Fibroblasts

WTNR6 cells, derived from the NIH 3T3 cell line, were obtained from Alan Wells at the University of Pittsburgh. This cell line is composed of mouse fibroblast 3T3 cells, lacking endogenous epidermal growth factor receptor (EGFR), which have been transfected to express human EGFR[167, 168]. Fluorescence-Assocated Cell Sorting (FACS) analysis has previously demonstrated the expression of $\alpha_v\beta_3$ and $\alpha_5\beta_1$ integrin receptors by this cell line[26], which are known to bind the RGD sequence[18].

WTNR6 cells were cultured using standard sterile technique in Modified Eagles' Medium-α, supplemented with 7.5% fetal bovine serum (FBS), 1% non-essential amino acids, 1% sodium pyruvate, 1% L-glutamine, 1% penicillin-streptomycin, and 1% Geneticin antibiotic. Cells were incubated at 37°C under 5% CO_2 in 75 cm^2 T culture flasks (Corning), and passaged near confluence with trypsin solution (10X).

PC12 Cells

PC12 cell culture and differentiation experiments were carried out by MIT Graduate Research Assistant Terry Johnson. PC12 cells, an adrenal tumor cell line derived from a rat phaeochromocytoma[156, 157, 169, 170], were obtained from American Culture Co. Cells were cultured in RPMI 1640 media supplemented with 1% penicillin-streptomycin, 5% fetal bovine serum and 10% heat-inactivated donor herd horse serum. Cells were incubated at 37°C in 5% CO_2, grown to confluence in 35 mm TCPS dishes (Falcon), then trypsinized and replated between passages. Passages 50 to 55 were used for experiments.

For differentiation experiments, tethered EGF substrates were prepared as described in section 6.2.1 using C1 comb polymer spincast on 10 mm glass coverslips. Unmodified C1 surfaces were used as a control. To support PC12 cell attachment on the protein-resistant tethered EGF surfaces and to provide a necessary co-signal for differentiation, rat tail collagen was incubated over the surfaces at high concentration to precipitate a low density of gelled collagen on the surface. Sterile 500 μg/mL collagen in PBS was incubated over surfaces for 2 hours at 4°C, then rinsed twice with PBS. 15,000 PC12 cells/cm^2 were seeded on surfaces in 48-well TCPS culture plates (Corning Costar) and cultured for 25 days. Cells were monitored for signs of differentiation (neurite growth) by phase contrast microscopy.

6.5.2 Cell Adhesion Measurements

Cell Attachment Assay

Fibroblast attachment was assayed by culturing WTNR6 cells in contact with surfaces 24 hours followed by counting the fraction adhered. Cell passages 16-26 were used for cell attachment experiments. Surfaces for cell culture were sterilized by exposure to a UV lamp 30 minutes prior to use. Fibroblasts to be seeded on samples were grown near confluence in T75 flasks, then

suspended using 10X trypsin-EDTA solution (Gibco). Cell concentrations were determined using a Coulter cell counter and diluted appropriately to seed surfaces. Cells were plated in 625 μL media/cm^2 surface area. For standard curves in DNA cell counting, three aliquots of the same number of cells seeded per sample were placed in eppendorf tubes, centrifuged 5 minutes at 10,000 g, media was aspirated and the cell pellets frozen at -70°C until the DNA assay was performed. Tissue culture poly(styrene) (TCPS, Corning Costar) was used as a control substrate in all cell experiments to monitor for irregularities in media or cell passages.

Cell numbers on polymer surfaces were quantified by direct manual counting of cells by phase contrast microscopy after culturing for the desired time course. Media was aspirated to remove unattached cells and fresh media applied. Manual cell number determination was performed by counting cells present in 5 fields at 100X in a phase contrast microscope (sample center, one field up, one field down, left, and right of center) on 3 samples. Cells counted in this manner are reported as # cells/field or percent adhered relative to a TCPS control surface.

Alternatively, quantification of total cell number on surfaces was carried out using a DNA-binding assay (CyQuant, Molecular Probes). After culturing cells on samples for the desired time course, media was aspirated and surfaces were rinsed 1X with 200 μL PBS. Samples were then immediately frozen at -70°C for 18 hours. Samples and frozen cell standards were then thawed at 25°C for one hour. Assay solution was prepared with cell lysis buffer (20X) and GR DNA dye (200X) in deionized water immediately prior to the assay. Cells on surfaces were lysed by applying 700 μL assay solution for 15 minutes, and cell standards were lysed in 600 μL assay solution. The proprietray dye exhibits a strongly enhanced fluorescence emission on binding of DNA. Three 200 μL aliquots from each cell sample were placed in different wells of a 96-well PS opaque spectrophotometer plate (Corning). In addition, 3 series were added to

wells by mixing 0, 5, 10, 25, 50, 100, or 200 μL of each of the lysed cell standards with assay solution to bring the total volume in each well to 200 μL. Fluorescence from the plate(s) was read immediately using a Molecular Devices Spectramax Gemini spectrophotometer with excitation at 480 nm and emission read at 520 nm. Total fluorescence was converted to cell number in each well using a standard curve prepared relating fluorescence to cell number in the cell standard wells. Cell number, surface densities, and % seeded cells adhered are reported as mean values of 3-5 samples ± standard error.

Cell Adhesion Strength Measurements

Adhesion strength of cells cultured on comb polymer surfaces as a function of total RGD surface density and ligand cluster size was determined by a centrifugation assay, as described previously[45, 171]. Cell adhesion strength experiments were carried out in collaboration with MIT Graduate Research Assistant Lily Y. Koo. Medias used for adhesion strength assays included a serum-free media (prepared as described above for WTNR6 culture without 7.5% FBS) and a HEPES assay media. Assay media was MEM-α with HEPES (25 mM), 1 mg/mL bovine serum albumin, 1% dialyzed fetal bovine serum, penicillin (100 U/mL), streptomycin (200 mg/mL), non-essential amino acids (1 mM), sodium pyruvate (1 mM), glutamine (2 mM), and G418 (350 μg/mL).

Comb/RGD-comb polymer surfaces for adhesion strength assays were prepared by solvent casting 0.002 g/mL 50/50 vol/vol water/ethanol solutions of C2/C2-RGD blends onto Falcon 96-well flat-bottom culture plates. Solutions were prepared of C2 mixed with one RGD-comb (C2-RGD1, C2-RGD2, C2-RGD3, or C2-RGD4). 10 μL of solution were cast in each well; plates were covered and allowed to dry at 25°C in air for 5 hours. Films were then dried 24

hours *in vacuo* at 25°C. RGD density at the surface of the comb/RGD-comb films was varied by varying the weight ratio of C2 to C2-RGD in the films.

Before cell seeding, comb polymer surfaces were equilibrated with serum-free media (100 μL per well) for 20 minutes. 5,000 WTNR6 cells were then added to each well in 100 μL media. Passages 9-15 were used for adhesion strength measurements. Cells were first plated in serum-free media for 12 hours, to arrest the cells in a quiescent state and prevent cell division from influencing the number of attached cells. This was followed by 8 hours incubation in assay media, and centrifugation of the culture plates.

Centrifugation was performed in a temperature-controlled Sorvall rotary centrifuge at 37°C, using a swing bucket tissue culture plate rotor. After 8 hours in assay media, the sample wells were filled to the rims with assay media and sealed with Falcon sealing tape. Sealed plates were centrifuged for 10 minutes each. After spinning, media was aspirated, surfaces were rinsed once with PBS, and samples frozen at -70°C until cell number was quantified. Cell number in each well was determined as described above using the CyQuant DNA assay. Fluctuations in the absolute level of cell adhesion from passage to passage due to variations in the cell line were accounted for in the experiments by using a control RGD surface (an 80:20 wt:wt C2:C2-RGD4 blend) inverted at 1 g force for each experiment. Cell numbers for each experiment were scaled by multiplying each sample's cell number by the ratio of cells attached to the control in a chosen reference experiment to the number of cells on the control for the current experiment. To facilitate comparison, cell number in each case is reported as a normalized fraction of adherent cells by dividing the number of attached cells at a given applied force by the number of cells adhered on the most adhesive RGD surface condition examined (at applied force > 0), which occurred for pure C2-RGD4 films at 600g applied force (~25% of the seeded cell number).

Adhesion results for comb/RGD-comb polymer films were compared with the force response of cells on two other substrates: a surface segregated PLA/comb/RGD-comb blend and fibronectin adsorbed on TCPS. These two control surfaces serve to address two questions: What is the role of substrate rigidity in the observed cell adhesion response? What differences are observed between the responses of cells signaled by the RGD oligomer vs. a full adhesion protein?

PLA blend samples were prepared as follows. 80:20 wt:wt poly(L-lactide):C2-RGD4 blends (5.4 RGD/comb) were spincoated as described above on clean 10mm glass coverslips. Samples were dried 18 hours at 25°C *in vacuo*, then glued to the bottom of wells in a 48-well tissue culture plate (Costar) using 5-minute epoxy. Samples were covered and the epoxy was allowed to cure in air for 2 hours. Culture plates were then immersed in a tub of filtered deionized water and annealed at 70°C for 24 hours. Blends were removed from water, sterilized under UV for 30 minutes, then used immediately for centrifugation experiments as described above. The number of cells per well was adjusted to arrive at a seeding density on the 48-well plate that was equivalent to that used for the 96-well comb/RGD-comb samples.

Adsorbed fibronectin surfaces for centrifugation experiments were prepared as described previously[172]. 33 μL of fibronectin in PBS (0.01 μg/mL, 1.0 μg/mL, or 3.0 μg/mL) was added to the wells of 96-well culture plates and incubated at 4°C for 18 hours. Fibronectin solutions were then aspirated and each well was rinsed twice with 33 μL PBS. Surfaces were blocked with bovine serum albumin by applying 33 μL BSA (1.0 mg/mL in PBS) to each surface for 2 hours. Finally, BSA solutions were aspirated and surfaces were rinsed twice with 33 μL PBS immediately prior to centrifugal adhesion assays.

7 Simulations of Cell-Surface Integrin Binding to Nanoscale-Clustered Adhesion Ligands

Monte Carlo simulations were developed in collaboration with MIT undergraduate Kerri-Ann Hue. Integrin clustering at points of contact between a cell and its substrate results in biochemical signaling and enhanced adhesion strength[28, 35, 36, 68, 137, 173, 174]. Effects of integrin clustering on adhesion strength were first predicted by a numerical model of Ward and Hammer[137], which they applied to cell adhesion strength data obtained by Lotz et al.[174]. Lotz et al. found that the force necessary to detach glioma cells from fibronectin in a centrifugation assay increased by an order of magnitude when focal contacts (or precursor focal contacts) were permitted to form over the initial 15 minutes of cell adhesion to fibronectin. Ward and Hammer's model accounted for differences in cell adhesion in the absence or presence of focal contacts by considering the mechanical force balance acting on a cell in each case. Predictions were made by assuming *a priori* the area contribution of focal contacts to the total contact area of the cell, using published fluorescence micrographs [37, 175-177] to estimate the size and density of focal adhesions. The required detachment force in the presence of these linkages for either a peeling or fracture model for cell detachment was calculated[137, 178]. Their model further

assumed a homogeneous ligand distribution, with receptor clustering at the focal contact being driven by a nonuniform distribution of talin within the cell at focal contacts. The calculated strength of fully formed focal adhesions was found to be in reasonable agreement with the cell adhesion data of Lotz et al.

This model successfully predicts the strength of mature focal contacts, but provides no insight into their development. Focal contact formation seems to rely on the close apposition of multiple integrin receptors[34]. Extracellular matrix proteins such as collagen or fibronectin that present binding sites for integrins are typically arranged in a fibrillar mesh about cells, providing spatially-localized ligand-bearing regions for cell attachment that may drive this receptor clustering[16]. If such nanoscale clusters can group a few receptors, this might serve to initiate recruitment of the cytosolic components of focal contacts. *In vivo*, such a trigger could be provided by local proximity of only a few adhesion proteins such as fibronectin, which have multiple binding sites for cell receptors [20, 25].

Clustering of integrins may lead to changes in receptor-ligand binding. Cells can modulate the affinity of their integrin receptors for extracellular ligand[179, 180]; it has been conjectured that changes in effective receptor-ligand interactions induced by receptor clustering and subsequent cytoskeletal interactions might lead to enhanced receptor binding when *ligand* is immobilized in clusters on a substrate [45]. Several of the biophysical changes induced by receptor clustering might increase the *effective* receptor-ligand affinity. Integrin-ligand binding could be influenced by integrin-cytoskeleton or integrin–crosslinking protein[181-183] interactions, receptor-receptor interactions, or interactions between integrins and signaling partners such as kinases or phosphatases. For example, Shaw et al. demonstrated that spreading of macrophages on laminin is triggered only under conditions where $\alpha_6\beta_1$ integrins are clustered in focal contacts, attached to

actin fibers of the cytoskeleton, and phosphorylated due to an exogenous signal [68]. Each of these interactions has the net result of increasing the effective affinity of the receptor for its ligand.

Experimentally, both the work described in this thesis and the studies of Maheshwari et al.[45] have demonstrated significant effects of clustered RGD ligand presentation on cell function . The theoretical work presented in this chapter was undertaken to examine the binding properties of cell-substrate systems where receptor clustering is driven by such *spatially inhomogeneous* ligand distributions on a substrate. A simple analytical model and lattice Monte Carlo simulations were used to study how integrin clustering might be induced at the interface between a cell membrane and substrate via ligand immobilized in small, randomly distributed clusters. Presenting ligand in high-density clusters forces some *de facto* clustering of receptors due to normal receptor-ligand equilibria. We first investigated whether such clustering could play a role in focal adhesion development by increasing the total number of receptor-ligand bonds compared to a uniform distribution at equal total ligand concentration. Secondly, we explored how increases in effective receptor-ligand affinity caused by receptor clustering would escalate local ligand binding, further driving focal contact formation and strengthening cell-substrate adhesion. We examined under what conditions (ligand distributions, local and average surface densities, and receptor-ligand binding energies) ligands presented in clusters modify the number of receptor-ligand bonds formed at the cell-substrate interface, an important factor in cell response. Simulations predict that for modest increases of the effective binding affinity on clustering, for even very small cluster sizes (2x2 or 3x3 ligand arrays), the total number of bonds formed at equilibrium can be increased by a factor of ~2-20 by clustering ligand over a broad range of total ligand densities.

7.1 Single State Binding Models

According to the single-state binding analytical model described in section 5.1.2, no increase in the total number of complexes is expected when ligand is clustered compared to a random ligand distribution. However, the analytical model neglects effects of receptor-receptor or receptor-complex steric interactions (receptor crowding or blocking within clusters). To study these effects, Monte Carlo simulations of receptor binding on clustered vs. unclustered ligand distributions were undertaken. Simulation results for the fraction of available receptors bound at equilibrium for D = 1, 2, 10, and 20 over a range of receptor-ligand binding energies are shown in Figure 7.1. In agreement with the analytical model presented in section 5.1.2, the simulations predict no increase in receptor binding by ligand clustering for a range of binding energies spanning from very weak (E = -0.2kT, p ~ 0.80, $K_D = 4.42 \times 10^{-4}$ M) to moderate binding (E = -6.0kT, p ~ 0.0025, $K_D = 1.38 \times 10^{-6}$ M). At very high binding energies (e.g. E = -20kT, p ~ 2.0×10^{-9}, $K_D = 1.14 \times 10^{-12}$ M), the fraction of receptors bound actually decreases for larger clusters. This is caused by "rings" of tightly bound complexes at the cluster perimeter that sterically block entry of additional receptors into the cluster interior. Figure 7.2 illustrates this effect for a system with D = 20 at high binding energy E = -20kT compared with a simulation of the same cluster size at a low binding energy E = -2.0kT. Although the ringed cluster structures are metastable (non-equilibrium), some receptor-ligand pairs are known to bind with even higher affinity (e.g. avidin-biotin, $K_D \sim 10^{-15}$ M [184, 185]). For high-affinity binding, these long-lived metastable states may persist through experimentally relevant timescales.

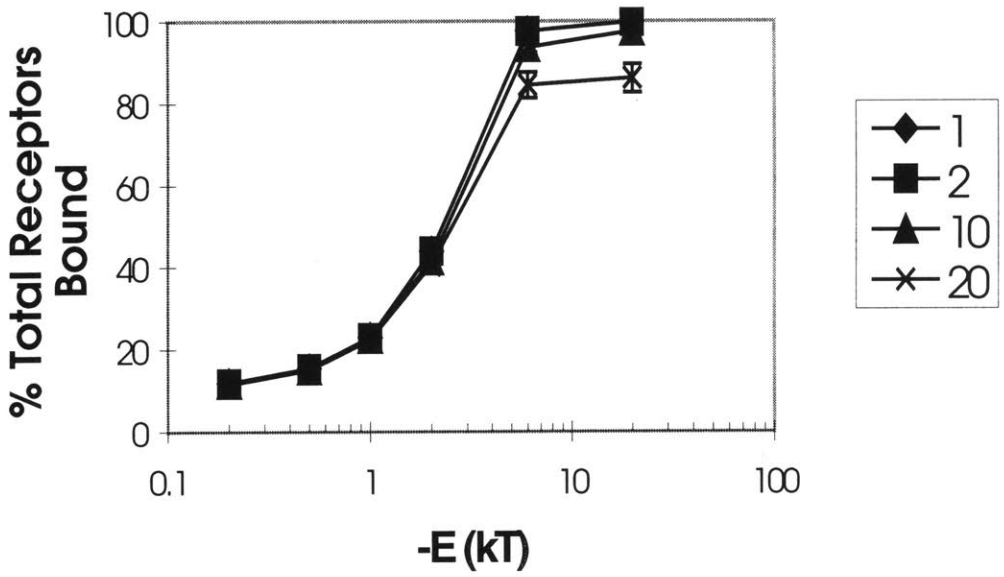

Figure 7.1. Monte Carlo results for receptor binding on clustered ligand surfaces using the single-state model. Equilibrium fraction of receptors bound was determined for four cluster sizes: D = 1, 2, 10, and 20, at a total ligand density of 10^3 ligands/μm^2.

7.2 Two-State Receptor Binding Model in Conjunction with Ligand Clustering

Next, the role of clustering was investigated assuming that nearest-neighbor complexes bind with a greater energy than isolated receptor-ligand pairs. First we examined whether clustering in this two-state model increases the number of bound receptors. Figure 7.3(a) shows the percent of available receptors bound at equilibrium for E_1 = -1.0kT (modeling low-affinity peptide ligands) as E_2 is varied from -1.0kT to -8.0kT. Increasing the clustered-state binding energy by a factor of 4 over the discrete energy gives rise to approximately twice the number of bound receptors for $D \bullet 5$.

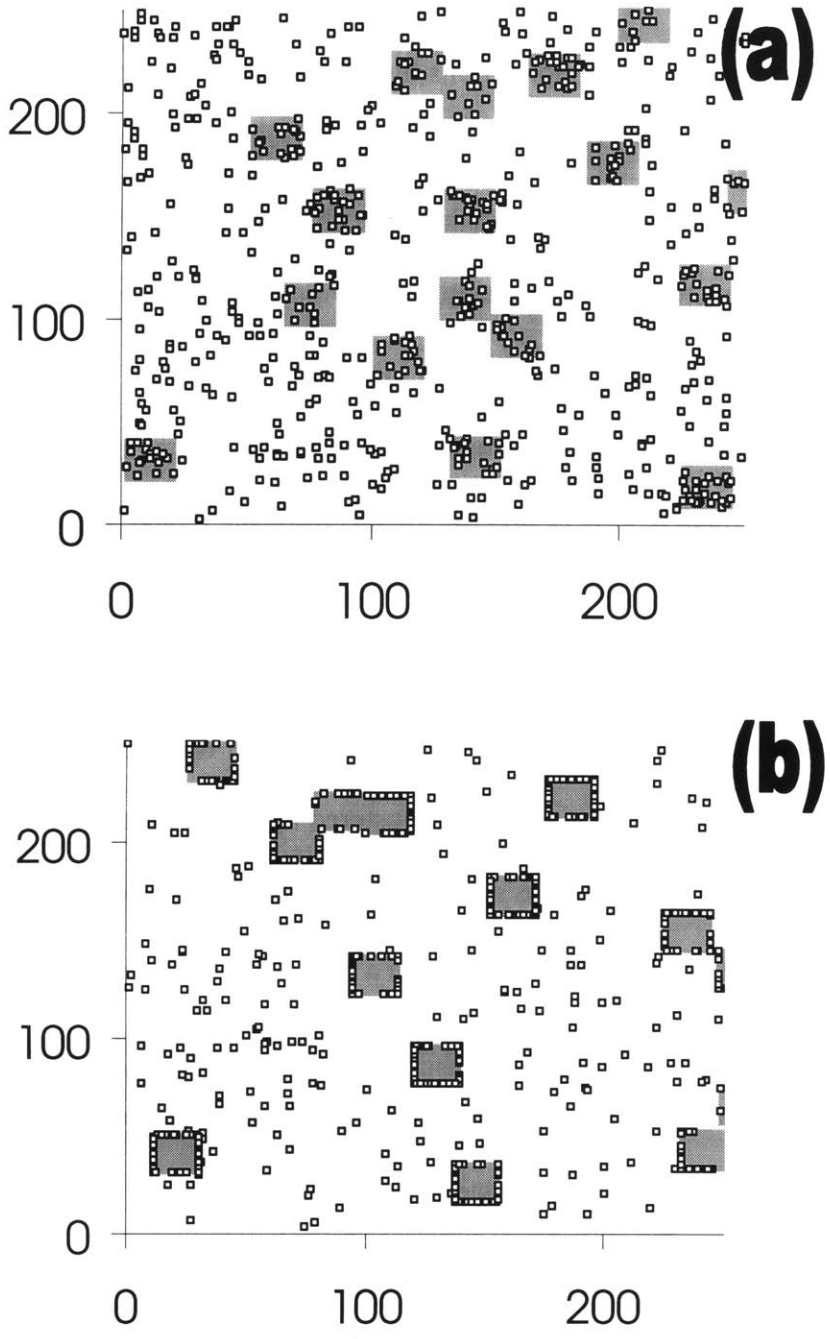

Figure 7.2. Steric blocking of ligand for high receptor-ligand affinities. Shown are snapshots of ligand and receptor lattice distributions from equilibrated systems with 10^3 ligands/μm^2. (a) A low binding energy simulation, E = -2.0kT. Receptors access ligand throughout clusters. (b) Ligand in the interior of clusters is blocked in a high affinity system: E = -20kT.

Significant increases in receptor binding vs. the unclustered ($D = 1$) case occur even for small clusters of only 4 ligands per group. At this ligand density, receptor binding plateaus when 25 or more ligands are clustered ($D \bullet 5$).

The effect of the relative magnitude of the clustered vs. unclustered binding state energies on the fraction of receptors bound is quantified in Figure 7.4. Percent receptors bound for E_1 = -1.0kT (total ligand density 1,000 ligands/μm^2) is plotted for a range of cluster sizes vs. the ratio of the clustered to unclustered binding energy (E_2/E_1). For a small perturbation in the binding energy ($E_2/E_1 = 2$), there is little or no effect from clustering ligand. However, over a range of E_2/E_1 = ~4 –8, clustering gives increases of up to approximately twice the number of complexes obtained on unclustered ($D = 1$) surfaces.

To model the higher binding affinity of integrins for full adhesion proteins, such as fibronectin, on a surface, we also simulated clustered ligand surfaces where the initial unclustered-state binding energy was significantly larger, E_1 = -5.0kT. At the ligand density plotted in Figure 7.3(a) (10^3 ligands/μm^2), such a high-affinity ligand will bind nearly all available receptors even in the unclustered state. However, clustering effects are observed at lower total ligand densities. Figure 7.3(b) shows the % receptors bound at a total ligand density of 100 ligands/μm^2 as a function of cluster size for E_1 = -5.0kT and E_2 = -6kT to -10kT. Receptor binding varies non-monotonically as cluster size is varied. Initially, clustering dramatically increases the level of receptor binding due to the increased affinity on clustering. For large cluster sizes, however, the number of receptors exceeds the number of perimeter cluster sites. Thus, complex formation around the perimeter blocks access to interior sites. This leads to the observed decrease in the fraction of bound receptors at $D > 5$. These metastable "ringed" states, as illustrated in Figure 7.2(b), persist for extremely long times (greater than the 10^8 cycles in our simulations) and may indicate that under certain conditions, an optimum cluster size exists

at low ligand densities for $|E_2| > 4$-6kT. Similar binding profiles are obtained at low total ligand density for smaller E_1 values (E_1 = -1.0kT).

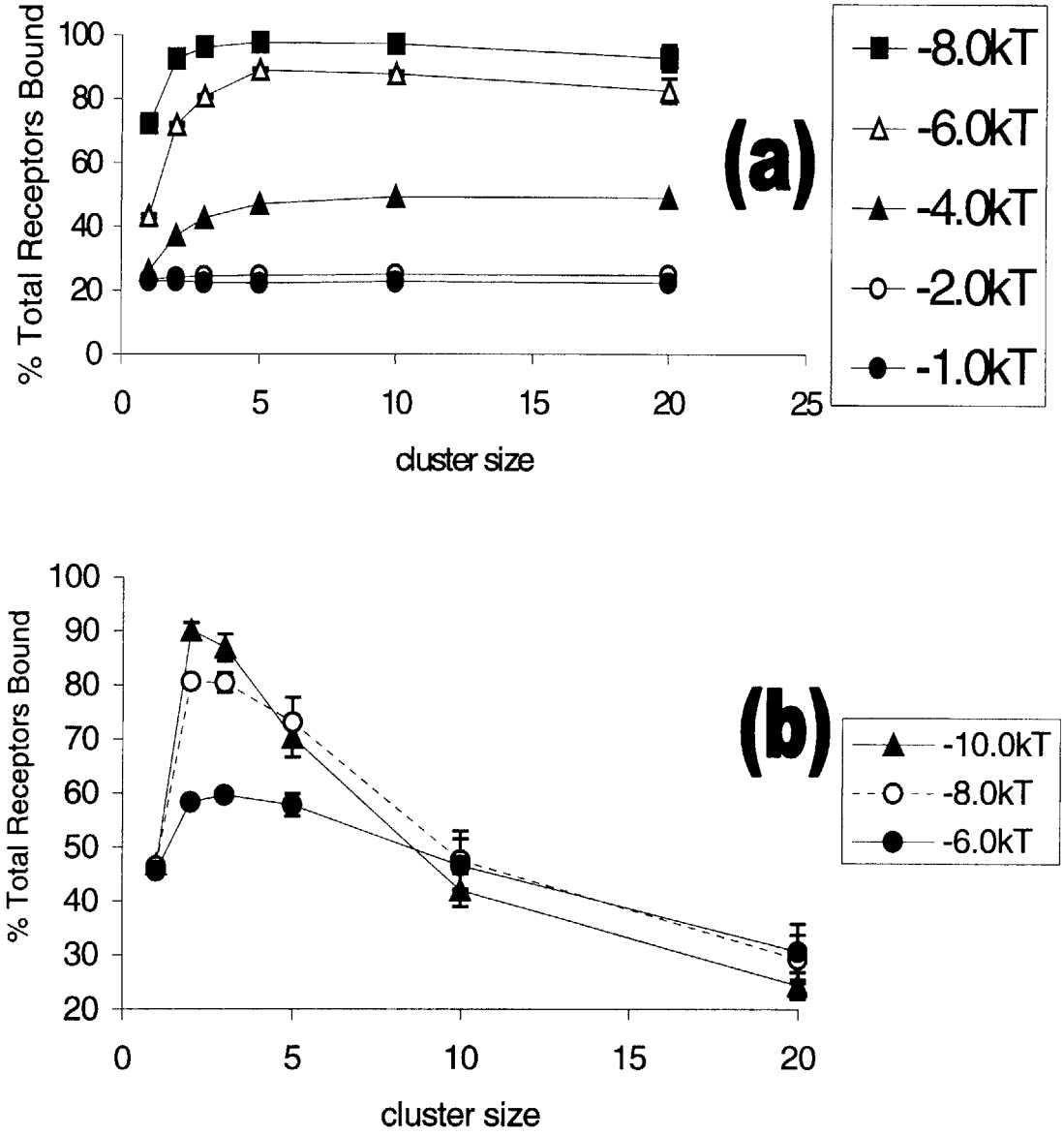

Figure 7.3. Receptor binding in the two-state model. Average percent of total available receptors bound at equilibrium from Monte Carlo simulations is plotted vs. cluster size for a series of clustered-state binding energies. (a) Total ligand density $10^3/\mu m^2$. Binding energies: E_1 was fixed at -1.0kT while E_2 was varied as shown in the legend. (b) Total ligand density of $10^2/\mu m^2$. Binding energies: E_1 was fixed at -5.0kT while E_2 was varied as shown in the legend.

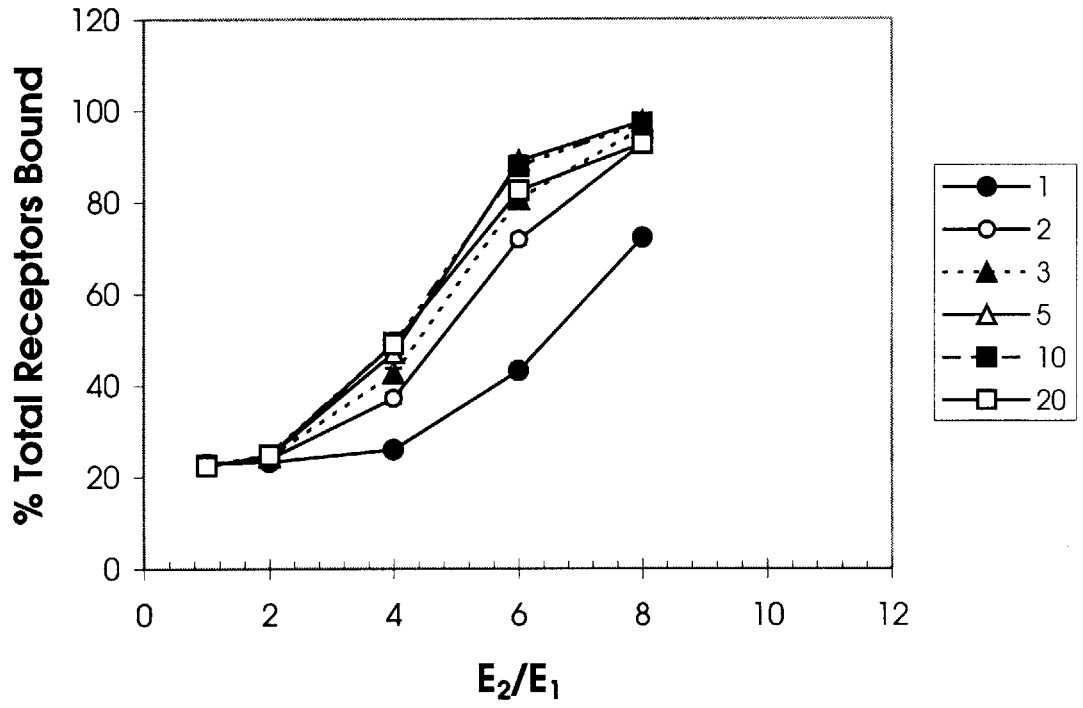

Figure 7.4. Relative strength of clustered vs. unclustered binding energy strongly influences receptor binding for the two-state binding model. Shown are simulation results for total ligand density $10^3/\mu m^2$, E_1 = -1.0kT, and a range of cluster sizes as denoted by the legend.

In addition to increasing the fraction of bound receptors, ligand clustering in the two-state model also drives aggregation of these receptors. Figure 7.5(a) shows the average number of receptors per cluster calculated from simulation results for the single-state model (with E = -1.0kT) compared to the two-state model (E_1 = -1.0kT, E_2 = -6.0kT) for total ligand density $10^3/\mu m^2$. Two-state binding drives clustering of receptors much more efficiently than the one-state model (by a factor of ~5 at all cluster sizes), due to the stronger affinity of the clustered receptors. Even at this high ligand density, the single-state binding model does not show more than 1 receptor per cluster for $D < 5$. In contrast, multiple receptors are bound in each cluster for D between 3 and 5 for the two-state model. Figure 7.5(b) shows the average number of receptors/cluster for a range of total ligand densities and cluster sizes in the two-state model for

E_1 = -1.0kT and E_2 = -6.0kT. Clustering ligand in the two-state model provides significant increases in the number of receptors/cluster over an order of magnitude range of ligand densities.

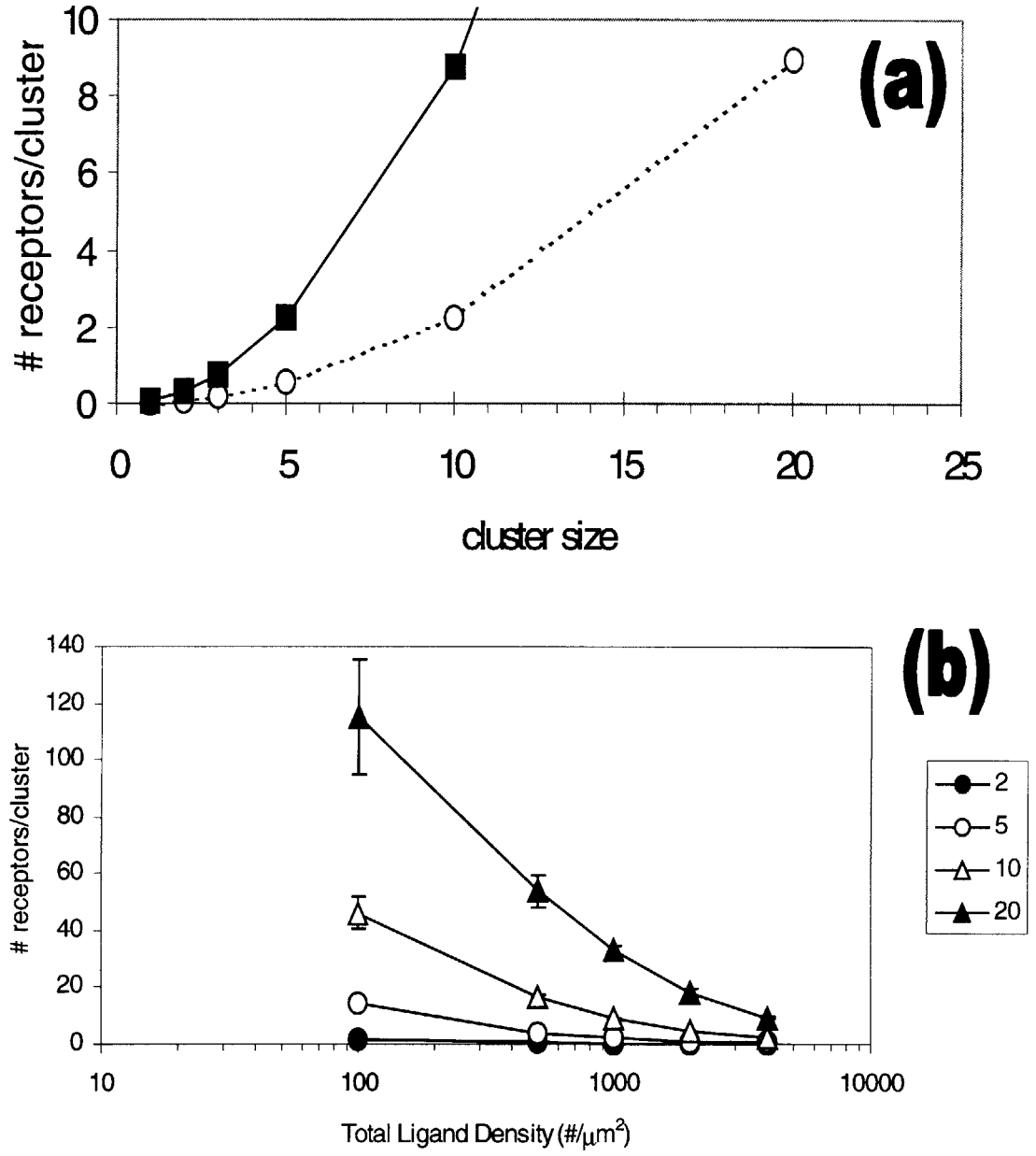

Figure 7.5. Receptor clustering induced by ligand clustering. (a) Average number of receptors per cluster is compared for the single-state binding model (•, E = -1.0kT) or the two-state binding model (•, E_1 = -1.0kT, E_2 = -6.0kT) at a total ligand density $10^3/\mu m^2$. (b) The average number of receptors per cluster from Monte Carlo simulations of two-state model with E_1 = -1.0kT and E_2 = -6.0kT is plotted for cluster sizes as denoted in the legend.

7.3 Role of Total Ligand Concentration

Total ligand concentration plays an important role in the pattern of receptor binding for the two-state binding model. Simulations were run with binding energies E_1 = -1.0kT and E_2 = -6.0kT. Figure 7.6 shows the fraction of receptors bound vs. cluster size for total ligand densities ranging from 30 ligands/μm^2 up to 4,000 ligands/μm^2. As already seen in Figure 7.3(b), at low total ligand densities the trend of receptor binding with increasing cluster size is non-monotonic, due to the competition between receptors for a finite number of available cluster perimeter sites. In contrast, at high ligand densities, all surfaces approach maximal binding of all available receptors and clustering does not significantly increase the level of receptor binding relative to the unclustered case. This is seen in Figure 7.7 where data is re-plotted to show total receptor binding at constant cluster size as total ligand density is varied. For total ligand densities approaching 4,000/μm^2, clustering effects become insignificant.

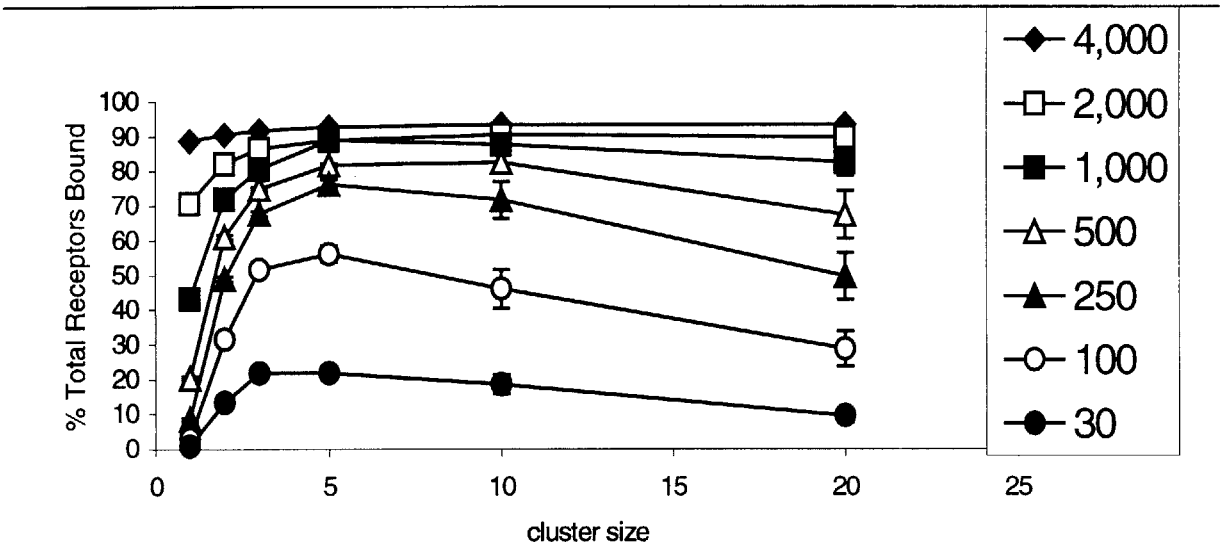

Figure 7.6. Effect of ligand concentration on receptor binding in two-state model. Average percent of total available receptors bound at equilibrium from simulations is plotted vs. cluster size for fixed binding energies E_1 = -1.0kT, E_2 = -6.0kT. Data is shown for a range of total ligand densities from 30 ligands/μm^2 to 4,000 ligands/μm^2 as denoted in the legend.

Even random ligand distributions (such as would be obtained by adsorption of protein to a homogeneous substrate) will show a nonlinear dependence of bond number on ligand density if clustering increases the effective receptor-ligand affinity. Plotted in Figure 7.7 is the binding profile for unclustered (D = 1, open squares) ligand in the single-state model with E = -1.0kT. The unclustered single-state simulation shows significantly fewer receptor-ligand bonds than the same "unclustered" ligand distribution in the two-state model (E_1 = -1.0kT, E_2 = -6.0kT; filled circles). This is because as ligand density increases, a stochastic distribution of ligand gives rise to an increasing number of nearest-neighbor ligands and thus increased receptor binding due to nearest-neighbor complex contacts.

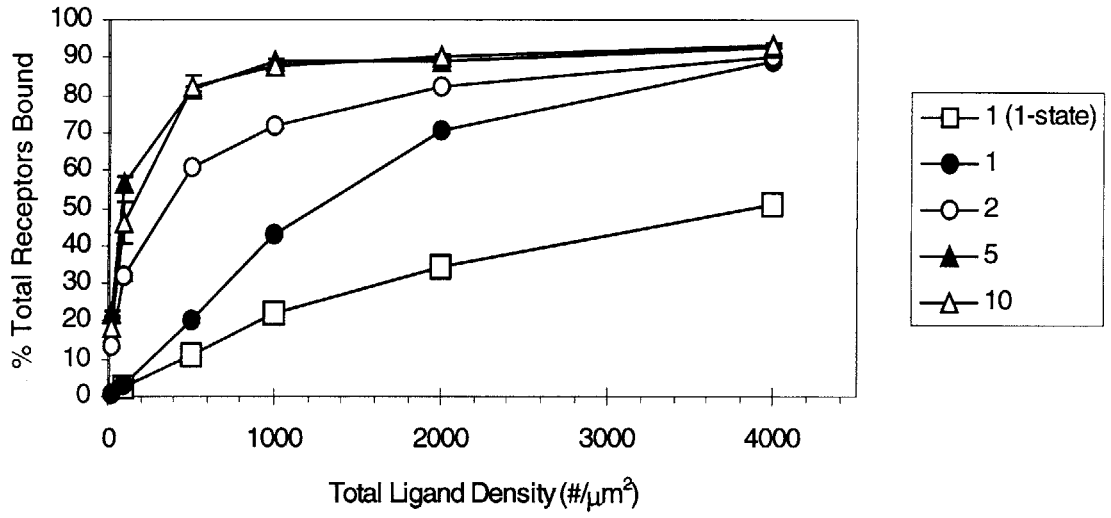

Figure 7.7. Receptor binding profiles for constant cluster size.
Results from simulations using E_1 = -1.0kT and E_2 = -6.0kT. (a) Shown is the percent receptors bound from simulations for D = 1-10 as noted in the legend. Also plotted for comparison is the binding curve for D = 1 in the 1-state binding model with E = -1.0kT.

7.4 Summary

Though integrin clustering and subsequent focal contact formation are well-known phenomena, the biophysical parameters that control these processes are yet unknown, and to our knowledge the model described herein is the first to study how integrin clustering might be induced by cell-ECM interactions. Simulations indicate that if receptor-ligand binding occurs with no change in binding affinity of neighboring ligands, the total number of receptors bound remains constant when comparing ligand presented in clusters vs. homogeneously distributed on the substrate. However, the local surface concentration of complexes at sites of ligand clustering *is* higher, which may itself facilitate focal contact formation due to the relative increase in local integrin concentration at such points of contact.

The presence of secondary interactions between ligated integrins and other molecular components will increase the effective affinity of the receptor for ligand immobilized on a substrate. Using a two-state binding energy model, we have modeled, in the simplest possible fashion, higher-order effects that occur in cell adhesion beyond simple receptor ligation. Two main conclusions are drawn from simulations of two-state binding. First, modest changes in the binding energy on receptor clustering significantly increase receptor binding on clustered ligand surfaces relative to random unimolecular ligand distributions. Increases in the binding energy, corresponding to solution K_D changes of approximately a factor of 10, give 2-3 times more bound receptors over a broad range of ligand densities. This relative increase in clustered receptor binding occurs for even very low affinity, discrete receptor-ligand pairs. As shown in Figure 7.7, receptor binding is most dramatically increased by clustering ligand at low total ligand densities; clustering can increase binding by an order of magnitude at low total density. Second, as the ligand density becomes comparable to the receptor density in the interface, the model predicts the existence of an optimum cluster size (10-25 ligands/cluster), when E_2 is •

6.0kT. The predicted decrease in receptor binding hinges on steric interactions between receptors, and would not occur if receptors are able to "shoulder their way through" the crowded cluster perimeter or if the cytoskeleton actively rearranges receptors.

The effect of the relative magnitude of the unclustered vs. clustered binding energies is shown in Figure 7.4. A weak dependence of clustering effects on cluster size is seen, with maximal binding obtained for groups of 25 to 100 ligands (D = 5-10). However, the present model considers only single nearest-neighbor complex-complex interactions, which may underestimate the possible changes in binding occurring with clustering. In real cells, multi-complex interactions may modify binding in a more elaborate manner, providing a large number of possible effective binding energies depending on the number of receptors in a cluster or second- or third-nearest neighbor interactions. Ligand grouping might thus even more dramatically alter receptor binding for large clusters.

Theoretical treatments have predicted that cell adhesion strength is proportional to the number of bonds between the cell and its substrate [137, 178]. Thus an experimental test of which model (single-state or two-state) more accurately describes real integrin-ligand interactions would be measurement of cell adhesion strengths on well-characterized surfaces presenting equal concentration of clustered vs. unclustered ligands. If secondary interactions that modify the receptor-ligand affinity are important, then clustered ligand surfaces should show significant increases in adhesion strength compared to homogeneous ligand distributions at the same total amount of ligand (below receptor saturation). Recent experiments by Maheshwari et al.[45] examining the adhesion strength of fibroblasts on nanoscale-clustered RGD peptides may be the first experimental evidence of such clustering effects. They found that presentation of RGD clustered on surfaces by star polymers (their maximum cluster size was ~9 RGD/cluster, and the size of the tethering star molecules was ~50 nm) led to dramatic increases in adhesion strength.

At equivalent total ligand densities, 9 RGD/cluster surfaces gave increases in adhesion strength by a factor of 2-3 over unclustered ligand across two orders of magnitude in ligand density. Assuming that bond number is an important determinant of adhesion strength, our model predicts that such dramatic effects of clustering require changes in the effective receptor-ligand affinity to drive complex formation.

Maheshwari et al. also observed similar trends in stress fiber formation within cells adhering to clustered RGD surfaces: 2-3 times more cells on 9 RGD/cluster surfaces showed well-developed stress fibers than on unclustered RGD surfaces at equal total RGD densities. This is intriguing, as the present simulations predict much stronger clustering of receptors in the two-state model relative to single-state binding. Assuming that localization of multiple receptors per cluster is a requirement for focal contact and subsequent stress fiber formation, the two-state binding model is more consistent with the results seen by Maheshwari et al.

Ligand clustering by ECM structures *in vivo* might be achieved in several ways. ECM proteins organized into fibrils, such as collagen and fibronectin, may present nanoscale clusters of ligand to cells due to the close spatial proximity of the assembled molecules. Cells actively assemble fibrils of ECM components such as fibronectin and collagen [25]. Because cells bind to these proteins by multiple receptors during matrix assembly, ligand clusters might even be effectively created directly by cells, which could then serve to drive clustering of integrins and focal contact formation. Alternatively, as shown in these simulations, adhesion proteins randomly adsorbed to an underlying basal lamina may present ligand clusters that trigger focal adhesion development at discrete sites.

Finally, for the development of novel biomaterials, these simulations indicate that if the binding energy of complexes is altered by clustering, increasing the number of ligands per cluster up to ~25 ligands in 2,500 nm^2 increases receptor binding. Thus ligand clustered in

domains of sizes up to ~100 nm may be effective in increasing the number of receptor-ligand bonds formed at the cell-substrate interface. The comb polymer studied in the next chapter provides a convenient way to prepare such clustered ligand surfaces. For larger-scale clustering domains, functionalized latex microspheres may be used to create 100-1000 μm domains of ligand at surfaces; investigations of these materials will also be presented in Chapter 8. Such nanoscale ligand clustering could then be used to improve cell adhesion strength on surfaces, manipulate cell migration rates, and control cell growth.

8 Control of Cell Responses to Surfaces Using Comb Polymers

In this chapter, experimental results defining the characteristics of cell-resistant and cell-signaling surfaces using comb polymer films, latex films, or embedded latexes are presented. The P(MMA-r-POEM) comb polymer is the surface-active component in each system, thus its chemistry and architecture was found to play an important role in determining the resistance of the surfaces to nonspecific cell adhesion. P(MMA-r-POEM) combs with short poly(ethylene oxide) side chains were found to give thin films effective in resisting cell adhesion when comprised of 40-50 wt% POEM monomers. To better understand the protein resistance of these surfaces, numerical SCF calculations of the interface between water and comb polymer films were made, which predict quasi-2D confinement of the comb polymer in the surface layer. Such alignment allows optimum presentation of the hydrophilic PEO side chains at the surface. The ability of these amphiphilic surfaces to restructure in water was studied by contact angle measurements, which indicate that comb surfaces are highly responsive to water. Comparison of contact angle and cell adhesion data on comb polymer thin films with that of comb-based latex

films or embedded latexes reveal similar surface properties for each material, indicating a similar surface layer structure in all three systems.

Cell-*resistant* surfaces were transformed into cell-*signaling* surfaces by presentation of tethered ligands. Two types of peptide ligand, tethered RGD peptides and tethered epidermal growth factor (EGF), were used to demonstrate control over different cell functions, and flexibility in the type of ligand that can be presented in an active conformation at surfaces. Low molecular weight (~600 g/mol) RGD peptides allow control over the attachment of cells to comb surfaces via integrin-mediated cell adhesion; the importance of adhesion in cell function has already been discussed at length. EGF, a larger peptide of ~6,100 g/mol, supports multiple cell functions. This growth factor has been intensely studied for its strong influence on cell migration[26, 45, 167], growth[44, 156, 186], and differentiation[156, 157, 169, 186]. We have demonstrated the use of this tethered peptide on comb surfaces for inducing the differentiation of a cultured neuronal cell line.

The chapter closes with a summary of the results in the context of current approaches for polymeric biomaterials. Parameters for the design of comb polymer surfaces eliciting predictable cell responses are identified.

8.1 Design of Cell-Resistant Surfaces Using Comb Polymers

8.1.1 Comb polymer thin films

Comb Composition and Architecture Effects

The effect of POEM side chain length on the resistance of comb polymer thin films to nonspecific cell adhesion was first examined. The total POEM content must be < 50 wt% to maintain water insolubility. For a fixed maximum POEM content, the comb could be prepared

with a few long side chains, or many short ones. However, use of high molecular weight PEO side chains to eliminate protein adsorption may conflict with effective signaling by tethered ligand at the surface. Low density, high molecular weight polymer brushes have chain ends distributed throughout the layer[144]; this might screen ligand from cell receptors, as depicted in Figure 8.1. Because the comb polymer must provide nanoscale ligand clustering in conjunction with protein resistance, short PEO tethers would be preferable to keep ligands spatially well-localized and prevent steric shielding. Thus we confined our studies of comb architecture to the examination of relatively short side chains ($\leq$ 45 repeat units).

Cell resistance of comb polymer films as a function of comb side chain length for a maximum water-stable POEM content (~45 wt% POEM) is shown in Figure 8.2. Cell adhesion is essentially eliminated for side chains with $\geq$ 9 EO repeat units; because a short tether length is desirable, 9-unit side chains were used for further studies.

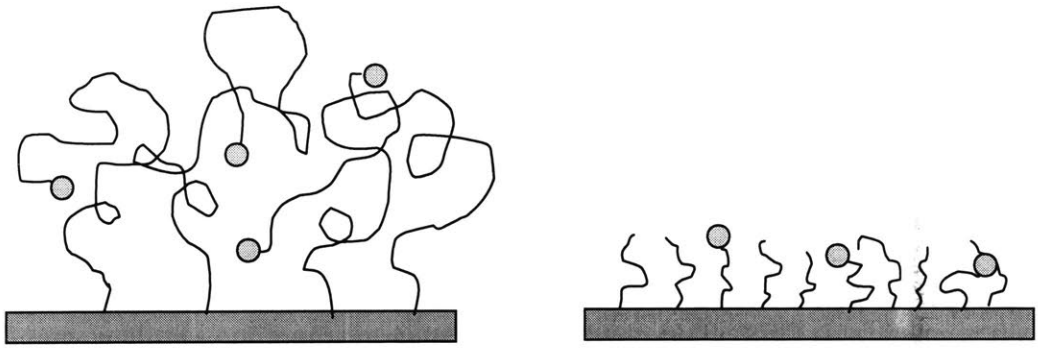

Figure 8.1. Comparison of chain end distributions in high molecular weight, low-density grafted layers vs. low-molecular weight, high-density layers. Chain ends bearing ligand within the layer of longer chains may be screened from cell receptors contacting the substrate.

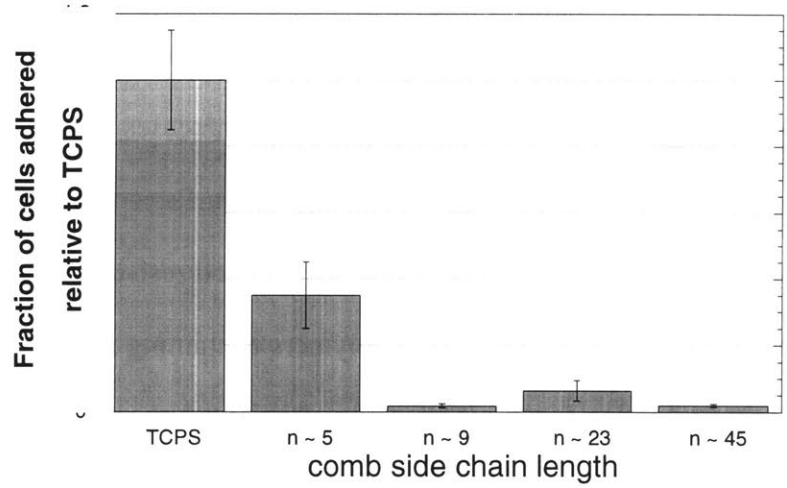

Figure 8.2. Cell adhesion to comb surfaces as a function of comb side chain length. WTNR6 fibroblasts (20,000 cells/cm^2) were seeded on TCPS or films of comb polymers bearing different numbers of ethylene oxide units (n) in the side chains. At 24 hours post seeding, cells adhered were counted manually, and data is plotted as fraction of cells adhered relative to TCPS (= # cells on surface/ # adhered to TCPS).

An estimate of the effective grafting density of 9-mer PEO chains at the water/comb interface can be made by assuming the comb minimizes water-PMMA contacts by creating a sharp interface between hydrated PEO side chains and an underlying layer composed of backbone units only. Then the grafting density σ (in PEO chains/area) is:

$$\sigma = x_{POEM}/a^2 \qquad \textbf{(Eqn 8.1)}$$

where x_{POEM} is the mole fraction of POEM units in the comb ($x_{POEM} \approx 0.15$) and a^2 is the surface area per backbone segment. Taking $a^2 \approx 25$ Å^2, the "grafting density" of the side chains at the interface would be ~0.6 chains/nm^2, or ~13 Å between PEO chains anchored at the surface.

The fully extended length of these very short side chains is ~18 Å; thus the PEO side chains appear to be providing protein resistance without being strongly stretched in the surface layer.

Increasing the fraction of PEO units in the comb polymer increases the grafting density in the surface brush layer, and thus should improve the resistance of surfaces to nonspecific cell attachment. The POEM content of comb polymers necessary for cell resistance at fixed chain length was assessed for a series of MMA/MPOEM copolymers containing 20, 30, or 45 wt% MPOEM with 9 ethylene oxide repeat units per side chain. Figure 8.3 shows that cell attachment to PMMA comb polymer surfaces in the presence of serum (relative to highly adhesive tissue culture polystyrene substrates) is effectively eliminated when the weight fraction of hydrophilic POEM units in the comb is ~ 30% or greater. Considering again the grafting density of PEO at these comb surfaces as calculated above, the mean distance between the side chains drops from ~22 Å at 20 wt% POEM to ~17 Å at 30 wt% POEM. Cell resistance thus appears to be obtained when the mean distance between side chains at the interface becomes less than the fully extended length of the short PEO teeth.

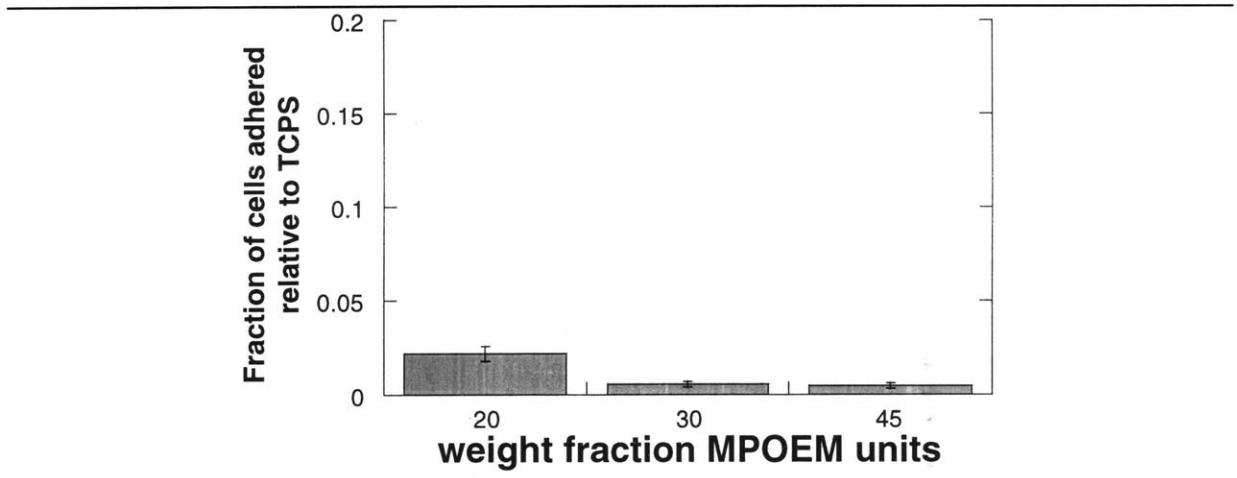

Figure 8.3. Cell attachment to comb surfaces with varying PEG content of polymer. WTNR6 Fibroblasts (20,000 cells/cm^2) were seeded in serum-containing media on thin films of comb polymer comprised of varied weight fractions of MPOEM (9 repeat unit side chains). Cells attached after 24 hours were manually counted; the ratio of cells attached to the comb surfaces vs. a highly adhesive tissue culture polystyrene control is plotted.

Further studies were carried out using two carboxylated comb polymers of cell-resistant composition (45 wt% 9-unit POEM), C1 and C2 (described in Chapter 6). The introduction of a small fraction of charged carboxyl groups (< 10 mole%), necessary for tethering ligands to the comb using NHS chemistry, did not affect the cell resistance of these comb polymers. Figure 8.4 shows quantitative measurement of the % WTNR6 cells attached to C1 before and after carboxylation and to control tissue culture polystyrene surfaces by DNA assay 24 hours post seeding. Typical phase contrast micrographs of the comb polymer surfaces at 24 hours are shown in Figure 8.5. The comb surfaces are highly cell-resistant; rare cells found on the comb surfaces always display a rounded, unspread morphology.

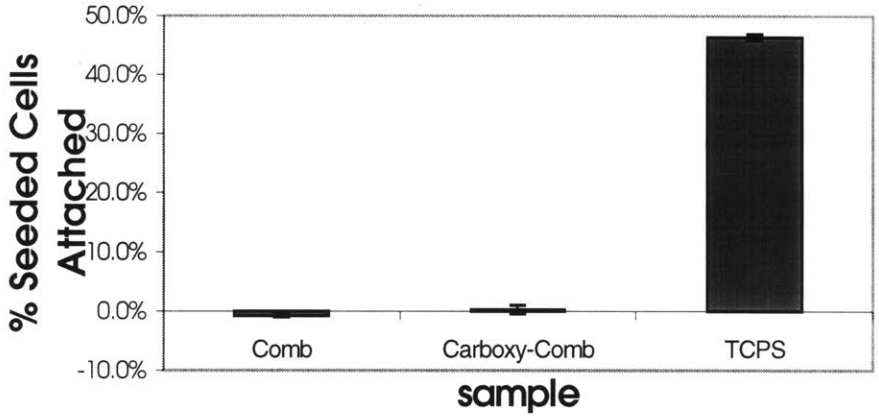

Figure 8.4. Cell resistance of C1 and carboxylated C1 surfaces. WTNR6 cells were seeded at 30,000 cells/cm^2 in serum-containing media, and cells attached were measured after 24 hours by DNA assay. Cell attachment to TCPS, a highly adhesive control, is shown for comparison.

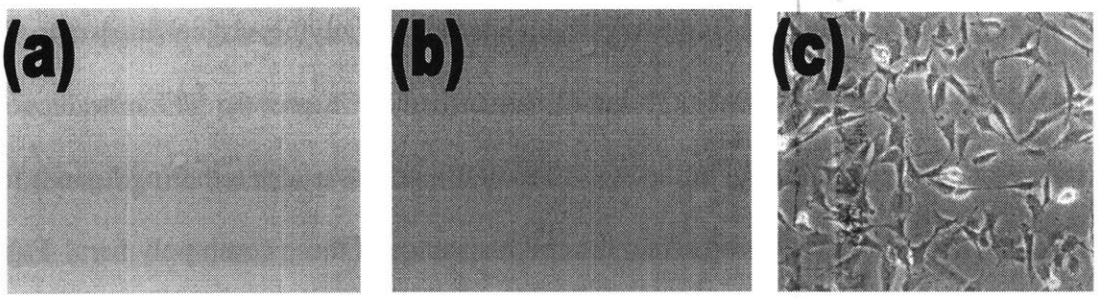

Figure 8.5. Phase contrast micrographs of WTNR6 fibroblast attachment to comb polymer surfaces vs. tissue culture plastic. Photomicrographs taken 24 hours post seeding on (a) C1, (b) carboxylated C1, or (c) TCPS.

SCF Predictions of Comb Surface Structure

To shed light on why comb polymers containing only short PEO side chains and > 50 wt% hydrophobic segments could be completely resistant to nonspecific cell adhesion, numerical modeling of the composition of the comb/water interface was performed. Calculations were made for a comb polymer architecture and composition comparable to comb C1. The chemical makeup of the comb was modeled by a comb architecture having hydrophobic backbone segments (chemical type *A*) and hydrophilic side chain segments (type *B*). Water was explicitly modeled as a single-segment molecule (chemical type *S*) in the calculations. χ parameters accounting for the energy of contacts between the chemical segments were set to model the comb polymer interacting with water: $\chi_{AB} = 0.0$, $\chi_{AS} = 2.5$, $\chi_{BS} = 0.4$. The predicted equilibrium concentration profiles for a film of comb polymer in contact with water are shown in Figure 8.6. Taking 5 Å as the segment size, SCF predicts that the outermost 10 Å of the polymer surface is composed almost entirely of water and PEO units. Due to the favorable interaction of the comb side chains with water, the backbone of the comb is preferentially localized within two layers at the interface. Hydrophilic segments *and* water are depleted from these two layers to accommodate the backbone by extending the side chains into the solvent. Alignment of the

comb backbone parallel to the interface minimizes the backbone/water contacts while maximizing favorable PEO - H_2O contacts. The volume fraction of side chain segments in the layer immediately above the backbone-enriched layers 107 and 108 (ϕ_{PEO}) provides an approximate measure of the effective grafting density of side chains at the interface:

$$\sigma = \phi_{PEO}/a^2 \qquad \textbf{(Eqn 8.2)}$$

where ϕ_{PEO} is the volume fraction of side chain segments localized in the "anchoring" layer, and a is the lattice spacing, here equal to the segment size (5 Å). In agreement with the simple calculations of PEO grafting density made above, the SCF theory predicts the side chains of C1 comb polymer are anchored at the interface with ~10 Å between them.

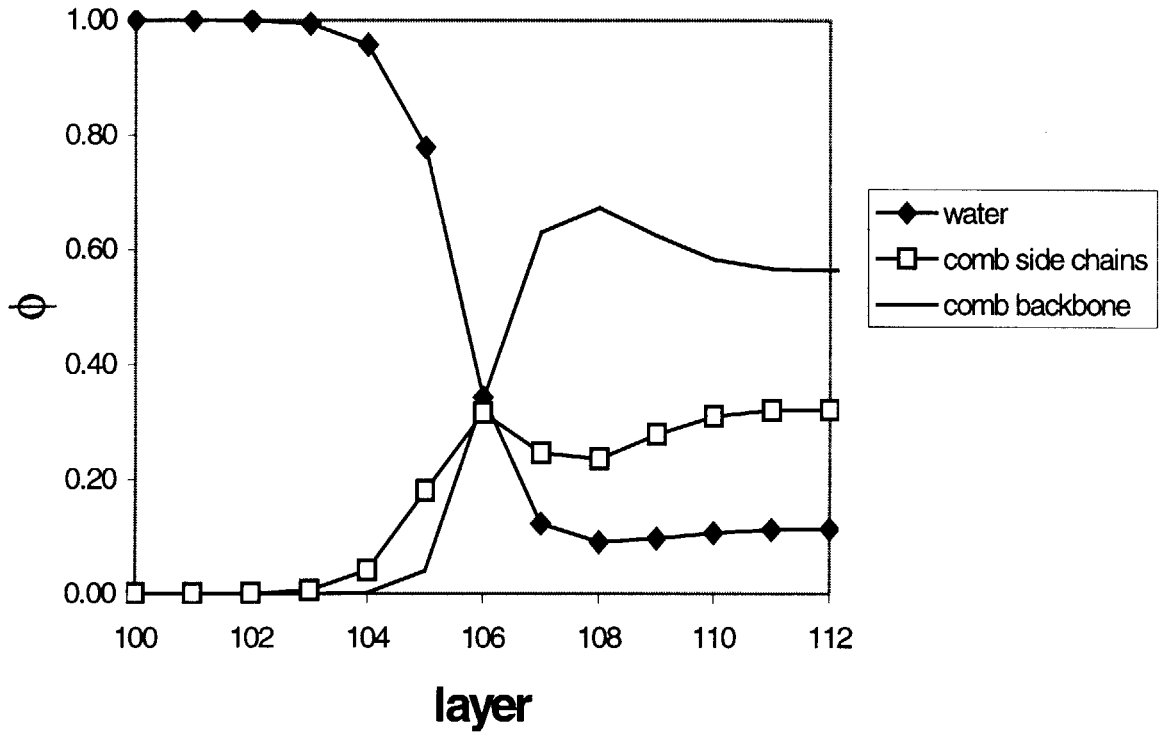

Figure 8.6. SCF prediction of comb polymer surface structure in water. Only the interfacial region of the calculated concentration profiles is shown.

Quasi-2D alignment of the comb polymer at the interface would have several important consequences for the surface properties of comb films. Perpendicular to the interface, segregation of the comb segments into a side chain-rich swollen brush layer atop a solvophobic layer at the surface explains the high cell resistance of comb polymer films even for compositions containing 50-60 wt% hydrophobic segments. The PEO teeth of the comb form a thin, highly hydrated and protein-resistant polymer brush at the surface.

The lateral distribution of comb molecules pinned in quasi-2D conformations at the surface should differ from that expected for the molecules in the bulk. The radius of gyration (R_G) of a polymer chain in the bulk is[145]:

$$\mathbf{R_G \approx N^{1/2} a 6^{-1/2}} \qquad \textbf{(Eqn 8.1)}$$

where N is the number of segments in the chain and a is the segment size. For comb C2, taking $N = 600$, and $a = 5$ Å yields an estimate for $R_G \approx 50$ Å. Confined at the interface, the comb backbones should be arranged as a 2D concentrated polymer solution; in this case R_G should scale with the number of segments as[187]:

$$\mathbf{R_{G,2D} \approx C N^{1/2} a \phi^{-1/2}} \qquad \textbf{(Eqn 8.2)}$$

The dramatic increase in the power law dependence of R_G with N indicates chains at the surface will take on an expanded dimension in 2D at the surface relative to the bulk.

A third consequence of 2D organization of the comb at the interface is that the molecules *exhibit little interpenetration.* In the bulk, the number of chains interpenetrating a given coil volume of size $\sim R_G^3$ can be quite large, scaling as $N^{1/2}$. However, chains confined to two dimensions do not interpenetrate even at bulk density[188, 189].

Thus, alignment and swelling of the comb at the interface apparently 1) segregates the teeth and backbone segments into a hydrophilic polymer brush atop a hydrophobic anchoring

layer, 2) increases the surface layer comb radius of gyration significantly and 3) arranges the surface layer molecules as non-interpenetrated disks at the surface, as depicted in Figure 8.7.

This molecular arrangement at the interface will greatly influence the surface presentation of clustered ligand. Were the chains organized as unperturbed three-dimensional coils at the interface, their small area contribution at the surface and extensive interpenetration would prevent single comb molecules from presenting ligand effectively.

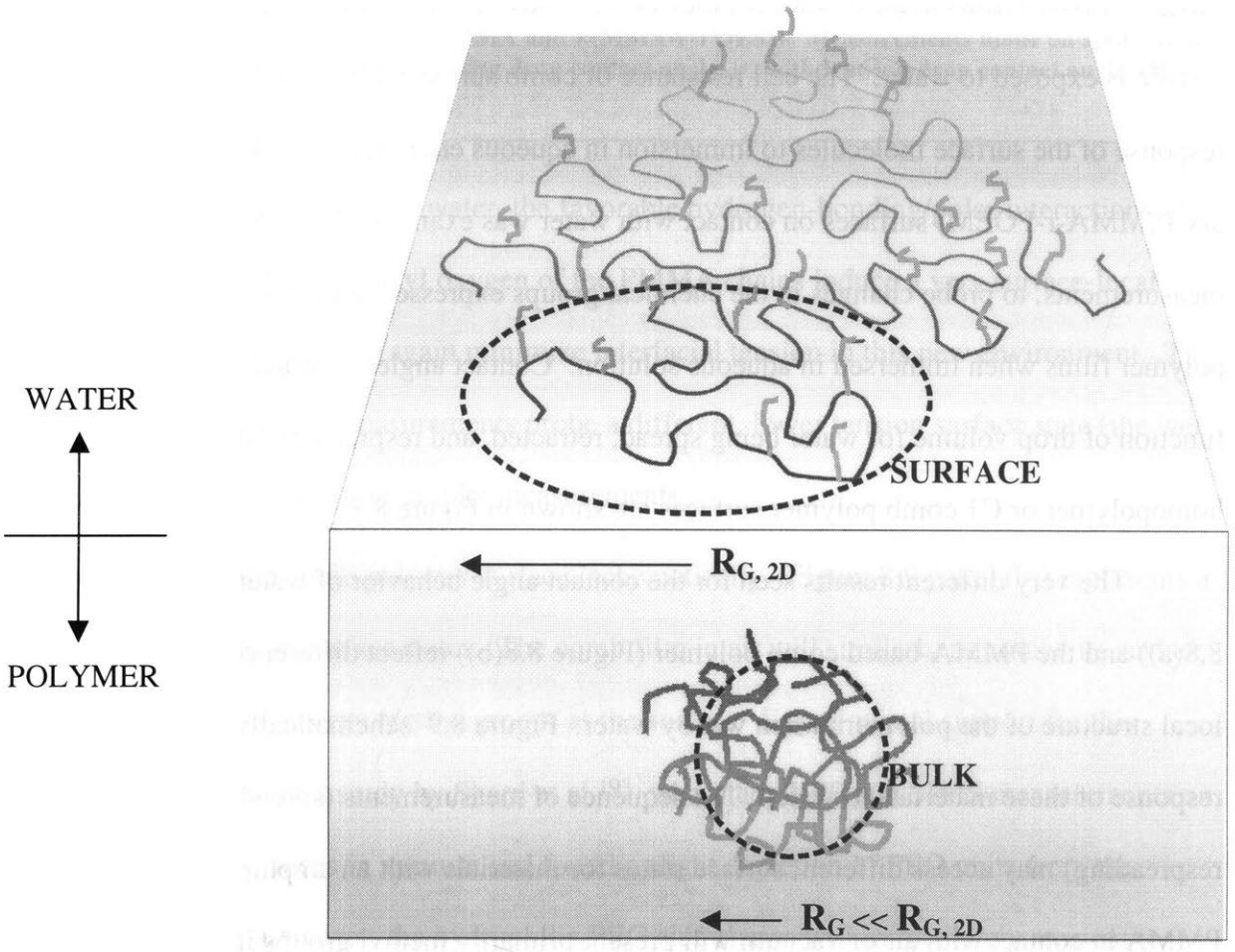

Figure 8.7. Schematic depiction of polymer quasi-2D alignment at the interface of comb polymer films and water.

A comb bearing 5 peptides might localize only one ligand (on average) accessible to receptors in the top surface layer while interpenetrated with ~$N^{1/2}$ other chains. Semi-confinement at the

interface, on the other hand, potentially allows access to every ligand on functionalized molecules in the surface layer.

Contact Angle Measurements

Amphiphilic polymer surfaces are not static, but rather respond by local segmental rearrangements at the surface to minimize the interfacial tension with the environment to which they are exposed[190-192]. Thus the arrangement of the backbone and side chain segments at the surface of comb films in air or vacuum may be very different from their organization when the surface is exposed to water. The cell resistance of comb surfaces is thus linked to the dynamic response of the surface molecules to immersion in aqueous environments. The rearrangement of dry P(MMA-r-POEM) surfaces on contact with water was examined by contact angle measurements, to probe changes in the chemical groups expressed at the surface of comb polymer films when immersed in aqueous solution. Contact angles of water droplets as a function of drop volume for water being spread, retracted, and respread on films of PMMA homopolymer or C1 comb polymer surfaces are shown in Figure 8.8.

The very different results seen for the contact angle behavior of water on PMMA (Figure 8.8(a)) and the PMMA-based comb polymer (Figure 8.8(b)) reflect differences in the surface-local structure of the polymers when wet by water. Figure 8.9 schematically illustrates the response of these materials to water. The sequence of measurements (spreading, withdrawing, respreading) may access different surface states for materials with an amphiphilic nature. PMMA in contact with air or vacuum will present primarily methyl groups in the surface layer to minimize the surface energy.

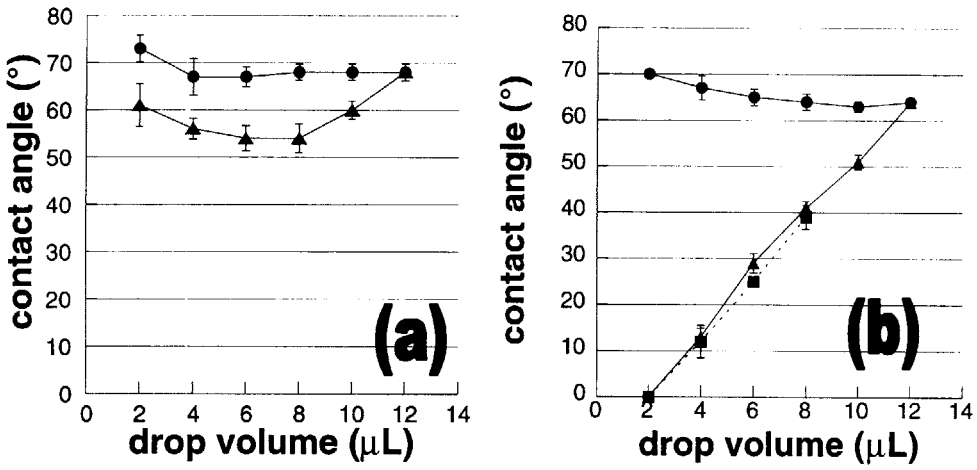

Figure 8.8. Contact angles of water on PMMA and P(MMA-r-POEM). Measurements made on spincoated films of (a) PMMA and (b) C1. (●) spreading drop contact angle, (•) withdrawing drop contact angle, (■) respreading contact angle.

However, as the surface is wet by water, the favorable hydrogen-bonding/polar interactions of water molecules with the carbonyl oxygen of the PMMA chains induce a very surface-local reorientation of the polymer to again minimize interfacial tension in this new environment. Thus withdrawing contact angle measurements probe a different, lower tension surface state (the wet PMMA surface) than spreading droplet measurements.

The case of the comb polymer surface (schematically, Figure 8.9 panel (b)) represents a more extreme change in surface states. The comb film in air will similarly minimize its surface energy by placing low-energy methyl groups at the surface. Experimental support for this arrangement comes from a study by Shard et al.[193], who made XPS and SIMS measurements on P(MMA-r-POEM) surfaces in vacuum and found a slight depletion of PEO units from the surface. On wetting, however, the hydrophilic PEG side chains will immediately reorient to contact the liquid, and water will absorb into the film. That absorption occurs is indicated by measurement of the equilibrium water content of bulk P(MMA-r-POEM) samples; a 16±3.1 % increase in weight was measured for the water-swollen comb, corresponding to approximately

1.1 water molecules per ethylene oxide repeat unit. Thus on withdrawal of the droplet across the wet film, the combination of absorbed water and reoriented surface groups provides a surface state having a very low interfacial tension with water. The droplet will thus reduce its contact angle instead of reducing its contact area with the surface. As the contact area of the drop on the surface remains constant, withdrawing water from the droplet leads to the steady drop in contact angle observed. Finally, absorbed water present at the surface of the film allows complete spreading of a droplet to the edge of the pre-wet contact area on the surface when respreading measurements are made on the comb polymer surface. Indeed, the respreading contact angles follow precisely the contact angles observed for withdrawing measurements as a function of drop volume. Consistent with the SCF surface structure predictions, these results imply that the comb polymer can be completely cell resistant by organization of the surface on contact with water to maximize the hydrophilicity of the top surface layer.

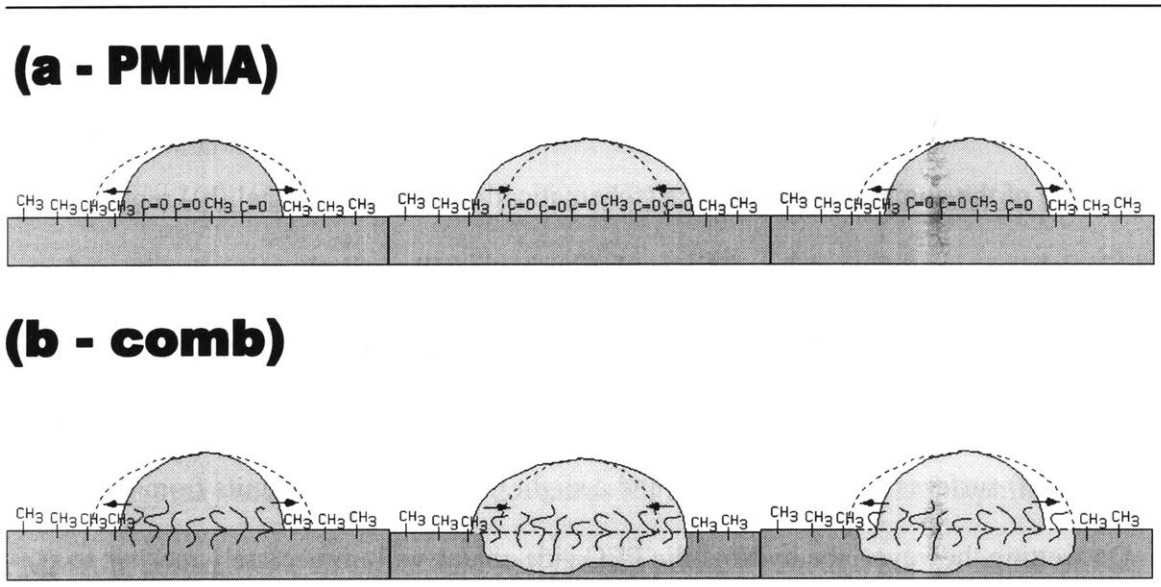

Figure 8.9. Schematic representation of contact areas in spreading, withdrawing, and respreading contact angle measurements. In panel (a), we show the case of water spreading over a nonpolar surface with little or no ability to present more polar groups through local surface chain motions. Panel (b) shows the case for a polymer surface that may reorient high-energy groups to the surface or even bind or absorb water in the surface layer.

8.1.2 Comb-Based Latex Films and Embedded Latex Surfaces

Previous work by Noda[194] showed that latexes prepared with a PEO-containing block copolymer stabilizer form films with hydrophilic surfaces. Based on these findings, we hypothesized that use of P(MMA-r-POEM) as a stabilizer for latex synthesis would allow preparation of protein and cell-resistant latex surfaces. In order to prepare latex films or embedded latexes resistant to nonspecific cell adhesion, C1 comb polymer was used as a stabilizer in the synthesis of PMMA latexes.

Cell-resistant surfaces were prepared by preparing films from comb-stabilized latexes or embedding the beads in films of comb polymer. Films formed by heating a confluent layer of nanospheres on a substrate were flat; however, the embedded latexes protrude above the comb polymer film, as shown in a representative AFM topography image and cross-section of an embedded latex surface, Figure 8.10. The latex beads used, having diameters of 200-2000 nm, protrude well above the underlying comb polymer layer, such that ligand-functionalized beads will present > 50% of their total surface area to cells in contact with these surfaces.

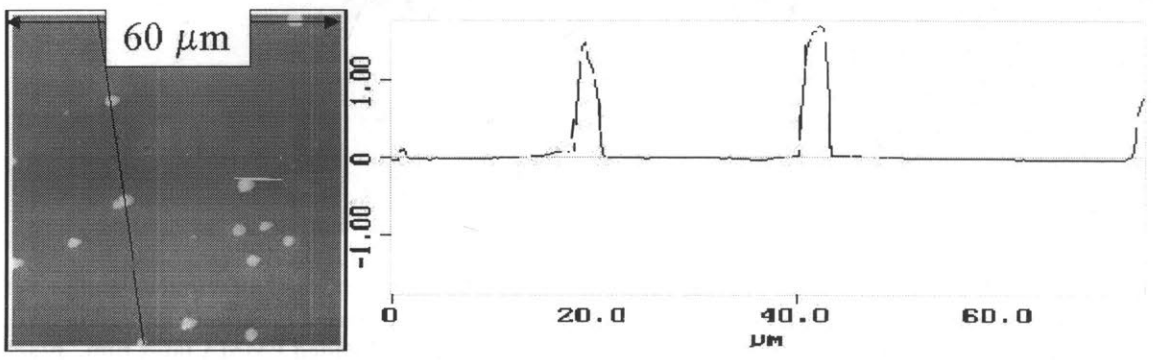

Figure 8.10. Representative AFM topography image and cross-section of embedded latex sphere surface. Cross-section y-axis is in μm.

Cell attachment to latex surfaces in the presence of serum-containing media was assessed by microscopy. Both coalesced films of the comb-stabilized latex and embedded latex bead surfaces were highly cell resistant. Example micrographs of WTNR6 cell attachment to a control film of pure PMMA, a coalesced PMMA latex film, and a film prepared by embedding the PMMA latex in an underlying comb polymer layer are shown in Figure 8.11, 24 hours after cell seeding.

The cores of the latexes all have different chemical compositions and each latex has a different glass transition temperature, yet all exhibit wetting properties strongly influenced by the surface-localized comb stabilizer. Figure 8.12 shows the contact angle results on films of coalesced latexes containing different acrylate or methacrylate cores. Variation in the value of the plateau spreading contact angle on different latexes indicates the contribution of different hydrophobic core segments at the surface in air, as in Figure 8.12(b) where some ethyl or butyl methacrylate units may be exposed to lower the surface energy (and raise the contact angle) in air. Withdrawing measurements then show a diminishing contact angle, revealing rearrangement of the surface to maximize PEO-water contacts.

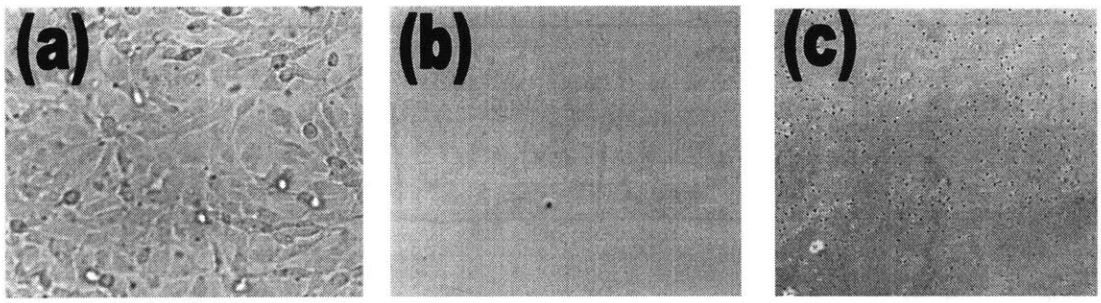

Figure 8.11. Comb-stabilized latexes provide surfaces resistant to nonspecific cell attachment similar to films of the pure comb polymer. WTNR6 Fibroblasts (30,000 cells/cm^2) were seeded in serum-containing media on (a) films of pure PMMA, (b) a coalesced PMMA latex film, or (c) an embedded PMMA latex film. Black dots in (c) are the embedded latex spheres (~2 μm diameter). Phase contrast micrographs were taken at 100X after 24 hours.

This can occur at the latex surface presumably by alignment of the comb backbone at the interface and extension of the PEO side chains into the water. However, the contact angle on withdrawal appears to plateau at a value of ~ 30° on the latex films (excepting the result obtained for the very low T_g P(BMA-co-EMA) latex), rather than continuing toward 0° as seen for films of pure comb polymer shown in Figure 8.8(b). The contact angles of the latex films more closely resemble those observed on PMMA films that cannot absorb water into the bulk (and where the contact angle decreases in withdrawal but reaches a plateau) than those observed on the pure comb polymer films. The plateau contact angle on withdrawal *is* notably lower on latex films than pure PMMA, since the comb at the surface does allow presentation of the multi-unit PEO side chains.

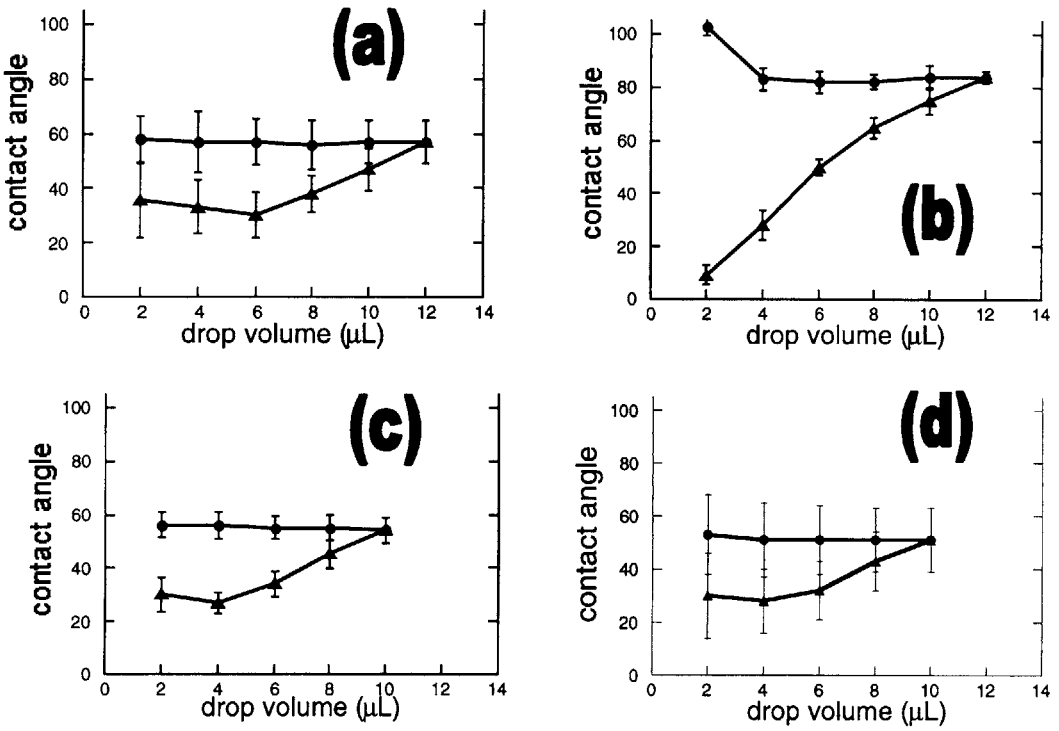

Figure 8.12. Contact angle measurements on comb-stabilized latex film surfaces. Measurements made on coalesced films of (a) PMMA latex, (b) P(BMA-co-EMA) latex, (c) P(MMA-co-BA) latex, or (d) P(MA-co-EMA) latex. (•) spreading contact angle measurements, (▲) withdrawing contact angle measurements.

8.2 Design of Cell-Signaling Comb Polymer Surfaces

8.2.1 Tethered RGD Surfaces

Comb Polymer Thin Films

Tethered RGD peptides can be used to control cell attachment, adhesion strength, differentiation, and migration at surfaces[39, 42, 43, 45, 51, 196]. RGD immobilization at comb polymer surfaces is effective whether coupling peptide to comb polymers in solution before film casting, coupling to the surface of chemically activated films, or *in situ* activation followed by coupling. Figure 8.13(a) compares the number of fibroblasts attached to GRGDSP-bearing surfaces prepared by each of these routes. Nonspecific adsorption of RGD in the surface-coupling approaches is apparently very low, as cell attachment was negligible on non-activated surfaces exposed to RGD. Ligand surface densities obtained by coupling peptide to *in situ* activated surfaces are ~ 30% lower than obtained by the solution phase pre-coupling method (as assessed by fluorescence labeling). However, the surface-coupling routes are useful for limiting the amount of precious peptides used, by confining the tethered ligand to the exterior surface of the film and allowing multiple uses of the same peptide solution. For example, if we consider application of the comb polymer as a biomaterial coating to control cell adhesion at the surface with a nominal thickness of 3,000 Å, then a maximally adhesive film prepared using the C1-RGD1 polymer alone will use ~$1x10^7$ peptides/μm^2, most of which is buried in the film. Approximately 1,000-fold less RGD tethered by the surface-coupling routes would provide a similar level of adhesion. This economy is of course traded for in robustness of the signaling layer, as the surface-coupled polymer will contain peptide only in the immediate surface layer. Further experiments with tethered RGD

discussed in this chapter and Chapters 9 and 10 were all performed using ligand immobilized by the solution pre-coupling method.

Cells attached and strongly spread on maximally-adhesive surfaces prepared by each of the coupling routes examined. Figure 8.13b shows a representative phase contrast micrograph of cell attachment to a C1-RGD1 thin film. RGD-mediated attachment supports a well-spread morphology for fibroblasts cultured on the surfaces.

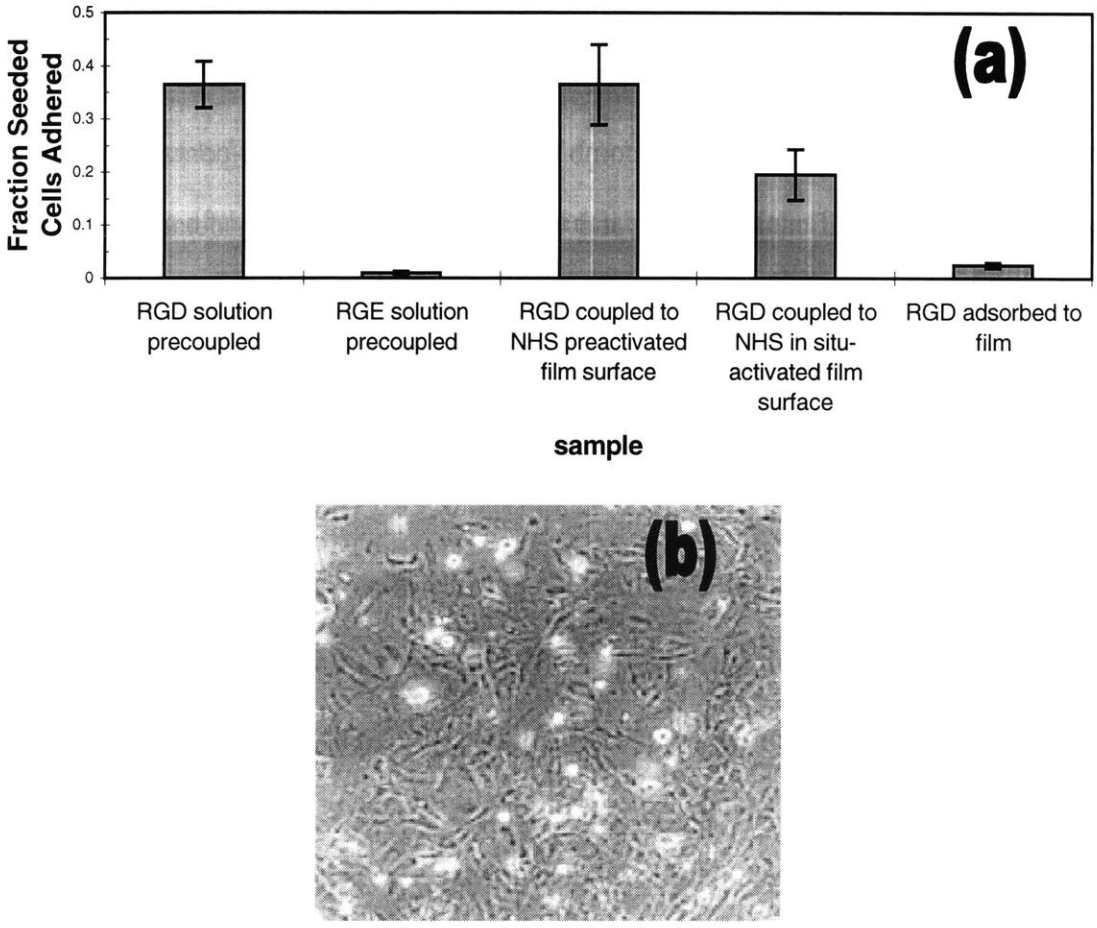

Figure 8.13. Cell adhesion on RGD-presenting surfaces prepared by different methods. WTNR6 cells (30,000 cells/cm^2) were seeded in serum-containing media on RGD surfaces prepared by several routes. (a) Fraction of seeded cells attached to RGD surfaces after 24 hours as measured by DNA assay. (b) Morphology of cells attaching to a tethered RGD surface prepared by the solution pre-coupling method (C1-RGD1), as seen by phase contrast microscopy of cells after 24 hours (100X). Cell attachment on RGD surfaces prepared by the other two chemical routes was qualitatively similar.

In order to control adhesion via tethered RGD, it is important that the ligand itself does not promote protein adsorption and that the only adhesion on the surface is due directly to RGD-integrin interactions. To test whether tethered RGD peptides supported cell adhesion by allowing protein adsorption, cell attachment to tethered GRGDSP was compared with that on tethered GRGESP, an inactive analog of RGD. These results are also shown in Figure 8.13 for surfaces prepared by the solution pre-coupling approach. Cells adhere and spread on RGD-presenting comb surfaces, but are unable to attach to tethered RGE surfaces despite culturing in the presence of 7.5% serum. The specificity of interaction between cells and tethered RGD surfaces was further probed by adding 85 μM soluble GRGDSP to the media of cells that had been allowed to attach 24 hours to RGD-comb thin films in 7.5% serum-containing media. Cells immediately showed significant rounding and within 4 hours completely detached from the surface, indicating that integrins responsive to RGD were the adhesion-promoting cell-surface linkage. Thus cell attachment even on surfaces of very high RGD density (~32 nm on average between RGD clusters, as discussed below) in the presence of serum is controlled by tethered RGD-integrin interactions.

The total surface density of RGD presented on comb polymer films can be controlled by blending RGD-combs with their non-functionalized counterparts in different weight ratios. Accessible RGD cluster densities obtained at the surface of comb/RGD-comb mixtures were measured by labeling surface ligand clusters with 30 nm-diameter fluorescent polystyrene nanospheres and measuring the total fluorescence from surfaces.

For this analysis, several assumptions must be made. First, the nanospheres are assumed to be able to access RGD presented at the surface in a manner comparable to integrin cell surface receptors; this is why a large label (with a diameter comparable to integrin heterodimers) was chosen. The nanospheres are unable to label ligand that might be present but buried in the

surface, out of reach of the cell receptors of interest. Second, it is assumed that a single ligand cluster (i.e. presented by one comb molecule) is labeled by only one nanosphere, and that each nanosphere labels only a single cluster. This assumption should be valid if the comb polymer is arranged in quasi-2D confinement at the surface of the films in a water-based environment. As discussed in section 8.1.1, 2D confinement of the comb at the interface implies arrangement of the molecules as non-interpenetrating disks at the surface. If only this surface layer of comb polymer presents accessible ligand, then 1) the minimum separation between ligand clusters will be determined by the comb dimension at the surface (and thus comb molecular weight), and 2) cluster separation will be simply determined by the relative area fraction of comb vs. RGD-comb at the surface.

The validity of this 2D model should be verifiable by the labeling results. If the comb is not semi-confined at the surface, multiple combs will contribute to the local RGD density at any given area due to chain interpenetration in the surface layer. Assuming the size of the nanosphere labels is comparable to the chain dimensions, labeling would be saturated (surfaces covered by a monolayer of labels) for any mixture of comb and RGD-comb where more than one RGD-comb was present per ~$N^{1/2}$ molecules; i.e. when more than one RGD-comb is present per R_G^2 area of the surface. For the C2 comb polymer, $N \approx 600$, meaning that $\phi^b_{RGD\text{-}comb} > 0.04$ (i.e. one RGD-comb per $N^{1/2} = 24$ chains, $\phi = 1/24$) would saturate surface labeling (the mean distance between RGD-bearing comb molecules at the surface would be smaller than the label size). Variations in label density would only be found at extremely low RGD-comb contents in the film.

Quasi-2D confinement at the interface:

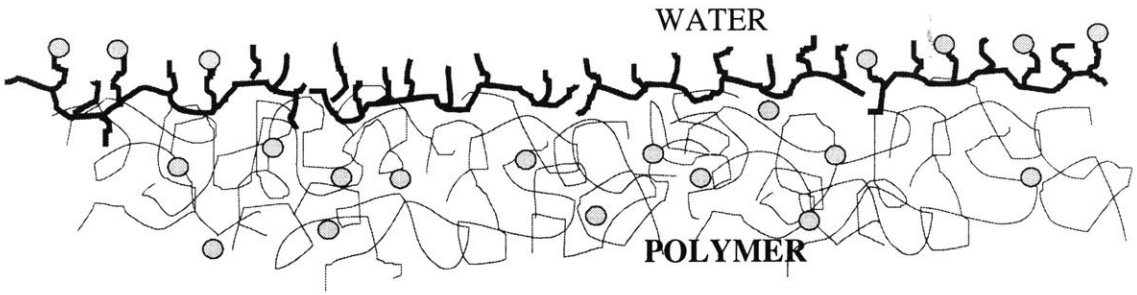

Chains uperturbed at interface:

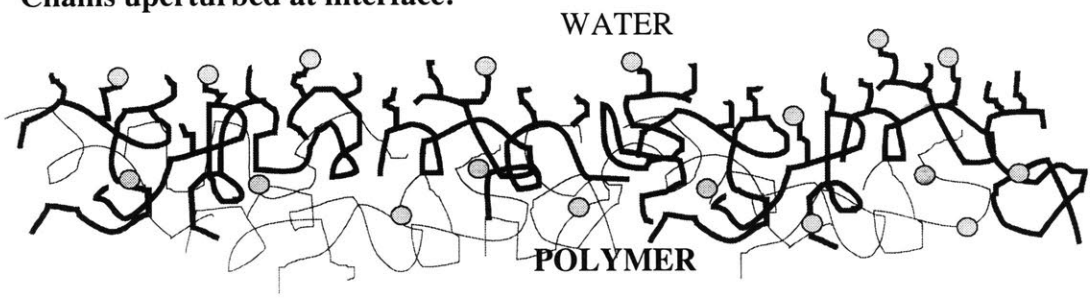

Figure 8.14. Consequences of chain confinement at the water-comb polymer interface on ligand distribution. Chains contributing to the surface layer are highlighted by heavy lines. (Top) Pinning of the comb backbone at the surface to allow presentation of a high density of comb side chains would arrange the molecules as non-interpenetrating disks at the surface. In this case the cluster density is determined by the ratio of comb to RGD-comb in the confined surface layer only and is strongly influenced by the size of the individual comb molecules. (Bottom) If the chains are not aligned at the interface, multiple combs within one R_G of the surface will contribute to the surface layer structure. Ligand distribution would appear uniform unless the fraction of RGD-comb in the film is extremely small, since up to $N^{1/2}$ chains could participate in the surface structure per R_G^2 surface area.

In sharp contrast, confinement of the comb at the interface would mean that large fractions of RGD-comb would be necessary to decrease the cluster separation; here the cluster separation would scale as $(\phi_{RGD\text{-}comb})^{-1/2}$. The surface structure for these two cases is compared in Figure 8.14.

Figure 8.15 shows the cluster surface density ρ_{clus} measured by nanosphere labeling as a function of the bulk volume fraction of C2-RGD3 ($\phi^b_{RGD\text{-}comb}$) in C2/C2-RGD3 blends. Also shown is a linear best fit to this data, obtained for $\rho_{clus} = 9.768 \times 10^{11} (\phi^b_{RGD\text{-}comb})$ (#/cm^2). This surface density is re-plotted in Figure 8.16(a) as an average cluster spacing on the surface d_{clus} =

$(\rho_{clus})^{-1/2}$. For the case of comb/RGD-comb blends where the top molecular layer is semi-confined at the interface, the expected average cluster spacing on the surface is $d_{clus} \sim d_{min}/\phi_{RGD\text{-}comb}^{-1/2}$, where d_{min} is a minimum cluster spacing obtained for films of the pure RGD-comb polymer. The data is well fit using this relationship ($\chi^2 = 0.792$). The best fit curve, shown in the figure, has $d_{min} = 32 \pm 1.0$ nm. Also plotted in Figure 8.16(a) is data from blends using C2-RGD4, where the number of peptides per comb is 5.4. The same overall cluster distribution is obtained, i.e. the number of peptides per cluster is changed but the separation of clusters at the surface for a given amount of RGD-comb in the film is the same.

The labeling data supports the hypothesis that the comb polymer is semi-confined at the water-polymer interface. The measured cluster separation is inconsistent with an unconfined arrangement of comb molecules at the interface, as labeling is not saturated for $\phi^b_{RGD\text{-}comb} >> 0.04$.

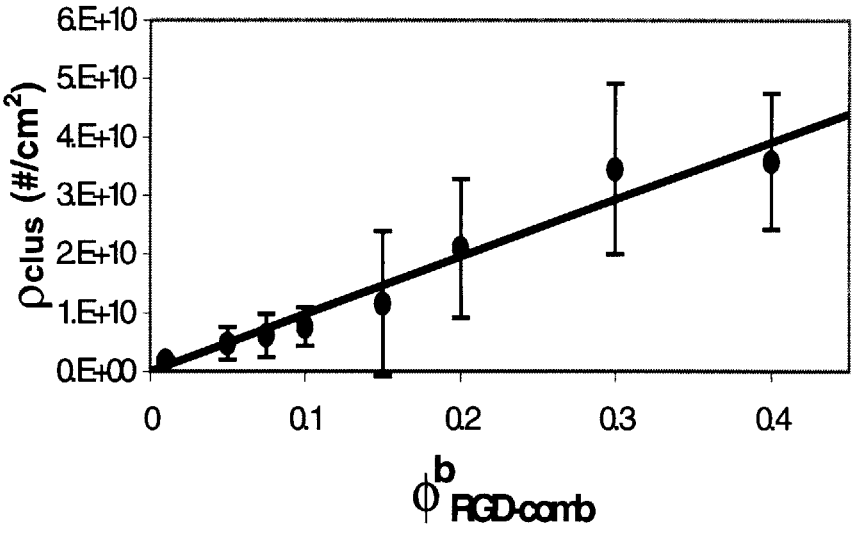

Figure 8.15. Ligand cluster surface density vs. bulk RGD-comb concentration in C2/C2-RGD3 blends. Solid line is a best fit to the data $\rho_{clus} = 9.768 \times 10^{11}(\phi^b_{RGD\text{-}comb})$ (#/cm^2).

From the data relating bulk RGD-comb concentration to ligand cluster density, the total average surface density of ligand obtained vs. the bulk concentration of RGD-comb for comb/RGD-comb blends with different cluster sizes can be calculated, as plotted in Figure 8.16(b). Shown is the accessible total ligand density range for the four RGD cluster sizes used in adhesion strength studies in Chapter 10, assuming that cluster spacing is not affected by the cluster size (# peptides/comb). For all four cluster sizes, the accessible peptide density on these comb polymer surfaces can be readily adjusted two orders of magnitude higher or lower than RGD densities reported in the literature to support fibroblast attachment and focal contact formation[51].

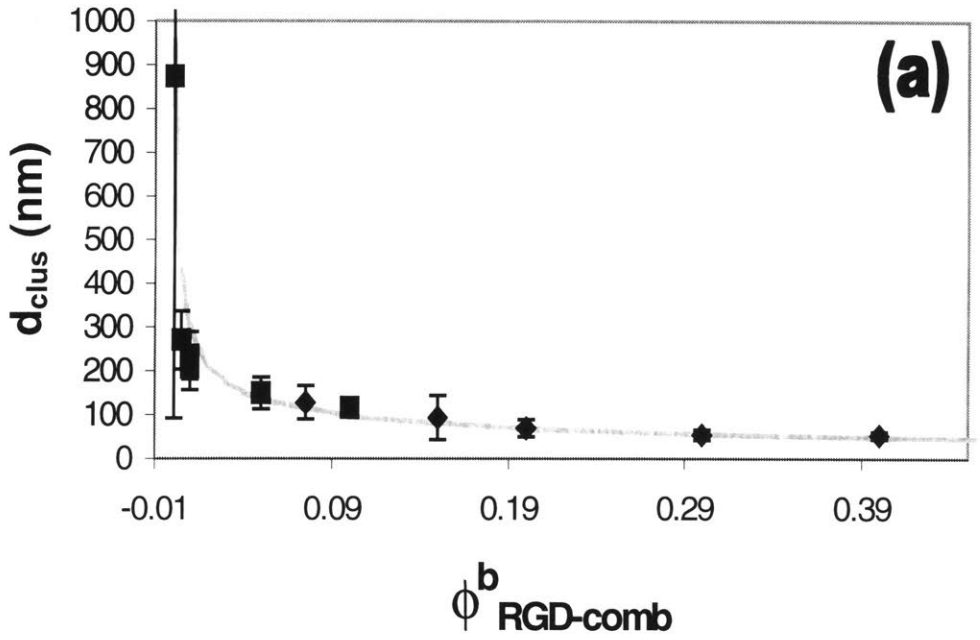

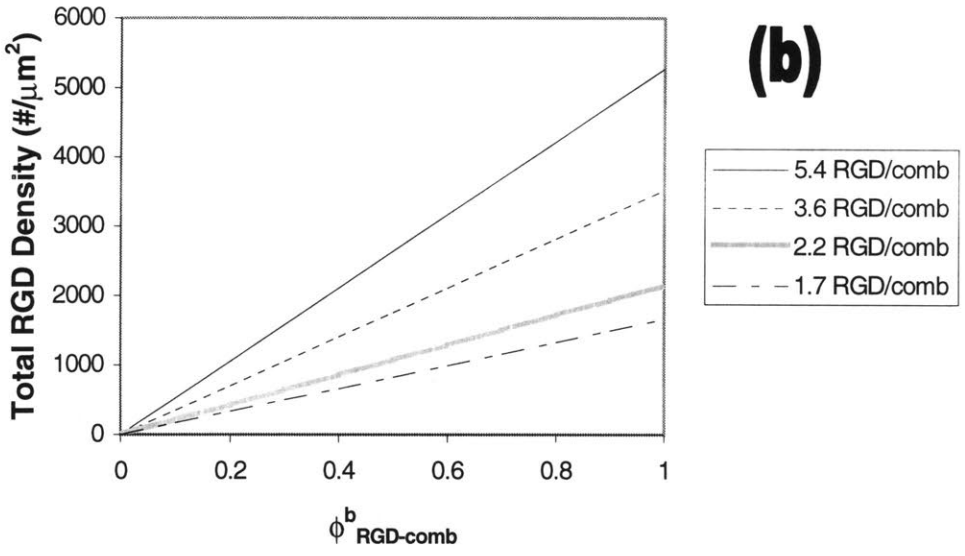

Figure 8.16. Average cluster separation and total RGD surface densities on C2/C2-RGD blends.
(a) RGD cluster spacing from cluster surface density data. Shown are results from two different cluster sizes: (♦) 3.6 peptides/comb (C2-RGD3), (•) 5.4 peptides/comb (C2-RGD4). Solid line is the best fit to the data $d_{clus} = d_{min}/\phi_{RGD\text{-}comb}^{-1/2}$, where $d_{min} = 32 \pm 0.98$ nm. (b) Total RGD surface densities obtained as a function of bulk RGD-comb concentration in comb/RGD-comb blends from cluster density data. Accessible surface densities for 4 different RGD-comb cluster sizes studied in this work are shown: 1.7 peptides/comb (C2-RGD1), 2.2 peptides/comb (C2-RGD2), 3.6 peptides/comb (C2-RGD3), and 5.4 peptides/comb (C2-RGD4).

Latex Films and Embedded Latex Surfaces

Latexes can also be used to present tethered RGD at the surface of biomaterials, allowing clustering of ligand by individual comb molecules and, on larger length scales, by the spheres themselves. We prepared RGD nanospheres having mean diameter 490 nm and total RGD surface densities ~2,500 molecules/μm^2. The morphology of WTNR6 fibroblasts cultured on RGD-comb polymer films, coalesced RGD-latex films, and the RGD-latex embedded in a comb polymer film are compared in Figure 8.17 and 8.19. Cells strongly attach and spread on RGD-latex films, similar to their response on RGD-comb polymer films with comparable ligand surface densities. This result strongly suggests that the top-layer surface structures of these systems are comparable. Cells also attach to embedded latex spheres, but presentation of RGD in 500 nm-diameter domains by the embedded RGD-latex, as shown in Figure 8.18, appears to have a significant effect on cell morphology. Figure 8.18(a), (b), and (c) show cell attachment at three different packing densities of the embedded latex, giving total average RGD densities ~230 RGD/μm^2, 1,300 RGD/μm^2, and 2,200 RGD/μm^2 for beads separated on average 2 μm, 1 μm, or close-packed, respectively. Cells show a more rounded morphology on the embedded latex surfaces than on comb polymer films or coalesced latex films at comparable total RGD densities (compare Figure 8.17(a) (comb polymer film), Figure 8.17(b) (latex film), and Figure 8.18(c) (embedded latex)). While the cell morphology differences seen here are only a semi-quantitative indicator, we will quantitatively demonstrate differences in cell adhesion due to ligand spatial distribution in Chapter 10.

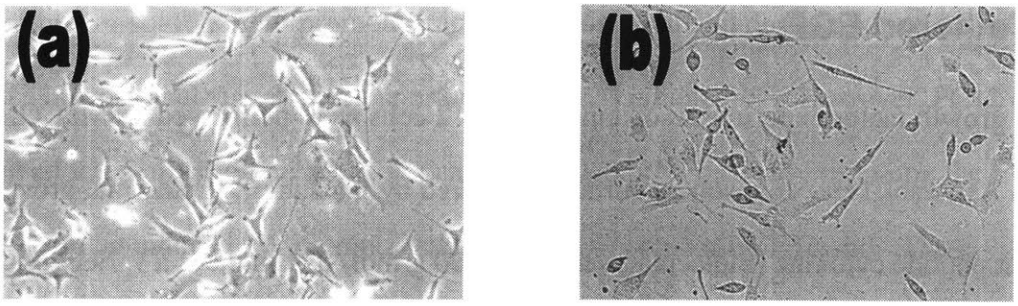

Figure 8.17. Comparison of cell attachment to RGD-comb and RGD-latex films. WTNR6 cells (30,000/cm^2) were seeded in serum-containing media on films prepared from (a) a C2/C2-RGD3 blend thin film or (b) RGD-latex nanospheres. Phase contrast micrograph taken 24 hours post-seeding at 100X. RGD density on each surface is ~2,500 molecules/μm^2.

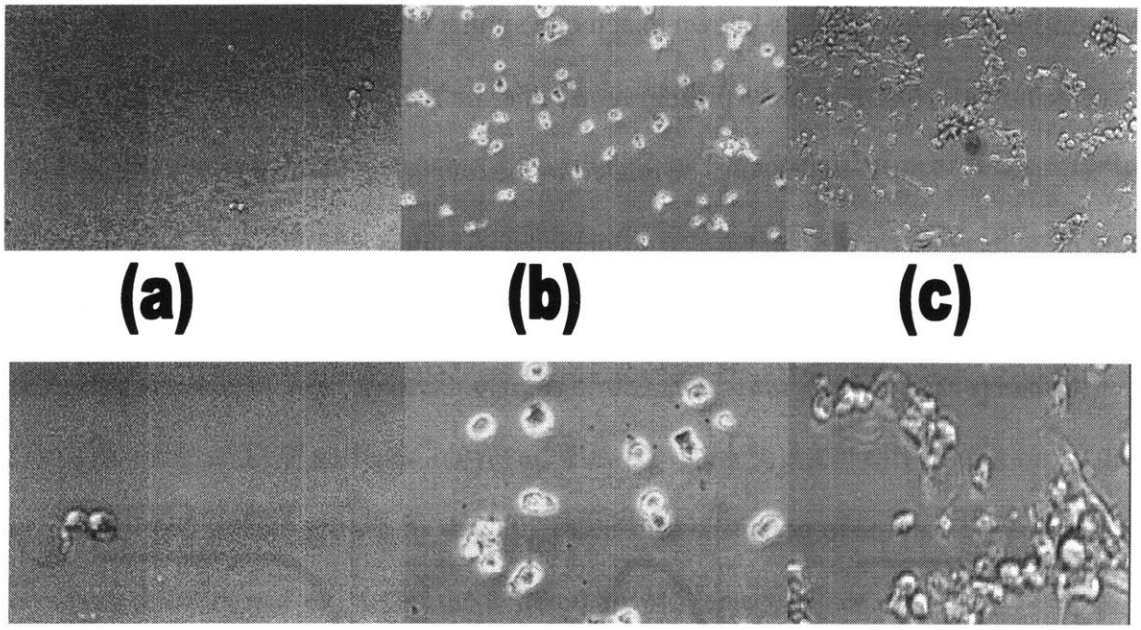

Figure 8.18. Cell attachment and morphology on embedded RGD-latexes. WTNR6 cells (30,000 cells/cm^2) were cultured on embedded RGD-latex surfaces 24 hours and phase contrast micrographs were taken at 100X (top row) and 200X (bottom row). Micrographs going left to right show increasing densities of RGD-latex beads, with average nanosphere separations of: (a) 2 μm (~230 RGD/μm^2), (b) 1 μm (~1,300 RGD/μm^2), and (c) spheres close packed (~2,200 RGD/μm^2).

8.2.2 Tethered EGF

Tethered growth factor experiments on cultured PC12 cells were performed by MIT Graduate Research Assistant Terry Johnson on surfaces prepared by the author. Epidermal growth factor is a potent peptide cytokine (molecular weight ~6,100 g/mol) that induces a variety of changes in cell function depending on the cell type and environment[186]. A few of the functions regulated by soluble EGF added to the media of cultured cells include proliferation, migration, and differentiation[5, 26, 45, 186]. We chose to study the response of an adrenal tumor cell line, PC12 cells, to EGF[170]. It is known that addition of soluble nerve growth factor (NGF) to PC12 cells induces differentiation of the cells into a neuronal phenotype[169]; the differentiated cells then grow axon-like neurites. EGF is known to activate similar chemical signaling pathways within PC12 cells, however, EGF induces proliferation rather than differentiation when added to media of the cell line[169]. This is believed to be related to the transience of the signal generated by EGF binding to its receptor on the cell surface, as depicted in Figure 8.19[167-170].

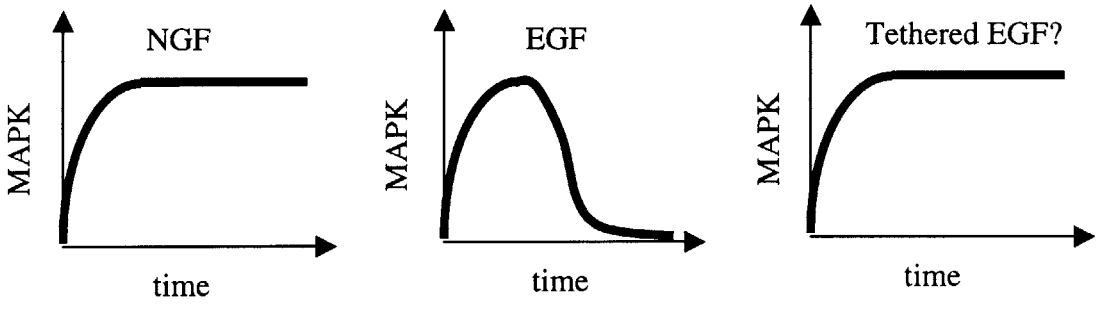

Figure 8.19. Differences in soluble NGF, soluble EGF, and tethered EGF signaling in PC12 cells. NGF or EGF binding by cell surface receptors generates a biochemical response within the cell by increasing the concentration of a signaling molecule (MAPK) in its activated state. However, activation of MAPK by EGF binding is transient (on the order of 20 minutes), possibly due to internalization of receptors. Tethered EGF might prevent receptor internalization and subsequent down-regulation of MAPK signaling, providing a sustained signal similar to NGF.

Binding of soluble EGF promotes rapid internalization and degradation of its receptor, leading to a biochemical signal with a short lifetime (~20 minutes)[169]. However, PC12 cells expressing an internalization-deficient mutant EGF receptor[167] or over-expressing the EGF receptor[168], can be induced to differentiate by addition of soluble EGF ligand. These experiments indicate that the difference in cell responses induced by EGF and NGF may be due to the short lifetime of the normal EGF signal. In a manner similar to the internalization-deficient receptor experiments, we proposed that receptors of non-mutant PC12 cells binding tethered EGF could not be internalized, and the sustained signal required for PC12 differentiation could be generated. Differentiation would indicate stability and activity of the tethered growth factor.

Tethered EGF surfaces were prepared as described in Chapter 6 using tresyl chloride-activated comb polymer films and PC12 cells were cultured on the substrates for 25 days. PC12s were also seeded on surfaces without tethered EGF. Phase contrast micrographs from surfaces at days 3 and 20 post seeding are shown in Figure 8.20. Cells cultured in the absence of EGF showed no signs of differentiation (Figure 8.20(a) and (b)). PC12 cells on tethered EGF surfaces, however, showed visible signs of differentiation by day 3 and well-developed neurite growth by day 20. PC12 differentiation over this time period indicates both stability and activity of the tethered growth factor surface.

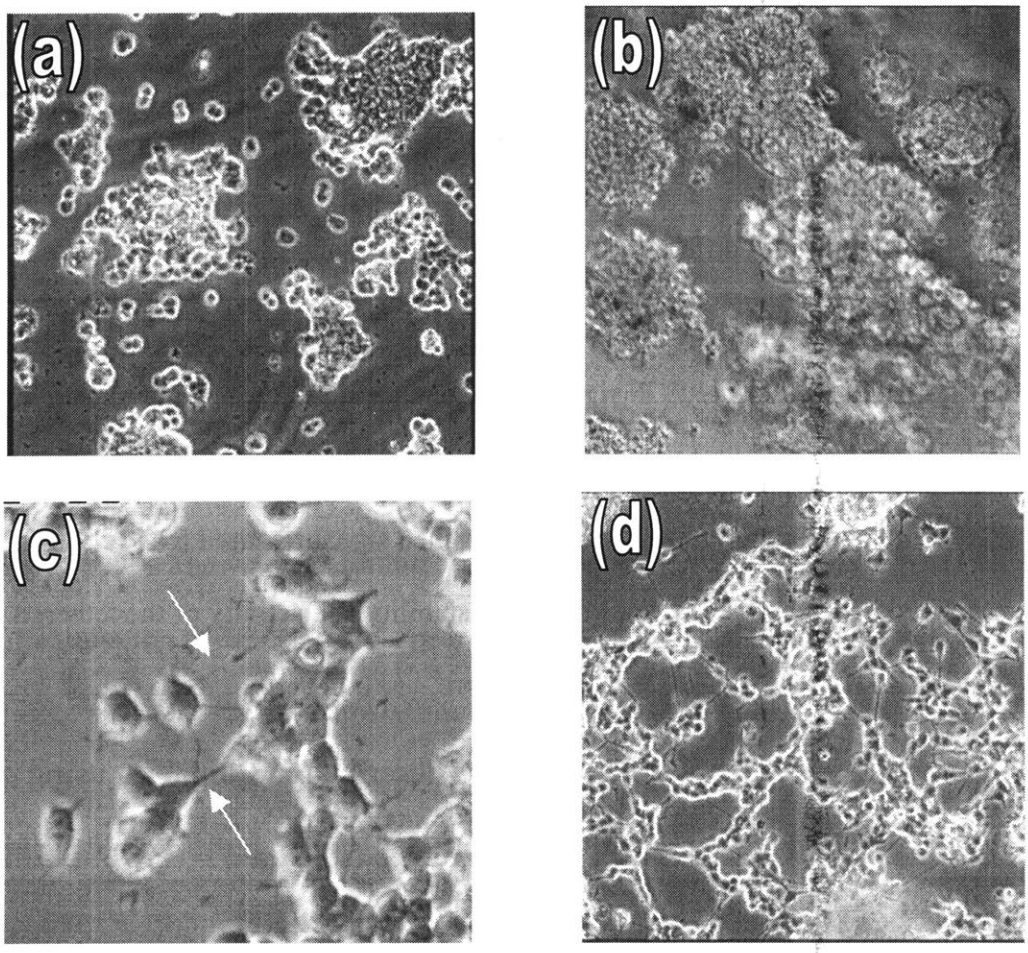

Figure 8.20. PC12 cell differentiation on tethered EGF and control comb polymer surfaces. (a)-(b) Comb polymer surfaces, no EGF. (c)-(d) Tethered EGF surfaces. Phase contrast micrographs taken at 3 days (a,c) or 20 days (b,d) in culture. Extending neurites at 3 days on a tethered EGF surface are denoted in (c) by white arrows.

8.3 Summary

A wide variety of biomedical applications would best be served by materials that guide specific cell responses by combining protein resistance with tethered ligand signaling[39, 40, 42, 43, 45, 46]. Several methods for the preparation of protein-resistant tethered ligand surfaces have been demonstrated in recent research, including the use of functionalized PEO hydrogels[40, 42, 45], grafted PEO monolayers[43], and PEO block copolymer thin films[46]. While each of these

approaches is attractive for certain applications, use of the comb polymers described here would have definite advantages in practical application outside a laboratory environment. Relative to all of these approaches, the comb polymer is inexpensively and simply prepared, and is compatible with typical industrial coating processes[197]. The solubility of these amphiphilic molecules in water/alcohol mixtures also eliminates the need for environmentally unsound organic solvents during processing. Comb-based latexes allow aqueous-based synthesis *and* processing- essentially acting as a bio-regulating paint. In addition, copolymerization of various acrylate or methacrylate monomers for latex cores allows the T_g of latexes to be varied from -30°C to 100°C while maintaining the hydrophilic surface properties of P(MMA-r-POEM). Thus both the temperature required to form films from the latex and the stiffness of these films *in vivo* can be tailored to suit the application of interest.

In addition, preparation of comb polymer surfaces, either by applying a thin comb polymer coating to biomaterials or by application of a comb polymer latex film, should provide a more robust surface layer than block copolymer films or grafted monolayers. Erosion of the top layer of a comb polymer film simply exposes more comb polymer, thereby remaining protein resistant. Further, in latex films the comb stabilizer is grafted to the core during synthesis, providing a highly entangled, high molecular weight anchor for each comb molecule at the surface.

Tethered ligand signaling from comb polymer surfaces as demonstrated in these studies is a powerful tool for engineering cell responses to surfaces. A constant signal is obtained by virtue of the apparent inability of cells to internalize tethered ligands, in contrast to drug-release biomaterials where biochemical signals can only be delivered for finite time periods and are susceptible to loss by diffusion and cell uptake[1, 3, 5]. Use of short side chain tethers allows the immobilized ligand to sample a range of conformations similar to its behavior free in solution,

while maintaining the chemical signal in a very surface-localized, unchanging state. Numerical SCF calculations of the structure of comb polymer/water interfaces predicts alignment of the backbone of comb chains at the surface, maximizing PEO-water contacts in the top surface layer; the experimental results for comb polymer films are consistent with this picture. Alignment of the comb at the surface in this manner leads to *highly efficient* nanoscale clustering of ligand at the surface: each ligand attached to a given comb molecule in the surface layer can potentially be accessed without steric hindrance from subsurface layers, as the surface is molecularly arranged to allow maximum exposure of the PEO side chains.

Comb polymers allow control over nanoscale clustering of peptide on two length scales (simultaneously, if desired). First, multiple side chains of a single comb molecule can be end-functionalized with peptide and blended with its bioinert counterpart to create clusters of ligand at the surface having dimensions of the comb molecule, on the order of 20-40 nm. Cluster spacing, number of peptides/cluster, and total ligand density are easily controlled by varying the fraction of RGD-comb used, comb molecular weight, the degree of functionalization, and the combination of these variables. Secondly, when tethered to latex nanosphere surfaces, ligand can be clustered on much larger length scales than individual comb molecules via mixed particle latex films or embedded latex surfaces, with ligand-bearing domains of 0.1-2.0 μm diameter. Such larger domain sizes may be of interest for controlling cell function when the size scale of individual comb molecules limits the size of peptide clusters that can be presented. Together these comb polymer systems provide access to a continuous range of clustered ligand domain sizes from a few nm up to several microns.

9 Implementation of Signaling Surfaces on a Resorbable Biomaterial

We investigated a method to surface modify poly(lactide) (PLA) compatible with current processing schemes for preparation of cell scaffolds, which might overcome the difficulties in surface modification of biodegradable polymers described in Chapter 4. The objective was to create a cell-signaling surface layer on PLA that can be prepared in a simple, economical manner as part of a scaffold fabrication process such as particulate leaching or phase inversion. The approach studied was surface segregation of P(MMA-r-POEM) comb polymers blended with a PLA matrix.

Segregation has been studied in polymer blends where the thermodynamic driving force for segregation is primarily enthalpic in nature, primarily entropic, or with important contributions from both parts of the surface free energy. In binary blends, segregation driven predominantly by enthalpy is achieved for the species with lower cohesive energy. Large surface excesses of the lower-energy component can accumulate when the difference in internal energies between components is large[115, 116],e.g. poly(tetrafluoroethylene)-containing polymers blended with polystyrene[124, 125]. Walton

et al.[80] demonstrated entropic surface segregation of a P(MMA-r-POEM) comb polymer additive in a PMMA matrix where the enthalpic contribution to the surface free energy actually favored depletion of the additive. The branched architecture of the comb polymer was utilized to entropically drive surface enrichment of the comb. Entropically-driven segregation of comb architectures was also theoretically predicted by Walton[126] and by Fredrickson[127] using SCF models. In linear matrices, comb surface segregation is attributed to favorable localization of chain ends at a surface. However, as the entropic contribution to the free energy in large molecule systems is small, any enthalpic competition between different segments in the system to reside at the surface may dominate the equilibrium structure of the blend[115].

Initial studies seeking to effect entropically-driven segregation of P(MMA-r-POEM) in PLA by vacuum annealing suggested no significant surface enrichment. We thus sought to promote surface segregation of the comb polymer by providing additional entropic and enthalpic thermodynamic driving forces to localize the additive at the surface of the blend. Considering the chemical components of the blend, (an amphiphilic comb having hydrophilic side chains blended with a hydrophobic matrix), we hypothesized that segregation could be driven in comb/PLA blends by annealing in contact with aqueous solution at the free surface. Localization of the hydrophilic comb side chains at the free surface of the blend would serve as a thermodynamic means for lowering the free energy of the blend/water interface, providing a highly comb-enriched surface structure suitable for controlling cell behavior at the surface. The driving force in this case would have both an entropic component (localization of branch ends at the surface and elimination of water ordering at the interface[11]) and an enthalpic component (favorable water-PEO contacts).

In this chapter, surface segregation in PLA/comb polymer blends is explored theoretically, using self-consistent field (SCF) lattice theory to make predictions of amphiphilic comb polymer/hydrophobic linear polymer blend surface composition profiles. The relative contributions of entropic and enthalpic driving forces to surface segregation are compared as a function of the interactions of the blend components with the surface. SCF predicts near-complete surface coverage of blends by comb polymer when even small enthalpic driving forces are present. Optimum composition and branch lengths for cell-signaling P(MMA-r-POEM) comb polymers were identified experimentally in Chapter 8. Here this information is used to make predictions of PLA/P(MMA-r-POEM) composition profiles for blends annealed in contact with water at the free surface. SCF calculations of blend-water interfaces show a surface alignment of comb in the top polymer surface layer similar to that predicted for pure comb polymer films in water. Molecular weight and film thickness effects on surface segregation are also examined.

These theoretical predictions are followed by an experimental study of PLA/P(MMA-r-POEM) blends, demonstrating how surface segregation can be used to control cell adhesion at the surface of PLA/comb polymer blend films. Miscibility studies of amorphous PLA with P(MMA-r-POEM) were carried out by rheology and small angle neutron scattering measurements to assess miscibility of the blend in the amorphous phase. Surface segregation studies were conducted on semicrystalline PLA/P(MMA-r-POEM) blends. Analysis of blend surfaces revealed significant surface enrichment of the comb polymer after water annealing. The surface properties of annealed blends were found to be similar to those of the pure comb polymer. In particular, PLA surface-modified with comb polymer shows increased resistance to

nonspecific cell adhesion for bulk comb concentrations of 10-20 wt%. Introduction of RGD-bearing comb polymer in the blend provides RGD-mediated cell attachment at the blend surface, similar to the comb mixtures studied in Chapter 9. These surfaces were stable in phosphate buffered saline over many weeks at physiologic temperature. The chapter closes with a summary of the results and the relative advantages/disadvantages of this approach for biomaterials surface modification.

9.1 Self-Consistent Field Theoretical Predictions of Surface Segregation in Comb Polymer/ Homopolymer Blends

9.1.1 Comb Polymer Surface Segregation

SCF theory was used to predict the structure of surface-segregated comb polymer/homopolymer blends, including blends with parameters chosen to represent the PLA/P(MMA-r-POEM) mixtures experimentally investigated. Calculations were made modeling the free surface of the blend as a hard wall. The architectural parameters of the blend were described in Chapter 5; they are summarized for convenience in Table 9.1. Architectural parameters remained fixed for all calculations except where comb polymer molecular weight effects were explicitly examined. The comb is 42 vol% B (solvophilic) units, comparable (by both mole and weight fraction of units) to the cell-resistant P(MMA-r-POEM) compositions studied in Chapter 8.

Surface Segregation of Comb Polymers Via Entropic Vs. Enthalpic Driving Forces

In comb polymer/linear homopolymer blends where no preferential enthalpic surface interactions are present, combs will surface segregate due to surface entropy differences between branched and linear polymers[80, 126, 127]. Figure 9.1 shows an example of segregation for a comb/homopolymer blend that has no enthalpic interactions, similar to the calculations of Walton and Mayes[126] ($\chi_{AB} = \chi_{AS} = \chi_{BS} = 0.0$).

Table 9.1. Blend polymer architectures for SCF calculations.

blend component	N_{bbone}	N_{teeth}	$N_{spacing}$	n_{teeth}	N_{total}	segment type
matrix homopolymer	1000	0	-	0	1000	A
comb copolymer	150	4	7	20	230	backbone: A teeth: B

N_{bbone} = number of backbone segments, N_{teeth} = number of segments per side chain, $N_{spacing}$ = number of segments along backbone between side chains of comb, n_{teeth} = total number of side chains per comb molecule, N_{total} = total number of segments per molecule.

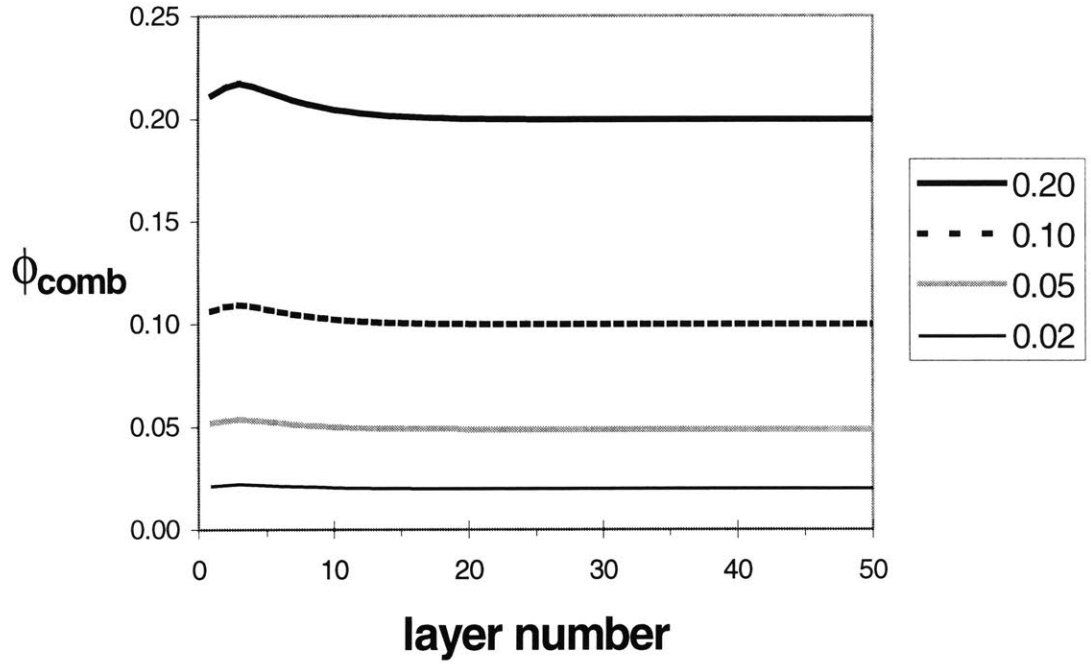

Figure 9.1. Entropically-driven surface segregation of comb polymers. Plotted is ϕ_{comb}, the volume fraction of comb polymer in a given layer of the blend. The hard-wall surface of the blend is located at layer 0. Concentration profiles for four bulk volume fractions of comb polymer in the blend (0.02, 0.05, 0.10, and 0.20) are shown.

The magnitude of excess comb polymer at the surface (above the bulk concentration) for the given blend architectural parameters is predicted to be small for this hard wall geometry. This is in contrast to the case where relatively favorable enthalpic interactions between the comb side chains and the surface are introduced. Figure 9.2 shows the concentration profiles for the same blend component architectures, but with the introduction of a surface repulsion of *A* units by increasing χ_{AS}. Figure 9.3 shows the near-surface volume fraction of comb polymer (ϕ^{s}_{comb}, the average comb concentration in the top 10 layers of the blend ~50 Å deep), and the comb concentration in the surface layer only (ϕ^{top}_{comb}) as a function of χ_{AS}.

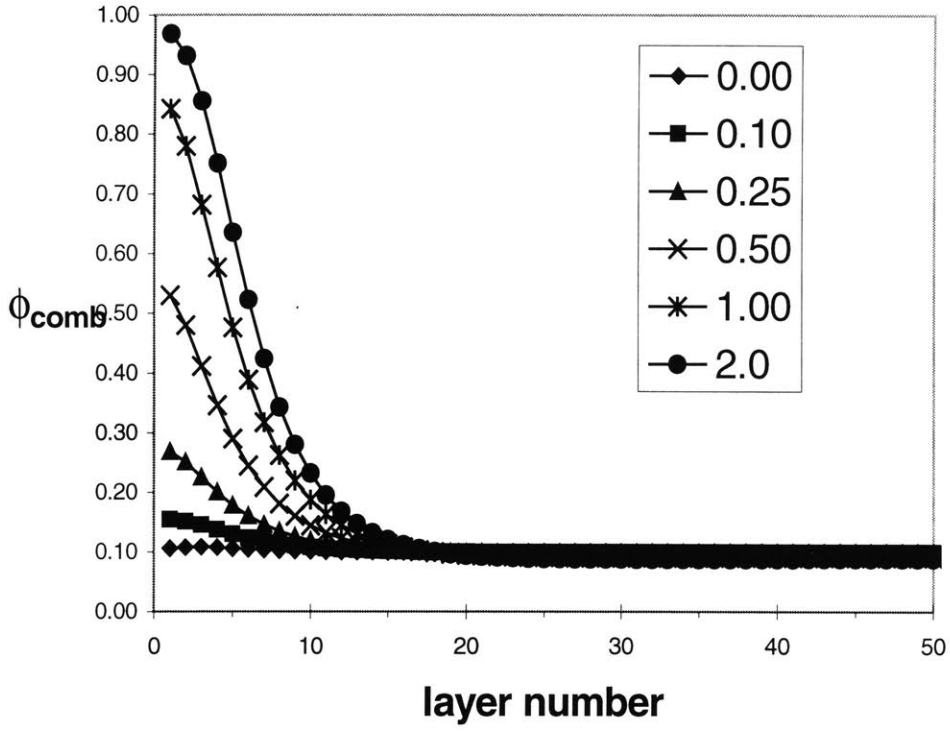

Figure 9.2. Enthalpically-driven comb polymer surface segregation. Concentration profiles for bulk comb volume fraction ϕ^{b}_{comb} = 0.10 are shown; χ_{AS} is varied from 0 to 2.0. $\chi_{AB} = \chi_{BS} = 0.0$.

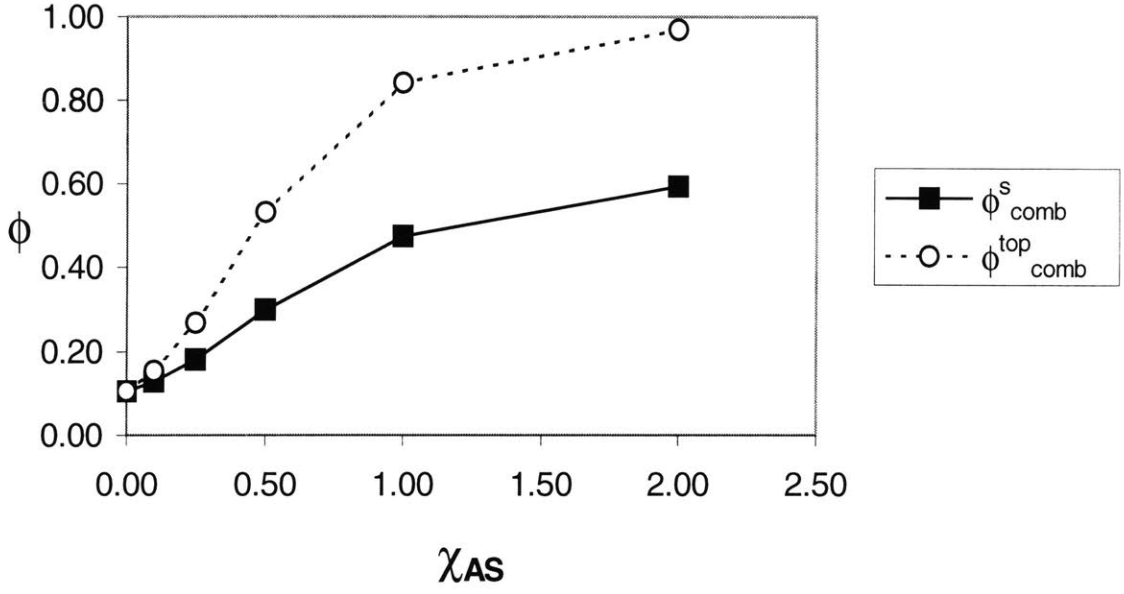

Figure 9.3. Near-surface volume fraction of comb additive and top-layer concentration of additive for enthalpically-driven comb segregation. Near-surface volume fraction ϕ^{s}_{comb} is the average comb volume fraction in top 10 layers of blend; ϕ^{top}_{comb} is the comb volume fraction in the top layer of the blend. Increasing χ_{AS} increases the relative attraction of the comb side chains for the blend surface.

The introduction of a relative enthalpic attraction of the comb side chains to the surface greatly amplifies the extent of surface segregation. The topmost surface layer of the blends is composed almost entirely of the comb additive for $\chi_{AS} = 2.0$ (modeling a matrix and backbone component with low water solubility). Enrichment of the additive is strongly surface-localized, providing only a thin surface layer of the comb polymer, and no evident depletion layer.

Practically, for blends of P(MMA-r-POEM) comb polymer with polylactide, an enthalpic attraction of the comb side chains to the surface can be achieved by annealing blends in contact with water. To model the interactions of PLA and comb polymers with an aqueous solution interface, we set $\chi_{BS} = 0.4$ (χ for poly(ethylene glycol) in water $\approx$ 0.4[146]) and $\chi_{AS} = 1.25$ (water is a nonsolvent for the backbone and matrix units). Since the basic repeat units of the experimental system (lactide, methyl methacrylate, and ethylene oxide) are miscible[131, 133], we set $\chi_{AB} = 0$. Architectural and composition parameters were kept as listed in Table 9.1.

Figure 9.4 shows the predicted equilibrium concentration profiles of blends with these interaction parameters for varying bulk comb concentrations. The inset plots the volume fraction of comb copolymer localized in the top surface layer (ϕ^{top}_{comb}) as a function of bulk comb volume fraction. The results predict a strong localization of the comb in the surface layer if a thermodynamic attraction between the comb side chains and the surface is introduced by water annealing. Bulk concentrations of only 2 vol% of the comb provide a concentration in the surface layer of nearly 90 vol%, and a large excess within the top ~ 50 Å of the blend. Though it discounts swelling at the water/polymer interface, the hard-wall surface model suggests that annealing PLA/P(MMA-r-POEM) blends in contact with aqueous solution should yield > 95%

surface coverage for bulk concentrations of ~10-20 vol% comb polymer. Figure 9.5 shows the predicted surface region volume fraction of comb polymer in comb/homopolymer blends (ϕ^{s}_{comb}) as a function of the bulk concentration in PLA. Because ϕ^{s}_{comb} provides a measure of the thickness of the surface segregated layer, larger values of ϕ^{s}_{comb} should identify surfaces that can absorb greater amounts of water. Figure 9.5 demonstrates that due to the rapid decay of the comb polymer enrichment away from the surface, the average surface composition within the top 50 Å will show a volume fraction of comb polymer significantly less the 1.0 even when the top surface of the blend is nearly 100% comb polymer.

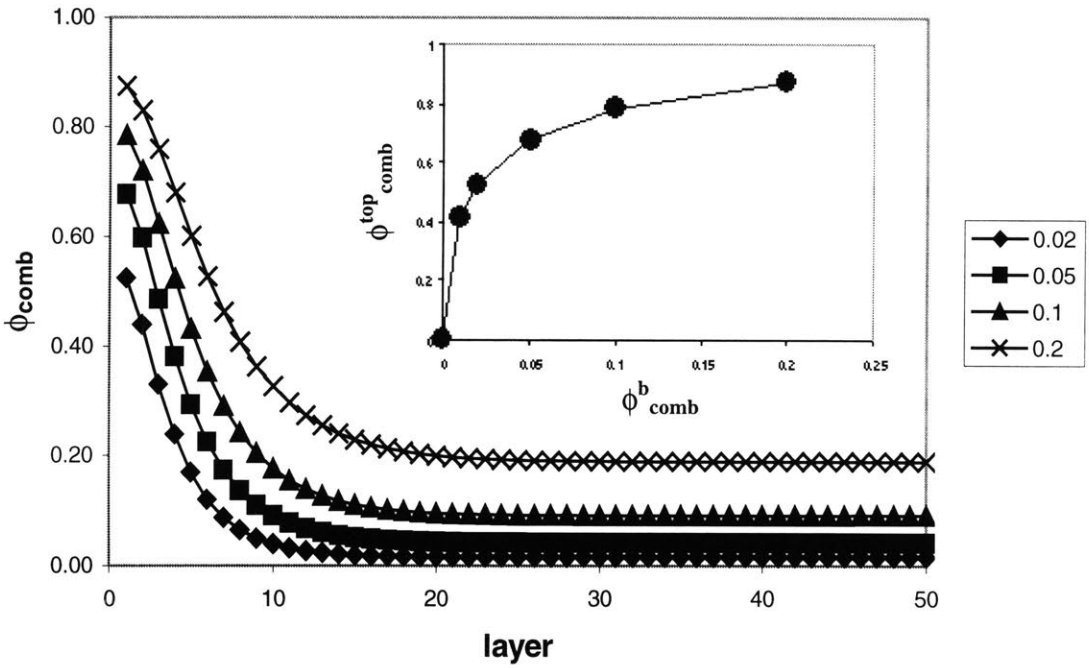

Figure 9.4. SCF predictions of P(MMA-r-POEM) surface segregation in polylactide. (Main Figure) Each curve is the calculated equilibrium volume fraction profile of the comb polymer blended with PLA in contact with water at layer 0. Bulk volume fractions of comb copolymer are (♦), 0.02; (•), 0.05; (•), 0.10; (×), 0.20. (Inset) Surface layer comb volume fraction for each of the bulk comb concentrations plotted in the main figure.

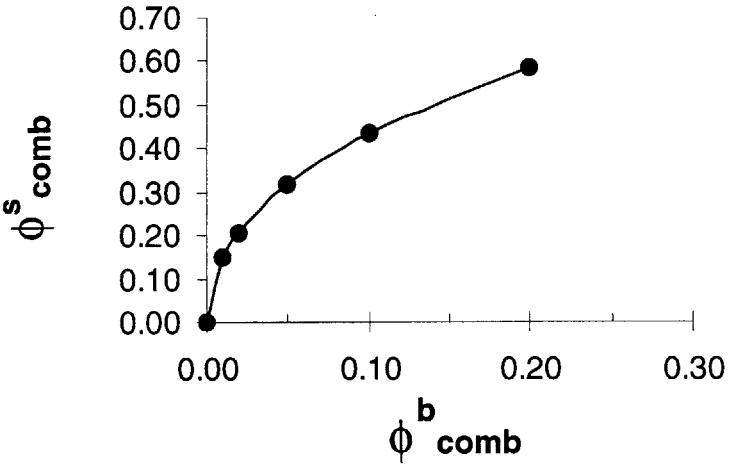

Figure 9.5. Surface region comb enrichment predicted for PLA/P(MMA-r-POEM) blends annealed in contact with water. Shown is the calculated average volume fraction of comb polymer in the top ~50 Å of blend thin films at equilibrium vs. the bulk concentration.

9.1.2 Swelling of Blend Surface Layers in Water

Further SCF calculations were made modeling the blend surface as a "soft-wall" interface by explicitly introducing water as a single-segment molecule immiscible with the blend polymers. This allowed swelling of the blend surface layer in water to be modeled. Computations were made with the same blend architectural parameters used in the previous calculations. Interaction parameters were set to $\chi_{AB} = 0.0$, $\chi_{BS} = 0.4$, and $\chi_{AS} = 2.5$. Note that a larger value of χ_{AS} is used here to model the insolubility of the hydrophobic units in water when the solvent is explicitly included in the calculation (instead of approximating the surface as a hard wall), to counteract entropy-driven mixing of the small molecule with the polymers. (In reality, this mixing entropy will be overcome by entropy loss due to the hydrophobic effect.) An example of the predicted equilibrium structure of the blend is shown in

Figure 9.6, for $\phi^{b}_{comb} = 0.015$. Significant swelling of the surface layer is predicted by SCF, and the presence of water in the surface layer orients the comb polymer in a manner similar to that predicted by SCF for pure comb polymer films in section 8.2.1. The concentration profile for the comb backbone peaks in 2 layers of the interphase. Side chains are depleted from these layers, extending into both the solvent and the bulk. Similar to the predicted structure of comb polymer films in water, the top few layers of the surface are composed almost entirely of hydrophilic side chain units and water. As discussed in section 8.2.1, quasi-confinement of the comb polymer at the interface implies arrangement of the molecules as non-interpenetrating disks at the surface.

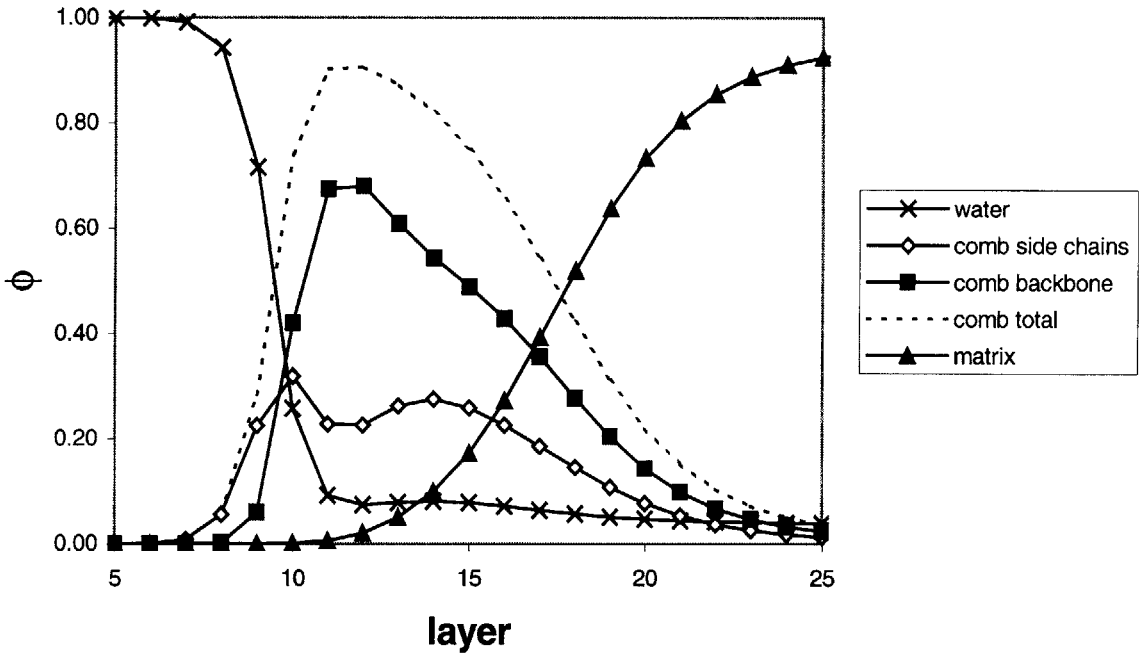

Figure 9.6. SCF prediction of blend surface swelling by equilibration in contact with water. Here, water was explicitly modeled as a monomeric solvent. The bulk concentration of comb polymer is $\phi^{b}_{comb} = 0.015$.

Ligand cluster density at the blend surface should thus be controlled by the area fraction of functionalized molecules at the surface, similar to comb polymer surfaces, and the size of individual clusters will be directly determined by the lateral coil dimensions at the interface.

9.1.3 Molecular Weight and Film Thickness Effects on Comb Segregation

The calculations made in section 9.1.1 considered a comb polymer having 150 units in the backbone; for P(MMA-r-POEM) comb polymers of equivalent architecture this corresponds to approximately a molecular weight of 25,000 g/mol. The SCF calculations of Walton and Mayes[126] predicted a strong dependence of comb surface excess on molecular weight for entropically-driven segregation. A significant molecular weight effect is also predicted here, and provides a handle by which ϕ^{s}_{comb} can be considerably increased. Figure 9.7 shows the change in ϕ^{top}_{comb} and ϕ^{s}_{comb} for $\phi^{b}_{comb} = 0.10$ (χ parameters modeling PLA/P(MMA-r-POEM) as in section 9.1.1) with increasing N_{bbone} of the comb for the hard-wall surface model. Quadrupling the molecular weight of the comb polymer by increasing N_{bbone} from 100 to 400 (keeping the spacing between side chains constant) gives rise to an increase in ϕ^{s}_{comb} of about 40%. Although we might expect further modest increases in ϕ^{s}_{comb} up to molecular weights of several hundred thousand g/mol, slower kinetics of diffusion for higher molecular weight chains (diffusivity ~ M^{-1}) become a practical limitation to surface segregation. Hence, optimal molecular weights in the range of 25-100K g/mol (N_{bbone} = 150-600 units in our calculations) should provide good surface coverage by the segregating additive while maintaining reasonable kinetics for equilibrating the blend.

Finally, a practical consideration in our experimental studies is the effect of film thickness on the surface structure. Previous theoretical and experimental studies of surface segregation have shown segregation may be reduced as the film thickness decreases due to decreasing differences in bulk vs. surface free energy[126, 194, 195]. Figure 9.8 shows the calculated surface concentrations of comb polymer in the top layer (ϕ^{top}_{comb}) and averaged over the top 10 layers of the blend (ϕ^{s}_{comb}) as a function of film thickness for χ parameters modeling a PLA/P(MMA-r-POEM) blend with $\phi^{b}_{comb} = 0.10$. Because the enthalpic driving force for this blend is expected to be quite strong ($\chi_{BS} << \chi_{AS}$), film thickness effects are only seen for films less than ~500 Å thick. Blend thin films with thicknesses > 500 Å should thus have surface segregated structures representative of much thicker polymer blend devices and bulk samples. These calculations were made assuming segregation only to the free surface of the blend; if surface energetics also favors segregation of comb to the substrate/polymer interface, these calculations will underestimate thickness effects for very thin films.

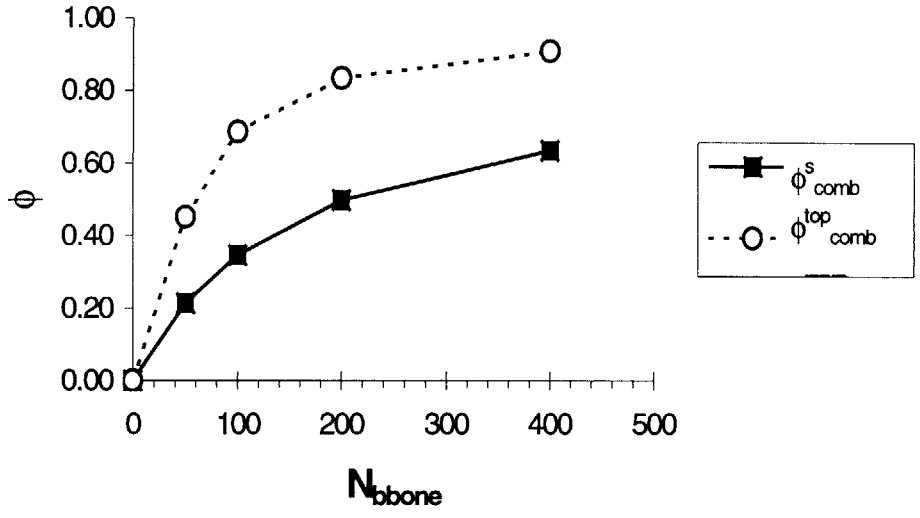

Figure 9.7. Effect of comb polymer molecular weight on surface segregation predicted for PLA/P(MMA-r-POEM) blends. N_{bbone} is increased while maintaining a constant side chain length of 4 units and spacing of 7 units. One additional side chain is added for every 7 units of added backbone to maintain constant comb composition.

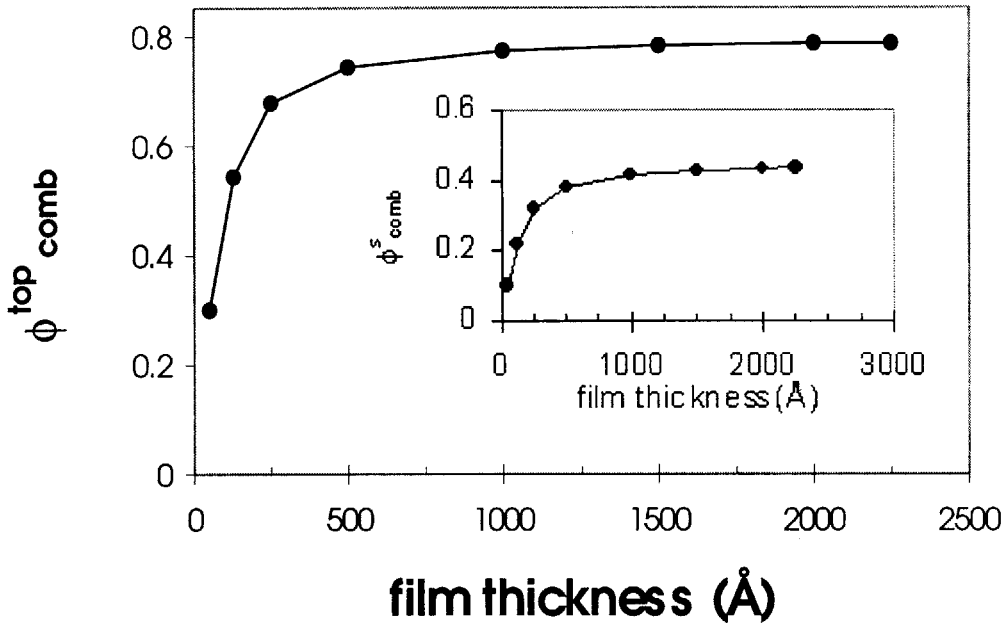

Figure 9.8. Film Thickness Effects. Variation in comb top surface layer volume fraction ϕ^{top}_{comb} (main figure) and top 50 Å average volume fractions ϕ^{s}_{comb} (inset) with film thickness.

9.2 Characterization of PLA/P(MMA-r-POEM) Blends

9.2.1 Miscibility of P(MMA-r-POEM) Comb Polymers With Amorphous PLA

Experimental assessment of miscibility of semicrystalline PLA with other polymers is made challenging by the inherent phase separation of crystalline and amorphous regions, which confuses attempts to elucidate mixing of a second component in the amorphous phase. We thus carried out miscibility analyses using the non-stereoregular isoform of PLA, poly(D,L-lactide), which does not crystallize and allows a clear determination of

amorphous mixing between the polyester and a second component[131]. Bulk miscibility of PLA and the comb polymer was assessed for PLA/C1 blends using dynamic rheological testing and small angle neutron scattering measurements on bulk melt-pressed blend samples. Miscibility of the comb polymer with PLA could not be determined by thermal analysis, as the T_gs of the comb (T_g = 43°C) and PLA (T_g = 57°C) are too close to effectively resolve in blends, especially in light of the broadening of the glass transition which is typically observed in miscible blends[196].

Dynamic Rheological Measurements of Blend Miscibility

Representative results from the rheological measurements on PLA/comb polymer blends are shown in Figure 9.9. The time-temperature superposition (tTS) principle[197] empirically relates the frequency dependence of the complex dynamic modulus (G*) of a material observed at temperature T to that at a given reference temperature according to:

$$G^*(\omega,T) = b_T G^*(\omega a_T, T_{ref}) \qquad \textbf{(Eqn 9.1)}$$

The modulus-scale shift factor b_T and frequency-scale shift factor a_T allow superposition of data at temperature T with that of the reference temperature (here, we have chosen T_{ref} = 140°C). Figure 9.9 shows tTS master curves for a 50:50 wt:wt PLA:C1 blend. Qualitatively, the data show a single plateau in the storage modulus at high frequency and one break in slope moving from high to low frequency, indicative of flow in a homogeneous blend. In contrast, immiscible blends show a second plateau in G' at low frequency due to a long time relaxation mechanism present in phase-separated microstructures[198]. Figure 9.10 shows a Han plot[199-203] of the 50:50 blend data. Two criteria for a fully homogeneous blend are temperature independence of the log G' vs. log G" curves and a terminal slope approaching 2; both requirements are met by the

PLA/comb blend. Similar rheological measurements on 80:20 and 90:10 wt:wt PLA:C1 blends indicate full miscibility of the polymers over this composition range.

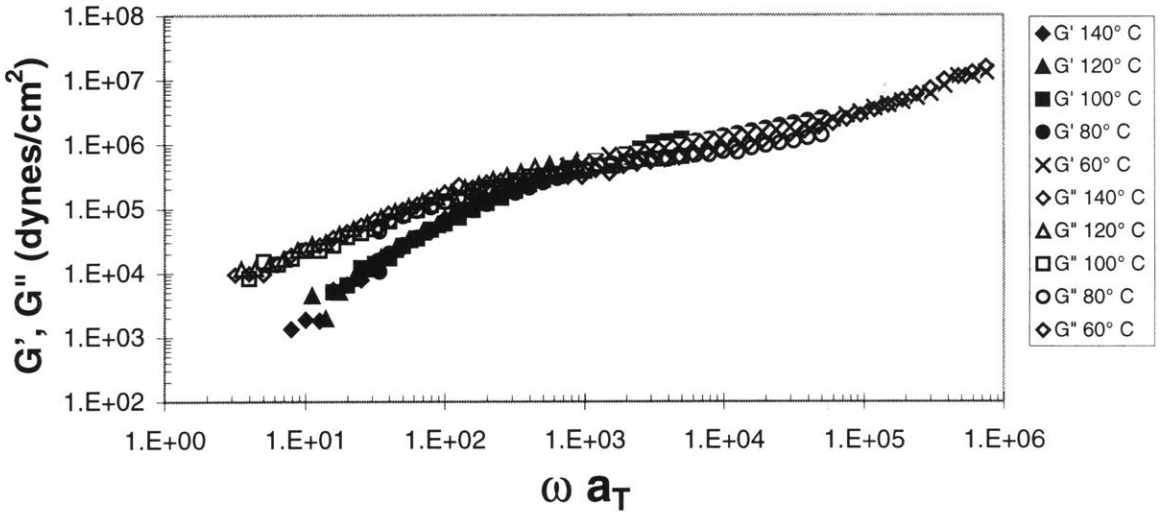

Figure 9.9. tTS master curves for a PLA/comb polymer blends prepared from dynamic rheological measurements. Legend shows temperature (in °C) of each shifted data set for a 50:50 wt:wt poly(D,L-lactide):C1 blend.

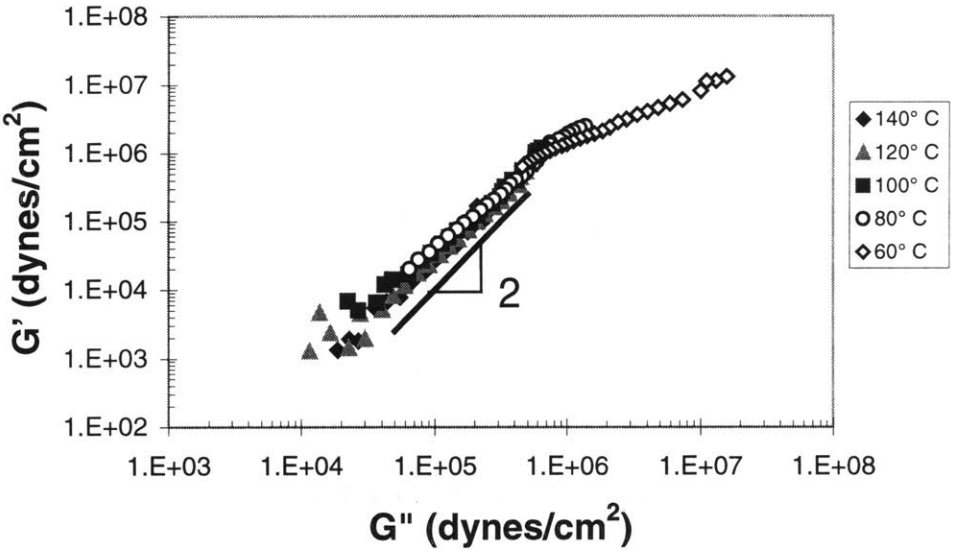

Figure 9.10. Han plot of rheological data for 50:50 wt:wt PLA:C1 blend.

SANS Measurements of Blend Miscibility

For further confirmation of the compatibility of PLA with the comb polymer, SANS measurements were made on melt-pressed bulk poly(D,L-lactide)/C1 blends. Phase separation gives two features in small-angle scattering[204, 205]. Porod scattering arises due to interphase boundaries at low Q; here the intensity scales as Q^{-4}.

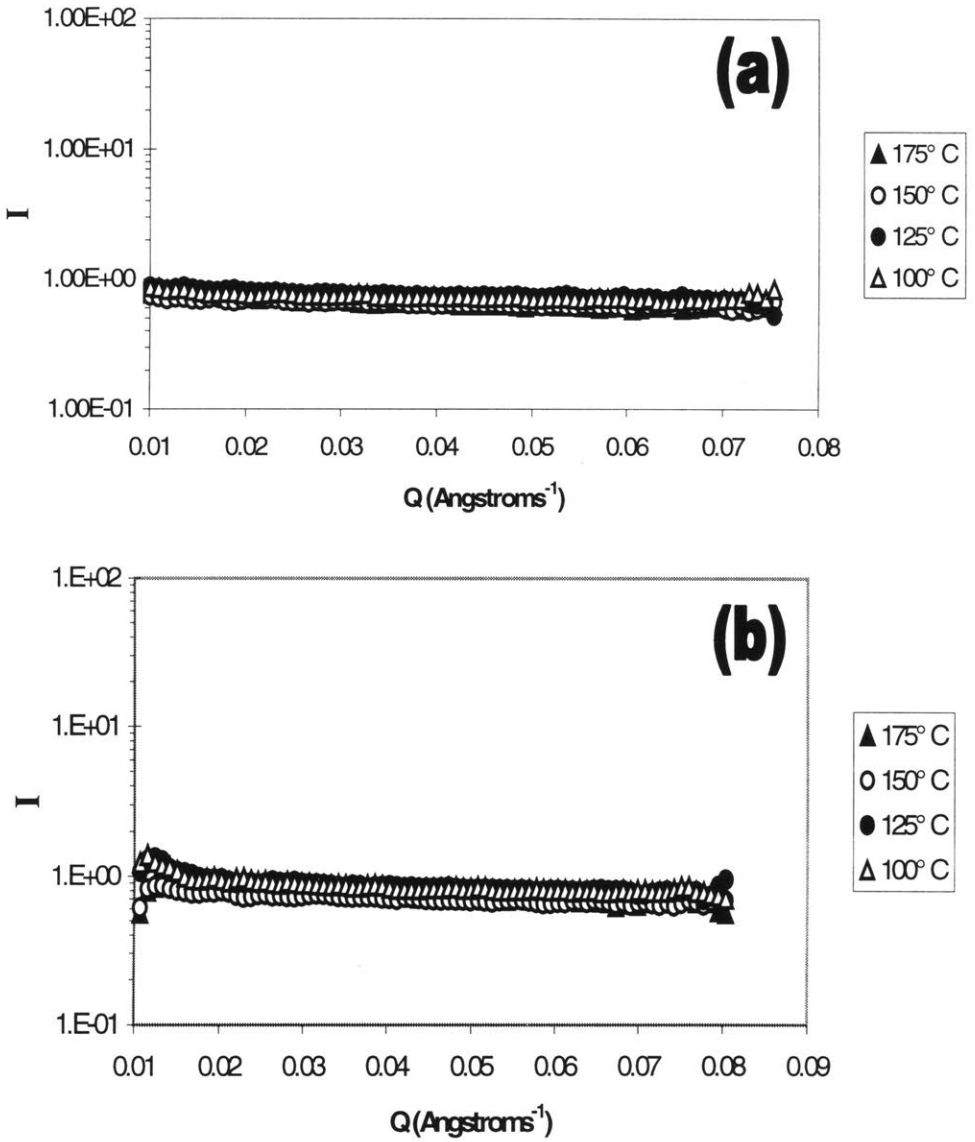

Figure 9.11. Scattering results for SANS measurements on PLA:C1 blends at several temperatures. Scans were made on the same sample moving from 175°C to 100°C in 25° increments. (a) 90:10 wt:wt PLA:C1 blend. (b) 80:20 wt:wt PLA:C1 blend.

(Q is the scattering vector, $Q = 4\pi\lambda^{-1}\sin\theta$ where λ is the wavelength of the incident neutrons and θ is the scattering angle). At higher Q the intensity scales as Q^{-2} (the Debye region) due to scattering from individual chains within different domains. Scattering profiles for a 90:10 wt:wt PLA:C1 blend and 80:20 wt:wt PLA:C1 blend are shown in Figure 9.11(a) and Figure 9.11(b) respectively. The samples show essentially background intensity over the entire scattering vector (Q) range examined. This is expected for a sample which has no source of contrast: for a mixture of two different polymers this is true when the blend is miscible and has little neutron scattering length density contrast.

9.2.2 Surface Segregation of P(MMA-r-POEM) in Poly(L-lactide)/Comb Blends

Surface Energy Measurements of Blend Components

Surface segregation in miscible polymer systems is thermodynamically controlled by surface free energy. For a given blend system at equilibrium, the component with the lowest surface free energy will typically be enriched at the surface of the blend. Measured surface free energies in air (surface tension in air) of PMMA, C1, and poly(L-lactide) are listed in Table 9.2. As expected, introduction of the hydrophilic PEG side chains in the comb polymer raises the surface energy (in air) of the comb polymer relative to pure PMMA. The measured surface energy of PLA is significantly lower than previously reported from experiments using an underwater contact angle method[58].

However, polymer surface energies derived from underwater contact angle measurements are known to be invariably too large (often twice as large as accepted values) due to adsorption of oils at the water-polymer interface[161]. As measured here, PLA shows a surface energy significantly lower than both PMMA and the comb polymer. Therefore blends of P(MMA-r-POEM) with PLA annealed in air or vacuum are expected to show a depletion of the comb polymer from the surface (enrichment of the lowest surface energy component, the matrix). However, if we consider the case of annealing the blend in contact with water, surface enrichment will be controlled by the relative values of the water/polymer interfacial tension rather than the air/polymer interfacial tension. The comb polymer has a calculated interfacial tension with water significantly below that of PLA/water, suggesting a driving force for comb surface segregation in blends annealed in contact with water, in line with results from SCF calculations in section 10.1.1.

Table 9.2. Measured surface energies of PMMA, P(MMA-r-POEM), and PLA.

Polymer	γ^d_p (dyn/cm)	γ^p_p (dyn/cm)	γ_p (dyn/cm)	γ_{pw} (dyn/cm)
PMMA	33±0.58	12±1.5	45±1.6	3.3±0.99
C1	33±0.37	15±0.59	48±0.70	2.6±0.19
PLA	26±1.7	13±4.4	38±4.7	5.6±1.8

Dispersive (γ^d_p), polar (γ^p_p), and total surface energies (γ_p) of polymers in air were calculated from sessile drop contact angle measurements on polymer surfaces. Interfacial energies of the polymers with water (γ_{pw}) were calculated using the equation of Girifalco and Good[162, 163], (Eqn 6.2).

XPS Analysis of Thin Film Blend Surface Compositions

Surface compositions of thin film PLA/C1 blends were assessed via X-ray photoelectron spectroscopy (as described in Chapter 6). Example raw data from high-resolution C_{1s} scans of two blends, 80:20 and 90:10 wt:wt PLA:C1, are shown in Figure

9.12 before and after annealing in water. Surface segregation of the comb polymer is indicated by the growing peak contribution to the spectra at ~286.5 eV (relative to the carbonyl peak at ~289 eV), characteristic of carbon bonded to oxygen in the comb side chains.

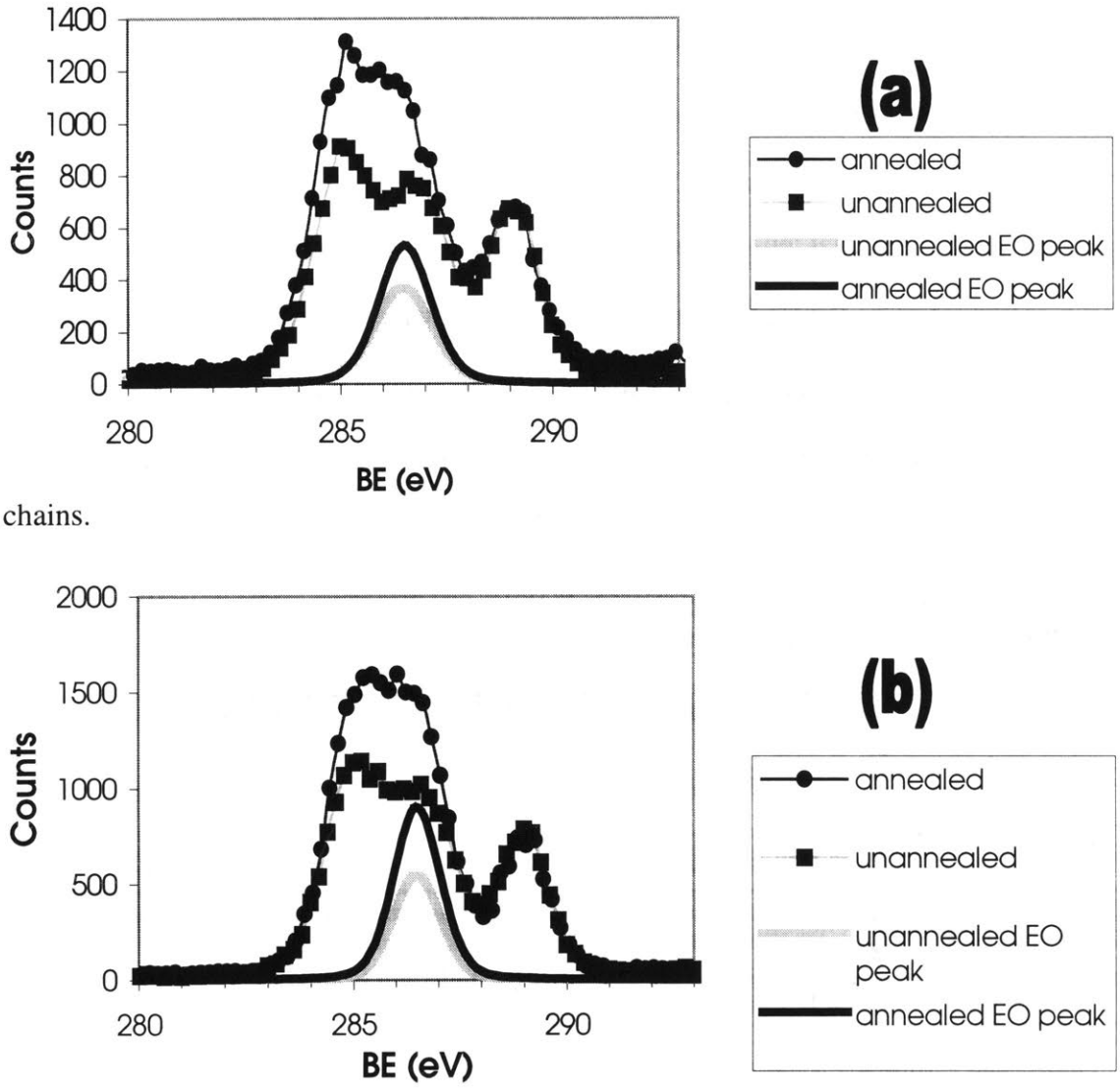

Figure 9.12. C_{1s} XPS data for PLA:C1 blends.
Data sets normalized to match COO peak areas of unannealed and annealed samples. (•) unannealed blend raw counts, (•) annealed blend raw counts, (▬) unannealed blend EO carbon environment peak, (▬) annealed blend EO carbon environment peak. (a) 90:10 wt:wt PLA:C1. (b) 80:20 wt:wt PLA:C1.

Figure 9.12 also plots the best-fit comb side chain ethylene oxide (EO) C_{1s} contribution to the spectra before and after annealing for each sample, showing the increase in this component at the surface upon annealing. The deconvoluted peaks and best fit for the two spectra of Figure 9.12 are given in Figure 9.13. Qualitatively, the contribution of EO units (and thus comb polymer) at the surface is significantly enriched after annealing.

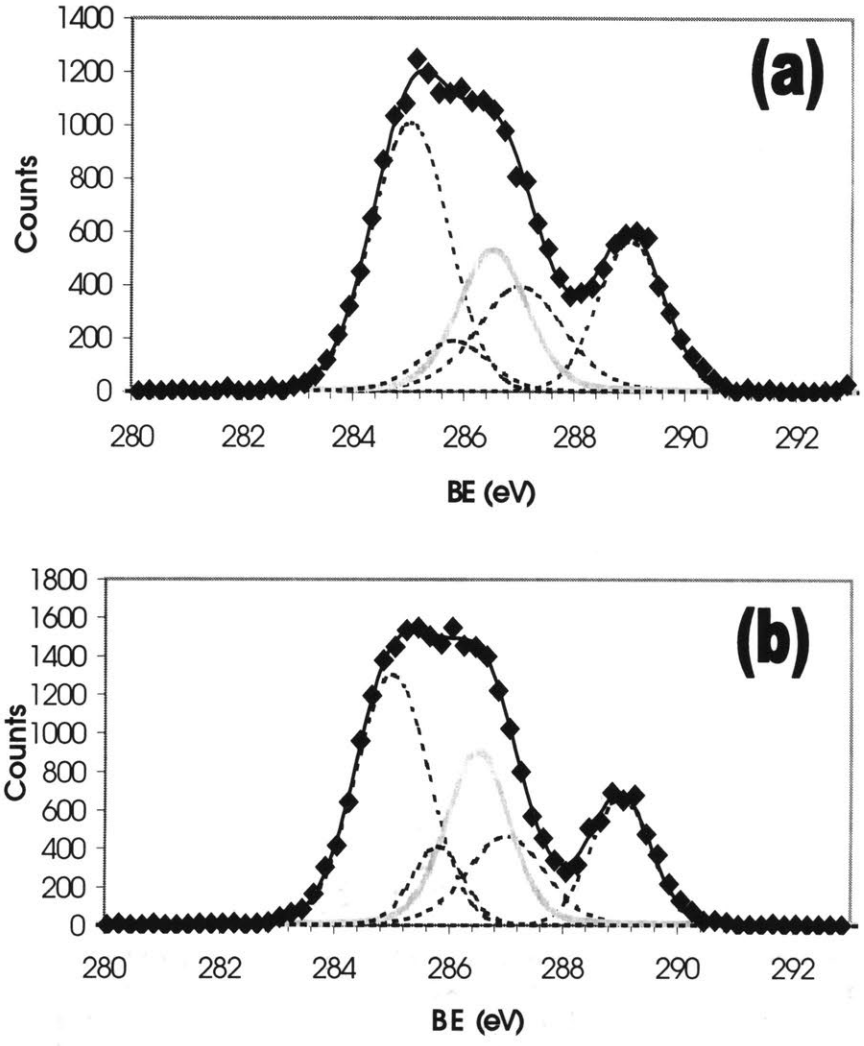

Figure 9.13. Example Best Fits to XPS Data and Deconvoluted Peaks. Samples are (a) 90:10 wt:wt PLA:C1 annealed blend, and (b) 80:20 wt:wt PLA:C1 annealed blend. Contributions due to the EO units of the comb side chain are highlighted by the gray solid lines. Dotted lines show the contributions to other C_{1s} bonding environments in the spectra.

Quantitative values of the near-surface volume fraction of comb polymer, ϕ^{s}_{comb}, were calculated from best fit data for each sample preparation condition. The near-surface comb volume fraction values are plotted as a function of bulk comb volume fraction in Figure 9.14(a) for take-off angles of 45°. XPS probes a depth of ~50 Å; the total measured ϕ^{s}_{comb} from the XPS data corresponds to a weighted average composition over this near-surface depth. Also plotted in Figure 9.14a is the equation $\phi^{s}_{comb} = \phi^{b}_{comb}$ (dashed line), the expected surface composition if no surface segregation or depletion occurs.

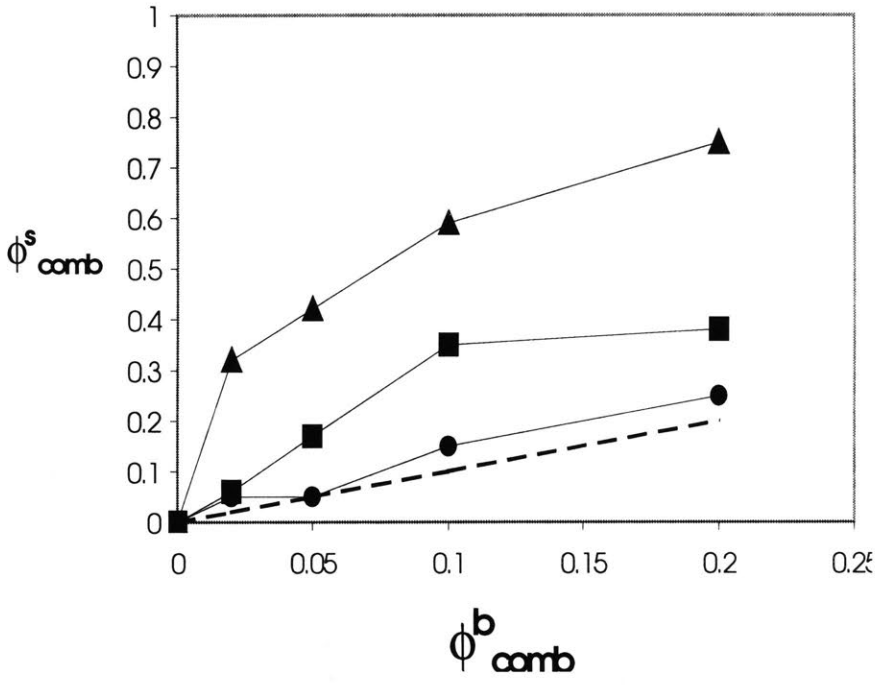

Figure 9.14. Surface segregation of comb polymer in PLA blends measured by XPS. Measured surface volume fraction of comb polymer from XPS data. (----) Expected surface composition for no segregation. (•) Surface volume fraction comb polymer calculated from XPS data for unannealed PLA/C1 blends. (•) Surface volume fraction comb polymer for blends annealed 4 days at 70° C in H_2O. (•) Surface volume fraction comb polymer for blends annealed 4 days in vacuum at 120°C.

Blend samples as cast show significant comb polymer surface segregation, presumably driven by surface entropy. Blends annealed in vacuum show a drop in the surface concentration of comb (Figure 9.14(a)), from the surface-enriched as cast condition to approximately the bulk concentration. Surface energy measurements suggest a *depletion* of comb from the surface under these conditions ($\phi^s_{comb} < \phi^b_{comb}$) might be expected. However, entropic chain end segregation still favors surface localization of the comb polymer in vacuum annealing. Annealing blends in contact with water led to strongly enhanced surface enrichment of the comb polymer over the as cast condition, in agreement with interfacial energy considerations and our model predictions.

To further understand the surface composition of annealed blends, expected XPS results were modeled using theoretical SCF concentration profiles for PLA/comb polymer blends. Model concentration profiles were used to generate expected values of $A_{EO\ blend}/A_{EO\ comb}$, the ratio of the ethylene oxide carbon C_{1s} peak in blends ($A_{EO\ blend}$) to that in the pure comb polymer ($A_{EO\ comb}$). Theoretical concentration profiles were calculated using the hard-wall surface model, in keeping with the high-vacuum environment of XPS. Representative χ parameters were used to model the PLA/comb blend: $\chi_{AB} = 0.0$, and $\chi_{BS} = 0.4$. The interaction parameter χ_{AS}, which is not explicitly known for this system, is the only adjustable parameter for the calculation. χ_{AS} was varied between 1.0 and 3.0 to obtain a best fit to measured values of $A_{EO\ blend}/A_{EO\ comb}$. Best fits were obtained for $\chi_{AS} = 1.25$; the measured XPS area ratios are compared to the SCF predicted values in Figure 9.15.

Concentration profiles that correspond to the predicted $A_{EO\ blend}/A_{EO\ comb}$ ratios are shown in

Figure 9.4, as discussed in section 9.1.1. The theoretical SCF concentration profiles for these parameters show a rapid decay of the comb concentration as one moves from the top layer of the blend into the bulk. Thus the concentration of comb in the top-most surface layer of the blend (based on the model predictions) may be significantly higher than the average surface concentration measured by XPS. The volume fraction of comb in the top layer of the blend predicted by SCF (ϕ^{top}_{comb}, ~5 Å deep) is plotted vs. comb bulk volume fraction in the inset of

Figure 9.4. Based on the model predictions, the total surface enrichment measured in XPS corresponds to ~90% coverage of the top surface layer of the blend by comb polymer when $\phi^{b}_{comb} = 0.20$.

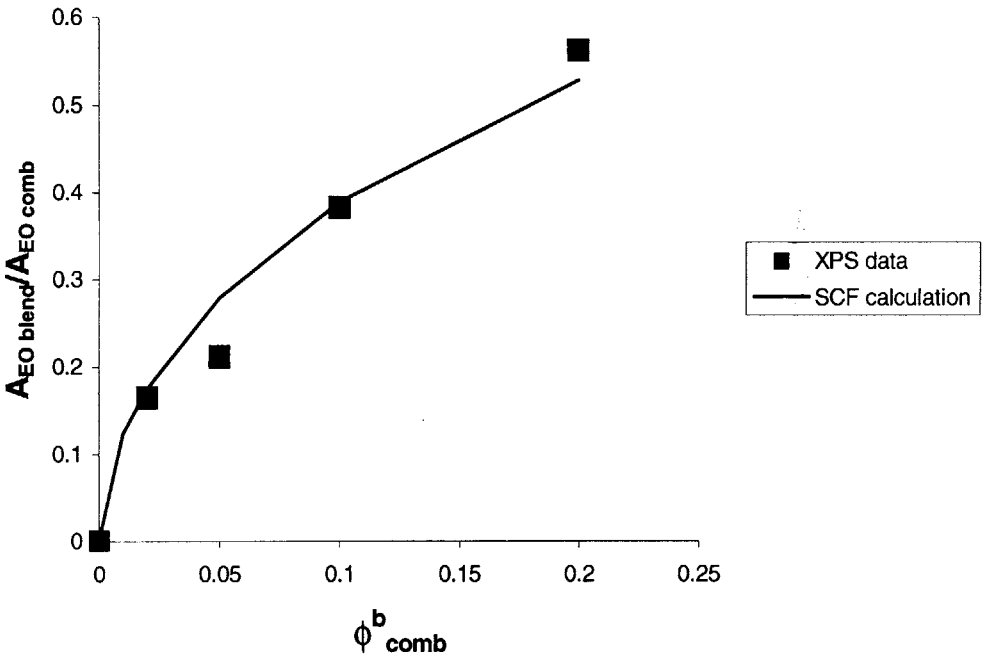

Figure 9.15. Comparison of experimental ethylene oxide C_{1s} carbon peak areas with best-fit SCF predictions. $A_{EO\ blend}/A_{EO\ comb}$ is the ratio of the C_{1s} EO carbon peak (BE = 286.5 eV) in blends to that in a film of pure comb polymer. (•) XPS data. (—) Best fit using theoretical SCF concentration profiles for blend.

Contact Angle Measurements on Blend Thin Films

Surface enrichment of the comb results in modified contact angles for water on the blend surfaces, as shown in Figure 9.16. Unannealed blends showed a decrease in the contact angle on withdrawal , indicating some restructuring of the surface under water. This is consistent with an excess of comb polymer at the as-cast surface, as detected in XPS. However, the surface excess of comb polymer in the as-cast blend appears insufficient to provide restructuring in water to a completely wetting surface. The contact angle drop plateaus at small drop volume rather than continuing to decline, in contrast to measurements made on pure comb polymer films (Figure 8.8). This may indicate either a very thin surface layer of comb polymer (comparable to the structure of latex films; contact angles shown in Figure 8.12), or incomplete coverage of the top surface by the hydrophilic side chains.

Contact angles on water-annealed blends, on the other hand, were qualitatively similar to those on comb films or latex films. Contact angles steadily declined with decreasing drop volume on annealed blends, corresponding to a constant area of contact of the spread water droplet on the surface, due to the presentation of PEG side chains at the reorganized surface. On respreading of a water drop on the annealed surface, the droplet immediately spread to the bounds of the pre-wet area due to absorption of water in the comb-enriched surface layer. Previous studies[80] of surface segregation of a similar amphiphilic comb polymer showed that the amount of water absorption in the comb-enriched surface layer can be significant (up to 40 vol% water at the top 50 Å of the blend). As noted in the following section, spincast PLA blends exhibit a rough surface morphology, and this may influence the observed contact angle result[161]; however the

observed trend is consistent with the surface composition measured by XPS- and comparable to the contact angle data obtained on smooth pure comb polymer surfaces.

AFM and XRD Investigations of Thin Film Blend Morphologies

Morphologies of pure poly(L-lactide) and 80:20 wt:wt poly(L-lactide):C1 blend films were investigated using atomic force microscopy and X-ray diffraction. The percent crystallinity determined from XRD spectra for pure PLA or PLA/C1 blends as cast and after annealing 4 days in water is listed in Table 9.3. AFM was performed on spincoated samples as cast or annealed 1 or 4 days in water. AFM images of samples annealed for 1 or 4 days were qualitatively similar; images after 1 day annealing are shown.

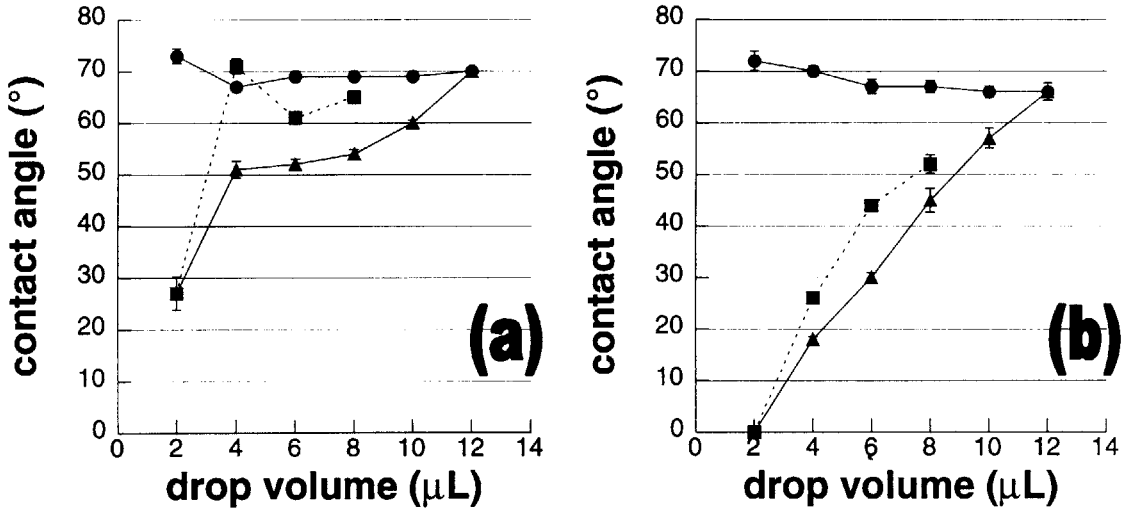

Figure 9.16. Water contact angles with 80:20 wt:wt PLA:C1 comb blends. Measurements made on spincoated films of blends, both (a) before and (b) after 4-day heat treatment at 70°C in water. (•) spreading drop contact angle, (•) withdrawing drop contact angle, (•) respreading contact angle.

Figure 9.17(a) shows surface topography of a pure PLA thin film observed by AFM. The spincast polymer film is initially transparent with a homogeneous flat surface showing no topographical or chemical/elastic features discernible by AFM. This is in contrast to the surface structure of the water-annealed film, shown in Figure 9.18(a) and (c). Formation of fibrous of crystalline lamellae on annealing leads to roughening of the (now opaque) film. The AFM phase data for the annealed surface reveals crystalline fibers distributed over the surface of the film. Separation of amorphous and crystalline domains within polymer films can occur over molecular distances (amorphous chains confined between lamellae) or microscopic distances (amorphous chains between lamellar fibers or between spherulites), depending on polymer molecular weight, chain mobility, crystallization rate, and the internal interactions of the chains[206-211]. Under AFM inspection, the PLA thin films prepared here by spincasting from chloroform appear to exhibit interfibrillar segregation of the amorphous component.

Spincoated blends of PLA with 20 wt% C1 exhibit significant differences in morphology. AFM topography images of an as cast poly(L-lactide)/C1 blend film are shown in Figure 9.17(b). The blend exhibits a pitted surface that might be attributed to phase separation.

Table 9.3. Percent crystallinity of PLA and 80:20 wt:wt PLA:C1 blends before and after water annealing.

sample	% crystallinity (as cast)	% crystallinity (annealed)
PLA	~0	21.7
PLA/C2 blend	5.2	19.2

Values determined from XRD spectra.

However, as cast blends of C2 with poly(D,L-lactide) show similar features, as seen in Figure 9.23(c). The films prepared were several thousand Å thick, apparently too large for thickness-induced phase separation[212]. Nor is the structure in the PLA blend likely attributable to crystalline/amorphous phase separation, as the as cast sample exhibits only ~5% crystallinity. Topography of thin films can be strongly influenced by the choice of solvent and sample preparation conditions[213]. Preferential interactions of one of the blend components with the solvent[214, 215] and rapid solvent evaporation during spincoating[216, 217] have both been observed to influence thin film topographies. Given that PLA was clearly miscible with C1 as assessed by rheology and SANS, it is likely that the topography seen in the as cast films is a non-equilibrium effect of the solvent and casting method rather than phase separation.

Upon annealing in water, crystal growth occurs in blends, as shown in Figure 9.18. X-ray diffraction spectra of PLA and PLA blends are shown are Figure 9.19. Comparable levels of crystallinity were measured in pure PLA and PLA/C1 blends annealed in water, although the morphologies of the annealed blends as seen by AFM differ considerably from annealed PLA films. Crystal growth in the blend is shown in Figure 9.18(f) to result in plate-like lamellae, while the pure PLA film (Figure 9.18(c)) shows branched fibrillar crystal growth.

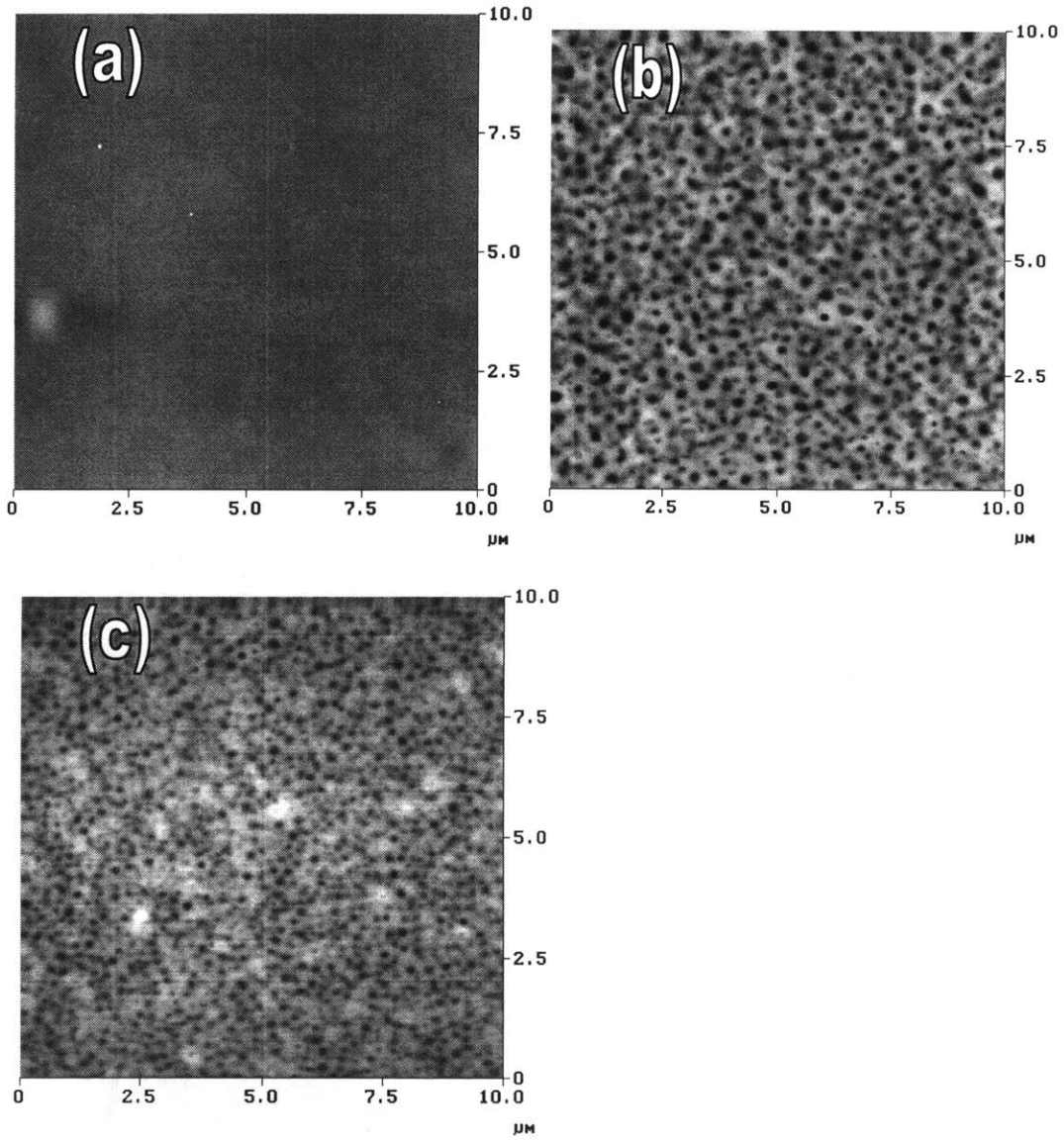

Figure 9.17. AFM topography images of as cast polymer thin film surfaces. (a) As-cast PLA thin film. Height grayscale is 20nm. (b) As-cast 80:20 wt:wt poly(L-lactide):C1 blend. Height grayscale is 100 nm. (c) As-cast 80:20 wt:wt poly(D,L-lactide):C1 blend. Height grayscale is 100 nm. Round dark features in as cast PLA blends are pits ~20-35 nm deep.

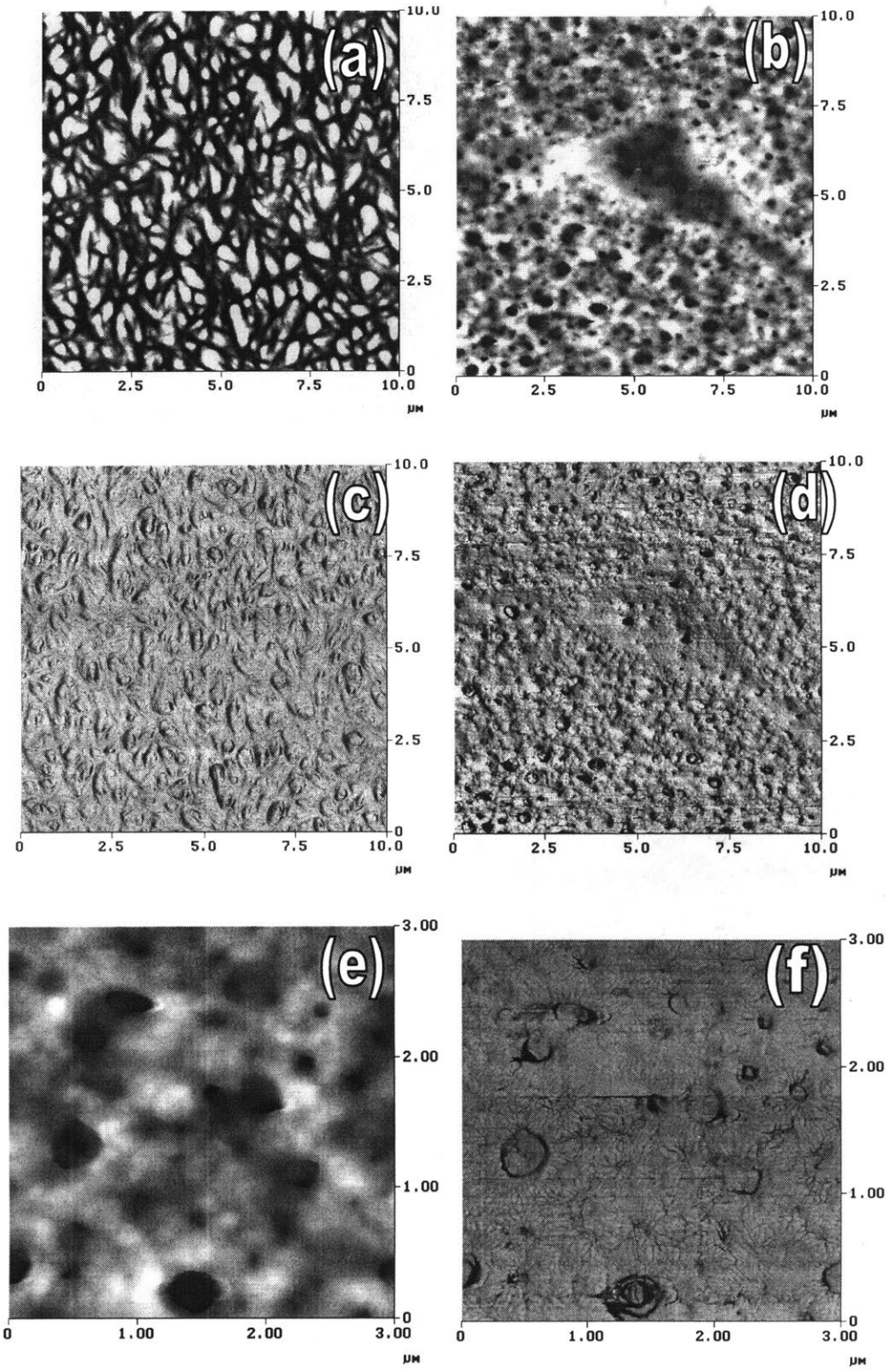

Figure 9.18. Morphological changes in PLA/comb polymer blend thin films induced by annealing. Shown are AFM topography (a,b,e) and phase (c,d,f) images. Topography grayscale is 200 nm. Phase grayscale is 60°. (a,c) PLA thin film after water annealing. (b,d,e,f): 80:20 wt:wt PLA:C1 blend after water annealing.

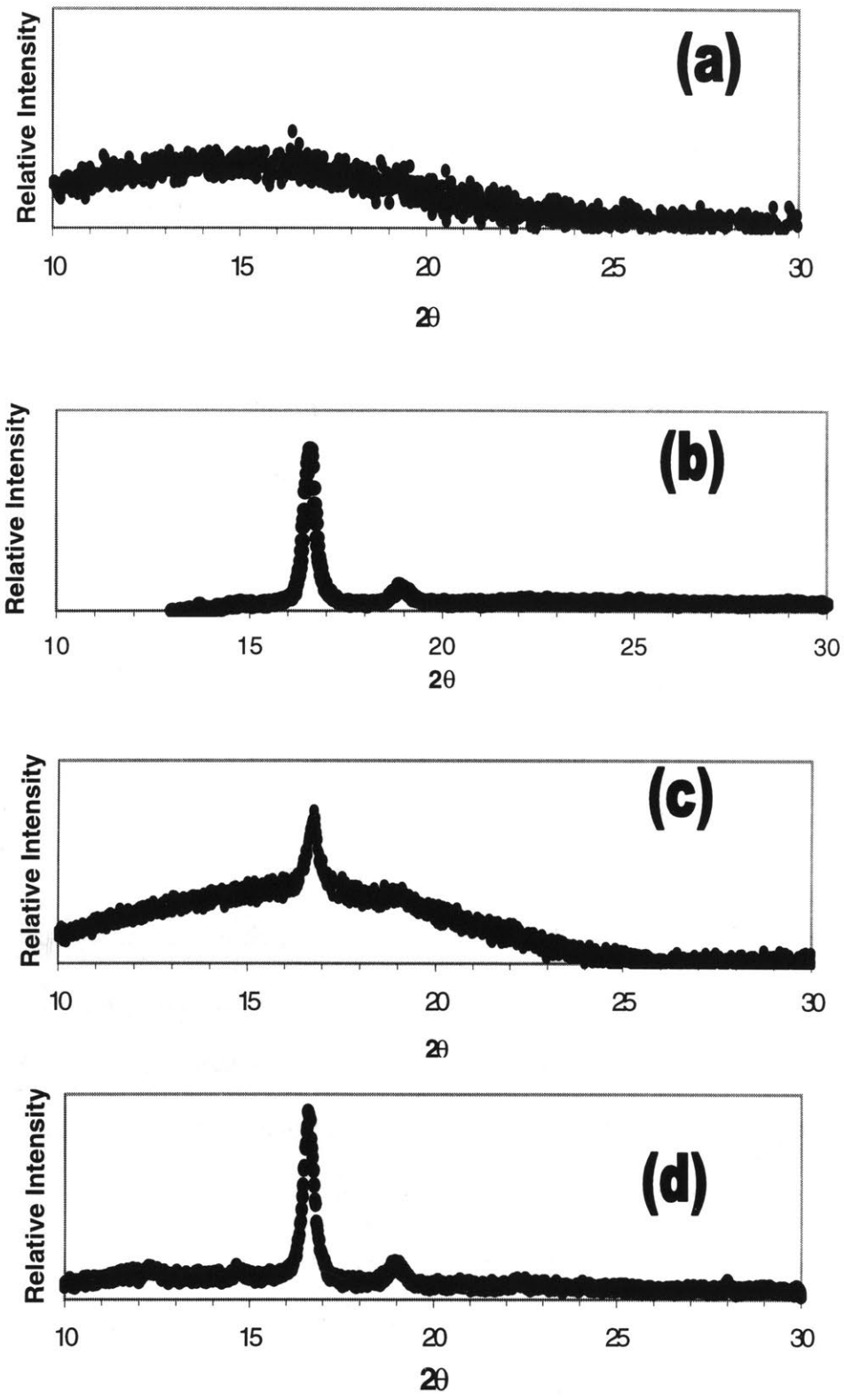

Figure 9.19. X-ray diffraction spectra of poly(L-lactide) and poly(L-lactide) blends. XRD patterns were obtained for solvent cast films of (a) PLA as cast, (b) PLA annealed in water, (c) 80:20 wt:wt PLA:C1 as cast, and (d) 80:20 wt:wt PLA:C1 annealed in water.

Accessible RGD Densities at PLA Blend Surfaces

Surface presentation of RGD ligand on PLA was achieved by blending with RGD-functionalized comb polymer. PLA/C2/C2-RGD3 and PLA/C2/C2-RGD4 blends were examined by AFM to determine the amount and distribution of surface-segregated RGD in water-annealed blends. Based on the combined SCF modeling and XPS data which showed a high surface coverage of blends by comb polymer for $\phi^b_{comb} = 0.20$, we chose to examine blends with a fixed total concentration of comb polymer (C2-RGD3 or C2-RGD4 + C2) of $\phi^b_{comb} = 0.20$. The relative amounts of ligand-modified and unmodified comb were varied in blends to alter the RGD surface density.

To assess the presentation of RGD peptides at the surface of the blend, 30 nm-diameter polystyrene nanospheres were covalently linked to ligand accessible at the surface of the blend, similar to the approach taken in section 8.3.1 for quantifying ligand density at the surface of comb/RGD-comb films, and AFM was performed on the labeled samples. This method allowed approximate average total cluster density determination, and also allowed examination of the local distribution of clusters at the surface of PLA/comb/RGD-comb blends. Representative AFM topography and phase images are presented in Figure 9.20 for blends containing 1, 5, or 10 wt% C2-RGD4. AFM phase data, depending on the sample under investigation, displays contrast arising from chemical or stiffness differences at or near the sample surface[218-230]. Thus the PS nanospheres (T_g ~ 100°C), which are significantly stiffer than the blend components at room temperature, are clearly defined in the phase image. Bright objects that we have

identified as the nanospheres in the phase image correlate with objects in the topography image of ~30 nm height. Blends exhibit immobilized nanospheres both on the top surface of the films and within the pits which were large enough for the AFM tip to effectively probe, indicating that the comb polymer is homogeneously present in the top surface layer of the uneven thin film blend surfaces.

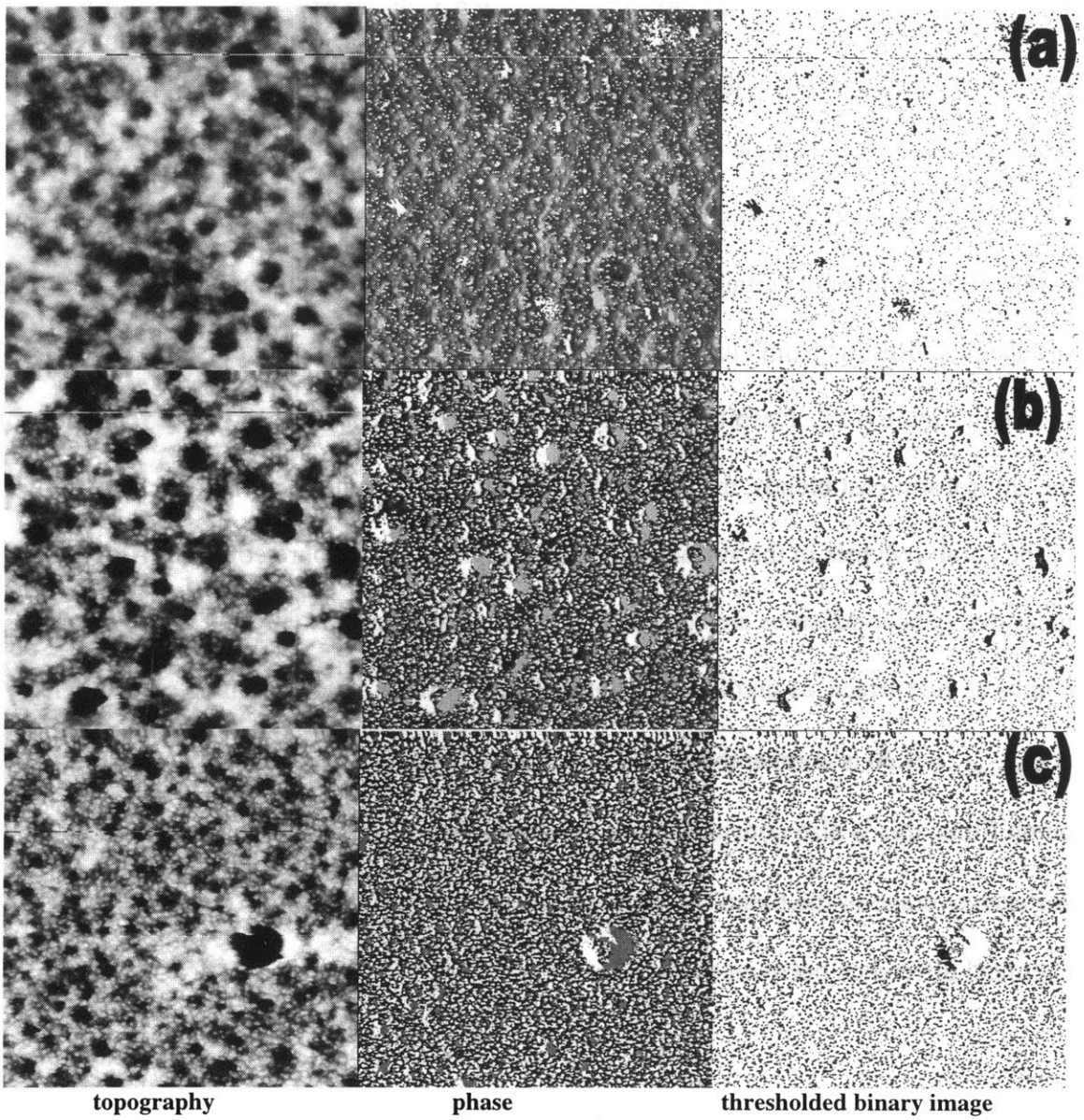

Figure 9.20. AFM images of nanosphere-labeled PLA:comb:RGD-comb blends. Shown are 5 μm x 5 μm AFM scans of water-annealed blends containing three different RGD-comb concentrations; the blend composition in each case was 80:20-x:x wt:wt:wt PLA:C2:C2-RGD4. Images left to right are AFM topography, AFM phase, and the processed phase image binarized to depict the nanospheres only. (a) 80:19:1 blend, (b) 80:15:5 blend, (c) 80:10:10 blend.

The extremely high contrast between the nanospheres and underlying blend surface in phase images was exploited to identify the effective cluster density at the surface of blends. Phase images were converted to binary (black/white) data and analyzed to obtain surface cluster densities and total ligand densities on blend surfaces. The analysis requires several assumptions as outlined in the discussion of ligand density determination on comb polymer films in section 8.3.1. Semi-2D confinement of the comb polymer backbone at the surface is assumed, as predicted by SCF, and nanospheres are assumed to label a single cluster at the surface. Due to the roughness of the spincast surfaces, we estimate the cluster densities determined here are likely only accurate to within 10%, as it is not certain that the AFM tip is able to probe to the bottom of all of the surface pits. Results from cluster-labeling analyses for two different cluster sizes are shown in Figure 9.21. Despite the uncertainty in label density caused by the roughness of the chloroform-cast blends, the cluster density data agrees with the predicted alignment of the comb polymer in the surface layer, similar to results on pure comb films. The measured cluster densities are consistent with a 2D, non-interpenetrating arrangement of combs at the surface, as predicted by the SCF calculations. The measured cluster density at $\phi^{b}_{\text{RGD-comb}} = 0.20$ is comparable to the maximum cluster density measured on pure RGD-comb films; this is also consistent with the results from XPS indicating near-complete surface coverage of the blend by comb polymer for $\phi^{b}_{\text{comb}} = 0.20$. The relatively small chemical difference between the RGD-

bearing combs (for the data shown, the peptides account for only ~4% by weight of the comb molecules) should mean that surface segregation of the RGD-bearing combs is

similar for all of the cluster sizes examined in these studies. This is supported by the data in Figure 9.21 for 5.4 RGD/comb and 2.2 RGD/comb surfaces, where the same cluster density was measured on these two different cluster sizes when equivalent bulk RGD-comb concentrations were blended. Assuming the comb and RGD-comb are driven to the surface to nearly equivalent coverage, the surface density of peptide clusters should be linear from 0 at $\phi^b_{RGD\text{-}comb} = 0$ to ~950 clusters/μm^2 at $\phi^b_{RGD\text{-}comb} \sim 0.20$. A linear dependence of cluster density on $\phi^b_{RGD\text{-}comb}$ appears to reasonably describe the cluster separation and total RGD density data.

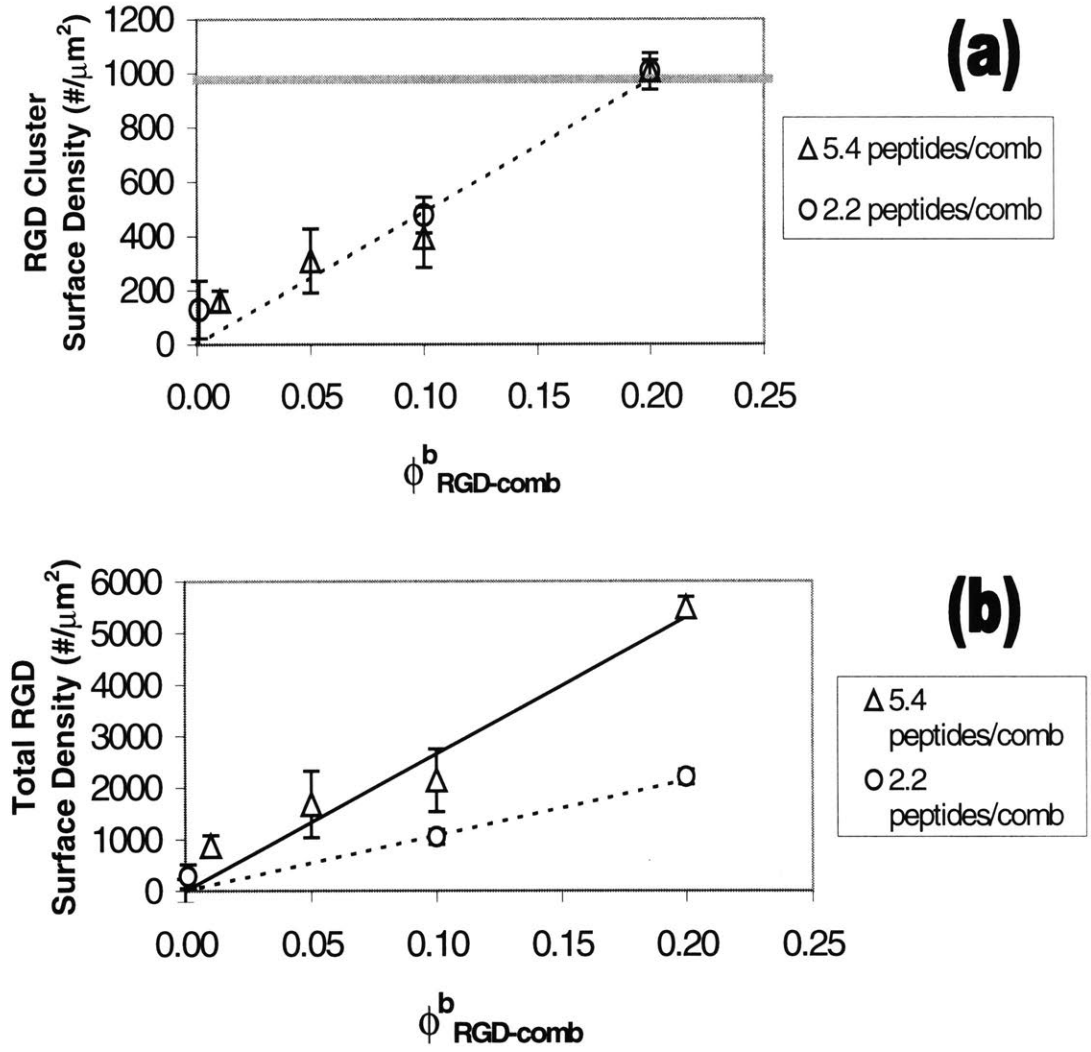

Figure 9.21. Peptide cluster density and total peptide density on blend surfaces. 80:20-x:x wt:wt:wt PLA:C2:C2-RGD blends were annealed 1 day in water and subsequently labeled with nanospheres. (a) Total cluster density for two cluster sizes, 5.44 peptides/comb (C2-RGD4) and 2.2 peptides/comb (C2-RGD2). Solid gray line is the maximum cluster density presented by pure RGD-comb films from section 8.3.1. Dashed line is a linear trend with maximum cluster density at $\phi^b_{RGD\text{-}comb} = 0.20$. (b) Total RGD density for two cluster sizes, 5.44 peptides/comb (C2-RGD4) and 2.2 peptides/comb (C2-RGD2) converted from total cluster surface density for each comb polymer. Lines show trends expected for rule of mixtures expression of C2-RGD2 or C2-RGD4 at the blend surface.

9.3 Cell Adhesion on PLA/P(MMA-r-POEM) Blends

9.3.1 Elimination of Nonspecific Cell Adhesion on PLA Blends

Nonspecific cell attachment to PLA is not as prominent as seen on some synthetic polymers, but is still significant[58]. Surface segregation of C1 in PLA was assessed for reducing nonspecific cell adhesion. WTNR6 fibroblasts were seeded on water-annealed PLA/C1 blends in media containing 7.5% serum and the number of cells attached after 24 hours was determined by a DNA quantification assay. Figure 9.22 shows the fraction of seeded cells adhered and the fraction of cells adhered relative to unmodified PLA as a function of the bulk concentration and as a function of the near-surface concentration of the comb polymer as determined by XPS. Consistent with the trend in surface enrichment of comb polymer with increasing bulk concentration, cell attachment is inversely correlated with the comb content of the blends.

Cell attachment on the modified PLA blends appears to require a minimum surface enrichment of comb polymer around $\phi^{s}_{comb} = 0.50$ in order to reduce cell attachment. The fraction of cells attaching to blends with $\phi^{b}_{comb} = 0.20$ is not as low as measured for pure comb polymer films, however, the absolute cell number on these surfaces is less than 5% of the total seeded. From this data it is evident that surface segregation reduces protein adsorption and nonspecific cell attachment on blends.

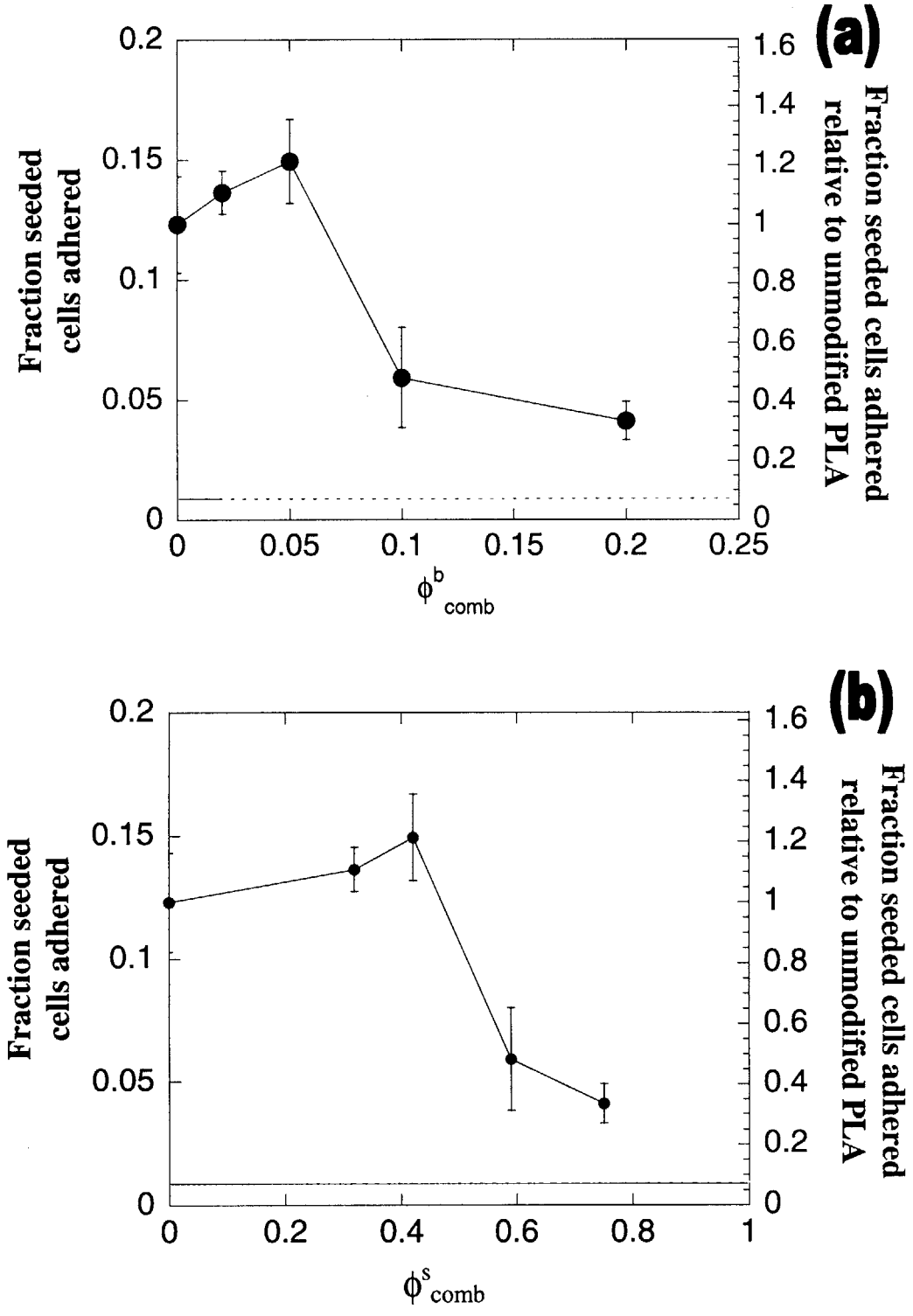

Figure 9.22. Adhesion of WTNR6 fibroblasts to PLA/C1 blends. WTNR6 fibroblasts were seeded at 30,000 cells/cm^2 in 7.5% serum-containing media. (a) Fraction of cells attached after 24 hours vs. comb polymer bulk volume fraction. Dashed line is the cell resistance exhibited by pure comb polymer films. (b) Attachment data re-plotted against the calculated surface volume fraction of comb polymer in the annealed PLA/comb blends. Dashed line is cell resistance of pure comb film.

9.3.2 RGD-Mediated Adhesion of Cells to PLA Blends

Surface segregation of RGD-modified combs allows tailored cell adhesion on PLA blends. The total volume fraction of comb polymer in blends for further tethered ligand studies was fixed at 0.20 to maximize resistance of the blends to nonspecific cell attachment; the relative ratio of comb to RGD-comb was varied but $\phi^b_{comb} + \phi^b_{RGD\text{-}comb} =$ 0.20 for each experiment. Figure 9.23 plots cell attachment vs. $\phi^b_{RGD\text{-}comb}$ for blend annealing times of 0, 1, or 4 days. As expected from the measurements of RGD surface density, after only 24 hours annealing in water, the surface density of RGD is sufficient to promote attachment and spreading of cells on the comb-modified blend. Further annealing does not increase the adhesivity of the surfaces.

Cell attachment as a function of RGD density was assessed on annealed PLA/ C2/C2-RGD4 blends. Figure 9.24 plots the fraction seeded cells attached vs. surface RGD density calculated from nanosphere-labeling measurements. Cell attachment saturates at a level comparable to that seen on highly adhesive TCPS controls for C2-RGD4 bulk concentrations of only 5 wt%, due to the strong surface segregation of the comb and the potency of tethered RGD peptides. RGD-expressing surfaces support much greater cell attachment than unmodified PLA. Figure 9.25 shows example phase contrast micrographs of cells attached to RGD-bearing blends with varying surface densities of ligand. Rounded cells (which appear in phase contrast micrographs as cells with bright borders) are prominent on PLA blends containing only 1 wt% C2-RGD4, but cell number and cell spreading both increase as the RGD content of the blend is increased. For only 5 wt% C2-RGD4 in the blend (~1,300 RGD/μm^2 at the surface) cells attach and strongly spread.

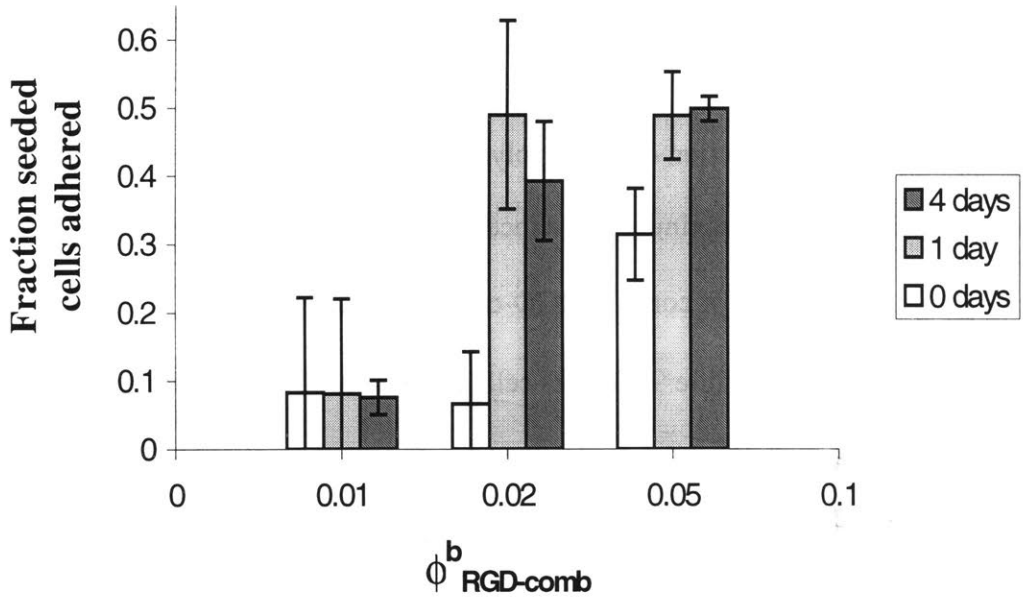

Figure 9.23. Cell adhesion on PLA/C1/C1-RGD1 blends. Fraction of seeded WTNR6 cells attached at 24 hours (30,000/cm^2 seeded) to blends unannealed or annealed 1 or 4 days. Legends show blend bulk weight fraction C1-RGD1. Total comb content (C1 + C1-RGD1) was 20 wt%.

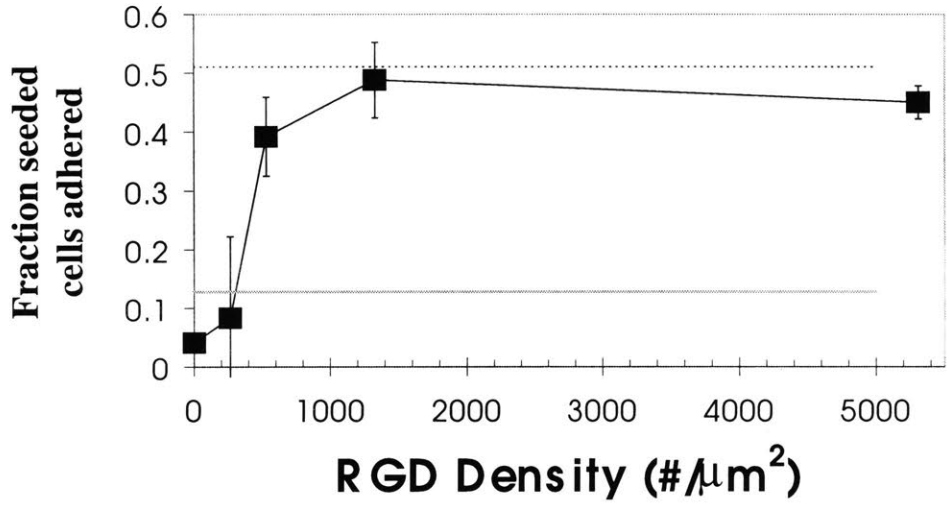

Figure 9.24. Cell adhesion on PLA/C2/C2-RGD4 blends with increasing RGD content. Comparison of WTNR6 fibroblast adhesion at 24 hours on blends with constant total content comb (20 wt%) but increasing fractions of C2-RGD4. The dotted line is the mean fraction seeded cells nonspecifically attached on TCPS control substrates in the same experiment. The solid gray line is the mean fraction seeded cells nonspecifically adhered to an unmodified PLA control.

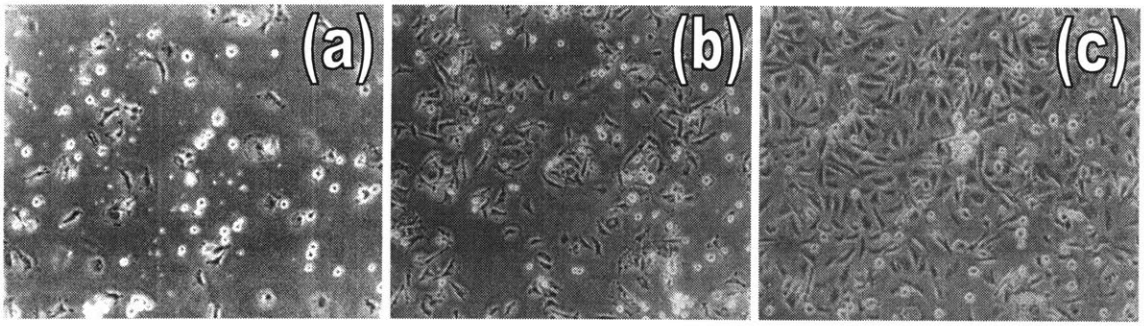

Figure 9.25. Phase contrast micrographs of cell morphology as a function of RGD density on PLA blends. (a) 80:19:1 wt:wt:wt PLA: C1:C1-RGD1. (b) 80:18:2 PLA: C1:C1-RGD1. (c) 80:15:5 PLA: C1:C1-RGD1.

Similar to results obtained for C2/C2-RGD4 blends, cell attachment on RGD-expressing PLA blends is mediated by specific RGD-integrin interactions. Addition of 85 μM soluble GRGDSP to the media of cells attached to RGD-comb-modified PLA promoted rapid rounding of the cells, and over 4 hours, > 90% cell detachment. Changing to fresh media after exposure to soluble RGD (before complete detachment), cells respread on the tethered ligand surfaces.

9.3.3 Degradation Kinetics of Comb/PLA Blends

A critical issue in the use of surface segregation for tissue engineering is the stability of the surface layer. Degradation of the system must be slow enough to allow cell behavior to be guided for an appropriate time period by the ligand-bearing surface. This is especially important since the comb is amphiphilic and will improve the ability of water to penetrate the bulk of the blend as it degrades. The time course of ligand loss from the surface of comb-segregated PLA blends was followed by monitoring the release of fluorescent nanosphere-labeled RGD peptides from thin films degraded over time under physiological conditions. Label loss from the surface of 80:20 wt:wt PLA:C2-RGD2 blends measured over time is shown in Figure 9.26. Ligand can be lost from the

degrading blend surface through either hydrolysis of the ester linkage between the RGD peptide and comb polymer, or via degradation-induced solubilization of surface-localized comb polymer. Ligand density at the surface of the blend is seen to decrease only very slowly under physiological conditions, retaining >90% of the labeled ligand after 3 weeks incubation in saline.

As a practical measure of short-term surface stability, we also assessed the ability of RGD-bearing PLA surfaces to support sustained cell attachment and growth of WTNR6 fibroblasts over 5 days in culture. The expansion of cells over this time period on surfaces presenting three different densities of RGD peptide is shown in Figure 9.27. At the end of this culture period, addition of 85 μm soluble GRGDSP to media of cells cultured on 10% C2-RGD3 blends promoted detachment of > 90% of the attached cells, again pointing to peptide-mediated adhesion even after several days in culture. Successful expansion of cells on these surfaces thus indicates stability of the tethered ligand surface over this time course.

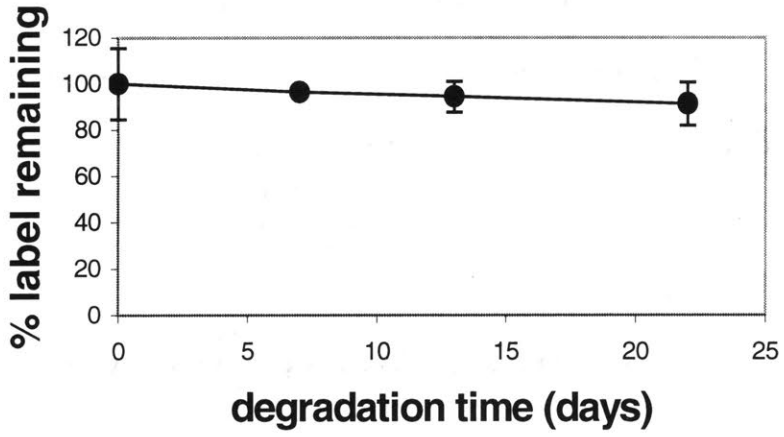

Figure 9.26. Labeled ligand loss from the surface of PLA/C2-RGD2 blends over time under physiological conditions.

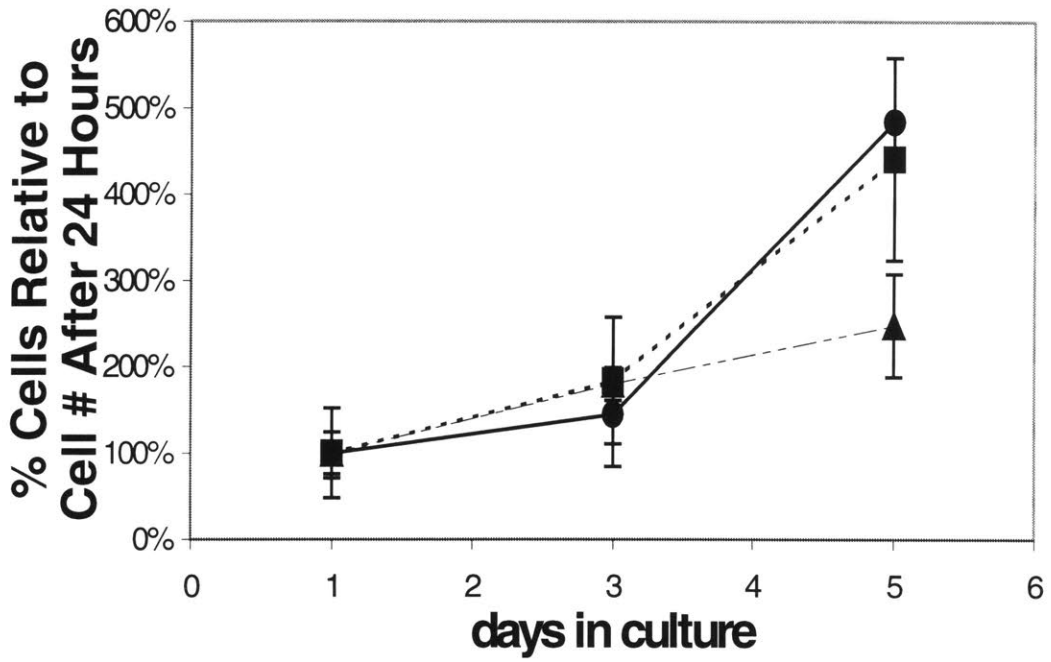

Figure 9.27. RGD-bearing PLA blends support cell attachment and growth over several days in culture. WTNR6 fibroblasts were seeded on PLA/ C2/C2-RGD3 containing (●) 615 RGD/μm^2, (■) 880 RGD/μm^2 or (•) 1,760 RGD/μm^2. Cell number was measured after 24, 72, and 120 hours in culture.

9.4 Summary

The results of these studies suggest surface segregation of the comb polymer as an additive in PLA (a material with suitable biodegradation and mechanical properties) as a suitable approach to create cell-signaling surfaces on a biodegradable device.

This approach is attractive for several reasons. As already discussed at length in Chapter 8, the comb polymer is inexpensive and easily prepared. Precious peptides are used sparingly since small amounts of ligand-bearing comb are strongly enriched at the surface by segregation. Only 5-10 wt% of RGD-bearing comb polymer in the blend provides confluent cell adhesion. Labeling of ligand at the surface of blends indicated that comb polymer is semi-confined at the blend-water interface, similar to the situation suggested by data for comb polymer films in water. Thus ligand clustering at the blend

surface is achieved effectively, since the combs in the top layer extend a maximal fraction of ligand into solution, rather than burying the peptide in the surface layer.

The blend is surface modified by thermodynamic self-assembly and thus preparation of cell-signaling surfaces on PLA devices may in some cases be achievable with *no additional processing steps*. Use of surface segregation to provide *in situ* surface modification during device fabrication has been demonstrated in a comparable comb polymer/semicrystalline matrix blend by Hester and Mayes[231], where surface segregation was achieved during casting of P(MMA-r-POEM)/poly(vinylidene fluoride) blend membranes by phase inversion in water. Similar processing approaches have been used for the preparation of PLA foams for cell scaffolds[90, 105]. Surface segregation might also be readily achieved by simply incorporating a water annealing step as part of other phase separation[57] or particulate-leaching[91, 92] scaffold fabrication methods. Because surface segregation is essentially a self-organizing process, all exterior surfaces of complex three-dimensional scaffolds can be modified. This is in contrast to line-of-sight coating methods for which modification of interior pores of scaffolds would be problematic.

Segregation of the comb polymer did not appear to provide cell resistance completely equivalent to that of pure comb polymer films, consistent with XPS results showing high but incomplete coverage of the blend surface by comb polymer. This could be an issue in some situations where a small fraction of nonspecific cell adhesion is unacceptable, for example in tissue engineering of vasculature[43, 48, 102], where selective adhesion of only endothelial cells on the interior graft surface is desired. However, further manipulation of the segregation process, for example, through a kinetic phase inversion process[231], might reveal conditions for preparation of blends with even higher comb surface coverage.

To facilitate analysis, thin film blends were studied here, and three-dimensional devices were not directly prepared. A potential limitation of this surface modification technique will be the effect of the comb polymer on the three-dimensional structure obtained by different fabrication routes. For example, incorporation of large comb fractions may affect the morphology of water-fabricated scaffolds[57, 231]. This might be addressed by manipulation of fabrication conditions, or through use of alternative processing schemes. For instance, scaffold fabrication by 3DP™ printing[54] or particulate leaching[90, 91, 104, 105] approaches may be relatively unaffected by the incorporation of the comb polymer.

10 Quantitative Cell Adhesion Studies on Clustered Ligand Surfaces

In this chapter, studies of the influence of adhesion ligand spatial distribution on cell adhesion using the comb polymer surfaces developed in Chapters 8 and 9 are presented. The adhesion of WTNR6 fibroblasts on comb surfaces presenting RGD peptides in clusters of ~1.5 – 5.5 RGD/cluster and total ligand densities of 200-5,500 RGD/μm^2 was measured by a centrifugation assay. These studies were performed in collaboration with MIT Graduate Research Assistant Lily Y. Koo, who conducted all of the adhesion measurements on surfaces prepared by D. Irvine. The ability of cells to respond to applied forces was found to depend on both cluster size and total ligand density. *Strengthening* of cell attachment with increasing applied force was observed for a range of detachment forces determined by cluster size and total RGD density on the surface. To compare with results obtained for tethered RGD peptides, adhesion strength measurements of cells on adsorbed fibronectin were also made. A strengthening of cell adhesion in response to increasing applied force was also observed on fibronectin. The chapter closes with a discussion of these results in the context of current theories of integrin signaling and cell attachment. A model developed in collaboration with Lily Koo is presented which can

qualitatively account for the observed behavior and which suggests ways to further probe this force-induced strengthening response.

10.1 Cell Adhesion Strengths on Clustered RGD

Clustered RGD surfaces were prepared using comb polymer thin films as described in section 6.4.1. As discussed in Chapter 8, alignment of the comb backbone at the water/polymer interface appears to organize the top layer of comb molecules as quasi-two dimensional, non-interpenetrating disks of diameter ~32 nm. Thus each ligand cluster is confined to an area of ~800 nm^2.

In order to analyze adhesion strength after seeded cells have had sufficient time to organize and remodel their cytoskeleton in response to the surface (a process which may continue for many hours[173]), measurements were taken 20 hours post seeding on surfaces. The normalized fraction cells remaining adhered (FA) measured as a function of applied detachment force (F_{app}) for surfaces presenting total RGD densities of 200 – 5,000 RGD/μm^2 is shown in Figure 10.1. For the lowest cluster size, 1.7 RGD/comb, the fraction adhered cells shows a monotonic decline with increasing F_{app}. However, for cluster sizes > 2 RGD/comb, the fraction of cells remaining attached is *non-monotonic with increasing detachment force*. Cell attachment over the measured range peaks at an applied force between 200 and 600g and a strengthening of adhesion occurs as the applied force is increased from low g up to this point. Peak position was relatively insensitive to ligand cluster density, however, the force at which peak adhesion is observed appears to depend on ligand cluster size: the position of the peak moves from ~600g to between 200 and 400g as cluster size is increased at constant total ligand density.

For the surfaces with 3.6 or 5.4 RGD/comb, very low fractions of cells remained attached at the lowest applied centrifugal forces (100 or 200 g). The clustered RGD surfaces thus appear

to show an initial rapid drop in attached cells at low forces as outlined schematically in Figure 10.2. Consistent with this picture, an initial drop in fraction cells adhered was observed for 2.2 RGD/comb surfaces at 540 and 1,100 RGD/μm^2, where the peak in adhesion occurred at a significantly higher force. In the schematic we introduce the notation F_{crit} for the critical applied force at which force-induced strengthening begins to occur and F_{max} for the applied force at peak adhesion. The fraction cells adhered at these points is FA_{crit} and FA_{max}, respectively.

Figure 10.3(a) plots FA_{max} for 3 cluster sizes. On the most adhesive surface (5.4 RGD/comb at 5,200 RGD/μm^2) peak adhesion was ~25% of the seeded cell number. For 1.7 RGD/comb, no peak was evident; therefore the low g force plateau FA value was plotted. At constant cluster size the peak fraction of adhered cells only begins to rise as the total RGD density rises above ~1,000 RGD/μm^2. The size of the peak ($FA_{max} - FA_{crit}$) also slowly increases with increasing total ligand density, as seen in Figure 10.3(b). Comparing the relative effect of increasing ligand density vs. increasing cluster size, cluster size appears to have a much stronger effect on the magnitude of adhesion strengthening observed.

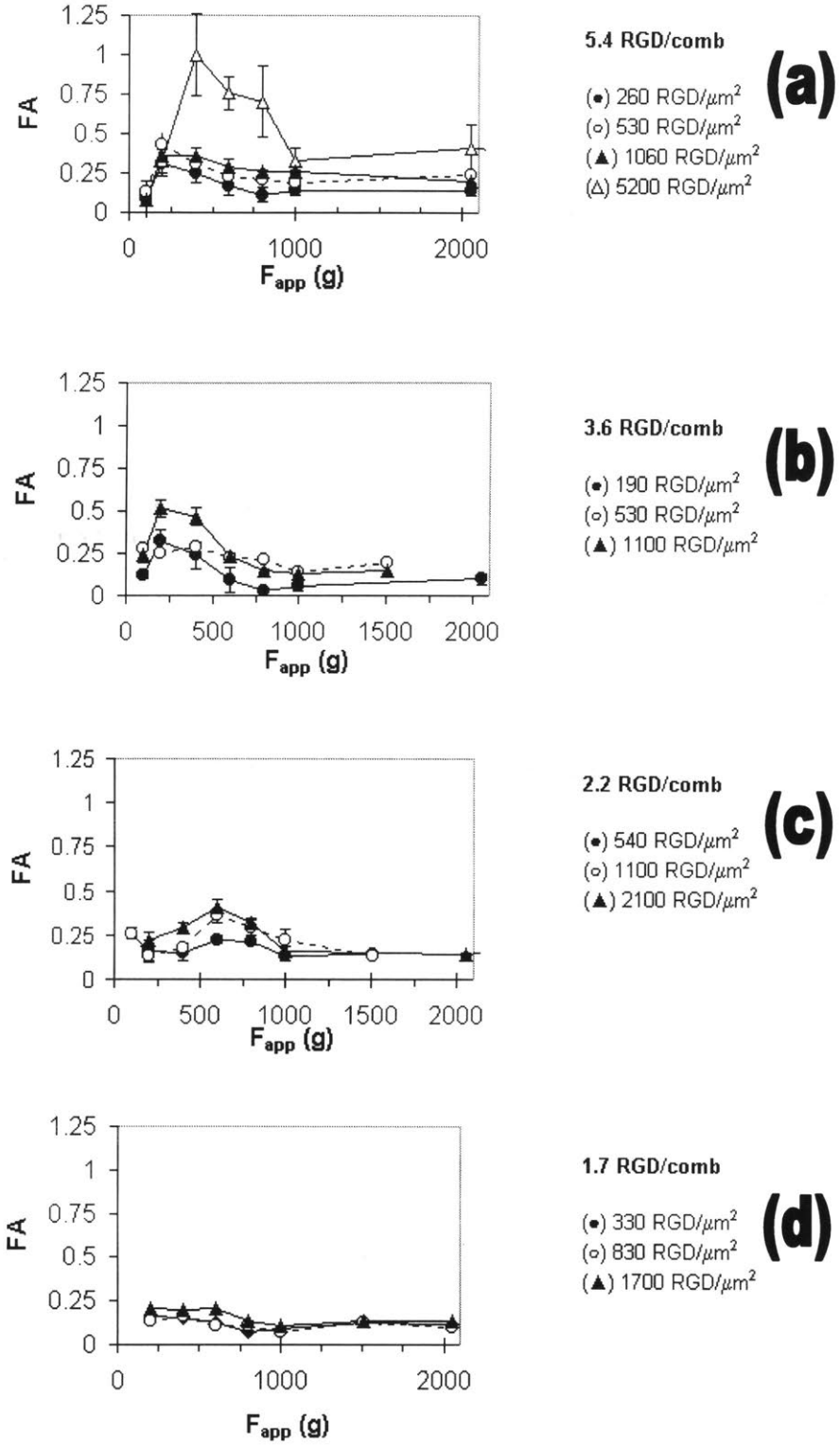

Figure 10.1.Normalized fraction of cells remaining adhered on clustered ligand surfaces as a function of the applied centrifugal detachment force. Shown are results for a range of total ligand densities on 4 different cluster sizes: (a) 5.4 RGD/comb, (b) 3.6 RGD/comb, (c) 2.2 RGD/comb, (d) 1.7 RGD/comb.

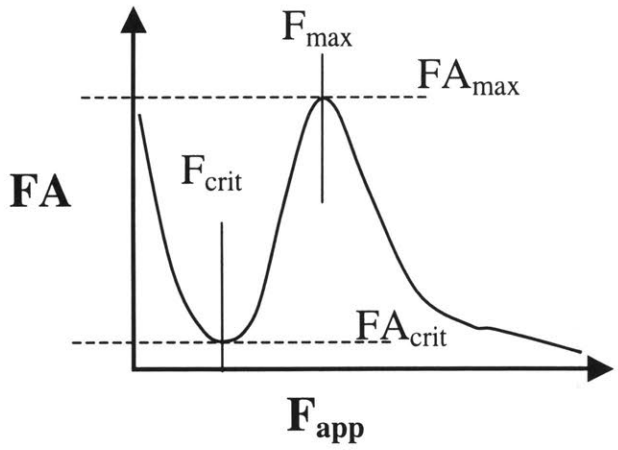

Figure 10.2. Proposed continuous force response curves for cell attachment on clustered RGD surfaces. Two points on the curve have been labeled: the critical applied force at which strengthening begins to occur (F_{crit}), and the applied force at maximum adhesion (F_{max}). The normalized fractions of adherent cells at these points are FA_{crit} and FA_{max}, respectively.

Clustering 3.6 RGD/comb at the lowest RGD density examined (~250 RGD/μm^2) increases FA_{max} by a factor of 3 over that on 1.7 RGD/comb surfaces, compared to only a 2-fold increase in FA_{max} obtained by increasing the total ligand density by an order of magnitude at constant cluster size.

In Figure 10.4, the entire force response curves of comparable total RGD densities at different cluster sizes are directly compared. Attachment strength of cells increases over the entire range of applied forces when ligand is clustered on the substrate. 5.4 RGD/comb surfaces provide better adhesion strength than 1.7 RGD/comb even when the total ligand density on 1.7 RGD/comb surfaces is nearly twice that on the larger cluster size. The increase in adhesion strength provided by clustering is most pronounced at $F_{app} = F_{max}$.

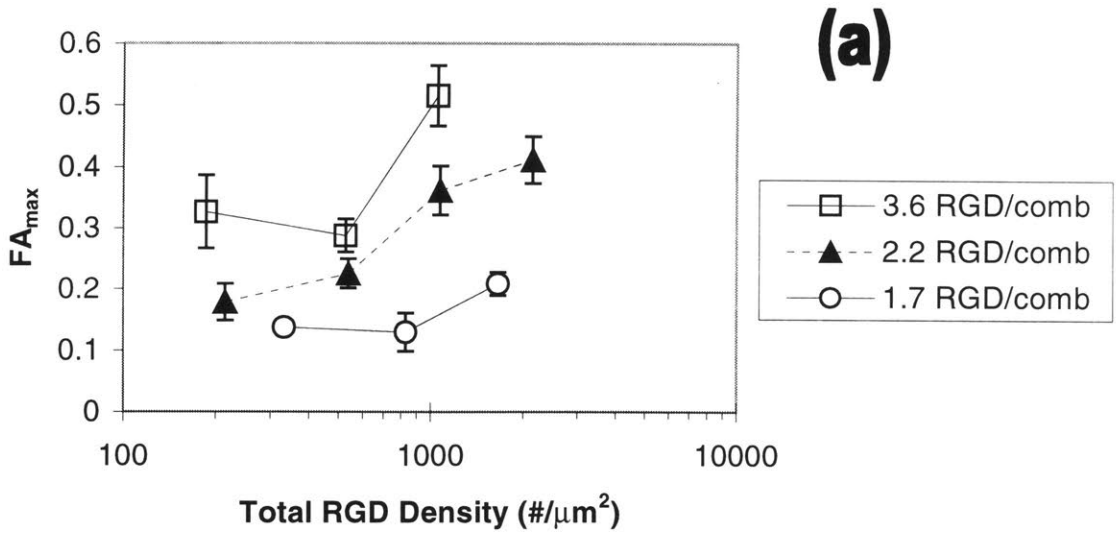

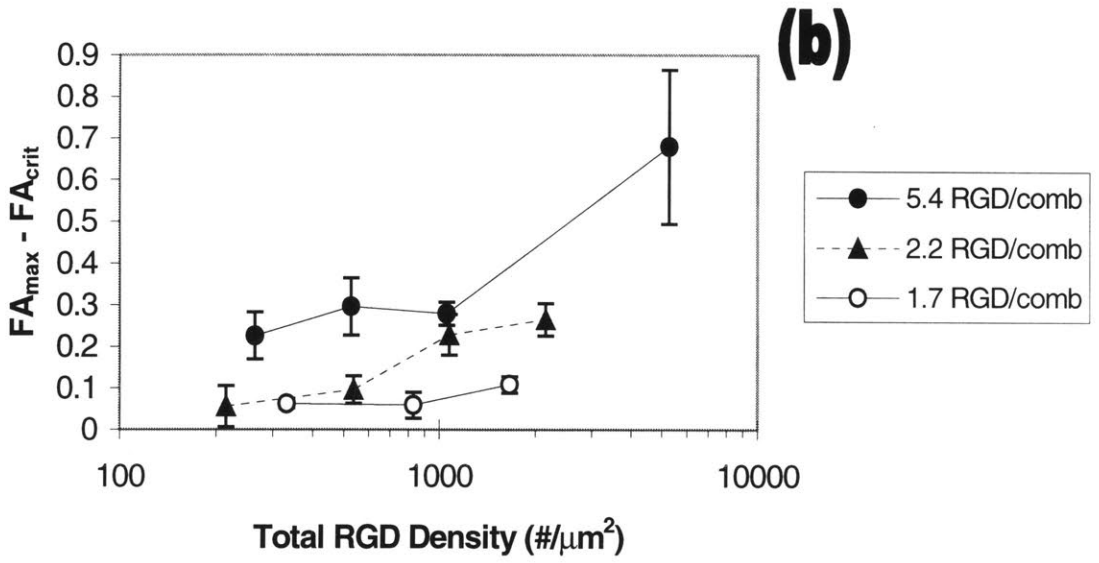

Figure 10.3. Clustering effects on cell responses to an applied force. Shown are (a) the peak fraction of cells adhering on clustered ligand surfaces and (b) the fraction adherent peak height for cells detached over a range of forces by centrifugation. Different cluster sizes are compared over a range of total ligand densities.

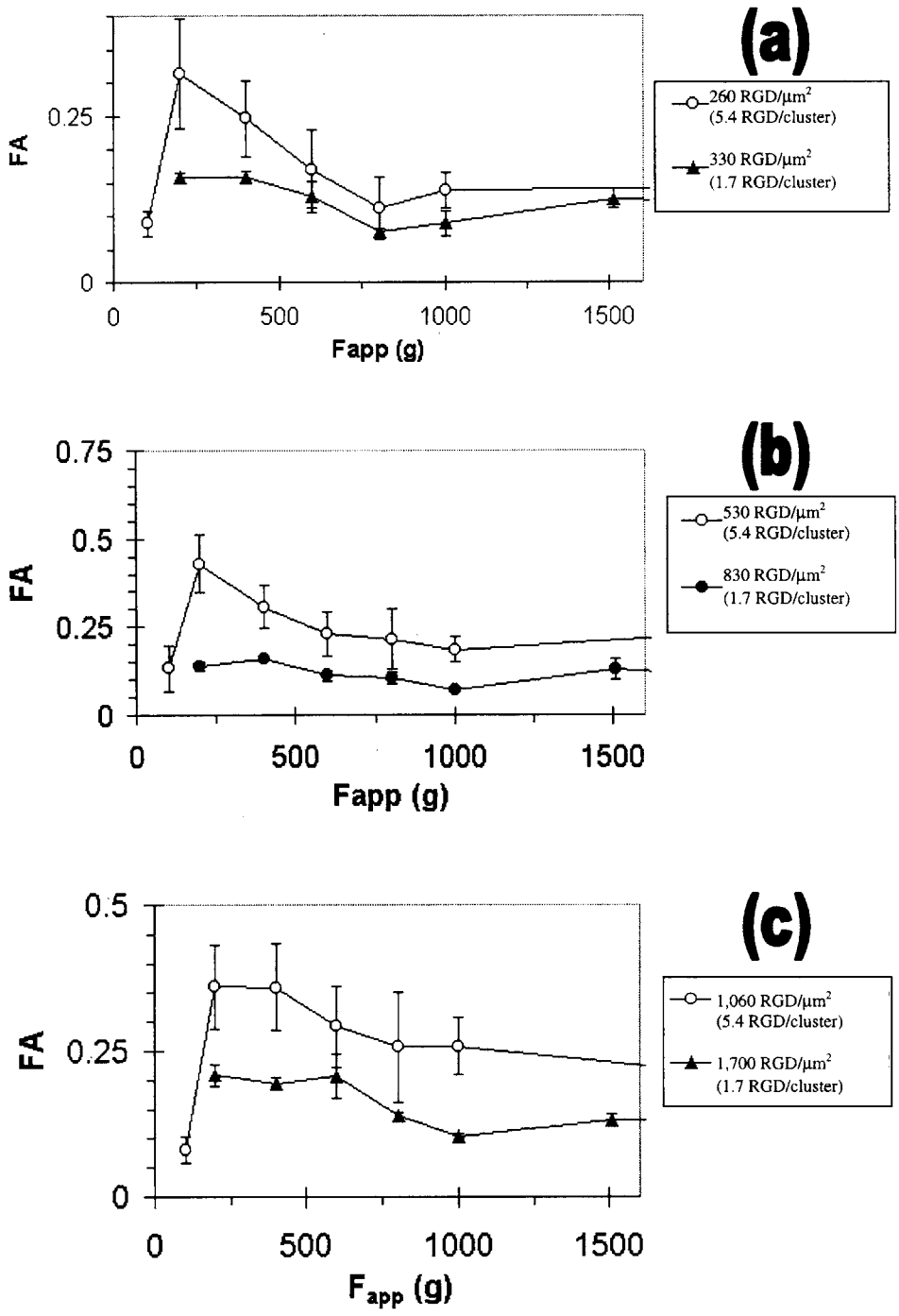

Figure 10.4. Comparison of force response curves for comparable total ligand densities presented in different cluster sizes.

10.2 Cell Adhesion Strengths on Adsorbed Fibronectin

In light of the dramatic influence spatial distribution of RGD peptides had on cell responses to applied forces, we wondered how these results might relate to the physiological response of cells to forces transmitted by integrin-ECM contacts. To compare with the results obtained on the synthetic tethered ligand surfaces, adhesion strength measurements were thus also carried out on surfaces prepared by adsorbing the ECM adhesion protein fibronectin (FN) to tissue culture polystyrene from 0.1 μg/mL, 1.0 μg/mL, or 3.0 μg/mL FN solutions. Results from these adhesion strength measurements are plotted in Figure 10.5. Qualitatively, adsorbed FN surfaces exhibit peaks in the fraction of adhered cells, similar to the observation on clustered RGD surfaces. However, cells attach more strongly at all forces for all three surface densities of FN relative to the RGD peptide surfaces; this is consistent with the 100-1,000-fold greater affinity of integrin receptors for the full adhesion protein. In agreement with the proposed qualitative shape of the continuous force responses on clustered RGD (Figure 10.2), an upturn in FA is observed for $F_{app} < F_{crit}$ on adsorbed FN. The peak in cell adhesion becomes more prominent and appears to move to higher applied force as the surface density of FN increases.

The qualitative similarity in cell force responses on FN and clustered RGD is striking, considering the large difference in binding affinity, the lack of any explicit spatial distribution control for adsorbed FN, and the fact that FN interacts with cells via multiple receptors[25]. However, adsorbed FN may generate cell responses similar to clustered RGD by at least two mechanisms. As discussed in the theoretical predictions of Chapter 7, multiple binding sites presented by each FN molecule may act as nanoscale ligand clusters analogous to comb-tethered RGD. In addition, stochastic adsorption of a few adjacent FN molecules may also give rise to effective clustering. Simulations of clustered ligand binding in Chapter 7 predicted that random adsorption could begin to elicit clustering effects at ligand densities on the order of 100

ligands/μm^2. Here the FN surface densities are within this range: approximately 50, 270, and 720 for FN adsorbed from 0.1, 1.0, or 3.0 μg/mL solutions, respectively[172].

10.3 Effect of Substrate Compliance on Adhesion Strengths

Previous studies have demonstrated a dependence of stiffness of the integrin-cytoskeletal linkages on substrate compliance[27, 28]. Thus differences in cell adhesion on adsorbed fibronectin vs. tethered RGD may be influenced by the greater rigidity of the polystyrene substrate relative to the comb polymer surfaces, which absorb ~15 wt% water at equilibrium. The prominence of the observed strengthening behavior might also depend on the compliance of the substrate. To examine how rigidity effects might influence the observed strengthening behavior on clustered RGD surfaces, cell adhesion strength was measured on surface-segregated 80:20 wt:wt PLA:C2-RGD4 (5.4 RGD/comb) blends, where the crystallinity of the matrix should impart stiffness to the tethered-RGD substrate.

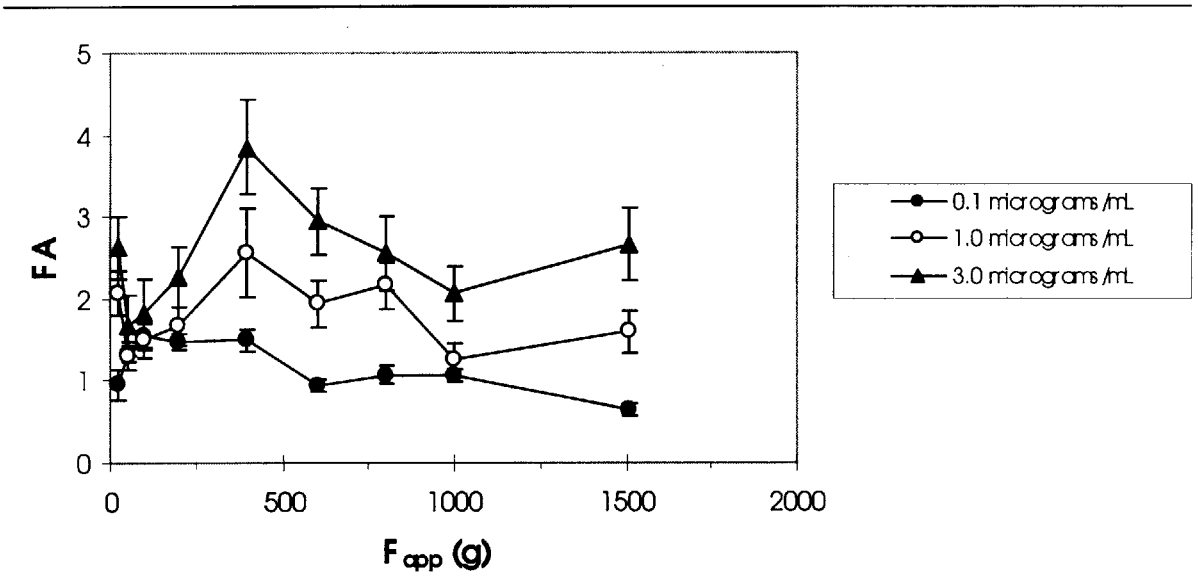

Figure 10.5. Cell adhesion strengths on adsorbed fibronectin.

Because these samples required different preparation conditions, a quantitative comparison of the fraction of adhered cells was not possible. However, Figure 10.6 compares the shape and position of the FA curve for the PLA blend tethered RGD substrate (normalized to the maximum adhesion on PLA blend surfaces) with comb polymer films expressing the equivalent total RGD density on separate axes. The peak in cell adhesion occurs at a significantly lower applied force for the rigid polymer substrate, and appears narrower. A model integrating these trends with the observed dependence of cell force responses on cluster size is presented in the following section.

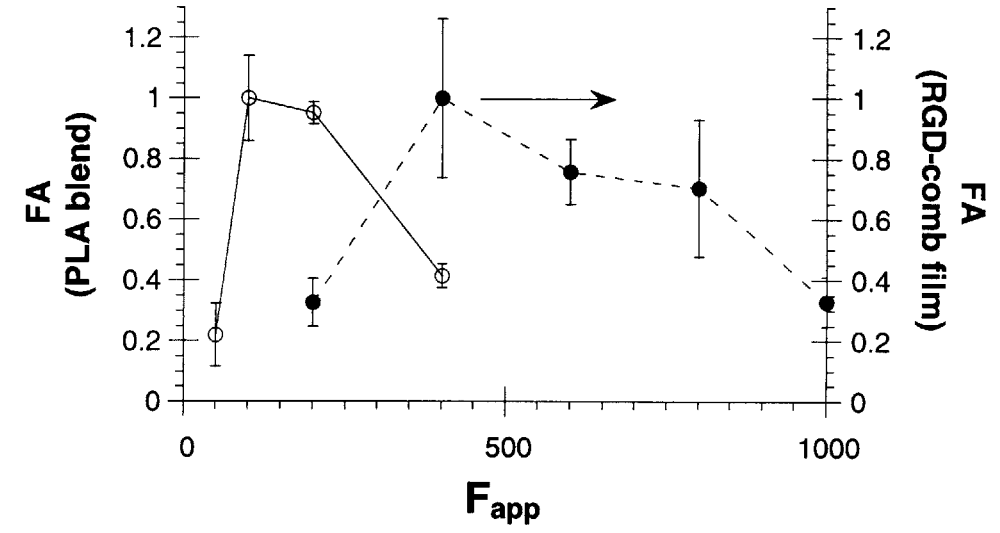

Figure 10.6. Cell adhesion strengths on a rigid RGD-presenting PLA blend vs. a water-absorbing RGD-comb polymer film. Surface density of RGD on both surfaces is ~5,200 RGD/μm^2.

10.4 Discussion

10.4.1 A Model for Force-Induced Adhesion Strengthening on Clustered Ligand Substrates

Using artificial substrates that present surface-tethered RGD peptide ligands for integrins in nanometer-scale clusters, we have demonstrated the adhesion strength of fibroblasts is sensitive both to the total ligand density and its spatial distribution in a manner dependent on the magnitude of the applied detachment force. Adhesion strength of cells on surfaces presenting clustered ligands shows a non-monotonic force dependence. This phenomenon has not been previously observed in published shear flow detachment assays[13, 232, 233]. However, assuming that integrin signaling in the cytoplasm is the source of the observed responses, signaling from multiple integrin clusters may be required rather than from only the small fraction of cell-substrate contacts at the peeling front. Clear evidence for a strengthening process has also not been published in other detachment experiments where the force is applied normal to the substrate[26, 45, 171]; however, no previous study has thoroughly examined as large a range of detachment forces as studied here. Although the apparent strength of receptor-ligand bonds is known to be dependent on loading rate[9], here we have clearly observed that spatial distribution of ligand at *constant* total ligand density affects the observed strengthening response. No cluster size effect would be expected if differences in cell adhesion at different applied forces were due simply to differences in loading rate during acceleration in the centrifuge.

To understand the detachment data, current understanding of integrin signaling, integrin-cytoskeletal linkages, and cytoskeletal mechanics must be considered together. Attachment of a cell to its substrate is supported via mechanical linkage of the cytoskeleton to immobilized

extracellular ligand via integrins. Studies of integrin-cytoskeletal linkages have demonstrated that these connections between the superstructure of the cell and the ECM are strengthened on a timescale of several seconds when a force is applied through the cell-ECM connection[27]. In particular, Choquet et al.[27] found the strength of integrin-cytoskeletal connections increased linearly with an applied force restraining beads bound by integrins on the cell surface. This strengthening in response to a locally-applied force appeared to have biochemical (i.e. signaling) origins.

Strengthening of integrin-cytoskeletal linkages via force-driven signaling may explain the observed strengthening behavior on the clustered RGD and adsorbed FN surfaces studied here. A simple model that can describe the observed force responses of cells attached via clustered ligands is depicted in Figure 10.7. We assume the mean force required to detach cells ($<F_{detach}>$) is proportional to an integrin-based signal (S). In the absence of this signal, $<F_{detach}>$ is a constant independent of the applied force. If the magnitude of S is a nonlinear function of the force transmitted to the cell, then $<F_{detach}>$ would in turn depend nonlinearly on the applied force. A hypothetical $<F_{detach}>$ vs. F_{app} curve assuming a sigmoidal dependence of S on F_{app} is drawn in Figure 10.7(a). If the population of cells attached to a surface is assumed to have a normal distribution of individual adhesion strengths distributed about $<F_{detach}>$ as depicted in Figure 10.7(b). Then the number of cells remaining attached at any given F_{app} will depend on the difference between F_{app} and $<F_{detach}>$. The number of cells attached (NA) will be:

$$\mathbf{NA} = \mathbf{NA_0}\left(\mathbf{1} - \int_0^{F_{app}} f(< F_{detach} >, F'_{app})\, dF'_{app}\right) \qquad \textbf{(Eqn 10.1)}$$

where NA_0 is the number of cells attached under 0 applied force and f is the fraction of the attached cell population (with mean attachment strength $<F_{detach}>$) removed by a given applied force F_{app}. This model gives rise to cell attachment curves as a function of the applied force as

shown in Figure 10.7(c). The qualitative trend observed for cell attachment vs. F_{app} is reproduced by this model: NA initially decreases with increasing F_{app}, until a critical applied force is reached, where force-driven signaling is turned on and begins to increase $<F_{detach}>$. Strengthening continues until the force signal *S* begins to saturate, at which point further increases in F_{app} begin to detach the maximally-strengthened cells.

The primary assumption of this model for force responses is the existence of an integrin-based signal that is influenced by ligand spatial distribution; in this model *clustering is required for signaling, and signaling is required for adhesion strengthening*. Clustering would act to shift integrin-based signaling (*S*) to lower applied forces and potentially increase the plateau level of signaling generated by the applied force, as shown in Figure 10.7(d). As cluster size increases, FA_{max} and FA_{crit} increase, while F_{max} and F_{crit} decrease, in agreement with the observed trends in adhesion strength. Evidence for force-dependent signaling by $\alpha_5\beta_1$ integrins has been found in experiments examining the response of integrin-cytoskeleton linkages to forces applied through ECM contacts[27, 28, 234]. Choquet et al. found that integrin-cytoskeleton linkages strengthened proportionally to a restraining force applied via ECM-coated microbeads restrained by a laser trap[27]. When they inhibited tyrosine phosphatases (which are important biochemical signal regulators) in cells using phenylarsine oxide (PAO) the force-induced strengthening of $\alpha_5\beta_1$ integrin linkages was disrupted. This appears to implicate a biochemical component to the strengthening response observed in their experiments. An integrin-derived biochemical signal has similarly been implicated in the response of cells to substrate rigidity[28]. Cells cultured on flexible substrates form dynamic, irregularly shaped focal adhesions relative to cells on rigid substrates. Addition of PAO to cells on flexible substrates restored the formation of stable focal adhesions.

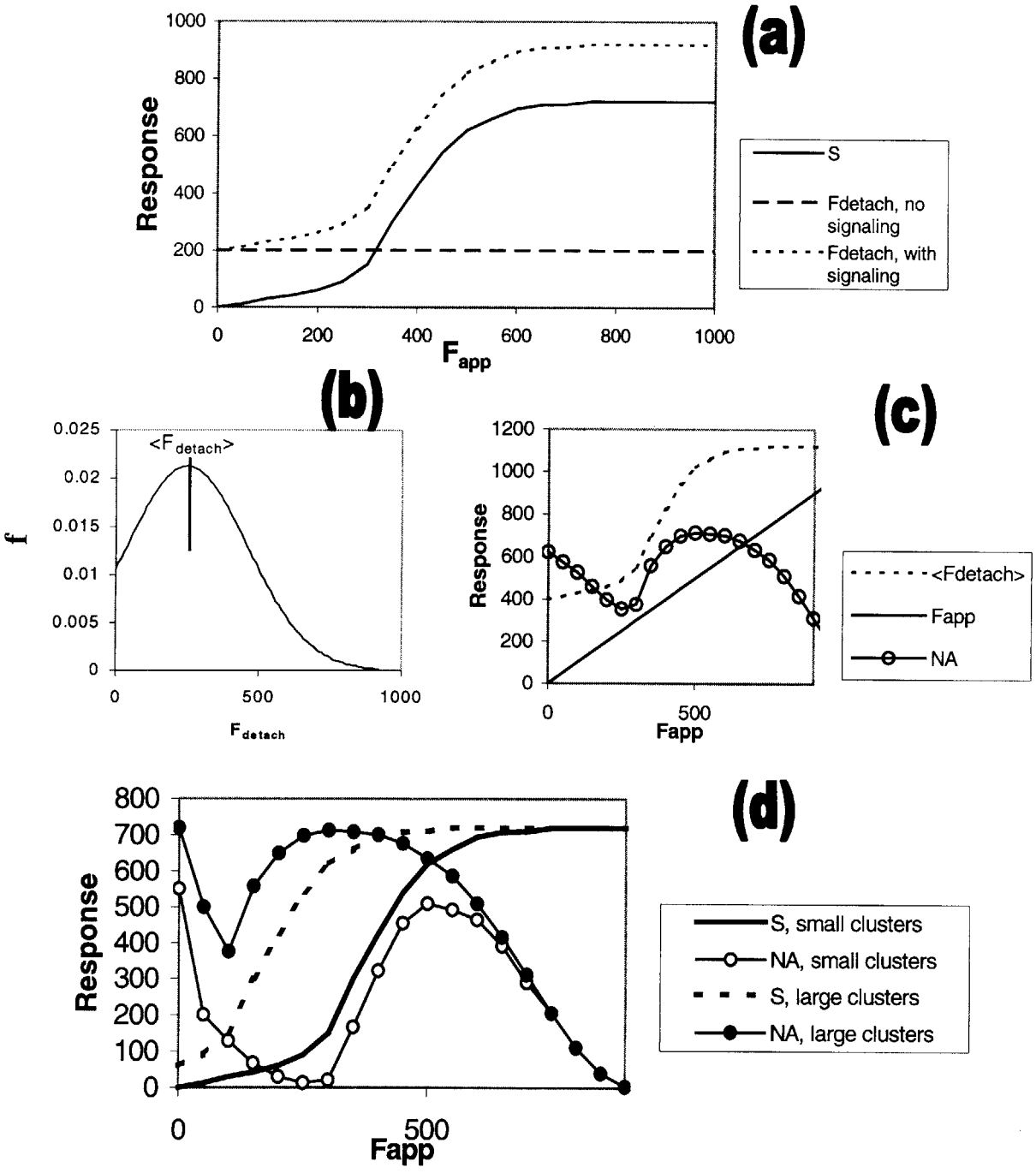

Figure 10.7. Hypothesis for force-induced adhesion strengthening on clustered ligand surfaces. (a) Required force to detach cells as a function of applied force in the absence or presence of integerin-based signaling. (b) Population distribution of forces required to detach cells from the substrate; *f* is the fraction of the cell population with a given F_{detach}. (c) Cell attachment profile expected for the proposed signaling model. (d) Efect of ligand clustering on cell adhesion responses.

The adhesion strengthening response observed in this study may in fact correspond to the strengthening response observed by Choquet et al.. In the laser trap experiments, beads were coated with 1,000 – 5,000 ligands per bead. Strengthening of integrin linkages was observed for restraining forces between 5 and 60 pN. Assuming half of the ligand presented by the beads was engaged by integrins, the applied forces range from 0.002 to 0.120 pN per receptor-ligand bond. In the present experiments, the force applied per cell is related to the applied centrifugal force by[26]:

$$\mathbf{F = F_{app}(V)(\rho_c - \rho_m)} \qquad \textbf{(Eqn. 10.1)}$$

where F_{app} is the applied centrifugal force (in units of *g*), *V* is the volume of the cell (approximately 800 μm^3, based on the observed diameter of WTNR6 cells in suspension), ρ_c is the density of the cell ($\rho_c \sim 1.03$ g/cm^3)[15], and ρ_m is the density of the culture media ($\rho_m \sim 1.0$ g/cm^3). Assuming 10^5 integrins/cell and full integrin engagement on the clustered RGD substrates (which should be reasonable at the higher ligand densities that are much larger than the integrin receptor density), the experimental forces applied here ranged from 0.047 pN per receptor-ligand bond at 200 *g* to 0.188 pN per receptor-ligand bond at 800 *g*. Thus the applied forces used in the current experiments appear comparable to the applied forces in the study of Choquet et al, and a signaling-based explanation of the strengthening response observed here appears consistent with their findings.

Alternatively, adhesion strengthening could be driven through the purely mechanical response of the cytoskeleton without biochemical signaling. Wang et al. showed that the stiffness of the cytoskeleton increases proportionately with stress applied through ECM-coated microbeads[14, 235]. This stiffening could be accounted for by a tensegrity model of the cell, where the entire cytoskeleton of the cell responses by global rearrangement of cellular mechanical

elements in response to applied forces. However, other experiments using locally-applied forces have shown no evidence of global cytoskeletal responses[27, 234]. Further, the inhibition of strengthening in these and other related experiments by PAO implicates biochemical signaling as a component of the response[27, 28].

The proposed relationship between integrin-derived signaling and ligand clustering is consistent with the two-state receptor binding model proposed in Chapter 7. Asthagiri et al.[172] found that integrin activation of two intracellular signaling pathways was proportional to integrin-ligand bond number on adsorbed fibronectin at early timepoints. Thus an increase in bond number caused by increased ligand clustering could raise the level of integrin signaling stimulated by the applied force at early times. Increases in total bond number can be explained by the two-state binding model for integrin-ligand interactions, providing the link between integrin signaling and cluster size. Physically, this model for the strengthening response consists of 3 stages: 1) integrins are bound in aggregates by clustered ligand and receptor-crosslinking within aggregates drives cluster size-dependent binding; 2) an integrin-based biochemical signal is generated which depends on bond number, the extent of clustering, and the force transmitted to the cell; and 3) cell-substrate connections are strengthened in response to integrin signaling.

Substrate rigidity in this model would affect the cell response by introducing a pre-stress on the cytoskeleton. More rigid substrates would support a greater pre-stress, and thus the applied force required to "switch on" integrin signaling would be lowered: the entire *S* curve would be shifted to lower forces. Substrate rigidity has been shown to play this role in determining the stiffness of the cytoskeleton in previous experiments[14].

10.4.2 Potential Roles for Force-Responsive Adhesion and Integrin Signaling

What role could force-induced strengthening of cell adhesion play *in vivo*? The ability of the cell to respond differentially to matrix rigidity or applied forces has consequences for many aspects of cell function in development, wound healing, and pathology. For example, the ability of a cell to generate traction through integrin-ECM contacts is a requirement for cell migration[24, 26, 236]. Previous studies have pointed to the utility of a cell's ability to respond to the rigidity of its substrate in order to regulate cell migration[27, 28]. Strengthening of cell-ECM linkages through ligand clustering may be a mechanism to generate traction at the leading edge of cells[236]. Further, fibroblasts cells both generate and respond to applied forces during contraction in wound healing. Mechanical stresses are also known to have a profound influence on developing tissue structure[237-239]. The observed adhesion behavior may thus serve as a "mechanotaxis" mechanism for guiding tissue architecture during wound healing and development[27].

The control of ligand spatial distribution at the surface of cell-signaling biomaterials holds promise for influencing the function of cells in contact with biomaterials in a manner mimicking the *in vivo* roles for force-dependent adhesion proposed above. Control of cell adhesion strength is of obvious importance for tissue engineering, especially for devices implanted with cells exposed to applied loads (e.g. cartilage or bone). Inappropriate cell attachment to scaffold devices remains a problem with many tissue engineering approaches; clustering adhesion ligands has been demonstrated here as a powerful means to increase the strength of cell adhesion. The experiments on nanoscale clustered RGD by Maheshwari et al. have already demonstrated dramatic effects of ligand clustering on cell migration[45]. Cell migration speed is directly correlated with adhesion strength[24, 45]; thus ligand clustering should also be a facile route to

manipulate cell migration speeds on biomaterial surfaces. Because integrins are implicated in regulation of many cell functions, including cell growth and differentiation, control of ligand clustering may be of further importance in many other aspects of cell behavior at surfaces. It remains to be seen how ligand spatial distribution influences cell proliferation and differentiation, but these important cell functions may be directly regulated by clustering as well.

11 Conclusions and Future Work

11.1 A Clinically-Applicable Paradigm for Tethered Ligand Signaling

We have demonstrated the use of P(MMA-r-POEM) comb polymers to provide protein resistance and tethered ligand presentation on biomaterials. The paradigm itself has been suggested by many researchers as a means to truly predetermine cell functions on surfaces[40-43, 45-47, 51], however, the current work represents the first example of such an approach produced in a practical system that allows control of ligand spatial distribution through clustering. These materials have been prepared in an economically and synthetically practical manner amenable to synthesis and processing on an industrial scale. Furthermore, we have demonstrated how biophysical control over ligand presentation at a surface (made possible by the use of a branched polymer architecture) can be used to tailor cell function (in the current work, cell adhesion). The present work represents the first use of molecular architecture to tailor ligand spatial distribution in an clinically-relevant system. Nanoscale adhesion ligand clustering using this system has been theoretically predicted to have strong effects on integrin binding; we have also experimentally demonstrated significant effects on cell adhesion strength and the response of cell to applied forces on clustered ligand surfaces.

Preparation of comb polymer surfaces, either as comb polymer thin films, comb-stabilized latex films, embedded latexes, or surface segregated blends provides extensive flexibility in the use of this system for surface modifying biomaterials. In each of these approaches, the top surface layer controls the properties of the polymer-water interface, and thus subsequent cell-materials interactions. The proposed approach is applicable to a variety of device fabrication schemes and materials, from permanent implant fixtures to resorbable cell scaffold devices.

We chose to develop our tethered ligand system using comb polymers due to their ease of synthesis and readily manipulated physical properties. However, the key physicochemical properties of such polymers should serve as a general guideline for the preparation of new cell-signaling materials. The required characteristics are that the polymer is amphiphilic and that is has a branched molecular architecture that allows the two segment types to be readily polarized spatially (i.e. locally segregated into hydrophilic and hydrophobic units). Comb polymers represent only one example of materials that can be designed with these structural characteristics; star polymers, dendrimers, and multiblock copolymers may also be useful surface modification agents. Further studies of this class of materials and the interactions of cells with their surfaces may lead to the first clinical materials able to truly direct cell function at the tissue-biomaterial interface.

11.2 Issues for future work

11.2.1 Mechanisms for clustered ligand effects

The Monte Carlo simulations of Chapter 7 showed that increases in effective receptor-ligand binding affinity through nearest-neighbor interactions give rise to dramatic binding increases

when ligand is immobilized at a surface in clusters. However, these simple models do not probe how such affinity changes might occur. An important unresolved question is at what biophysical level might clustering affinity changes occur? Experimental evidence exists for changes in effective receptor affinity induced directly by ligand binding[179, 180], or due to changes induced by proteins recruited to the site of ligation inside the membrane[68]. Understanding where and how these effective affinity changes are controlled may shed light on which parameters are key for controlling receptor binding and clustering, as well as how clustering may affect the synergistic interactions between multiple signaling pathways (e.g. adhesion ligand and growth factor signaling).

11.2.2 Force-Induced Adhesion Strengthening Studies

Several question remain unanswered from the studies carried out here of cell adhesion strengths on clustered RGD or adsorbed fibronectin. First is whether the observed strengthening response is definitively equivalent to the strengthening observed in laser trap microbead studies[27]. Experiments demonstrating a change in the force response curves in the centrifugation assay in the presence of the biochemical inhibitor PAO used by Choquet et al. in those studies would support this hypothesis. Also of interest is what molecules within the cytosol control the integrin-based signaling affected by ligand clustering. One potential regulator is the protein calpain, a focal contact-localized protease that cleaves integrin-cytoskeletal linkages[240-242]. Calpain can be selectively inhibited by calpain inhibitor I[180]; experiments probing cell adhesion strengths in the presence of this inhibitor might reveal this protease's role in integrin signaling on clustered ligands. Such experiments will be key in further illuminating this putative combined biophysical/biochemical integrin signaling pathway and its importance in controlling cell function.

11.2.3 Fully Degradable Comb Polymer Systems

The comb polymers used in the current surface segregation studies are composed of water-soluble PEO side chains anchored to a hydrophobic, non-degradable methacrylate backbone. Degradation of PLA/comb polymer blends may leave residual comb polymer at the site of an implant, whose influence on the inflammatory response to the device is unknown. Fully resorbable comb polymers, comprised of a hydrolytically- or enzymatically-degradable backbone might be desirable to improve the biocompatibility of PLA blend devices for tissue engineering. Synthesis of poly(lactide)-backbone PEO-side chain comb polymer was attempted for this work, but to date no reliable synthetic approach has been developed. Synthesis of PLA-backbone copolymers with short grafted PEO side chains has been recently been reported by a route we also examined, however, this approach leaves no means for functionalization of the chain ends of the resulting copolymers. As an alternative to using PLA as the backbone component, other hydrophobic degradable monomer units compatible with PLA might be useful; synthetic approaches using degradable lactone and lactide-family monomers are of continued research interest.

11.2.4 Comb Polymer Systems for Biophysical Separation of Multiple ECM Signals

One exciting aspect of the comb polymer systems developed in this work not examined in the current thesis is the ability of comb polymer surfaces or latex surfaces to present multiple ECM ligands in a spatially-segregated manner. For example, as depicted in Figure 11.1, latexes bearing two different ECM ligands might be embedded in protein-resistant comb polymer films. The resulting surface would present segregated signaling domains comprised of one or the other

ECM ligand. Such surfaces could be used to probe the effects of spatial distribution on the synergistic signaling between, for example, integrins and growth factor receptors. Growth factor receptors are known to co-localize at focal adhesions with integrin receptors[33, 38]; the comb polymer systems would provide a convenient means to control whether co-localization can occur and examine the response of cells in the presence or absence of signal biophysical segregation.

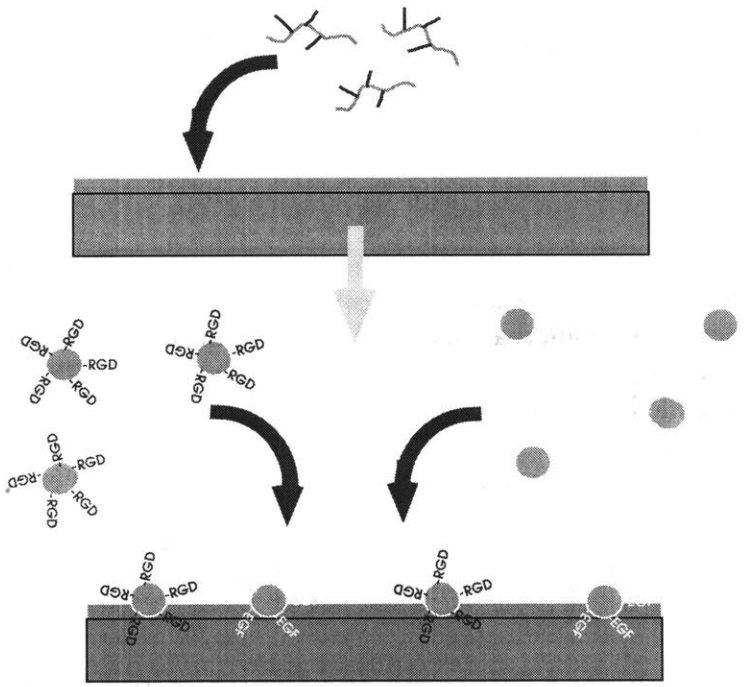

Figure 11.1. Spatial segregation of multiple ECM signals using embedded latexes.

12 Appendix A: Experimental Protocols

12.1 P(MMA-r-POEM) Comb Polymer Synthesis

Reagents

(amounts represent a typical synthesis)
21 mL methyl methacrylate (MMA) = 19.7 g = 0.197 mol)
5.95 mL poly(oxyethylene glycol) methacrylate (POEM) (= 6.55 g = 0.0187 mol, M ~ 360 g/mol)
6.06 mL methoxy poly(oxyethylene glycol) methacrylate (MPOEM) (= 6.55 g = 0.0139 mol, M ~ 475 g/mol)
0.239 g azo(bis)isobutyronitrile (AIBN) (0.00146 mol)
500 mL tetrahydrofuran (THF)
2000 mL 8:1 vol:vol petroleum ether:methanol
20-50 mg 1-methoxyphenol

Apparatus

1000 mL reaction flask (round-bottom)
large oil bath at 70° C
large stirbar
stirring hotplate
retort stand
rubber septa
nitrogen tank
nitrogen hose with needle
vent needle
cold water condenser
disposable plastic syringes (2)

Prior to Synthesis

1. Dry reactor, stir bar, syringes, needles, cannicula, and reflux column in oven overnight.

Procedure

1. Remove glassware from oven.
2. Fill reactor with THF.
3. Inject MMA, POEM, and MPOEM into reactor while stirring at room temperature.
4. Dissolve AIBN in 1-5 mL of THF and add to reactor.
5. Seal reactor, attach condensor. Vent condensor with low-gauge needle.
6. Bubble reaction solution with N_2 for 20 minutes.
7. Immerse reactor with condensor in oil bath at 70° C.

8. Continue reaction for 18h at 70° C with stirring.
9. Terminate reaction by the addition of 1-methoxyphenol.
10. Concentrate solution by rotoevaporation, and precipitate into 2000 mL pet ether/methanol.
11. Redissolve in THF and reprecipitate in pet ether/methanol 1-2 times until product is monomer-free.
12. Collect polymer and vacuum dry.

Theory

Figure 12.1 through Figure 12.3 depict the free radical initiation and polymerization of methyl methacrylate and the poly(ethylene glycol)-based monomethacrylate monomers, as well as potential side reactions with the azo(isobutyl nitrile) initiator. The poly(ethylene glycol) methacrylate macromonomers are susceptible to transfer of radicals to the side chain leading to crosslinked gels under conditions which favor chain transfer under certain conditions[243, 244]. Thus reactions at high monomer concentration and high initiator concentration will lead to crosslinked products. Exact conditions to avoid crosslinking vary with the lengths of the PEG monomer side chains and the concentration of monomers and initiator used. The relative reactivity of POEM monomers and MMA varies with the PEO chain length[245], however, we found in practice that compositions of copolymers generally matched the monomer feed ratio for side chain lengths n = 5,6, or 9 ethylene oxide units.

Methoxyphenol terminates the free radical synthesis by scavenging radicals, which its benzene ring stabilizes[246].

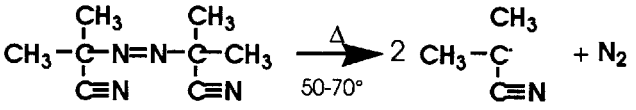

Figure 12.1. AIBN Decomposition.

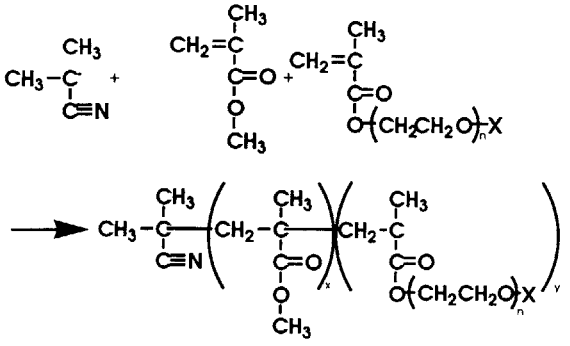

Figure 12.2: Random copolymer synthesis. X is a methyl or hydroxyl group, depending on whether the monomer is MPOEM or POEM.

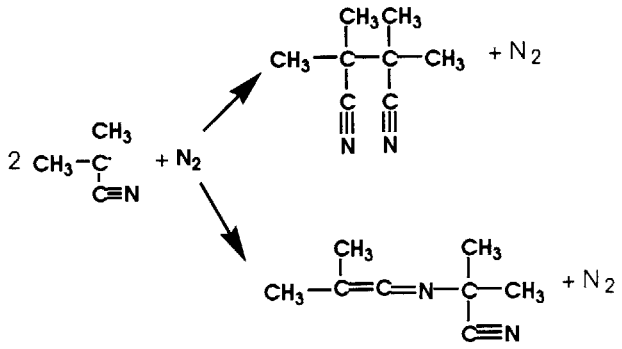

Figure 12.3: AIBN side reactions

12.2 Comb Polymer Carboxylation

Reagents

8 g P(MMA-r-POEM) = 4.0×10^{-3} mol -OH = 1X -OH groups
4 g succinic anhydride (10X)
0.048 mL N-methylimidazole
200 mL anhydrous dichloroethane

Apparatus

500 mL round-bottom flask with septum and magnetic stir bar
reflux condensor
heating bath or mantle

Procedure

1. Mark 200 mL fill line on RB. Dry stir bar and RB flask in oven over night.
2. Remove RB from oven, quickly add stir bar, polymer, and succinic anhydride while flask is still hot. Cap with rubber septum and purge nitrogen or argon until flask is cool.
3. Cannulate 200 mL of anhydrous dichloroethane into reactor.
4. With stirring, polymer will dissolve, but succinic anhydride remains suspended. Add N-methylimidizole dropwise to stirring reactor; solution will become clear.
5. Uncap RB and quickly attach to condensor. Immerse in heating bath and reflux over night at 65-70° C.

Theory

Reaction of an anhydride with an alcohol is a basic chemistry reaction. The procedure used is based on an example from the literature[153].

12.3 NHS-Activation of Carboxylated Comb Polymer

Apparatus and reagents are listed for a typical synthesis, using carboxylated comb polymer prepared as in the protocol of section 12.2.

Reagents

4.75g carboxylated P(MMA-r-POEM) = 0.76 g POEM = 0.00211 mol –COOH = 1X
0.486g N-hydroxy succinimide (NHS) = 0.00422 mol = 2X
0.871g dicyclohexylcarbodiimide (DCC) = 0.00422 mol = 2X
50mL dichloroethane
50-100mL ethyl acetate
1600-2000mL anhydrous ether

Apparatus

200mL round bottom flask with magnetic stir bar and rubber septum
stir plate
Funnel and filter paper
crystallization dish for precipitating polymer

Procedure

1. Dry stir bar and RB flask in oven over night.
2. Remove RB from oven, quickly add stir bar while flask is still hot. Cap with rubber septum and purge with nitrogen or argon until flask is cool.
3. Remove septum, quickly add NHS, comb polymer, and 45mL dichloroethane. Recap, and stir while bubbling nitrogen 15 minutes.
4. Dissolve DCC in 5mL dichloroethane and add via syringe dropwise to stirring comb polymer solution.
5. Stir 24 hours at room temperature. Within 10 minutes, precipitation of dicyclohexylurea side product begins.
6. Add 50mL ethyl acetate to bring polymer concentration to ~0.05 g/mL. Filter into 800-1000mL stirring anhydrous ether (filter removes most of precipitated side product).
7. Decant ether and dry precipitated product 1 hour *in vacuo* at room temperature.
8. Redissolve at 0.05 g/mL in ethyl acetate, and precipitate again in 800-1000mL anyhydrous ether.
9. Dry *in vacuo*, then aliquot 100mg of polymer into vials. Seal vials with parafilm and store at

-20°C.

Approximate Yield: 50 wt%

Theory

Carbodiimides react with carboxyl groups to form amine-reactive intermediates. However, these intermediates are unstable in water and hydrolyze on a timescale of seconds, making the yields in coupling reactions of a carbodiimide-activated polymer and peptide very low. Alternatively, good yields of peptide coupling can be obtained by activating carboxyl groups with carbodiimide in the presence of the peptide, which will be immediately linked to the activated carboxyl. However, this approach makes cross-linking of the peptide possible since the carbodiimide present will activate *both* the polymer carboxyl groups and the carboxyl groups of the peptide. To overcome this problem, N-hydroxy succinimide groups can be used to activate the polymer carboxyls instead of carbodiimide. NHS is significantly more stable to hydrolysis in water, having a half-life ~40 minutes. Here we use carbodiimide to activate the carboxy groups in the presence of NHS, followed by immediate linkage of NHS to the carboxy group. The NHS polymer can then be reacted with peptide in the presence of water with relatively high yields.

12.4 Solution-Phase Coupling of GRGDSP and GRGDSPK to NHS-Activated Comb Polymer

Apparatus and reagents are listed for a typical synthesis, using NHS-activated comb polymer prepared as in the protocol of section 12.3. Degree of peptide functionalization of NHS-activated polymers was controlled by increasing or decreasing the concentration of RGD added during this reaction- the particular protocol shown was used for the preparation of C2-RGD3.

Reagents

2.5 mg GRGDSPK
2 mL PBS, pH 7.4
100 mg NHS-activated P(MMA-r-POEM)
2 mL anhydrous dimethylformamide (DMF)
3 mL 50/50 vol/vol water/ethanol solution
[0.5 N KOH in methanol]

Apparatus

2 vials (5mL size) with magnetic stir bars
stir plate
3,500 g/mol-cutoff dialysis cassette (Pierce Chemical Co. Slide-a-lyzer)

Procedure

1. Dissolve GRGDSPK in PBS.
2. Dissolve comb polymer in DMF.
3. Chill solutions at 4°C 30 minutes while dissolving.
4. Add comb polymer solution to RGD solution dropwise by Pasteur pipette while stirring RGD solution. Polymer will show some precipitation at first few drops added. As addition continues, an emulsion is formed (solution turns milky- reaction takes place rapidly, with RGD-modified comb emulsifying the mixture).
5. Allow reaction to continue with stirring at 4°C for 24 hours.
6. Pour milky solution onto a watch glass and evaporate solution under low/no heat.
7. Redissolve in 3mL water/ethanol. If polymer will not dissolve, add 0.5N KOH in methanol (20 μL at a time) until RGD-comb dissolves (KOH makes a salt of the carboxy groups and makes the polymer more soluble).

8. Load RGD-comb solution into 3,500 MWCO dialysis cassette and dialyze 48 hours against pure water/ethanol to remove unreacted RGD and hydrolyzed NHS.
9. Unload solution from cassette and evaporate solvent to recover RGD-comb polymer product.

Theory

NHS-activated carboxyl groups react with the N-terminal amines of the peptide to form an amide covalent bond. NHS has a half-life in water at pH 7.4 of ~40 minutes, which is further increased in this reaction by using a water/organic solvent mixture. Note that the amines of the lysine side chain in GRGDSPK peptides are much less reactive than the N-terminus and do not lead to appreciable product (Pierce Chemical Co.).

12.5 Tresyl Chloride-Activation of Comb Polymer

Reagents

150 mg P(MMA-r-POEM)
25 ml distilled or anhydrous toluene
200 µl distilled triethylamine
250 mg 2,2,2-trifluoroethanesulfonyl chloride (tresyl chloride)
50 ml dry, septum-sealed, nitrogen-purged round bottom flask with magnetic stir bar
magnetic stir plate
0.2 µm large-capacity syringe filter
500-700 ml petroleum ether

Procedure

1. Mark 25 ml fill line on round bottom flask. Dry copolymer in round bottom flask with stir bar overnight under low heat (50-70° C) in vacuo.
2. Cap round bottom flask and purge with nitrogen until cool.
3. Chill distilled TEA and tresyl chloride at 5° C.
4. Add toluene to flask by cannula, and stir to dissolve copolymer. Cool to 5° C.
5. Add TEA at 5° C, allow 10 minutes to equilibrate.
6. Add tresyl chloride, stir at 5° C 3 hours. On addition of tresyl chloride, HCl vapor will be seen over the solution inside the flask and the solution will become immediately cloudy on formation of TEA salts.
7. Centrifuge reaction mixture 15 minutes at 3400 rpm to remove bulk of salts.
8. Load solution into syringe and filter mixture into vigorously stirring petroleum ether to remove salts and separate polymer from unreacted TEA/tresyl chloride.
9. Decant petroleum ether and dry recovered copolymer *in vacuo*.
10. Store tresylated copolymer *in vacuo* at room temperature until use to prevent loss of activity due to hydrolysis.

12.6 Solution-Phase Coupling of GRGDSP to Tresyl-Activated Comb Polymer

Reagents

100 mg tresylated P(MMA-r-POEM)
5 mL anhydrous tetrahydrofuran
0.5 mL GRGDSP (1 mg/mL in PBS)
3 mL 50/50 vol/vol water/ethanol
2000 mL 50/50 vol/vol water/ethanol bath

Apparatus

Stir/hot plate
10 mL vial with cap and magnetic stir bar
3.5K MWCO dialysis cassette (Pierce Chemical Co., Slide-A-Lyzer™)

Procedure

1. Dissolve tresylated comb polymer in THF at 4°C with stirring. Chill GRGDSP solution at 4°C.
2. Add GRGDSP solution dropwise to stirring comb polymer solution at 4°C.
3. Continue stirring at 4°C 3 hours.
4. Evaporate solvent in fume hood under low heat (30-40°C).
5. Redissolve functionalized comb polymer in water/ethanol. Inject into dialysis cassette and dialyze against pure water/ethanol 2-3 days.
6. Recover product by removing solution from dialysis cassette and evaporating solvent under low heat (30-40°C) in fume hood.

Theory

Tresyl chloride-acitvated hydroxyl groups react with amines to provide covalent amide linkages[155]. The yield of reactions carried out in aqueous solution is limited by the competition between coupling and hydrolysis of the labile tresylate group. By reacting in a THF/water mixture, the hydrolysis reaction should be significantly depressed.

12.7 Comb Polymer-Stabilized Latex Synthesis

Reagents (Protocol for synthesis of PMMA latex)

1.3 g P(MMA-r-POEM) comb polymer
50 mL 50/50 vol/vol water/ethyl alcohol
0.57 g ammonium persulfate
5.3 mL methyl methacrylate

Apparatus

100 mL conical flask with magnetic stir bar and rubber septum
stirring/hot plate

Procedure

1. Dissolve comb polymer in water/alcohol media.
2. Add methyl methacrylate and ammonium persulfate.
3. Degas by bubbling nitrogen with stirring for 20 minutes.
4. Initiate polymerization by immersing flask with stirring in oil bath thermostated at 60°C. Dispersion will become milky typically within 30 minutes.
5. Allow polymerization to proceed 16-20 hours, then remove from oil bath.
6. Purify unreacted stabilizer and monomer by centrifuging the suspension, decanting supernatant, and resuspending in water/ethanol via sonication. Repeat 5-6 times to fully remove unreacted reagents.

Theory

Dispersion polymerization is used for the preparation of microspheres of a variety of polymers in both aqueous and organic media[77, 87-89, 247]. This method of polymerization is distinguished from emulsion polymerization as it begins as a homogeneous single phase and becomes two phase only after polymerization has begun[83].

12.8 Anthracenemethyl methacrylate monomer synthesis

Reagents

2 g (0.0096 mol) 9-anthracenemethanol (M = 208.3 g/mol, Aldrich)
1.03 mL (0.011 mol, 1.1X excess) methacryloyl chloride (M = 104.5 g/mol, ρ = 1.070 g/mL, Aldrich)
1.53 mL (0.011 mol, 1.1X excess) distilled triethylamine (M = 101.2 g/mol, ρ = 0.726 g/mL, Aldrich)
50 mL distilled tetrahydrofuran (Aldrich)
methylene chloride
2% aqueous sodium hydroxide
deionized water
anhydrous sodium sulfate

Apparatus

Ice bath chilled with sodium chloride
100 mL round-bottom flask with magnetic stir bar and rubber septum
stir plate
2 2-mL glass syringes with needles
filter paper
funnel
conical flask for washes

Prior to Synthesis

1. Dry flasks, stir bars, syringes, and needles in oven.
2. Distill THF.
3. Distill triethylamine.
4. Equilibrate ice bath at 0° C.

Synthesis

1. Add anthracenemethanol to hot RB containing stir bar, seal, and purge with dry nitrogen until cool.

2. Cannulate dry THF to RB, cool on ice bath.
3. Add triethylamine.
4. Add methacryloyl chloride slowly with stirring, react 2 hours at 0° C.
5. Allow to continue overnight at room temperature.
6. Filter mixture.
7. Evaporate solvent, redissolve in methylene chloride.
8. Wash with 2% aqueous NaOH.
9. Wash with several fractions of DI water until pH of aqueous phase remains neutral.
10. Dry organic fraction over sodium sulfate.
11. Decant solution through filter, concentrate by rotoevaporator.
12. Store product at 4° C.

Theory

This procedure is a modification of the Schotten Bauman scheme for preparation of acrylic derivatives under mild conditions which will not polymerize the vinyl group.

12.9 CyQUANT cell number assay

Reagents (sufficient for 18 12-well plate samples)

CyQUANT cell proliferation assay kit (Molecular Probes, C-7026):
- 0.925 mL Cell lysis buffer (20X)
- 92 µL GR dye (400X in DMSO)[1] (200X)

17.5 mL Deionized water

Apparatus

50 mL PP centrifuge tube wrapped in aluminum foil
96-well fluorescence plate

Prior to Assay

5. Aliquot media+cells plated during experiment into 3 Eppendorf tubes to prepare cell standards. Centrifuge tubes 5 minutes at 10,000 rpm, aspirate media, and freeze tubes at -70° C.
6. At the completion of cell culture experiment, aspirate media, wash samples 1X with PBS, and freeze at -70° C.

Procedure

13. Thaw frozen cell standards and samples. Thaw cyquant reagents, protected from light.
14. Wrap GR dye in aluminum foil to avoid light damage. Keep all plates and samples containing the cyquant solution during preparation covered to avoid light degradation.
15. Prepare cyquant solution by adding cell lysis buffer and dye to deionized water in centrifuge tube. Vortex tube 1 minute to mix.
16. Resuspend each cell standard in 600 µL cyquant solution. Vortex tubes briefly.
17. Add 650 µL cyquant solution to each well of samples.
18. Add cyquant solution and cell standard suspensions to wells of 96-well plate according to the following amounts:

[1] Molecular Probes recommends the use of double gloves when working with this reagent, as it binds nucleic acids it should be treated as a potential mutagen. In addition, DMSO is known to facilitate the entry of organic molecules into tissues.

µL cyquant solution	µL cell suspension
200	0
195	5
190	10
175	25
150	50
100	100
50	150
0	200

19. Add 200 mL of solution from samples to each of 3 wells on 96-well plate.
20. Read fluorescence emission of samples at 520 nm with excitation at 480 nm.
21. Find best-fit line for fluorescence of standards vs. known cell number, use this equation to calculate cell number from fluorescence of unknown samples.

Theory

This assay provides a convenient measure of the density of cells present in a culture, providing a linear detection range of ~50 to 50,000 cells in a 200 µL volume[9]. Increasing the dye concentration in the assay increases the linear working range to 250,000 cells. The assay is based on the use of a proprietary dye which exhibits strong fluorescence enhancement when bound to nucleic acids. Applying the dye to lysed cells, the fluorescence of the sample is directly proportional to the number of cells present in the sample.

12.10 Centrifugation Cell Adhesion Strength Assay

Reagents

WTNR6 fibroblasts cell line
Serum-free NR6 media
NR6 assay media:
- MEM-α with HEPES (25 mM)
- 1 mg/mL bovine serum albumin
- 1% dialyzed fetal bovine serum
- penicillin (100 U/mL)
- streptomycin (200 mg/mL)
- non-essential amino acids (1 mM)
- sodium pyruvate (1 mM)
- glutamine (2 mM)
- G418 (350 μg/mL)

Polymer surfaces to be tested cast in 96-well TCPS plates, including 1g control samples.

Apparatus

Incubator at 37°C, 5% CO_2
Sorvall temperature-controlled centrifuge

Prior to Assay

1. Prepare polymer surfaces in 96-well plate. Cast comb/RGD-comb samples by preparing 0.002 g/mL solutions of polymer in 50/50 vol/vol water/ethanol. Cast surfaces by adding 10 μL solution to each sample well, covering and allowing to dry in air 5 hours, followed by drying *in vacuo* at room temperature over night. Cast 3 samples of each surface in wells of 7 plates, to allow 7 different centrifugal forces to be tested. In addition, cast 6 samples of control surface in a separate plate to be inverted at 1g.
2. Prepare serum-free and assay media.
3. Bring WTNR6 cells to confluence.

Procedure

1. Add 100 μL serum-free media to each sample well.
2. Passage WTNR6 cells and seed 5,000 cells/well in 100 μL serum-free media (total volume in each well 200 μL).
3. Allow cells to attach under serum-free conditions 12 hours at 37°C and 5% CO_2.
4. Aspirate media and add 200 μL assay media. Incubate 8 hours.

5. Top up all sample wells with assay media.
6. Seal wells of plate with sealing film.
7. Centrifuge plates at 37°C 10 minutes: one plate each at 100g, 200g, 400g, 600g, 800g, 1000g, and 1510g.
8. Invert sealed 1g control plate 10 minutes.
9. Unseal plates, aspirate media, rinse 1X with PBS, aspirate, and freeze plates at -70°C.
10. Assay cell number on each surface by CyQuant assay. Normalize cell number from different experiments by comparing number cells attached to 1g controls in each experiment.

Theory

This assay was first developed by McClay et al.[171] to measure the strength of cell adhesion to substrates.

13 Appendix B: Self-Consistent Field Theory

13.1 Model Equations

Self-Consistent Field (SCF) calculations were made for a model of the blend system under investigation using the basic method of Scheutjens and Fleer[140, 141]. In this lattice model, polymer chains having N units are represented as segments occupying sites of the lattice, with connectivity of the chain maintained by the restriction that adjacent segments of the chain occupy neighboring sites. Concentration profiles are assumed to vary only perpendicular to the substrate. The concentration of segments within a given layer (denoted by its z coordinate) is determined by a potential $U_I(z)$:

$$U_I(z) = U'(z) + \sum_{J \neq I} \chi_{IJ} kT[< \phi_J(z) > - \phi_J^b] \qquad \textbf{(Eqn 13.1)}$$

where $U'(z)$ is a "hard core" potential fulfilling the condition of incompressibility, χ_{IJ} is the Flory-Huggins interaction parameter, $<\phi_I(z)>$ is the average volume fraction of J-type segments adjacent to site (z), and ϕ_J^b is the bulk volume fraction of J segments. (The convention used in this notation is capital subscripts refer to "chemical" types of segments present in the

system and lower case subscripts refer to molecule types.) $<\phi_I(x,z)>$ is where the mean field approximation is made:

$$<\phi_J(z)>=\lambda_0\phi_J(z)+\lambda_1\phi_J\ (z-1)+\lambda_1\phi_J(z+1) \qquad \textbf{(Eqn 13.2)}$$

where λ_0 is the fraction of nearest neighbors in the same layer, and λ_1 is the fraction of nearest neighbors at *z-1* or *z+1*. a particular direction. For a hexagonal lattice, $\lambda_0 = 6/8$ and $\lambda_1 = 2/8$. The potential $U_I(x,z)$ is related to a Boltzmann factor for the occupation of the lattice site by a given segment type *I* by

$$G_I(z)=e^{-U_I(z)/kT} \qquad \textbf{(Eqn 13.3)}$$

This Boltzmann factor represents the probability of a free segment being located on the lattice site. For the probability of the *s*th segment of type *I* of the polymer chain to be located in layer *z* of the lattice, the free segment statistical weight of (Eqn 14.3) must be multiplied by the probabilities that the statistical walk of the chain from the initial and terminal free ends reaches the particular site of interest in *s* steps and (*N-s*) steps, respectively. To calculate the statistical weight of *s*-step random walks from any lattice site *(z')* from the end of the polymer chain, we start with the statistical weight $G_I(z)$ of the free end located at *(z)*. We then calculate the statistical weight of the next segment lying adjacent to that site (connectivity requires that the next step of the random walk lie in an adjacent site):

$$<G_{1,I}(x,z)>=\lambda_0 G_{1,I}(z)+\lambda_1 G_{1,I}(z+1)+\lambda_1 G_{1,I}(z-1) \qquad \textbf{(Eqn 13.4)}$$

for all *(x,z)*. Now the statistical weight for the second segment at each site is the free segment probability (Eqn 14.3) multiplied by the probability that the end segment is in an

adjacent site (Eqn 14.4). Equations (14.3) and (14.4) are recursively repeated to calculate the statistical weight for the location of each segment of the chain.

The concentration of the *sth* type *I* segments of all the polymer chains in the system within a particular lattice layer *(z)* is given by:

$$\phi_{s,I}(z) = \frac{\phi_I^b}{N} G_I(z, s \mid e_1, ..., e_n) \qquad \textbf{(Eqn 13.5)}$$

where ϕ_I^b is the bulk concentration of the type *I* segments and $G_I(z,s|e_1,...,e_n)$ is the normalized probability that segment *s* lies in layer *(z)* given that the other *n* chain ends of the polymer may be anywhere in the system. The total polymer concentration in each layer is obtained by summing over all segments of all the polymer chains in the system.

The equilibrium distribution of segments for the system must be obtained in a self-consistent manner, as the concentration of segments depends on the potential $U_I(z)$ and the potential is in turn determined by the segment concentrations. The solution is found by iterating from some starting guess for the potential toward a potential and concentration distribution that are self-consistent, subject to the constraint of incompressibility (The sum of the volume fractions from each type of monomer in the system at each lattice site must be one). The part of the potential that fulfills the requirement of incompressibility is given by:

$$\alpha_J(z) = \frac{U_J(z) - U_J^{ref}}{kT} - \sum_J \chi_{IJ} \frac{< \phi_J(z) >}{\sum_K \phi_K(z)} \qquad \textbf{(Eqn 13.6)}$$

where the capital subscripts refer to a particular segment type and U^{ref} is given by:

$$\frac{U_J^{ref}}{kT} = \sum_j \frac{\phi_j^b}{N_j} + \frac{1}{2} \sum_{J,K} \chi_{JK} \phi_J^b \phi_K^b - \sum_I \chi_{IJ} \phi_I^b \qquad \textbf{(Eqn 13.7)}$$

where χ_{ij} is the Flory-Huggins interaction parameter[145], defined in the usual manner as:

$$\chi_{ij} \equiv \frac{z}{kT}\left[\omega_{ij} - \frac{(\omega_{ii} + \omega_{jj})}{2}\right] \qquad \textbf{(Eqn 13.8)}$$

where z is the lattice coordination number and ω_{ij} is the interaction energy of i with j per segment. In this model dependencies of χ_{ij} on molecular weight of the molecules or concentration of the chemical species are neglected. Note that in calculations of polymer blends in contact with a hard wall surface, we follow Evers et al.[141] in defining the interactions of each component with the surface separately, e.g. for a binary blend the parameters are χ_{AS} and χ_{BS} for the interaction of A or B segments with the surface, respectively. These parameters are related to the adsorption energy difference χ_S[115, 141]:

$$\chi_S = u_A/kT - u_B/kT = -\lambda_1(\chi_{AS} - \chi_{BS}) \qquad \textbf{(Eqn 13.9)}$$

where u_i is the adsorption energy per segment of component i.

At equilibrium, the Lagrange multipliers $\alpha_j(z)$ must all have the same value (i.e. the potential is self-consistent with the volume fraction of all components at all lattice sites,) and the volume fraction of all components at each site must sum to 1. We can define a function

$$f_I(z) = \sum_i \phi_{i,}(z) - \frac{1}{\sum_i \phi_{i,I}(z)} + \alpha_I(z) - \overline{\alpha} \qquad \textbf{(Eqn 13.10)}$$

where $\overline{\alpha} = \Sigma\alpha(z)/\Sigma\ 1$. Equilibrium is found when $f(z) = 0$ for all components at all sites. Practically speaking, convergence is taken as $f < 1\text{x}10^{-7}$. This minimum in f with respect to the potential and component volume fractions is found using standard numerical methods such as discussed by Dennis[147].

14 Bibliography

1. B. D. Ratner, A. S. Hoffman, F. J. Schoen, and J. E. Lemons, *Biomaterials Science: An Introduction to Materials in Medicine,* Academic Press, New York, NY, 484 pages, (1996).
2. R. P. Lanza, R. Langer, and W. L. Chick, *Principles of Tissue Engineering,* R.D. Landes Company, Georgetown, TX, 808 pages, (1997).
3. E. Mathiowitz, J. S. Jacob, Y. S. Jong, G. P. Carino, D. E. Chickering, P. Chaturvedi, C. A. Santos, K. Vijayaraghavan, S. Montgomery, M. Bassett, and C. Morrell, "Biologically erodable microspheres as potential oral drug delivery systems," *Nature* **386**, 410-414 (1997).
4. D. K. Pettit and W. R. Gombotz, "The development of site-specific drug-delivery systems for protein and peptide biopharmaceuticals," *TIB Tech.* **16**, 343-349 (1998).
5. W. M. Saltzman, "Growth-factor delivery in tissue engineering," *MRS Bull.* **21**, 62-65 (1996).
6. D. J. Lyman and S. M. Rowland, "Biomaterials," in *Encyclopedia of Polymer Science and Engineering*, edited by H. F. Mark and J. I. Kroschwitz (Wiley, New York, NY, 1985), Vol. 2, p. 267-286.
7. A. G. Mikos, M. G. Papadaki, S. Kouvroukoglou, S. L. Ishaug, and R. C. Thomson, "Mini-Review: Islet transplantation to create a bioartificial pancreas," *Biotechnol. Bioeng.* **43**, 673-677 (1994).
8. D. A. Cieslinski and H. D. Humes, "Tissue engineering of a bioartificial kidney," *Biotechnol. Bioeng.* **43**, 678-681 (1994).
9. D. A. Lauffenburger and J. J. Linderman, *Receptors: Models for Binding, Trafficking, and Signaling,* Oxford University Press, New York, NY, 362 pages, (1993).
10. S. I. Jeon and J. D. Andrade, "Protein-surface interactions in the presence of polyethylene oxide," *J. Colloid Interf. Sci.* **142**, 159-166 (1991).
11. J. H. Lee, H. B. Lee, and J. D. Andrade, "Blood compatibility of poly(ethylene oxide) surfaces," *Prog. Polym. Sci.* **20**, 1043-1079 (1995).
12. M. D. Garrison, D. J. Iuliano, S. S. Saavedra, and W. M. Reichert, "Post-adsorption changes in the emission maximum of acrylodan-labelled bovine serum albumin using TIRF," *J. Coll. Interf. Sci.* **148**, 415-422 (1992).

13. D. J. Iuliano, S. S. Saavedra, and G. A. Truskey, "Effect of the conformation and orientation of adsorbed fibronectin on endothelial cell spereading and the strength of adhesion," *J. Biomed. Mater. Res.* **278**, 1103-1113 (1993).
14. N. Wang and D. E. Ingber, "Control of cytoskeletal mechanics by extracellular matrix, cell shape, and mechanical tension," *Biophys. J.* **66**, 2181-2189 (1994).
15. B. Alberts, D. Bray, J. Lewis, M. Raff, K. Roberts, and J. D. Watson, *Molecular Biology of the Cell,* Garland Publishing, Inc., New York, NY, 1294 pages, (1994).
16. H. Lodish, D. Baltimore, A. Berk, S. L. Zipursky, P. Matsudaira, and J. Darnell, *Molecular Cell Biology,* Scientific American Books, New York, NY, 1344 pages, (1995).
17. J. M. Edelman, P. A. DiMilla, and S. M. Albelda, "The integrin cell adhesion molecules," in *Principles of cell adhesion*, edited by P. Richardson and M. Steiner (CRC Press, New York, NY, 1995), p. 163-186.
18. E. Ruoslahti and M. D. Pierschbacher, "New perspectives in cell adhesion - RGD and integrins," *Science* **238**, 491-497 (1987).
19. E. Ruoslahti and B. Obrink, "Common principles in cell adhesion," *Exp. Cell Res.* **227**, 1-11 (1996).
20. S. K. Akiyama, S. Aota, and K. M. Yamada, "Function and receptor specificity of a minimal 20-kilodalton cell adhesive fragment of fibronectin," *Cell Adhes. Commun.* **3**, 13-25 (1995).
21. J. Graf, R. C. Ogle, F. A. Robey, M. Sasaki, G. R. Martin, Y. Yamada, and H. K. Kleinman, "A pentapeptide from the laminin-b1 chain mediates cell-adhesion and binds the 67000-laminin receptor," *Biochem.* **26**, 6896-6900 (1987).
22. S. P. Massia and J. A. Hubbell, "Vascular endothelial-cell adhesion and spreading promoted by the peptide REDV of the IIICS region of plasma fibronectin is mediated by integrin $\alpha_4\beta_1$," *J. Biol. Chem.* **267**, 14019-14026 (1992).
23. W. D. Staatz, K. F. Fok, M. M. Zutter, S. P. Adams, B. A. Rodriquez, and S. A. Santoro, "Identification of a tetrapeptide recognition sequence for the $\alpha_2\beta_1$ integrin in collagen," *J. Biol. Chem.* **266**, 7363-7367 (1991).
24. P. A. DiMilla, J. A. Stone, J. A. Quinn, S. M. Albelda, and D. A. Lauffenburger, "Maximal migration of human smooth muscle cells on fibronectin and type IV collagen occurs at an intermediate attachment strength," *J. Cell Biol.* **122**, 729-737 (1993).
25. K. M. Yamada, S. Aota, S. K. Akiyama, and S. E. LaFlamme, "Mechanisms of fibronectin and integrin function during cell adhesion and migration," *Cold Spring Harbor Symp. Quant. Biol.* **57**, 203-211 (1992).
26. G. Maheshwari, A. Wells, L. G. Griffith, and D. A. Lauffenburger, "Biophysical integration of effects of epidermal growth factor and fibronectin on fibroblast migration," *Biophys. J.* **76**, 2814-2823 (1999).
27. D. Choquet, D. P. Felsenfeld, and M. P. Sheetz, "Extracellular matrix rigidity causes strengthening of integrin-cytoskeleton linkages," *Cell* **88**, 39-48 (1997).
28. R. J. Pelham Jr. and Y.-L. Wang, "Cell locomotion and focal adhesions are regulated by substrate flexibility," *Proc. Natl. Acad. Sci. USA* **94**, 13661-13665 (1997).
29. J. Folkman and A. Moscona, "Role of cell shape in growth control," *Nature* **273**, 345-349 (1978).
30. M. J. Bissell, H. G. Hall, and G. Parry, "How does extracellular matrix direct gene expression?," *J. Theor. Biol.* **99**, 31-68 (1982).

31. D. Mooney, L. Hansen, J. Vacanti, R. Langer, S. Farmer, and D. Ingber, "Switching from differentiation to growth in hepatocytes: control by extracellular matrix," *J. Cell Physiol.* **151**, 497-505 (1992).
32. D. E. Ingber, J. A. Madri, and J. D. Jamieson, "Basement membrane as a spatial organizer of polarized epithelia: exogenous basement membrane reorients pancreatic epithelial tumor cells *in vitro*," *Am. J. Pathol.* **122**, 129-139 (1986).
33. F. G. Giancotti and E. Ruoslahti, "Integrin signaling," *Science* **285**, 1028-1032 (1999).
34. S. Miyamoto, H. Teramoto, O. A. Coso, J. S. Gurkind, P. D. Burbelo, S. K. Akiyama, and K. M. Yamada, "Integrin function: molecular heierarchies of cytoskeletal and signaling molecules," *J. Cell Biol.* **131**, 791-805 (1995).
35. K. Burridge, K. Fath, T. Kelly, G. Nuckolls, and C. Turner, "Focal adhesions: Transmembrane junctions between the extracellular matrix and the cytoskeleton," *Ann. Rev. Cell Biol.* **4**, 487-525 (1988).
36. K. Burridge and M. Chrzanowska-Wodnicka, "Focal adhesions, contractility, and signaling," *Annu. Rev. Cell Dev. Biol.* **12**, 463-519 (1996).
37. K. Fath, C.-J. Edgell, and K. Burridge, "The distribution of distinct integrins in focal contacts is determined by the substratum composition," *J. Cell Sci.* **92**, 67-75 (1989).
38. S. Miyamoto, H. Teramoto, J. S. Gutkind, and K. M. Yamada, "Integrins can collaborate with growth factors for phosphorylation of receptor tyrosine kinases and MAP kinase activation: Roles of integrin aggregation and occupancy of receptors," *J. Cell Biol.* **135**, 1633-1642 (1996).
39. P. Banerjee, D. J. Irvine, A. M. Mayes, and L. G. Griffith, "Polymer latexes for cell-resistant and cell-interactive surfaces," *J. Biomed. Mater. Res.* **50**, 331-339 (2000).
40. J. P. Bearinger, D. G. Castner, and K. E. Healy, "Biomolecular modification of P(AAm-co-EG/AA) IPNs supports osteoblast adhesion and phenotypic expression," *J. Biomater. Sci. Polym. Ed.* **9**, 629-652 (1998).
41. F. E. Black, M. Hartshorne, M. C. Davies, C. J. Roberts, S. J. B. Tendler, P. M. Williams, K. M. Shakesheff, S. M. Cannizzaro, I. Kim, and R. Langer, "Surface engineering and surface analysis of a biodegradable polymer with biotinylated end groups," *Langmuir* **15**, 3157-3161 (1999).
42. P. D. Drumheller, D. L. Elbert, and J. A. Hubbell, "Multifunctional poly(ethylene glycol) semi-interpenetrating polymer networks as highly selective adhesive substrates for bioadhesive peptide grafting," *Biotech. Bioeng.* **43**, 772-780 (1994).
43. J. A. Hubbell, S. P. Massia, N. P. Desai, and P. D. Drumheller, "Endothelial cell-selective materials for tissue engineering in the vascular graft via a new receptor," *Bio/Tech.* **9**, 568-572 (1991).
44. P. R. Kuhl and L. G. GriffithCima, "Tethered epidermal growth factor as a paradigm for growth factor-induced stimulation from the solid phase," *Nature Medicine* **2**, 1022-1027 (1996).
45. G. Maheshwari, G. Brown, D. A. Lauffenburger, A. Wells, and L. G. Griffith, "Cell adhesion and motility depend on nanoscale RGD clustering," *J. Cell. Sci.* **113**, 1677-1686 (2000).
46. N. Patel, R. Padera, G. H. W. Sanders, S. M. Cannizzaro, M. C. Davies, R. Langer, C. J. Roberts, S. J. B. Tendler, P. M. Williams, and K. M. Shakesheff, "Spatially controlled cell engineering on biodegradable polymer surfaces," *FASEB J.* **12**, 1447-1454 (1990).
47. Y. W. Tong and M. S. Shoichet, "Enhancing the interaction of central nervous system neurons with poly(tetrafluoroethylene-co-hexafluoroproplylene) via a novel surface amine-

functionalization reaction followed by peptide modification," *J. Biomater. Sci. Polym. Ed.* **9**, 713-729 (1998).
48. S. K. Williams, D. G. Rose, and B. E. Jarrell, "Microvascular endothelial cell sodding of ePTFE vacular grafts: improved patency and stability of the cellular lining," *J. Biomed. Mater. Res.* **28**, 203-212 (1994).
49. M. Rupnick, A. Gardner, and J. Glover, "Endothelialization of vascular prosthetic surfaces after seeding or sodding with human microvascular endothelial cells," *J. Vasc. Surg.* **9**, 788-795 (1989).
50. B. D. Ratner, "Template-imprinted nanostructured surfaces for protein recognition," *Nature* **398**, 593-597 (1999).
51. S. P. Massia and J. A. Hubbell, "An RGD spacing of 440 nm is sufficient for integrin $\alpha_V\beta_3$-mediated fibroblast spreading and 140 nm for focal contact and stress fiber formation," *J. Cell Biol.* **114**, 1089-1100 (1991).
52. J. A. Hubbell, "Biomaterials in Tissue Engineering," *Bio-Technology* **13**, 565-576 (1995).
53. D. K. Han, K. D. Park, J. A. Hubbell, and Y. H. Kim, "Surface characteristics and biocompatibility of lactide-based poly(ethylene glycol) scaffolds for tissue engineering," *J. Biomater. Sci. Polym. Ed.* **9**, 667-680 (1998).
54. A. Park, B. Wu, and L. G. Griffith, "Integration of surface modification and 3D fabrication techniques to prepare patterned poly(L-lactide) substrates allowing regionally selective cell adhesion," *J. Biomater. Sci. Polym. Ed.* **9**, 89-110 (1998).
55. A. M. Reed and D. K. Gilding, "Biodegradable polymers for use in surgery - poly(gycolic)/poly(lactic acid) homo and copolymers: 2. *In vitro* degradation," *Polymer* **22**, 494-498 (1981).
56. C. Schugens, V. Maquet, C. Grandfils, R. Jerome, and P. Teyssie, "Polylactide macroporous biodegradable implants for cell transplantation. II. Preparation of polylactide foams by liquid-liquid phase separation," *J. Biomed. Mater. Res.* **30**, 449-461 (1996).
57. P. van de Witte, H. Esselbrugge, P. J. Dijkstra, J. W. A. van den Berg, and J. Feijen, "Phase transitions during membrane formation of polylactides. I. A morphological study of membranes obtained from the system polylactide-chloroform-methanol," *J. Mem. Sci.* **113**, 223-236 (1996).
58. A. Park and L. Griffith Cima, "*In vitro* cell response to differences in poly-L-lactide crystallinity," *J. Biomed. Mater. Res.* **31**, 117-130 (1996).
59. J. H. Lee, P. Kopeckova, J. Kopecek, and J. D. Andrade, "Surface-properties of copolymers of alkyl methacrylates with methoxy (polyethylene oxide) methacrylates and their application as protein-resistant coatings," *Biomaterials* **11**, 455-464 (1990).
60. K. L. Prime and G. M. Whitesides, "Adsorption of proteins onto surfaces containing end-attached oligo(ethylene oxide): a model system using self-assembled monolayers," *J. Am. Chem. Soc.* **115**, 10714-10721 (1993).
61. J. M. Harris, *Poly(ethylene glycol) Chemistry: Biotechnical and Biomedical Applications,* Plenum Press, New York, NY, 385 pages, (1992).
62. D. J. Irvine, A. M. Mayes, S. K. Satija, J. G. Barker, S. J. Sofia-Allgor, and L. G. Griffith, "Comparison of grafted star and linear poly(ethylene oxide) polymers for protein-resistant surfaces," *Journal of Biomedical Materials Research* **40**, 498-509 (1998).
63. K. D. Park, W. G. Kim, H. Jacobs, T. Okano, and S. W. Kim, "Blood compatibility of SPUU-PEO-heparin graft-copolymers," *J. Biomed. Mater. Res.* **26**, 739-756 (1992).

64. Y. C. Tseng and K. Park, "Synthesis of photoreactive poly(ethylene glycol) and its application to the prevention of surface-induced platelet activation," *J. Biomed. Mater. Res.* **26**, 373-391 (1992).
65. M. Amiji and K. Park, "Surface modification of polymeric biomaterials with poly(ethylene oxide), albumin, and heparin for reduced thrombogenicity," *J. Biomater. Sci., Polym. Ed.* **4**, 217-234 (1993).
66. M. S. Sheu, A. S. Hoffman, J. G. A. Terlingen, and J. Feijen, "A new gas discharge process for preparation of non-fouling surfaces on biomaterials," *Clin. Mater.* **13**, 41 (1993).
67. E. Ruoslahti and J. C. Reed, "Anchorage dependence, integrins, and apoptosis," *Cell* **77**, 477-478 (1994).
68. L. M. Shaw, J. M. Messier, and A. M. Mercurio, "The activation dependent adhesion of macrophages to laminin involves cytoskeletal anchoring and phosphorylation of the $\alpha_6\beta_1$ integrin," *J. Cell Biol.* **110**, 2167-2174 (1990).
69. D. K. Han, K. D. Park, G. H. Ryu, U. Y. Kim, B. G. Min, and Y. H. Kim, "Plasma protein adsorption to sulfonated poly(ethylene oxide)-grafted polyurethane surface," *J. Biomed. Mater. Res.* **30**, 23-30 (1996).
70. S. J. Sofia, V. Premnath, and E. W. Merrill, "Poly(ethylene oxide) grafted to silicon surfaces: grafting density and protein adsorption," *Macromol.* **31**, 5059-5070 (1998).
71. N. P. Desai, S. F. A. Hossainy, and J. A. Hubbell, "Surface-immobilized polyethylene oxide for bacterial repellence," *Biomaterials* **13**, 417-420 (1992).
72. A. S. Sawney, C. P. Pathak, and J. A. Hubbell, "Bioerodible hydrogels based on photopolymerized poly(ethylene glycol)-co-poly(α-hydroxy acid) diacrylate monomers," *Macrmol.* **26**, 581-587 (1993).
73. A. M. Mayes, D. J. Irvine, and L. G. Griffith, "Tailored Polymer Surfaces for Controlled Cell Interactions," *MRS Symp. Proc.* **530**, 73-84 (1998).
74. C. Roberts, C. S. Chen, M. Mrksich, V. Martichonok, D. E. Ingber, and G. M. Whitesides, "Using mixed self-assembled monolayers presenting RGD and (EG)(3)OH groups to characterize long-term attachment of bovine capillary endothelial cells to surfaces," *Journal of the American Chemical Society* **120**, 6548-6555 (1998).
75. I. Szleifer, "Protein adsorption on surfaces with grafted polymers: a theoretical approach," *Biophys. J.* **72**, 595-612 (1997).
76. S. L. McGurk, R. J. Green, G. H. W. Sanders, M. C. Davies, C. J. Roberts, S. J. B. Tendler, and P. M. Williams, "Molecular interactions of biomolecules with surface-engineered interfaces using Atomic Force Microscopy and surface plasmon resonance," *Langmuir* **15**, 5136-5140 (1999).
77. J. V. Dawkins, D. J. Neep, and P. L. Shaw, "Non-aqueous polystyrene dispersions: steric stabilization by partially hydrolysed poly(vinyl alcohol) in methanolic media," *Polymer* **35**, 5366-5368 (1994).
78. C. FreijLarsson, T. Nylander, P. Jannasch, and B. Wesslen, "Adsorption behaviour of amphiphilic polymers at hydrophobic surfaces: Effects on protein adsorption," *Biomaterials* **17**, 2199-2207 (1996).
79. L. M. Zhu, O. Gunnarsson, and B. Wesslen, "An amphiphilic graft copolymer as a surface-modifying additive for poly(methyl methacrylate)," *Journal of Polymer Science Part a-Polymer Chemistry* **33**, 1257-1265 (1995).
80. D. G. Walton, P. P. Soo, A. M. Mayes, S. J. Sofia-Allgor, J. T. Fujii, L. G. Griffith, J. F. Ankner, H. Kaiser, J. Johansson, G. D. Smith, J. G. Barker, and S. K. Satija, "Creation of

stable poly(ethylene oxide) surfaces on poly(methyl methacrylate) using blends of branched and linear polymers," *Macromol.* **30**, 6947-4956 (1997).
81. J. H. Lee, Y. M. Ju, W. K. Lee, K. D. Park, and Y. H. Kim, "Platelet adhesion onto segmented polyurethane surfaces modified by PEO- and sulfonated PEO-containing block copolymer additives," *Journal of Biomedical Materials Research* **40**, 314-323 (1998).
82. D. K. Han, K. D. Park, and Y. H. Kim, "Sulfonated poly(ethylene oxide)-grafted polyurethane copolymer for biomedical applications," *Journal of Biomaterials Science-Polymer Edition* **9**, 163-174 (1998).
83. R. M. Fitch, *Polymer Colloids: A Comprehensive Introduction,* Academic Press Ltd., London, 346 pages, (1997).
84. J. Ugelstad, A. Berge, T. Ellingsen, R. Schmid, T.-N. Nilsen, P. C. Mork, P. Stenstad, E. Hornes, and O. Olsvik, "Preparation and application of new monosized polymer particles," *Prog. Polym. Sci.* **17**, 87-161 (1992).
85. D. Bastos-Gonzalez, J. L. Ortega-Vinuesa, F. J. De Las Nieves, and R. Hidalgo-Alvarez, "Carboxylated latexes for covalent coupling antibodies, I," *J. Coll. Interf. Sci.* **176**, 232-239 (1995).
86. R. Puchades and A. Maquiera, "Recent developments in flow injection immunoanalysis," *Crit. Rev. Anal. Chem.* **26**, 195-218 (1996).
87. A. J. Paine and J. McNulty, "Dispersion polymerization of styrene in polar solvents. 6. Influence of reaction parameters on particle size and molecular weight in poly(N-vinylpyrrolidone)-stabilized reactions," *Macromol.* **23**, 3104-3109 (1990).
88. S. Shen, E. D. Sudol, and M. S. El-Aasser, "Control of particle size in dispersion polymerization of methyl methacrylate," *J. Polym. Sci. A, Polym. Chem.* **31**, 1393-1402 (1993).
89. C. K. Ober and K. P. Lok, "Formation of large monodisperse copolymer particles by dispersion polymerization," *Macromol.* **20**, 268-273 (1987).
90. D.-M. Liu and V. Dixit, in *Materials Science Forum* (Trans Tech Publications, Switzerland, 1997), Vol. 250, p. 241.
91. S. J. Peter, M. J. Miller, A. W. Yasko, M. J. Yaszemski, and A. G. Mikos, "Polymer concepts in tissue engineering," *J. Biomed. Mater. Res.* **43**, 422-427 (1998).
92. M. C. Wake, P. K. Gupta, and A. G. Mikos, "Fabrication of pliable biodegradable polymer foams to engineer soft tissues," *Cell Transp.* **5**, 465-473 (1996).
93. M. C. Peters and D. J. Mooney, "Synthetic extracellular matrices for cell transplantation," *Mater. Sci. Forum* **250**, 43-52 (1997).
94. C. A. Vacanti, W. Kim, J. Upton, M. P. Vacanti, D. Mooney, B. Schloo, and J. P. Vacanti, "Tissue-engineered growth of bone and cartilage," *Transplant Proc.* **25**, 1019-1021 (1993).
95. L. M. Wilkins, S. R. Watson, S. J. Prosky, S. F. Meunier, and N. L. Parenteau, "Development of a bilayered living skin construct for clinical applications," *Biotechnol. Bioeng.* **43**, 747-756 (1994).
96. I. V. Yannas, "Models of organ regeneration processes induced by templates," in *Bioartificial Organs*, 1997), Vol. 831, p. 280-293.
97. I. V. Yannas, E. Lee, D. P. Orgill, E. M. Skrabut, and G. F. Murphy, "Synthesis and characterization of a model extracellular-matrix that induces partial regeneration of adult mammalian skin," *Proc. Natl. Acad. Sci. USA* **86**, 933-937 (1989).
98. D. L. Ellis and I. V. Yannas, "Recent advances in tissue synthesis *in vivo* by use of collagen-glycosaminoglycan copolymers," *Biomaterials* **17**, 291-299 (1996).

99. R. Bellamkonda and P. Aebischer, "Review: Tissue engineering in the nervous system," *Biotechnol. Bioeng.* **43**, 543-554 (1994).
100. M. H. Spilker, I. V. Yannas, H. P. Hsu, T. V. Norregaard, S. K. Kostyk, and M. Spector, "The effects of collagen-based implants on early healing of the adult rat spinal cord," *Tissue Eng.* **3**, 309-317 (1997).
101. L. J. Chamberlain, I. V. Yannas, A. Arrizabalaga, H. P. Hsu, T. V. Norregaard, and M. Spector, "Early peripheral nerve healing in collagen and silicone tube implants: Myofibroblasts and the cellular response," *Biomaterials* **19**, 1393-1403 (1998).
102. L. E. Niklason, J. Gao, W. M. Abbott, H. K.K., S. Houser, R. Marini, and R. Langer, "Functional arteries grown *in vitro*," *Science* **284**, 489-493 (1999).
103. S. Uyama, P. M. Kaufmann, T. Tadeka, and J. P. Vacanti, "Delivery of whole liver-equivalent hepatocyte mass using polymer devices and heptotrophic stimulation," *Transplantation* **55**, 932-935 (1993).
104. M. C. Wake, C. W. Patrick, and A. G. Mikos, "Pore morphology effects on the fibrovascular tissue growth in porous polymer substrates," *Cell Transp.* **3**, 339-343 (1994).
105. R. C. Thomson, M. C. Wake, M. J. Yaszemski, and A. G. Mikos, "Biodegradable polymer scaffolds to regenerate organs," in *Biopolymers II*, edited by N. A. Peppas and R. S. Langer (Springer-Verlag, New York, NY, 1995), Vol. 122, p. 245-274.
106. K. Whang, C. H. Thomas, K. E. Healy, and G. Nuber, "A novel method to fabricate bioabsorbable scaffolds," *Polymer* **36**, 837-842 (1995).
107. D. A. Barrera, E. Zylstra, P. T. Lansbury, and R. Langer, "Copolymerization and degradation of poly(lactic acid-co-lysine)," *Macromol.* **28**, 425-432 (1995).
108. T. Ouchi, A. Fujino, K. Tanaka, and T. Banba, "Synthesis and antitumor activity of conjugates of poly(α-malic acid) and 5-fluorouracils bound via ester, amide or carbamoyl bonds," *J. Contr. Rel.* **12**, 143-153 (1990).
109. D. N. Theodorou, "Microscopic structure and thermodynamic properties of bulk copolymers and surface-active polymers at interfaces. 2. Results for some representative chain architectures," *Macromol.* **21**, 1422-1436 (1988).
110. D. T. Wu, G. H. Fredrickson, J.-P. Carton, A. Ajdari, and L. Leibler, "Distribution of chain ends at the surface of a polymer melt: Compensation effects and surface tension," *J. Polym. Sci. B, Polym. Phys.* **33**, 2373-2389 (1995).
111. I. Hopkinson, F. T. Kiff, R. W. Richards, S. Affrossman, M. Hartshorne, R. A. Pethrick, H. Munro, and J. R. P. Webster, "Investigation of surface enrichment in isotopic mixtures of poly(methyl methacrylate)," *Macromol.* **28**, 627-635 (1995).
112. R. A. L. Jones, E. J. Kramer, M. H. Rafailovich, J. Sokolov, and S. A. Schwarz, "Surface enrichment in polymer blends: Simple theory and an experimental test," *Mater. Res. Soc. Symp. Proc.* **153**, 133-141 (1989).
113. R. A. L. Jones, E. J. Kramer, M. H. Rafailovich, J. Sokolov, and S. A. Schwarz, "Surface enrichment in an isotopic polymer blend," *Phys. Rev. Lett.* **62**, 280-283 (1989).
114. R. J. Composto, R. S. Stein, E. J. Kramer, R. A. L. Jones, A. Mansour, A. Karim, and G. P. Felcher, "Surface enrichment in polymer blends- A neutron reflection test," *Physica B* **156-157**, 434-436 (1989).
115. A. Hariharan, S. L. Kumar, and T. P. Russell, "Surface segregation in binary polymer mixtures: A lattice model," *Macromol.* **24**, 4909-4917 (1991).
116. P. Cifra, F. E. Karasz, and W. J. MacKnight, "Surface segregation in polymer blends: A Monte Carlo simulation," *Macromol.* **25**, 4895-4901 (1992).

117. M. Sikka, N. Singh, F. S. Bates, A. Karim, S. Satija, and C. F. Majkrzak, "Surface segregation in model symmetric polyolefin diblock copolymer melts," *J. Phys. II France* **4**, 2231-2248 (1994).
118. A. Turturro, E. Gattiglia, P. Vacca, and G. T. Viola, "Free surface morphology of block copolymers: 1. Styrene-butadiene diblock copolymers," *Polymer* **36**, 3987-3996 (1995).
119. M. A. Carignano and I. Szleifer, "Surface segregation in diblock copolymers and polymer blend thin films," *Europhys. Lett.* **30**, 525-530 (1995).
120. M. Sikka, N. Singh, A. Karim, F. S. Bates, S. Satija, and C. F. Majkrzak, "Entropy-driven surface segregation in block copolymer melts," *Phys. Rev. Lett.* **70**, 307-310 (1993).
121. C. J. Jalbert, J. T. Koberstein, R. Balaji, Q. Bhatia, L. Salvati Jr., and I. Yilgor, "Surface depletion of end groups in amine-terminated poly(dimethylsiloxane)," *Macromol.* **27**, 2409-2413 (1994).
122. J. F. Elman, B. D. Johs, T. E. Long, and J. T. Koberstein, "A neutron reflectivity investigation of surface and interface segregation of polymer functional end groups," *Macromol.* **27**, 5341-5349 (1994).
123. A. M. Botelho do Rego, J. D. Lopes da Silva, M. Rei Vilar, M. Schott, S. Petitjean, and R. Jerome, "End chain segregation effects in polymer surfaces observed by HREELS: A preliminary study," *Macromol.* **26**, 4986-4988 (1993).
124. S. Affrossman, M. Hartshorne, T. Kiff, R. A. Pethrick, and R. W. Richards, "Surface segregation in blends of hydrogenous polystyrene and perfluorhexane end-capped deuterated polystyrene, studied by SSIMMS and XPS," *Macromol.* **27**, 1588-1591 (1994).
125. T. F. Schaub, G. J. Kellogg, A. M. Mayes, R. Kulasekere, J. F. Ankner, and H. Kaiser, "Surface modification via chain end segregation in polymer blends," *Macromol.* **29**, 3982-3990 (1996).
126. D. G. Walton and A. M. Mayes, "Entropically driven segregation in blends of branched and linear polymers," *Phys. Rev. E* **54**, 2811-2815 (1996).
127. G. H. Fredrickson, "Effect of architecture in the surface segregation of polymer blends," *Macromol.* **29**, 7919-7930 (1996).
128. T. P. Russell, "Copolymers at surfaces and interfaces," *Curr. Op. Coll. Interf. Sci.* **1**, 107-115 (1996).
129. F. E. Bailey Jr. and J. V. Koleske, *Alkylene oxides and their polymers,* Dekker, New York, NYpages, (1991).
130. D. Gersappe, D. Irvine, A. C. Balazs, Y. Liu, J. Sokolov, M. Rafailovich, S. Schwarz, and D. G. Pfeiffer, "The use of graft copolymers to bind immiscible blends," *Science* **265**, 1072-1074 (1994).
131. J. L. Eguiburu, J. J. Iruin, M. J. Fernandez-Berridi, and J. S. Roman, "Blends of amorphous and crystalline polylactides with poly(methyl methacrylate) and poly(methyl acrylate): A miscibility study," *Polymer* **39**, 6891-6897 (1998).
132. H. Younes and D. Cohn, "Phase separation in poly(ethylene glycol)/poly(lactic acid) blends," *Eur. Polym. J.* **8**, 765-773 (1988).
133. A. J. Nijenhuis, E. Colstee, D. W. Grijpma, and A. J. Pennings, "High molecular weight poly(L-lactide) and poly(ethylene oxide) blends: Thermal characterization and physical properties," *Polymer* **37**, 5849-5857 (1996).
134. J.-M. Yang, H.-L. Chen, J.-W. You, and J. C. Hwang, "Miscibility and crystallization of poly(L-lactide)/poly(ethylene glycol) and poly(L-lactide)/poly(ε-caprolactone) blends," *Polym. J.* **29**, 657-662 (1997).

135. J.-L. Duband, G. H. Nuckolls, A. Ishihara, T. Hasegawa, K. M. Yamada, J. P. Thiery, and K. Jacobson, "Fibronectin receptor exhibits high lateral mobility in embryonic locomoting cells but is immobile in focal contacts and fibrillar streaks in stationary cells," *J. Cell Biol.* **107**, 1385-1396 (1988).
136. G. I. Bell, M. Dembo, and P. Bongrand, "Cell adhesion: Competition between nonspecific repulsion and specific binding," *Biophys. J.* **45**, 1051-1064 (1984).
137. M. D. Ward and D. A. Hammer, "A theoretical analysis for the effect of focal contact formation on cell-substrate attachment strength," *Biophys. J.* **64**, 936-959 (1993).
138. N. Metropolis, A. Rosenbluth, M. Rosenbluth, A. Teller, and E. Teller, "Equations of state calculations by fast computing machines," *J. Chem. Phys.* **21**, 1087-1092 (1953).
139. Y. Xiao and G. A. Truskey, "Effect of receptor-ligand affinity on the strength of endothelial cell adhesion," *Biophys. J.* **71**, 2869-2884 (1996).
140. J. M. H. M. Scheutjens and G. J. Fleer, "Statistical theory of the adsorption of interacting chain molecules. 1. Partition function, segment density distribution, and adsorption isotherms," *J. Phys. Chem.* **83**, 1619-1635 (1979).
141. O. A. Evers, J. M. H. M. Scheutjens, and G. J. Fleer, "Statistical thermodynamics of block copolymer adsorption. 1. Formulation of the model and results for the adsorbed layer structure," *Macromol.* **23**, 5221-5233 (1990).
142. G. J. Fleer, M. A. Cohen Stuart, J. M. H. M. Scheutjens, T. Cosgrove, and B. Vincent, *Polymers at Interfaces,* University Press, Cambridge, UK, 502 pages, (1993).
143. D. N. Theodorou, "Structure and thermodynamics of bulk homopolymer/solid interfaces: A site lattic model approach," *Marcomol.* **21**, 1400-1410 (1988).
144. D. J. Irvine, A. M. Mayes, and L. Griffith-Cima, "Self-consistent field analysis of grafted star polymers," *Macromol.* **29**, 6037-6043 (1996).
145. P. J. Flory, *Principles of Polymer Chemistry,* Cornell Univ. Press, Ithaca, NYpages, (1953).
146. A. F. M. Barton, *CRC Handbook of Polymer-Liquid Interaction Parameters,* CRC Press, Boca Raton, FLpages, (1990).
147. J. E. Dennis Jr. and R. B. Schnabel, *Numerical methods for unconstrained optimization and nonlinear equations,* Prentice-Hall, Inc., Englewood Cliffs, NJ, 378 pages, (1983).
148. D. Van Krevelen, *Properties of Polymers: Their Correlation With Chemical Structure, Their Numerical Estimation and Prediction from Group Contributions,* Elsevier, New York, NY, 875 pages, (1990).
149. E. W. Fisher, H. J. Sterzel, and G. Wegner, "Investigation of the structure of solution grown crystals of lactide copolymers by means of chemical reactions," *G. Kolloid-Zeitschrift Zeitschrift Polym.* **251**, 980-990 (1973).
150. S. Iannace and L. Nicolais, "Isothermal crystallization and chain mobility of poly(L-lactide)," *J. Appl. Polym. Sci.* **64**, 911-919 (1997).
151. S.-A. C. Company, *Product Index,* pages, (1999-2000).
152. J. Brandrup and E. H. Immergut, (Wiley, New York, NY, 1989).
153. R. F. Storey and T. P. Hickey, "New epoxy-terminated oligoesters - precursors to totally biodegradable networks," *J. Polym. Sci. A Polym. Chem.* **31**, 1825-1838 (1993).
154. S. Jo and A. G. Mikos, "Modification of poly(ethylene glyol)-tethered poly(propylene-co-fumurate) with RGD peptide," *ACS Polym. Preprints* **40**, 183 (1999).
155. K. Nilsson and K. Mosbach, "Immobilization of ligands with organic sulfonyl chlorides," *Meth. Enzymol.* **104**, 56-69 (1984).
156. C. J. Marshall, "Specificity of receptor tyrosine kinase signaling - transient versus sustained extracellular signal-regulated kinase activation," *Cell* **80**, 179-185 (1995).

157. S. Traverse, N. Gomez, H. Paterson, C. Marshall, and P. Cohen, "Sustained activation of the mitogen-activated protein (MAP) kinase cascade may be required for differentiation of PC12 cells. Comparison of hte effects of nerge frowth factor and epidermal growth factor," *Biochem. J.* **288**, 351-355 (1992).
158. B. Kalb and A. J. Pennings, "General crystallization behavior of poly(L-lactic acid)," *Polymer* **21**, 607-612 (1980).
159. F. J. Balta-Calleja, *X-ray Scattering of Synthetic Polymers,* Elsevier, New York, NY, 317 pages, (1989).
160. J.-R. Sarasua, R. E. Prud'homme, M. Wisniewski, A. Le Borgne, and N. Spassky, "Crystallization and melting behavior of polylactides," *Macromol.* **31**, 3895-3905 (1998).
161. S. Wu, *Polymer Interface and Adhesion,* Marcel Dekker, Inc., New York, NY, 630 pages, (1982).
162. L. A. Girifalco and R. J. Good, "A theory for the estimation of surface and interfacial energies. I. Derivation and application to interfacial tension," *J. Phys. Chem.* **61**, 904-909 (1957).
163. R. J. Good, "Intermolecular and Interatomic Forces," in *Treatise on Adhesion and Adhesives*, edited by R. L. Patrick (Marcel Dekker, Inc., New York, NY, 1967), Vol. 1, p. 9-68.
164. G. Beamson and D. Briggs, *High Resolution XPS of Organic Polymers,* Wiley, New York, NY, 295 pages, (1992).
165. G. C. Smith, *Quantitative Surface Analysis for Materials Science,* Institute of Metals, Brookfield, VT, 173 pages, (1991).
166. D. T. Clark and H. R. Thomas, "Application of ESCA to polymer chemistry. XVI. Electron mean free paths as a function of kinetic energy in polymeric films determined by means of ESCA," *J. Polym. Sci. Polym. Chem.* **15**, 2843-2867 (1977).
167. P. Chen, K. Gupta, and A. Wells, "Cell movement elicited by epidermal growth factor receptor requires kinase and autophosphorylation but is separable from mitogenesis," *J. Cell Biol.* **214**, 547-555 (1994).
168. R. M. Pruss and H. R. Herschman, "Variants of 3T3 cells lacking mitogenic response to epidermal growth factor," *Proc. Natl. Acad. Sci. USA* **74**, 3918-3921 (1977).
169. M. Yamada, T. Ikeuchi, S. Aimoto, and H. Hatanaka, "PC12h-R cell, a subclone of PC12 cells, shows EGF-induced neuronal differentiation and sustained signaling," *J. Neurosci. Res.* **43**, 355-364 (1996).
170. S. Traverse, K. Seedorf, H. Paterson, C. J. Marshall, P. Cohen, and A. Ullrich, "EGF triggers neuronal differentiation of PC12 cells that overexpress the EGF receptor," *Curr. Biol.* **4**, 694-701 (1994).
171. D. R. McClay, G. M. Wessel, and R. B. Marchase, "Intercellular recognition: Quantitation of initial binding events," *Proc. Natl. Acad. Sci. USA* **78**, 4975-4979 (1981).
172. A. R. Asthagiri, C. M. Nelson, A. F. Horwitz, and D. A. Lauffenburger, "Quantitative relationship among integrin-ligand binding, adhesion, and signaling via focal adhesion kinase and extracellular signal-regulated kinase 2," *J. Biol. Chem.* **274**, 27119-27127 (1999).
173. K.-L. Paul Sung, L. Yang, D. E. Whittemore, Y. Shi, G. Jin, A. H. Hsieh, W. H. Akeson, and L. A. Sung, "The differential adhesion forces of anterior cruciate and medial collateral ligament fibroblasts: Effects of tropomodulin, talin, vinculin, and α-actinin," *Proc. Natl. Acad. Sci. USA* **93**, 9182-9187 (1996).

174. M. M. Lotz, C. A. Burdsal, H. P. Erickson, and D. R. McClay, "Cell adhesion to fibronectin and tenascin: quantitative measurements of initial binding and subsequent strengthening response," *J. Cell Biol.* **109**, 1795-1805 (1989).
175. E. A. Wayner, R. A. Orlando, and D. A. Cheresh, "Integrins $\alpha_V\beta_3$ and $\alpha_V\beta_5$ contribute to cell attachment to vitronectin but differentially distribute on the cell surface," *J. Cell Biol.* **113**, 919-929 (1991).
176. K. Burridge and L. Connell, "Talin: A cytoskeletal component concentrated in adhesion plaques and other sites of actin-membrane interaction," *Cell Motil.* **3**, 405-417 (1983).
177. G. H. Nuckolls, C. E. Turner, and K. Burridge, "Functional studies of the domains of talin," *J. Cell Biol.* **110**, 1635-1644 (1990).
178. M. Dembo, D. C. Torney, K. Saxman, and D. Hammer, "The reaction-limited kinetics of membrane-to-surface adhesion and detachment," *Proc. R. Soc. Lond. B* **234**, 55-83 (1988).
179. M. H. Ginsberg, X. Du, and E. F. Plow, "Inside-out integrin signaling," *Curr. Op. Cell Biol.* **4**, 766-771 (1992).
180. A. Huttenlocher, M. H. Ginsberg, and A. F. Horwitz, "Modulation of cell migration by integrin-mediated cytoskeletal linkages and ligand-binding affinity," *J. Cell Biol.* **134**, 1551-1562 (1996).
181. K. K. Wary, F. Mainiero, S. J. Isakoff, E. E. Marcantonio, and F. G. Giancotti, "The adaptor protein Shc couples a class of integrins to the control of cell cycle progression," *Cell* **87**, 733-743 (1996).
182. K. K. Wary, A. Mariotti, C. Zurzolo, and F. G. Giancotti, "A requirement for caveolin-1 and associated kinase Fyn in integrin signaling and anchorage-dependent cell growth," *Cell* **94**, 625-634 (1998).
183. Y. Wei, X. Yang, Q. Liu, J. Wilkins, and H. Chapman, "A role for caveolin and the urokinase receptor in integrin-mediated adhesion and signaling," *J. Cell Biol.* **144**, 1285-1294 (1999).
184. A. Chilkoti and P. S. Stayton, "Molecular origins of the slow streptavidin-biotin dissociation kinetics," *J. Am. Chem. Soc.* **117**, 10622-10628 (1995).
185. P. C. Weber, D. H. Ohlendorf, J. J. Wendoloski, and F. R. Salemme, "Structural origins of high-affinity biotin binding to streptavidin," *Science* **243**, 85-88 (1989).
186. L. B. Nanney and L. E. King Jr., "Epidermal growth factor and transforming growth factor-α," in *The Molecular and Cellular Biology of Wound Repair*, edited by R. A. F. Clark (Plenum Press, New York, NY, 1996), p. 171-194.
187. P. H. Nelson, T. A. Hatton, and G. C. Rutledge, "General reptation and sclaing of 2d athermal polymers on close-packed lattices," *J. Chem. Phys.* **107**, 1269-1278 (1997).
188. Y. Rouault, "Chain radius dependence on concentration in a 2D living polymer system," *Eur. Phys. J. B* **4**, 321-324 (1998).
189. I. Carmesin and K. Kremer, "Static and dynamic properties of two-dimensional polymer melts," *J. Phys. France* **51**, 915-932 (1990).
190. M. Miyama, Y. Yang, T. Yasuda, T. Okuno, and H. K. Yasuda, "Static and dynamic contant angles of water on polymeric surfaces," *Langmuir* **13**, 5494-5503 (1997).
191. M. X. Xu, W. G. Liu, J. Wang, W. Gao, and K. D. Yao, "Surface rearrangment of vinyl acetate and acrylate terpolymer adhesives investigated by dynamic contact angles," *Polym. Int.* **44**, 421-427 (1997).

192. S. Takahashi, T. Kasemura, and K. Asano, "Surface molecular mobility for copolymers having perfluorooctyl and/or polyether side chains via dynamic contact angle," *Polymer* **38**, 2107-2111 (1997).
193. A. G. Shard, M. C. Davies, S. J. B. Tendler, C. V. Nicholas, M. D. Purbrick, and J. F. Watts, "Surface characterization of methyl methacrylate-poly(ethylene glycol) methacrylate copolymers by secondary ion mass spectrometry and X-ray photoelectron spectroscopy," *Macromol.* **28**, 7855-7859 (1995).
194. A. Hariharan, S. K. Kumar, M. H. Rafailovich, J. Sokolov, X. Zheng, D. Duong, S. A. Schwarz, and T. P. Russell, "The effect of finite film thickness on the surface segregation in symmetric binary polymer mixtures," *J. Chem. Phys.* **99**, 656-663 (1993).
195. P. P. Hong, F. J. Boerio, and S. D. Smith, "Effect of annealing time, film thickness, and molecular weight on surface enrichment in blends of polystyrene and deuterated polystyrene," *Macromol.* **27**, 596-605 (1994).
196. A. Alegria, J. Colmenero, K. L. Ngai, and C. M. Roland, "Observation of the component dynamics in a miscible polymer blend by dielectric and mechanical spectroscopies," *Macromol.* **27**, 4486-4492 (1994).
197. J. D. Ferry, *Viscoelastic Properties of Polymers,* Wiley, New York, NY, 641 pages, (1980).
198. M. Yamaguchi and H. Miyata, "Influence of stereoregularity of polypropylene on miscibility with ethylene-1-hexene copolymer," *Macromol.* **32**, 5911-5916 (1999).
199. C. D. Han and M. S. Jhon, "Correlations of the first normal stress difference with shear stress and of the storage modulus with loss modulus for homopolymers," *J. Appl. Polym. Sci.* **32**, 3809-3840 (1986).
200. C. D. Han and J. Kim, "Rheological technique for determining order-disorder transition of block copolymers," *J Polym. Sci., Polym. Phys.* **25**, 1741-1764 (1987).
201. C. D. Han and J. K. Kim, "Molecular theory for the viscoelasticity of compatible polymer mixtures. 2. Tube model with reptation and constraint release contributions," *Macromol.* **22**, 4292-4302 (1989).
202. P. T. Mather, A. Romo-Uribe, C. D. Han, and S. S. Kim, "Rheo-optical evidence of a flow-induced isotropic-nematic transition in a thermotropic liquid-crystalline polymer," *Macromol.* **30**, 7977-7989 (1997).
203. C. D. Han and S. S. Kim, "Shear-induced isotropic-to-nematic transition in a thermotropic liquid-crystalline polymer," *Macromol.* **28**, 2089-2092 (1995).
204. R. G. Alamo, W. W. Graessley, R. Krishnamoorti, D. J. Lohse, J. D. Londono, L. Mandelkern, and F. C. Stehling, "Small angle neutron scattering investigations of melt miscibility and phase segregation in blends of linear and branched polyethylenes as a function of the branch content," *Macromol.* **30**, 561-566 (1997).
205. J. D. Londono and G. D. Wignall, "The Flory-Huggins interaction parameter in blends of polystyrene and poly(*p*-methylstyrene) by small-angle neutron scattering," *Macromol.* **30**, 3821-3824 (1997).
206. H.-L. Chen, L.-J. Li, and T.-L. Lin, "Formation of segregation morphology in crystalline/amorphous polymer blends: Molecular weight effect," *Macromol.* **31**, 2255-2264 (1998).
207. G. Defieuw, G. Groeninckx, and H. Reynaers, "Diffusion and segregation phenomena in miscible binary polymer blends during crystallization," *Polym. Commun.* **30**, 267-270 (1989).

208. G. Defieuw, G. Groeninckx, and H. Reynaers, "Miscibility and morphology of binary polymer blends of polycaprolactone with solution-chlorinated polyethylene," *Polymer* **30**, 595-603 (1989).
209. S. D. Hudson, D. D. Davis, and A. J. Lovinger, "Semicrystalline morphology of poly(aryl ether ether ketone)/poly(ether imide) blends," *Macromol.* **25**, 1759-1765 (1992).
210. P. P. Huo, P. Cebe, and M. Capel, "Dynamic-mechanical relaxation and X-ray-scattering study of poly(butylene terephthalate) polyarylate blends," *Macromol.* **26**, 4275-4282 (1993).
211. B. S. Hsiao and B. B. Sauer, "Glass transition, crystallization, and morphology relationships in miscible poly(aryl ether ketones) and poly(ether imide) blends," *J. Polym. Sci., Polym. Phys. Ed.* **31**, 901-915 (1993).
212. K. Tanaka, J. S. Yoon, A. Takahara, and T. Kajiyama, "Ultrathinning-Induced Surface Phase-Separation of Polystyrene Poly(Vinyl Methyl-Ether) Blend Film," *Macromolecules* **28**, 934-938 (1995).
213. T. K. Mandal and E. M. Woo, "Phase behaviour and borderline miscibility in blends of syndiotactic polystyrene with poly(vinyl methyl ether)," *Polymer* **40**, 2813-2820 (1999).
214. S. Walheim, M. Boltau, M. Jurgen, G. Krausch, and U. Steiner, "Structure formation via polymer demixing in spin-cast films," *Macromol.* **30**, 4995-5003 (1997).
215. S. Walheim, M. Ramstein, and U. Steiner, "Morphologies in ternary polymer blends after spin-coating," *Langmuir* **15**, 4828-4836 (1999).
216. S. Affrossman, T. Kiff, S. A. O'Neill, R. A. Pethrick, and R. W. Richards, "Topography and surface composition of thin films of blends of poly(methyl methacrylate) and poly(ethylene oxide)," *Macromol.* **32**, 2721-2730 (1999).
217. E. Kumacheva, L. L, M. A. Winnik, D. M. Shinozaki, and P. C. Cheng, "Direct imaging of surface and bulk structures in solvent cast polymer blend films," *Langmuir* **13**, 2483-2489 (1997).
218. N. A. Burnham, O. P. Behrend, F. Oulevey, G. Gremaud, P. J. Gallo, D. Gourdon, E. Dupas, A. J. Kulik, H. M. Pollock, and G. A. D. Briggs, "How does a tip tap?," *Nanotechnology* **8**, 67-75 (1997).
219. X. Chen, S. L. McGurk, M. C. Davies, C. J. Roberts, K. M. Shakesheff, S. J. B. Tendler, P. M. Williams, J. Davies, A. C. Dawkes, and A. Domb, "Chemical and morphological analysis of surface enrichment in a biodegradable polymer blend by phase-detection imaging atomic force microscopy," *Macromol.* **31**, 2278-2283 (1998).
220. S. J. T. Van Noort, J. O. Van der Werf, B. G. De Grooth, N. F. Van Hulst, and J. Greve, "Height anomalies in tapping mode atomic force microscopy in air caused by adhesion," *Ultramicroscopy* **69**, 117-127 (1997).
221. D. Krüger, B. Anczykowski, and H. Fuchs, "GET THIS," *Ann. Phys.* **6**, 341-??? (1997).
222. S. N. Magonov, V. Elings, and M. H. Whangbo, "Phase imaging and stiffness in tapping-mode atomic force microscopy," *Surf. Sci.* **375**, L385-L391 (1997).
223. I. Schmitz, M. Schreiner, G. Friedbacher, and M. Grasserbauer, "Phase imaging as an extension to tapping mode AFM for the identification of material properties on humidity-sensitive surfaces," *Appl. Surf. Sci.* **115**, 190-198 (1997).
224. A. Tamayo and R. Garcia, "Deformation, contact time, and phase contrast in tapping mode scanning force microscopy," *Langmuir* **12**, 4430-4435 (1996).
225. T. Kajiyama, K. Tanaka, I. Ohki, S. R. Ge, J. S. Yoon, and A. Takahara, "Imaging of dynamic viscoelastic properties of a phase-separated polymer surface by forced oscillation atomic force microscopy," *Macromol.* **27**, 7932-7934 (1994).

226. T. Kajiyama, I. Ohki, K. Tanaka, S. R. Ge, and A. Takahara, "Direct observation of surface morphology and surface viscoelastic properties of polymeric solids based on scanning force microscopy," *Proc. Jpn. Acad. Ser. B: Phys. Biol. Sci.* **71**, 75-80 (1995).
227. R. Viswanathan, J. Tian, and D. W. M. Marr, "Morphology characterization in multicomponent macromolecular systems using scanning probe phase microscopy," *Langmuir* **13**, 1840-1843 (1997).
228. P. Leclère, R. Lazzaroni, J. L. Brédas, J. M. Yu, P. Dubois, and R. Jérôme, "Microdomain morphology analysis of block copolymers by atomic force microscopy with phase detection imaging," *Langmuir* **12**, 4317-4320 (1996).
229. S. O. Akari, E. W. Van der Vegte, P. C. M. Grim, G. F. Belder, V. Koutsos, G. Tenbrinke, and G. Hadziioannou, "Imaging of single polymer chains based on their elasticity," *Appl. Phys. Lett.* **65**, 1915-1917 (1994).
230. B. Keita, L. Nadjo, E. Gachard, and H. Remita, "Phase imaging in tapping mode AFM: discrimination between metal clusters and the surfactant polymer," *New J. Chem.* **21**, 851-855 (1997).
231. J. F. Hester, P. Banerjee, and A. M. Mayes, "Preparation of protein-resistant surfaces on poly(vinylidene fluoride) membranes via surface segregation," *Macromol.* **32**, 1643-1650 (1999).
232. R. S. Cargill II, K. C. Dee, and S. Malcolm, "An assessment of the strength of NG108-15 cell adhesion to chemically modified surfaces," *Biomaterials* **20**, 2417-2425 (1999).
233. J. S. Burmeister, J. D. Vrany, W. M. Reichert, and G. A. Truskey, "Effect of fibronectin amount and conformation on the strength of endotheial cell adhesion to HEMA/EMA copolymers," *J. Biomed. Mater. Res.* **30**, 13-22 (1996).
234. S. R. Heidemann, S. Kaech, R. E. Buxbaum, and A. Matus, "Direct observations of the mechanical behaviors of the cytoskeleton in libing fibroblasts," *J. Cell Biol.* **145**, 109-122 (1999).
235. N. Wang, J. P. Butler, and D. E. Ingber, "Mechanotransduction across the cell surface and through the cytoskeleton," *Science* **260**, 1124-1127 (1993).
236. M. P. Sheetz, D. P. Felsenfeld, and C. G. Galbraith, "Cell migration: regulation of force on extracellular matrix-integrin complexes," *Trends in Cell Biol.* **8**, 51-53 (1998).
237. Y. C. Fung, *Biomechanics: Mechanical Properties of Living Tissues,* Springer-Verlag, New York, NYpages, (1988).
238. D. W. Thompson, *On Growth and Form,* Cambridge University Press, New York, NYpages, (1977).
239. E. S. Russell, *Form and Function,* University of Chicago Press, Chicago, ILpages, (1982).
240. S. P. Palacek, A. Huttenlocher, A. F. Horwitz, and D. A. Lauffenburger, "Physical and biochemical regualtion of integrin release during rear detachment of migrating cells," *J. Cell Sci.* **111**, 929-940 (1998).
241. A. Huttenlocher, S. P. Palacek, Q. Lu, W. Zhang, R. L. Mellgren, D. A. Lauffenburger, M. H. Ginsberg, and A. F. Horwitz, "Regulation of cell migration by the calcium-dependent protease calpain," *J. Biol. Chem.* **272**, 32719-32722 (1997).
242. M. C. Beckerle, K. Burridge, G. N. DeMartino, and D. E. Croall, "Colocalization of calcium-dependent protease II and one of its substates at sites of cells adhesion," *Cell* **51**, 569-577 (1987).
243. P. Gramain and Y. Frere, "Preparation of monomethoxy-poly(ethylene oxide) acrylate and methacrylate and its polymerization: self-gelling polymers," *Polymer Commun.* **27**, 16-18 (1986).

244. Y. Frere, Y. Guilbert, and P. Gramain, "Gel effect and subsequent degradation process in radical polymerization of poly(ethylene oxide) acrylate and methacrylate macromers," *New Polym. Mater.* **3**, 175-186 (1992).
245. K. Ito, H. Tsuchida, A. Hayashi, T. Kitano, E. Yamada, and T. Matsumoto, "Reactivity of poly(ethylene oxide) macomonomers in radical copolymerization," *Polymer J.* **17**, 827-839 (1985).
246. G. G. Odian, *Principles of Polymerization,* Wiley, New York, NY, 768 pages, (1991).
247. A. J. Paine, "Dispersion polymerization of styrene in polar solvents. I. Grafting mechanism of stabilization by hydroxypropyl cellulose," *J. Coll. Interf. Sci.* **138**, 157-169 (1990).

15 Biographical Note

Darrell J. Irvine

Education

Massachusetts Institute of Technology Cambridge, MA
PhD Candidate; Thesis: "Spatially Controlled Presentation of Biochemical Ligands on Biomaterial Surfaces Using Comb Polymers."

University of Pittsburgh Pittsburgh, PA
B.S. Engineering Physics from the School of Engineering May 1995.
B.Phil. Engineering Physics from the Honors College, May 1995.

Awards

Runyon-Winchell Postdoctoral Fellowship from the Cancer Research Fund of the Damon Runyon-Walter Winchell Foundation, 2000
Finalist, American Physical Society Padden Award for Graduate Student Research, 1999
Winner, Graduate student "best in show", MIT Program in Polymer Science and Technology/Amoco Poster Contest, 1998
National Science Foundation Graduate Fellow (1995 - 1998)

Research Experience

MIT Department of Materials Science and Engineering and Center for Biomedical Engineering Cambridge, MA
Advisors: Anne M. Mayes and Linda G. Griffith
Explored the use of polymer architecture and surface segregation to modify the surface of materials for use in biomedical applications. The use of star polymers for surface modification was explored theoretically using a self-consistent field theory and experimentally using neutron reflectivity. A design strategy was developed for creating protein-resistant, cell-signaling surfaces on bulk materials using comb polymer segregation. This paradigm was reduced to practice for biodegradable matrix materials, currently used for tissue engineering scaffolds. Applications of comb copolymers as films or as latex microsphere coatings were explored as cell-signaling surfaces.
(September 1995 - present)

University of Pittsburgh Department of Materials Science and Engineering Pittsburgh, PA
Advisor: Anna C. Balazs
Applied Monte Carlo simulations and Self-Consistent Mean Field Theory to problems in the equilibrium

structure of polymer systems. Studies included the structure of random copolymers at the interface between immiscible homopolymers, the aggregation behavior of amphiphilic comb copolymers in solution, and the segregation of linear and comb copolymers to the interface between immiscible phases.
(May 1993 - September 1995)

Teaching Experience

Co-developed and taught undergraduate course "Biomedical Applications of Materials," Fall – Spring 1998, Massachusetts Institute of Technology.

Accepted to NSF Engineering Education Scholars Program April 1998. Attended week-long training session for future faculty at the University of Wisconsin-Madison, July 1998.

Guest lecturer for graduate course "Statistical Mechanics of Polymers", Spring 1998, Massachusetts Institute of Technology.

Undergraduate tutor in Materials Science and Engineering, September 1994-March 1995, University of Pittsburgh.

Professional Activities and Memberships

American Physical Society, Division of High Polymer Physics, member.
National Society for Biomaterials, member.
American Institute of Chemical Engineers, member.
Materials Research Society, member.
Chair, Symposium on Soft Biomaterials Poster Session, Spring 2000 MRS National Meeting.

Invited Presentations

"Spatially Controlled Presentation of Biochemical Ligands on Biomaterial Surfaces Using Comb Polymers," D.J. Irvine, L.Y. Koo, A.M. Mayes, and L.G. Griffith, Mater. Res. Soc. National Meeting, San Francisco, CA, April 2000.

"Controlling Ligand Presentation to Cells at Surfaces Using Comb Polymers," D.J. Irvine, A.M. Mayes, and L.G. Griffith, invited seminar, Nat. Inst. Stand. Tech., Gaithersburg, MD, November 1999.

"Design of Cell-Signaling Surfaces Using Comb Copolymers," D.J. Irvine, A.M. Mayes, and L.G. Griffith, invited seminar, University of Washington, Seattle, WA, April 1999.

"Design of Cell-Signaling Surfaces Using Comb Copolymers," D.J. Irvine, A.M. Mayes, and L.G. Griffith, invited seminar, Massachusetts Institute of Technology, Cambridge, MA, March 1999.

"Design of Cell-Signaling Surfaces Using Comb Copolymers," D.J. Irvine, A.M. Mayes, and L.G. Griffith, invited seminar, University of California, Irvine, CA, February 1999.

"Design of Cell-Signaling Surfaces Using Comb Copolymers," D.J. Irvine, A.M. Mayes, and L.G. Griffith, invited seminar, Stanford University, Stanford, CA, February 1999.

"Design of Cell-Signaling Surfaces Using Comb Copolymers," D.J. Irvine, A.M. Mayes, and L.G. Griffith, invited seminar, Northwestern University, Evanston, IL, February 1999.

"Design of Polymeric Cell-Signaling Surfaces and Their Application as Biomaterials." D. J. Irvine, A. M. Mayes, and L. G. Griffith, Amer. Chem. Soc. National Meeting, Boston, MA, August 1998.[2]

"Design of Tailored Polymeric Materials for Cell Biology and Tissue Engineering," D.J. Irvine, A.M. Mayes, and L.G. Griffith, 3rd Annual User Group Meeting, Los Alamos Neutron Science Center, Los Alamos, NM, August 1998.

"Control of Cell Behavior Via Polymer Surface Engineering." D. J. Irvine, A. M. Mayes, and L. G. Griffith, seminar for the MIT Program in Polymer Science, Cambridge MA, December 1997.

"Controlled Presentation of Clustered Ligands on Protein-Resistant Surfaces." D. J. Irvine, A. M. Mayes, and L. G. Griffith, 1st International Symposium on Ordered Proteins at Interfaces, Univ. of Washington, Seattle, WA, August 1997.

Publications

"Polymer Latexes for Cell-Resistant or Cell-Interactive Surfaces," P. Banerjee, D.J. Irvine, A.M. Mayes, and L.G. Griffith, *J. Biomed. Mater. Res.*, **50**(3) 331-339 (2000).

"Tailored Polymer Surfaces for Controlled Cell Interactions," A.M. Mayes, D.J. Irvine, and L.G. Griffith, *Mater. Res. Soc. Symp. Proc.*, **530**, 73-84 (1998).

"Comparison of Tethered Star and Linear Poly(Ethylene Oxide) for Control of Biomaterials Surface Properties," D.J. Irvine, A.M. Mayes, S.K. Satija, J.G. Barker, S.J. Sofia-Allgor, and L.G. Griffith, *Journal of Biomedical Materials Research*, **40**(3) 498-509 (1998).

"Design of Biocompatible Surfaces," A.M. Mayes, D.G. Walton, D.J. Irvine, and L. Griffith, *Amer. Chem. Soc. Proc. Div. Mat. Sci. Eng.*, **75**, 78-79 (1996).

"Self-Consistent Field Analysis of Grafted Star Polymers," D.J. Irvine, A.M. Mayes, and L. Griffith-Cima, *Macromolecules*, **29**(18) 6037-6043 (1996).

"Computer Simulations of Self-Assembling Comb Copolymers," D.J. Irvine, D. Gersappe, and A.C. Balazs, *Langmuir*, **11**(10) 3848-3855 (1995).

"The Use of Graft Copolymers to Bind Immiscible Blends," D. Gersappe, D. Irvine, A.C. Balazs, Y. Liu, J. Sokolov, M. Rafailovich, S. Schwarz, and D.G. Peiffer, *Science*, **265**(5175) 1072-1074 (1994).

"Contrasting the Compatibilizing Activity of Comb and Linear Copolymers," D. Gersappe, P.K. Harm, D. Irvine, and A.C. Balazs, *Macromolecules*, **27**(3) 720-724 (1994).

Patents

"Comb Polymers for Controlled Cell-Surface Interactions," A.M. Mayes, L.G. Griffith, and D.J. Irvine, U.S. Provisional Patent filed April 13, 1998.